University of Modena and Reggio Emilia

Department of Engineering "Enzo Ferrari"

International Doctorate
Information and Communication Technologies

XXXV Cycle

Optoelectronics Methods and Instrumentation for Human Vision Science

---

Tutor:
Prof. Luigi Rovati

PhD Thesis of:
Giovanni Gibertoni

Doctorate Course Coordinator:
Prof. Sonia Bergamaschi

Modena, 2023

Abstract

Recent advancements in biomedical optics and engineering have revolutionized the visualization of the human body and opened up new avenues for analyzing its physiological and pathological features. Innovative photonics techniques proved to be of crucial importance for the diagnosis and treatment of different visual impairments. Despite these advances, there are still many fields in which biomedical optics research plays a critical role, with ophthalmology being one of them. In fact, as recent statistics highlights, the prevalence of eye diseases, including *Diabetic Retinopathy* (DR), A*ge-related Macular Degeneration* (AMD), and *glaucoma* is expected to double. Early diagnosis of these conditions is essential for mitigating or slowing their progression, thereby preventing further damage to the eyes or vision loss. As a result, there is an increasing demand for biomedical instruments that can detect these diseases in their initial phase.

As demonstrated by recent findings, the integration of electronics, optics, and artificial intelligence is leading to groundbreaking discoveries in vital areas of medicine. However, to fully realize the potential of these technologies, new methods, and techniques are still required to make them more accessible, user-friendly, and accurate. Keeping this in mind, the objective of this study is to explore innovative and easily accessible ophthalmic techniques that could be utilized in clinical practice to detect common visual impairments at an early stage.

One of the focal points of this research endeavor pertains to the development of methodologies and instruments for studying image-forming and non-image-forming visual processes that can be leveraged to investigate and comprehensively assess various critical brain-stem functions. Among the diverse range of techniques, the *Pupillary Light Reflex* (PLR) proves to be a highly compelling modality for probing the human visual-nervous system, as it encompasses numerous sensory and motor functions of the eye. Additionally, this investigation will concentrate on the photoreceptor-mediated signal processing pathways, such as rods, cones, and *intrinsically photosensitive retinal ganglion cells* (ipRGCs).

A second topic of the work presented concerned the investigation of another diagnosis technique regarding the analysis of the *Anterior Chamber Angle* (ACA) for *Primary Angle Closure Glaucoma* (PACG) prevention. The findings show that the Van Herick procedure is a very promising approach to accessing the information on the preliminary state of advancement of this common disease. In this research, a newly designed instrument is proposed to perform this technique in an automatic and objective manner, thereby utilizing a combination of modern and compact photonics components and *Artificial Intelligence* (AI) classification techniques.

Finally, the experimental research activities presented in the last part of this work involved a series of in-vivo experiments aimed at assessing the performance and real-world applicability of the proposed systems. These endeavors, together with future efforts, hold significant potential to drive progress and innovation in the field of visual research. The findings from this study will hopefully contribute to enhancing access to more reliable and accurate ophthalmic devices for everyday human eye healthcare.

Contents

Introduction **1**

I State of The Art 5

1 Human Visual System 7
1.1 Anatomy of the eye . . . 7
1.1.1 The Retina . . . 8
1.1.2 Photoreceptors . . . 10
1.2 Pupillary Light Reflex . . . 14
1.2.1 The iris muscle plant . . . 14
1.2.2 Accomodation . . . 16
1.2.3 Rod, Cone, and Melanopsin contributions to human pupil . . . 16
1.3 Model For The Human Pupillary . . . 17
1.3.1 Introduction . . . 17
1.3.2 Muscle Plant Model . . . 18

2 Color Vision 21
2.1 Basics of Colorimetry . . . 21
2.1.1 Color Matching Functions . . . 21
2.1.2 XYZ and RGB Color Spaces . . . 22
2.2 Silent Substitution Technique . . . 24
2.2.1 Silent substitution methodology . . . 25
2.2.2 System Optimization . . . 27

3 Optical Notions 29
3.1 Optical Elements . . . 29
3.1.1 Lenses . . . 29
3.1.2 Other optical elements . . . 34
3.2 Basics of Light Systems . . . 35
3.2.1 Types of Illumination Source . . . 36
3.2.2 Photometry and radiometry . . . 37
3.3 Viewing Geometry . . . 38
3.3.1 Maxwellian View . . . 40
3.3.2 Retinal illuminance . . . 40

4 Opthalmic Technologies **43**
4.1 Visual-Based Techniques . . . 43
4.1.1 Expert Systems . . . 44
4.1.2 Machine Learning . . . 45
4.2 Pupillometry . . . 46
4.2.1 Measurement of the human pupil . . . 47
4.3 Primary Angle Closure Glaucoma . . . 52
4.3.1 Prevention . . . 53
4.3.2 Van Herick Technique . . . 54

II Materials and Methods **58**

5 PLR Measurement Intrumentation **60**
5.1 Related Works . . . 61
5.1.1 Reference Techniques . . . 61
5.1.2 Pupil Tracking . . . 62
5.2 System Design . . . 64
5.2.1 Light Sources . . . 64
5.2.2 Optical Elements . . . 69
5.2.3 Acquisition Device . . . 72
5.2.4 Hardware . . . 74
5.2.5 Software . . . 78
5.2.6 Mounting and Component Housing . . . 82
5.3 Realized Prototypes . . . 82
5.3.1 Maxwellian Monocular Pupillometer . . . 83
5.3.2 Maxwellian Binocular Pupillometer . . . 84
5.4 System Performance . . . 88
5.4.1 Exit Pupil Spot Size Measurement . . . 88
5.4.2 Image acquisition: Resolution . . . 90
5.4.3 Light Sources Characterization . . . 91

6 Automatic ACA Measurement Instrument **97**
6.1 Related Works - Van Herick Grading . . . 97
6.2 System Design . . . 98
6.2.1 System Optical Diagram . . . 98
6.2.2 General Description . . . 98
6.2.3 Realized Prototype . . . 101
6.2.4 Software . . . 103
6.2.5 Safety Considerations . . . 105

III Results and Discussion **108**

7 Pupillometry **110**
7.1 Modeling of the oculomotor system . . . 110
7.1.1 Instrument . . . 110
7.1.2 Methods . . . 111

7.1.3 Results and Discussion . . . 113
7.1.4 Conclusions . . . 115
7.2 Silent Substitution experiments . . . 115
7.2.1 Experiment 1: PLR Induced Response of M-Cones and ipRGCs . . . 116
7.2.2 Experiment 2: Comparing ERG and PLR . . . 120

8 Vision-Based Image Classification **127**
8.1 Pupil Position Classification . . . 127
8.1.1 PopEYE Dataset . . . 128
8.1.2 Vision-based Image Selection . . . 130
8.1.3 Results . . . 134
8.1.4 Conclusion . . . 139
8.2 Image Classification for ACA Objective Measure . . . 140
8.2.1 Experimental Setup and Research Goals . . . 140
8.2.2 ML-based classification Technique . . . 141
8.2.3 Neural Network Evaluation . . . 144
8.2.4 Test results . . . 146
8.2.5 Conclusions and Future Work . . . 150
8.3 Preliminary Experiment for Automatic Detection of the Van Herick Grade . . . 152
8.3.1 Goals . . . 152
8.3.2 Methods . . . 152
8.3.3 Results . . . 154
8.3.4 Discussion and Conclusion . . . 155

Conclusion **157**

Appendices **161**
Output luminance - Measurement . . . 162

Publications List **169**

Bibliography **169**

List of Tables

3.1 Unit of Measures for common Radiometric and Photometric quantities . . . 37

4.1 Van Herick grading scheme. . . . 56

5.1 Summary table of methods available for eye status classification. . . . 64
5.2 Specifications of selected Roithner LEDs used for eye stimulation . . . 65
5.3 45° AOI, 35.0mm Square, Hot Mirror Specifications . . . 71
5.4 Camera and Lens Specifications . . . 74
5.5 CORE DUE Specifications . . . 76
5.6 LEDs Measured Spectral Output . . . 92
5.7 Safety exposure limits for maximum optical power. . . . 95

6.1 Basler Camera Specification . . . 100
6.2 Characteristics of the LEDs and the power emitted through the projector optics . . . 105
6.3 Measurement of the emission solid angle of a Texas Instrument DLP2010 device . . . 106

7.1 Luminous flux levels of the baseline and peak for the three experiments. . . . 112
7.2 Fitted parameters from the model outputs . . . 114
7.3 Sum squared relative errors of the model fitting for the three experiments. . . . 115
7.4 Experiment's equivalent $\alpha - opic$ illuminance specifications . . . 117
7.5 Parameters Constraints of the double-term exponential fitting function. . . . 119
7.6 Fitted parameters. Results of the PLRs analysis . . . 119
7.7 Experiments specifications for silent stimulations of L and S cones . . . 123
7.8 Average ERGs response statistics . . . 123
7.9 Average PLR waveforms values for 200 ms flashes at 40% and 70% Michelson Contrast . . . 126

8.1 *PopEYE* dataset composition across the six different annotated classes. . . . 130
8.2 Train and test splitting used in *PopEYE* dataset for both ML and DL approaches. . . . 134
8.3 Hardware specification of the devices used to compute the SFPT across all experiments. . . . 135
8.4 Accuracy and timing performance of the ES algorithm over the Desktop Computer . . . 135
8.5 Accuracy and speed performance obtained with Neural Network classifiers . . . 138
8.6 Classification accuracy and speed performance comparison across the three investigated approaches. . . . 138
8.7 Classification Method Comparison . . . 142
8.8 Data Augmentation Setup Parameters. . . . 144
8.9 Train Data Set Properties. . . . 144
8.10 CNN training settings. . . . 145
8.11 New dataset properties. . . . 149

8.12 Mean and standard deviation of the error E between the limbus and the light line position for different iris pigmentation. 150
8.13 Enrolled subjects data. 153
8.14 Number of images collected for each VHG. 153
8.15 Dataset used for the training and validation of the network. 154

List of Figures

1.1 Schematic diagram of the human eye . . . 8
1.2 Distribution and arrangement of the photoreceptors in the retina . . . 9
1.3 Retinal distributions of eye's photoreceptors around the horizontal optical axis. . . . 10
1.4 Photoreceptor's absorptions and vision regime of the human eye . . . 11
1.5 Pupillary Light Reflex pathways . . . 15
1.6 Pupil iris muscle plant . . . 15
1.7 Rods, cones, melanopsin contribution to PLR . . . 17
1.8 Human Pupillary Muscle Plant . . . 19

2.1 Color Matching Functions . . . 22
2.2 CIE RGB Color Space . . . 24
2.3 CIE luminous efficiency and photoreceptor sensitivities . . . 25

3.1 Thin Lens ray tracing diagram . . . 29
3.2 Thick Lens . . . 30
3.3 Spherical Aberrations . . . 32
3.4 Chromatic Aberrations . . . 32
3.5 Astigmatism . . . 33
3.6 Coma aberration . . . 33
3.7 Field curvature . . . 34
3.8 Typical Distortion on a square images . . . 34
3.9 Emission spectra of different light sources . . . 36
3.10 The Newtonian-view . . . 39
3.11 Ganzfeld-View . . . 39
3.12 Principle of Maxwellian view . . . 41
3.13 Maxwellian Illumination . . . 41

4.1 Artificial Intelligence Subcategories . . . 44
4.2 Expert Systems . . . 45
4.3 Four steps in the analysis of pupil shape . . . 48
4.4 Influence of corneal geometry on pupil estimation . . . 49
4.5 Ellipse geometry . . . 51
4.6 Radius Equation for an Ellipse . . . 52
4.7 Primary Angle Closure Glaucoma Effect . . . 53
4.8 Goldmann Goniolens . . . 53
4.9 Optical scheme used for Van Herick manoeuvre . . . 54
4.10 The Van Herick method to evaluate ACA . . . 55

5.1 NeurOptics Hand-Held Pupillometer . . . 61
5.2 Hitomiru®binocular pupillometer . . . 62
5.3 Optical diagram of the Maxwellian-View monocular pupillometer . . . 65
5.4 Infrared LEDs placement on a printed circuit board. . . . 66
5.5 Optical fiber emission angle . . . 67
5.6 Illumination Assembly on SolidWorks . . . 68
5.7 Design of the fiber coupling . . . 68
5.8 Optical fiber NA . . . 69
5.9 Effect of non-infinitesimal point source dimension . . . 70
5.10 Correct layout of collimator . . . 70
5.11 45° Hot Mirror . . . 71
5.12 3D view of the board level CMOS camera . . . 73
5.13 Pupillometer control block diagram . . . 74
5.14 Core Due Microcontroller Board. . . . 75
5.15 CAT4238 typical application circuit . . . 77
5.16 LED Driving Schematics . . . 78
5.17 Automatic pupil recognition steps . . . 80
5.18 Maxwellian-View monocular pupillometer instrument . . . 83
5.19 Binocular pupillometer's different parts . . . 85
5.20 Optical diagram of the binocular pupillometer design . . . 86
5.21 Technical Characteristics of Optic Prism . . . 86
5.22 Dual pupil acquisition with a single camera. . . . 87
5.23 3D rendering of the realized binocular pupillometer device . . . 87
5.24 (a) Spot size image on a CMOS sensor. (b) Plot of the spot size luminosity horizontal profile at the center. . . . 89
5.25 Spatial resolution reference measure . . . 90
5.26 Graphical measure of the paper graph square size acquired on the camera . . . 90
5.27 Normalized output spectra of the selected LEDs . . . 92
5.28 Source output spectral power analysis. . . . 93

6.1 Optical Scheme of the modified ACA measurement setup . . . 99
6.2 Basler Camera Dart Series - 3D view . . . 100
6.3 Working principle of a DMD-based light projector . . . 101
6.4 The DLP 2010 development board by Texas Instrument . . . 102
6.5 Realized Instrument for Automatic Anterior Chamber Angle Width. . . . 102
6.6 Front window aperture on the component housing . . . 103
6.7 ACA User Interface . . . 104
6.8 DLP Field of View Projection . . . 107

7.1 The VR pupillometer prototype. . . . 111
7.2 Schematic diagram of autonomic nervous activities in response to a short light flash . . . 111
7.3 Temporal diagram for the experiment to model pupil muscle plant . . . 112
7.4 Boxcar averaged pupil response from a 250ms green flashes among two subjects . . . 113
7.5 Experimental temporal phases for 1-second flash response silent stimulations . . . 116
7.6 Spectral distribution of two colors used for the silent stimulation od ipRGCs and M-Cones 117
7.7 Average pupil light response to ipRGC and M-cones silent stimulation . . . 118
7.8 Pupil recovery phase after ipRGC and M-cones silent stimulation . . . 119

7.9 Experimental temporal phases for testing silent cone responses to 200ms light flashes . . . 122
7.10 Spectral distribution of light stimuli used for the silent substitution for L and S cone stimulations . . . 124
7.11 ERGs electrical response to L and S cones silent stimulation . . . 125
7.12 Normalized and averaged PLR response among the three subjects for 200 ms flash-driven response . . . 125

8.1 Example of images collected from different subjects of the *PopEYE* dataset . . . 129
8.2 Visual aids used for the data annotation phase . . . 130
8.3 General overview of the proposed analysis. . . . 131
8.4 Flowchart of the image processing steps performed by the developed ES algorithm . . . 132
8.5 Classification accuracy of the three Machine Learning-based classifiers . . . 136
8.6 Comparison of the average (SFPT) plus the prediction time, of the three ML classifiers running on a Desktop computer . . . 137
8.7 FOM heatmap for different values of A and SFPT. Red stars * indicates the score of selected approaches from each category. . . . 139
8.8 Timing performance comparison across the different platforms . . . 139
8.9 Example of a set of images acquired during a scan. . . . 140
8.10 The implemented AlexNet structure. . . . 143
8.11 The implemented VGG-16 structure. . . . 143
8.12 Precision and Recall: (a) AlexNet and (b)VGG-16 . . . 146
8.13 Typical reference image used to estimate the limbus position . . . 148
8.14 Typical *center* image used to estimate the light line position . . . 148
8.15 Histogram of occurrences of the error between the limbus and line position . . . 149
8.16 Histogram of occurrences of the error between the limbus and line position in pixel for the new dataset . . . 149
8.17 Histograms of occurrences of the error E between the limbus and the light line position for different eye pigmentation . . . 151
8.18 Histogram of the mean intensity of the light line for each different eye color. . . . 151
8.19 VHG Image Examples . . . 153
8.20 Accuracy VHD CNN . . . 155
8.21 Confusion matrix for the GoogLeNet (a), ResNet (b), and AlexNet (c). . . . 156

Introduction

The number of people who are visually impaired is rapidly increasing due to the growth of the aging population. According to the *World Health Organization*, there are 285 million people worldwide with visual impairment, with 39 million classified as blind. The majority of visually impaired individuals are over 50 years old, and the top causes of visual impairment are uncorrected refractive errors and cataracts, whereas cataracts and glaucoma are the leading causes of preventable blindness. The distribution of visually impaired people is uneven and is correlated to the distribution of financial resources, with higher prevalence in China, India, South-Eastern Asia, and the Eastern-Mediterranean area. These regions have low socio-economic development, limited access to basic ophthalmic care, and a genetic predisposition also plays a key role in the development of ocular diseases.

The visual impairment trends in most western developed nations show that high investments in healthcare usually correspond to a lower prevalence of visual impairment and higher life expectancy. In these countries, visual impairments primarily originate from eye pathologies such as *age-related macular degeneration*, *glaucoma* and *diabetic retinopathy*, while more typical impairments such crystalline lens opacities or refractive errors are not the main sources of eye diseases. Such common diseases can be corrected and treated through non-invasive and routine medical procedures, therefore access to basic eye care can reduce the number of visually impaired individuals in the world.

According to the *National Eye Institute*, the number of Americans suffering from severe eye pathologies has limited treatment choices and is anticipated to double by 2050, despite the fact that the advancement of these ocular diseases frequently results in blindness. Effective and accessible treatments are urgently needed to address this impending public health issue. Clinical procedures and medicines can only slow down the rate of vision loss, and in the best cases, eyesight loss can be stopped, but not restored. It is important to get a comprehensive dilated eye exam at least once a year to monitor and detect ocular pathologies early, but usually, the diagnosis relies on a qualitative and subjective evaluation by the ophthalmologist. Therefore, there is an increasing need for biomedical instrumentation that can detect these diseases at an early stage using optoelectronic instruments as well as high repeatability and reliability methodologies. The cost of preventing visual impairment worldwide may be high, but the improvements in terms of life quality and cost reduction for the healthcare system justify an increase in medical research investment. People affected by avoidable causes of visual impairment and those who will develop ocular diseases in the future would benefit from such change and could have an enormous advantage in fighting and defeating visual impairment and blindness in the world. As a result of the development of new methods and technology, the field of vision research has experienced considerable breakthroughs in recent years.

Overall, this manuscript explores the utilization of techniques for investigating the visual system and its associated disorders. The research presented here focuses on the design, fabrication, and characterization of optoelectronic devices, as well as the implementation of these devices for in-vivo and in-vitro studies and experiments. As previously discussed, ophthalmic instrumentation plays a critical role in the diagnosing of eye diseases, therefore, this thesis focuses on providing a useful understanding for the devel-

opment of optoelectronic devices that aim at improving the diagnostic capabilities of existing techniques.

In this work, the two main focuses concern the *Pupillary Light Reflex* (PLR) analysis and the assessment of the *Anterior Chamber Angle* (ACA) for *Primary Angle Closure Glaucoma* (PACG) by using the Van Herick technique.

On one hand, the pupillary light reflex proved to play an essential aspect in the visual system, and its measurement can provide valuable information about the functioning of the eyes and brain. Therefore, the instrumentation developed and presented in this work purpose to enhance the accuracy and reliability of PLR measurements, allowing access to a more accurate and deep understanding of the human visual system.

PACG on the other hand is a severe eye disease characterized by the closure of the angle where the iris meets the cornea, which can lead to increased intra-ocular pressure and damage to the optic nerve. Early detection and diagnosis of PACG are crucial for preventing vision loss, and the Van Herick technique is a valuable candidate for early estimation and detection of patients at risk of such disease. The instrumentation developed in this thesis aims to make this technology more accessible to non-expert users, thus reducing the need for expert ophthalmologists and optometrists.

The scope of this thesis work is therefore to present a useful breakdown of optoelectronic methods and instrumentation for vision research. moreover, the work presented focuses on the design, realization, and characterization of specific optoelectronic devices, as well as the practical evaluation of these appliances for in vivo and in vitro experiments. Starting from a general knowledge of the human visual system, the goal is to deliver an advanced understanding of the engineering and development of new diagnostic and therapeutic tools and instruments with the intention to make the prevention of common vision disorders more accessible.

Thesis Outline

This thesis is organized as follows:

Part I - State of The Art In the first part of this manuscript, an overview of all the notions and theoretical aspects faced during the research is presented. A general description of the human visual system will be presented, starting with a description of the anatomy of the eye, as well as the mechanism and the photosensitive cells that allow us to sense and process visual information. Moreover, a general description of the main functions of the human visual system is described, thus including the pupillary light reflex which is a simple physiological response of the iris muscle plant to light changes, but as it is mediated by sympathetic and parasympathetic nervous systems it measurement can provide valuable information about the functioning of the eye and the brain. Additionally, a comprehensive overview of the fundamentals of color vision, including colorimetry and current standards for representing perceived colors, is provided. This forms the foundation for modern techniques used to investigate the individual contribution of photosensitive cells to visual perception, commonly referred to as the *Silent Substitution* technique. As will be presented, this technique could be exploited to extract additional information about the contribution of the ipRGCs to several eyes diseases, e.g. retinitis pigmentosa or glaucoma or to simply study them from a scientific viewpoint [1]. Currently, the knowledge about ipRGCs is poor, since they have been studied for relatively few decades and their contribution to the PLR is not yet satisfactorily understood [2], being this still a hot research field [3].

Afterward, starting from the basic concepts of optics, which include optical elements such as thick lenses, and mirrors prisms, the fundamentals of light systems, thus including the most common viewing geometries used in ophthalmic instrumentation, will be discussed. At the conclusion of the first theoretical section, an examination of the various cutting-edge technologies that are currently the focus of research

in the field of ophthalmic instrumentation will be conducted. Therefore, visual-based approaches, that can be used accordingly with *Artificial Intelligence* (AI) applications to enhance the diagnostic capabilities and improve the accuracy of these measurements will be covered. Moreover, a metrological approach to pupillometry and the assessment of angle closure glaucoma (PACG) with reference techniques will be discussed as well. The goal of this chapter is to present a complete review of the current state of the art in these specific techniques, highlighting the most recent advances as well as the field's current concerns. This will lay the groundwork for the reader to fully comprehend the choices and motives of the next sections of this thesis.

Part II - Materials and Methods In this second part, a technical approach to the realization of two specific ophthalmic instruments will be covered. As lately presented, the first Chapter entitled "PLR Measurement Intrumentation" foresees our technical approach toward the realization of a Maxwellian-View-based pupillometer. The second Chapter instead, i.e. "6", concerns our proposal for the realization of an objective and automated approach for the measurement of Anterior Chamber Angle (ACA) with the aforementioned Van Herick technique. The goal of this research is to provide precise and dependable measuring techniques for pupillometry and ACA estimates, which are critical diagnostic tools in the field of ophthalmology.

A review of commercially and scientifically available pupillometry equipment developed by previous researchers will be conducted and followed by a detailed examination of the main technical elements, optical components, and requirements at the base of any pupillometry system. The steps presented will include some overview of the system's optics, such as lenses and camera, hardware, such as LED driving techniques, and software, thus including data elaboration and innovative analysis methodologies.

In the last Chapter, a full discussion of the details, components, and design choices of our approach toward a fully automated ACA measurement system will be discussed as well. Following the same structure presented for the pupillometry device, some recently developed and commercially available optoelectronics components, such as a compact *digital light projector*, and their working principle will be examined. In fact, these technologies can be used to replace traditional components, thus enabling superior performances and modularity. Moreover, the importance to design easy-to-use software interfaces and how safety can be accessed when realizing laboratory instrumentation will be assessed.

It should be noted that the technical aspects described in this part are critical for understanding the methodologies employed in this study and to allow other researchers to replicate the in-vivo results described in the last part of this manuscript. Additionally, the aim is to showcase the significant advancements of the developed systems and their potential to enhance the diagnostic accuracy and reliability of ophthalmic measurement and diagnosis techniques. It is our thought that the guidelines, precautions, and technical notions, as well as the drawbacks and benefits of the presented solutions, can help other researchers in the realization of simple, economical, accessible but at the same time accurate instrumentation for the early assessment of common visual impairments.

Part III Results and Discussion This last part will cover the findings and related discussion of the studies conducted on human participants, which is one of the primary phases to be undertaken throughout the development of ophthalmic devices. As a consequence, a practical use case of the methodologies and instrumentation described in Part II, as well as a hands-on adoption of all the considerations and pieces of knowledge presented in the theoretical background, together with implications and findings relative to the obtained experimental results are presented in this part. Furthermore, this part is organized into the following chapters:

- **Pupillometry:** In this Chapter 7 all the experiments and relative results concerning Pupil Light

reflex measurements on human subjects will be presented and discussed. In particular, three experiments with and related preliminary results obtained concerning pupillometry and associated physiological effects are described. The first experiment concern preliminary research to construct a novel model for the iris oculomotor system. The proposed model showed to be suited for the simulation of short-light-flash-induced transient PLR responses. In the second and third experiments, a simple approach to the Silent Substitution technique allowed us to analyze the contribution of the individual photoreceptors to PLR. The tests conducted on human volunteers showed that this approach enables a deep understanding of the contribution of single photoreceptor types, as well as ipRGCs to both image-forming and non-image-forming functions of the human visual system. Moreover, simultaneous observation of PLR and Electroretinogram (ERG) signals with silent substitution proved to be a very promising approach to retrieve many insights into the human visual pathway in an overall faster, less invasive, and more comprehensive way. This will make access to and easier investigation and potential detection of common optic-nervous system disorders.

- **Vision-Based Image Classification:** In this last Chapter three research works that exploit Visual-Based techniques are presented. The utilization of AI algorithms showed to be very promising and to potentially increase the accuracy and objectiveness of the realized systems. More specifically, in the first study, some Vision-Based classification algorithms to improve the acquisition quality of the pupillometer device are investigated. Different fields, *i.e.* Expert Systems, Machine Learning, and Deep Learning, have been used to determine the position of the pupil in input images in order to filter out bad and incorrect acquisitions. In the last two chapters, Visual-based techniques have been used to improve the objectivity in the determination of the Van Herick grade, index of PACG prevention. At this scope, an extensive measurement campaign has been carried out and proved to be of fundamental importance to collect a realistic statistical number of samples. Therefore, all these measures have been taken in different environmental conditions and labeled by expert medical personnel. More specifically, CNN networks proved to perform better in terms of precision and accuracy if compared to ML techniques for this case. VGG-16 proved to be the most accurate with over 98% classification accuracy while maintaining optimal computational complexity also for embedded systems. The last Chapter describes how CNNs can be used to estimate the Van Herick grade as a second stage of the first study case. Moreover, the overall accuracy in VH grade classification is in the order of 80% in the best case, showing good accuracy even if the training dataset is still limited.

In the last section, some general conclusions as well as future works regarding this research activity will be presented.

Part I

State of The Art

Introduction

The field of ophthalmology is constantly evolving, with new technologies and techniques being developed to improve our understanding of the human visual system and to provide better diagnosis and treatment of ocular conditions. This chapter, entitled "State of the Art," provides an overview of the current state of research in several key areas of ophthalmology. In particular, we will discuss the human visual system, including the anatomy of the eye, the pupillary light reflex, and models for the human pupil. We will also delve into the topic of color vision, covering the basics of colorimetry and the silent substitution technique. Additionally, we will examine optical notions such as optical elements and the basics of light systems and view geometries such as Newtonian-View and Maxwellian-View. Finally, we will discuss the various ophthalmic cutting-edge technologies that are currently a hot topic in this research field, including visual-based techniques, pupillometry, and the assessment of angle closure glaucoma (PACG). The aim of this chapter is to provide a comprehensive overview of the state of the art in ophthalmology, highlighting the most recent advances and the current challenges in the field. This will build the basis for the reader to fully understand the choices and motivations of the following parts of this thesis.

Chapter 1

Human Visual System

The human eye is one of the most complex organs in the entire body. Among the five senses, the eye provides a huge quantity of sensitive information about the surrounding environment.
Like a camera, the eye system is able to convert photons energy to a chemical signal that is sent to various parts of the human brain. The human eye can provide a three-dimensional, colored moving image in a wide variety of conditions: from very dark scenarios, e.g. night without moon $10^{-6}\ cd/m^2$ to the lightest sunny day $10^{8}\ cd/m^2$, a huge range of $10^{14}\ cd/m^2$. Moreover, the human eye is capable to differentiate among 10 million colors and to collect light over approximately $100°$ vertical and $145°$ horizontal field of view. The human eye is also responsible to provide non-image-forming information: ipRGC (*Intrinsically photosensitive ganglion cells*) are essential to control the adjustment of the size of the pupil and regulation/suppression of the hormone melatonin that is of fundamental importance for the *circadian rhythm* or *body clock*. In this section, the basic anatomy and main functionality of the human eye are described.

1.1 Anatomy of the eye

The shape of the eyeball is not like a perfect sphere, rather it is a fused two-piece unit composed of the anterior segment and the posterior segment (See Fig. 1.1). The anterior segment is made up of the *cornea*, *iris*, *pupil*, and *lens*. The *cornea* is transparent and more curved and is the outer layer of the eyeball anterior segment. The cornea is typically about 11.5 mm in diameter, and 500 μm in thickness near its center. The larger posterior section on the eyeball is composed of the *vitreous humor*, *retina*, *choroid*, and an outer white shell called the *sclera*. The posterior chamber constitutes the remaining 5/6 of the eyeball.

The dimensions of the eye are reasonably constant, varying among normal individuals by only one or two millimeters; the vertical diameter of the eyeball is around 24 mm and is usually less than the transverse diameter. The weight of the eyeball is about 7.5 gr and its volume is about 6.5 cm^3. As introduced, the posterior sector of the eye is made up of three coats that enclose the optically clear aqueous humor, lens, and vitreous body. The outer parts of two sectors, so the cornea and the sclera are connected by an area termed the *limbus*. The circular part that characterizes the visible color of our eyes is the *iris* and the white part around it is the visible part of the sclera. The iris concentrically surrounds the center of the eye, the pupil, which appears to be black. The size of the pupil, which controls the amount of light entering the eye, is adjusted by the iris' dilator and sphincter muscles(See section 1.2.1). Light rays enter the eye through the cornea (which is transparent to visible light), then pass through the pupil and the lens in order to be focused on the retina, where the photoreceptors are located. The lens shape is changed to perform accommodation (focus distance, see 1.2.2) and is controlled by the *ciliary muscle*. Photons of light falling on the light-sensitive cells of the retina (photoreceptor cones and rods) are converted by chemical

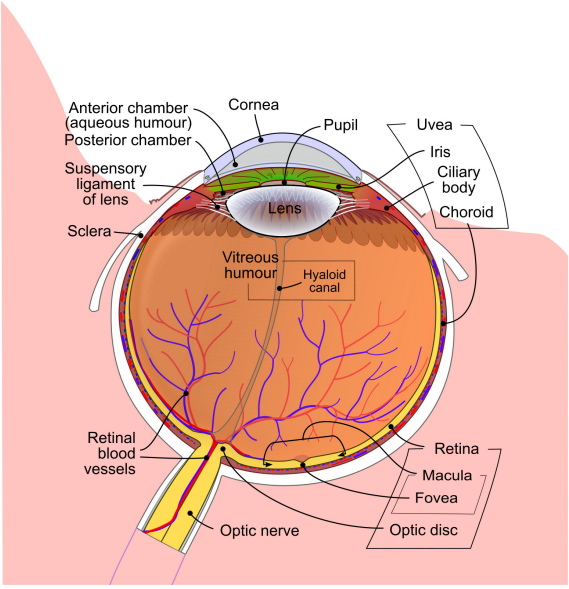


Figure 1.1: Schematic diagram of the human eye

reactions into electrical signals that are transmitted to the brain by the optic nerve and interpreted as sight and vision [4]. The parts here briefly introduced that are of main interest for understanding the research work addressed, will be described in this section.

1.1.1 The Retina

The retina is the innermost, light-sensitive layer of tissue of the eye. The optics of the eye create a focused two-dimensional image of the visual world on the retina, which translates that image into electrical-neural impulses and sent them to the brain to create visual perception. The retina has the same function as the film or image sensor in a digital camera. The retina consists of several layers of neurons interconnected by synapses and is supported by an outer layer of pigmented epithelial cells. The primary light-sensing cells in the retina are the photoreceptor cells, which are of two types: *rods* and *cones*. Rods function mainly in dim light and provide black-and-white vision. Cones function in well-lit conditions and are responsible for the perception of color, as well as high-acuity vision used for tasks such as reading (See Figure 1.4). A third type of light-sensing cell recently discovered, the photosensitive ganglion cell (ipRGC), is important for the regulation of *circadian rhythms* and reflexive responses such as the *pupillary light reflex*.
The light that enters the eye and reaches the retina induces a cascade of chemical and electrical events that ultimately trigger nerve impulses. These impulses are then sent to various visual centers of the brain through the *fibers* of the *optic nerve*. Neural signals from the rods and cones undergo processing by other neurons, whose output takes the form of electrical potentials in retinal ganglion cells. Several important features of visual perception can be traced to the retinal encoding and processing of light inside the retina. As shown in the Figure 1.2, the vertebrate retina is composed of many different layers that can be briefly described from the closest to the vitreous body to the farthest, as follows: [5]

1. Inner limiting membrane – basement membrane elaborated by *Müller* cells.
2. Nerve fiber layer – axons of the ganglion cell nuclei (note that a thin layer of Müller cell footplates exists between this layer and the inner limiting membrane).
3. Ganglion cell layer – contains nuclei of ganglion cells, the axons of which become the optic nerve fibers for messages and some displaced *amacrine* cells.

4. Inner plexiform layer – contains the synapse between the bipolar cell axons and the dendrites of the ganglion and amacrine cells.
5. Inner nuclear layer – contains the nuclei and surrounding cell bodies of the amacrine cells, bipolar cells, and horizontal cells.
6. Outer plexiform layer – projections of rods and cones ending in the rod *spherule* and cone *pedicle*, respectively. These make synapses with dendrites of bipolar cells and horizontal cells.
7. Outer nuclear layer – cell bodies of rods and cones.
8. External limiting membrane – layer that separates the inner segment portions of the photoreceptors from their cell nuclei.
9. Inner segment / outer segment layer – inner segments and outer segments of rods and cones. The outer segments contain a highly-specialized light-sensing apparatus [6, 7].
10. Retinal pigment epithelium – a single layer of cuboid epithelial cells (with extrusions not shown in the diagram). This layer is closest to the choroid and provides nourishment and support functions to the neural retina.

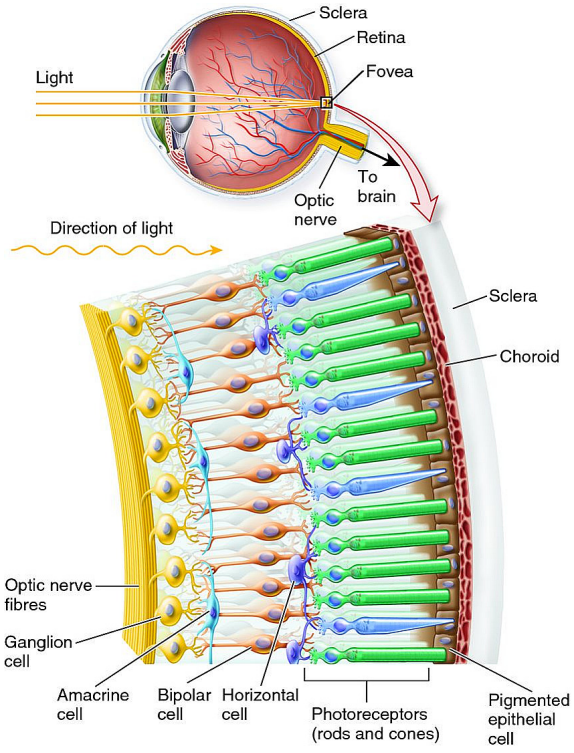


Figure 1.2: Distribution and arrangement of the photoreceptors in the retina

These layers can be grouped into 4 main processing stages: photo-reception; transmission to bipolar cells; transmission to ganglion cells, which also contain photoreceptors, the photosensitive ganglion cells (ipRGC); and transmission along the optic nerve. At each synaptic stage there are also laterally connecting horizontal and *amacrine* cells. The optic nerve is a central tract of many *axons*[1] of ganglion cells connecting

[1] An axon, or nerve fiber, is a long, slender projection of a nerve cell, or neuron, in vertebrates, that typically conducts electrical impulses known as action potentials away from the nerve cell body. The function of the axon is to transmit information to different neurons, muscles, and glands.

primarily to the *lateral geniculate body*, a visual relay station in the *diencephalon* (the rear of the *forebrain*). In adult humans, the entire retina is approximately 72% of a sphere about 22 mm in diameter. The entire retina contains about 7 million cones and from 75 to 150 million rods. The optic disc, a part of the retina sometimes called "*the blind spot*" due to lack of photoreceptors, is located at the *optic papilla*, where the optic-nerve fibers leave the eye. It appears as an oval white area of 3 mm^2. Temporal (in the direction of the temples) to the optic disc there is the *macula* region, at whose center there is the *fovea*. The fovea is a pothole that is responsible for our sharp central vision but is actually less sensitive to light because its lacks rods. Figure 1.3, show the spatial distribution of photoreceptors on the retina.

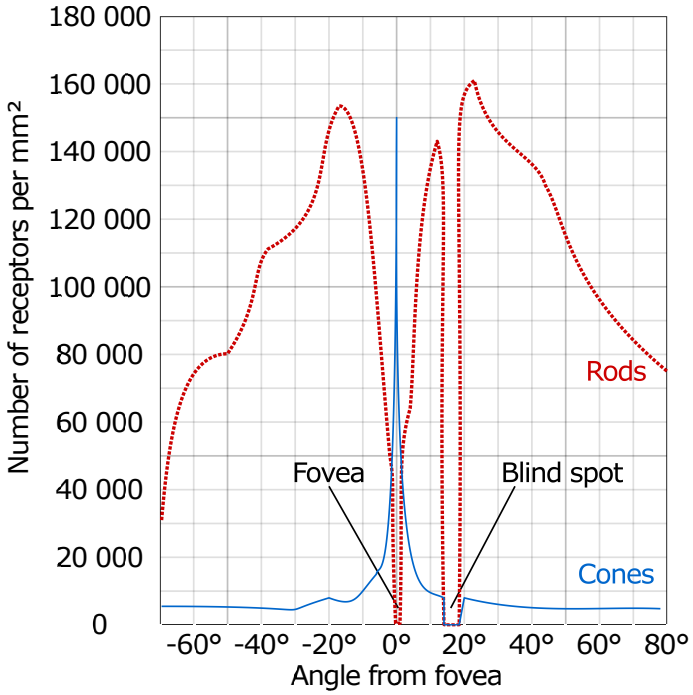


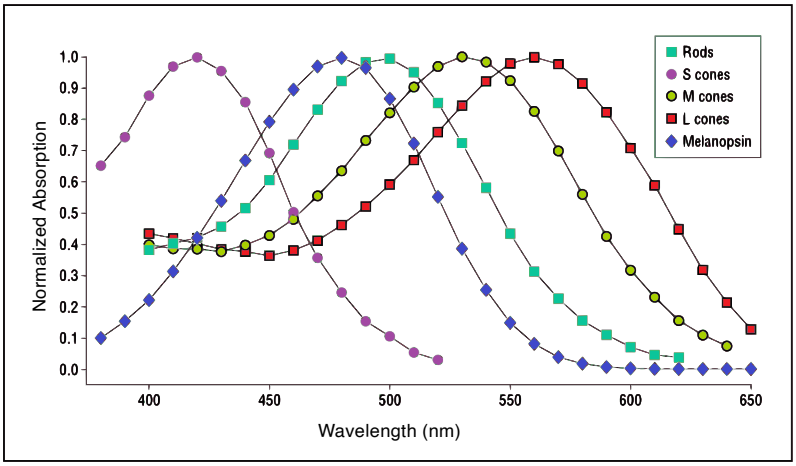
Figure 1.3: Retinal distributions of eye's photoreceptors around the horizontal optical axis.

1.1.2 Photoreceptors

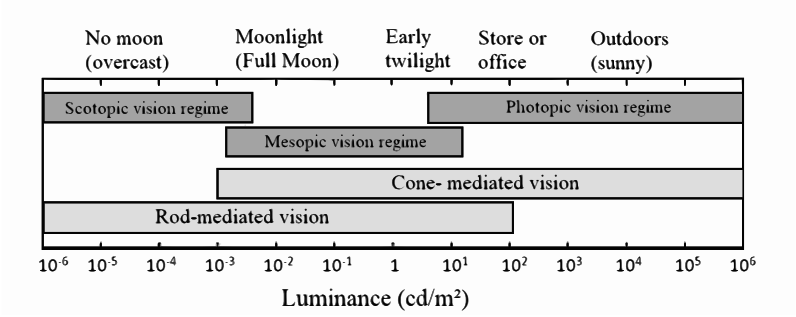
A photoreceptor cell is a particular type of *neuro-epithelial* cell found in the retina that is capable of visual *phototransduction*. Photoreceptors are directly connected to the optical nerve through ganglion cells. The considerable biological importance of photoreceptors is that they convert light (visible electromagnetic radiation) into signals that can stimulate biological processes. More deeply, photoreceptor proteins in the cell absorb photons, triggering a change in the cell's membrane potential [4]. The human eye has three types of photosensitive cells: cones(L, M, H), rods, and *intrinsically photosensitive retinal ganglion cells* ipRGC. As one may suggest, our eyes can detect different colors in the visible light spectrum. This is possible because photoreceptors react differently to various wavelengths and light intensities. Figure 1.4 shows both spectral response and light intensity response of the eye's photoreceptors. The following sections briefly describe the characteristics of these photopigments.

Rods

Rod cells are photoreceptor cells in the retina of the eye that can function in less intense light than the other type of visual photoreceptor, cone cells. Rods are usually found concentrated at the outer edges of the retina and are used in peripheral vision. Rod cells are more sensitive than cone cells and are almost



(a)



(b)

Figure 1.4: a) Shows, the spectral absorptions of the eye's photo-sensitive cells. The five peaks for these photoreceptor absorptions curves, listed in order from shorter to longer wavelengths, are S-cones (short-wavelength cones in purple) with a peak absorption at around 420 nanometers, Intrinsically photosensitive retinal ganglion cells (ipRGCs, or Melanopsin expressing photopigment, in blue) with a peak absorption at around 480 nanometers, Rods (cyan) with a peak absorption at around 498 nanometers, M-cones (medium-wavelength cones in green) with a peak absorption at around 535 nanometers, and L-cones (long-wavelength cones in red) with a peak absorption at around 565 nanometers. b) Shows the photoreceptor's luminance regime.

entirely responsible for night vision. Looking at the Figure 1.4b, the rods-mediated vision is also called *scotopic regime* that goes from 10^{-6} to $10^{-3}cd/m^2/$. However, rods have little role in color vision, for this reason, colors are much less apparent in dim light, and not at all at night. Rods are physically a little longer and leaner than cones but have the same basic structure. *Opsin*[2]-containing disks lie at the end of the cell adjacent to the retinal pigment *epithelium*, which in turn is attached to the inside of the eyeball. The stacked-disc structure of the detector portion of the cell allows for very high efficiency. Rods are much more common than cones, with about 100 million rod cells compared to 7 million cone cells. On average, there are approximately 92 million rod cells in the human retina [8]. Like cones, rod cells have a synaptic terminal, an inner segment, and an outer segment. The synaptic terminal forms a synapse with another neuron, usually a bipolar cell or a horizontal cell (See Figure 1.2). The inner and outer segments are connected by a cilium, which lines the distal segment. The inner segment contains organelles and

[2]Opsins are a group of proteins, made light-sensitive, via the *chromophore* retinal found in photoreceptor cells of the retina. Five classical groups of opsins are involved in vision, mediating the conversion of a photon of light into an electrochemical signal, the first step in the visual transduction cascade.

the cell's nucleus, while the rod outer segment (abbreviated to ROS), which is pointed toward the back of the eye, contains the light-absorbing materials [9]. A human rod cell is about 2 microns in diameter and 100 microns long. Rods are not all morphologically the same; in mice, rods close to the outer plexiform synaptic layer display a reduced length due to a shortened synaptic terminal [10].

Cones

Cone cells are photoreceptor cells in the retinas of the human eye. They respond differently to light of different wavelengths and are thus responsible for colored vision and function best in relatively bright light (See Figure 1.4). Cone cells are located near the *fovea*, a region with 0.3 mm diameter free of rod and with high amount of densely packed cones, which quickly reduce in number towards the periphery of the retina (See Figure 1.3). There are about six to seven million cones in the human eye. However, different sources in the literature reveal different estimations of cone numbers. The work attained by Curcio et al. [8] (1990) indicate an average of close to 4.5 million cone cells and 90 million rod cells in the human retina for each eye. Cones are less sensitive to light than the rod cells in the retina (which support vision at low light levels), but allow the perception of color. They are also able to perceive finer detail and more rapid changes in images because their present a faster response to stimuli than rods. As said before, cones are normally of three types, each with different pigments, namely: S-cones, M-cones, and L-cones. The first responds the most to the light of long wavelengths, peaking at about 560 nm; this type is sometimes designated as L-cones ('L' for long wavelength). The second type responds the most to the light of medium wavelength, peaking at 530 nm, and is abbreviated M-cones, 'M' for medium. The third type responds the most to short-wavelength light, peaking at 420 nm, and is designated S-cones for short. Because humans usually have three kinds of cones with different *photopsins*, which have different response curves and thus respond to variation in color in different ways, we have 'tri-chromatic' vision. Particular cases of individuals with color blind are related to the absence of one or more types of cones or that present a deviation from the standard spectral response. Individuals with four or more types of cones are also possible, giving them four-chromatic vision. The three pigments responsible for detecting light have been shown to vary in their exact chemical composition due to genetic mutation; as a consequence, different individuals will have cones with different color sensitivity.

The three types have peak wavelengths near 564–580 nm, 534–545 nm, and 420–440 nm, respectively, depending on the individual. While it has been discovered that there exists a mixed type of bipolar cells that bind to both rod and cone cells, bipolar cells still predominantly receive their input from cone cells.

Shape and arrangement: Cone cells are somewhat shorter than rods, but wider and tapered, and are much less numerous than rods in most parts of the retina, but greatly more densely concentrated than rods in the *fovea*. Structurally, cone cells have a cone-like shape at one end where a pigment filters incoming light, giving them their different response curves. They are typically 40–50 μm long, and their diameter varies from 0.5 to 4.0 μm, being the smallest and most tightly packed at the center of the eye at the fovea. The S cone spacing is slightly larger than the others. *Photobleaching*[3] can be used to determine cone arrangement. This is accomplished by exposing the dark-adapted retina to a specific wavelength of light, which paralyzes the specific type of cone sensitive to that wavelength for up to thirty minutes, rendering it white in contrast to the grey dark-adapted cones when a photograph of the retina is taken. The findings show that S cones are distributed at random and appear substantially less frequently than M and L cones. Different people with normal vision have quite different ratios of M and L cones (for example, values of 75.8% L with 20.0% M against 50.6% L with 44.2% M in two male patients) [11]. Like rods, each

[3] In optics, photobleaching (sometimes termed fading) is the photochemical alteration of a dye or a fluorophore molecule such that it permanently is unable to reflect light.

cone cell has a synaptic terminal, an inner segment, and an outer segment as well as an interior nucleus and various *mitochondria*. The synaptic terminal forms a synapse with a neuron such as a bipolar cell. The inner and outer segments are connected by a cilium. The inner segment contains organelles and the cell's nucleus, while the outer segment, which is pointed toward the back of the eye, contains light-absorbing materials. Unlike rods, the outer segments of cones have windings of their cell membranes that create stacks of membranous disks. Photopigments exist as trans-membrane proteins within these disks, which provide more surface area for light to affect the pigments. In cones, these disks are attached to the outer membrane, whereas they are pinched off and exist separately in rods [12].

ipRGCs

The retina of a mammal's eye contains a specific type of neuron known as intrinsically photosensitive retinal ganglion cells (ipRGCs) or melanopsin-containing retinal ganglion cells (mRGCs). Rod- and cone-deficient animals nonetheless reacted to light stimulation in 1923 by constricting their pupils [13], indicating that ipRGCs are present in addition to rods and cones as the retina's primary light-sensitive neurons. Advanced studies on these cells didn't start until later, in the 1980s [14]. Recent research has demonstrated that ipRGC are innately photosensitive [15], unlike other retinal ganglion cells, due to the presence of melanopsin[4], a light-sensitive protein. Therefore they constitute a third class of photoreceptors, in addition to rod and cone cells [16]. Compared to the rods and cones, the ipRGCs respond more slowly and react to the presence of light over the long term. They a present in a very small subset of the retinal ganglion cells, only in about 1% of them. Their functional roles are non-image-forming and fundamentally different from those of pattern vision; they provide a stable representation of ambient light intensity. Among others, they have at least three primary functions.

- They play a major role in synchronizing circadian rhythms to the 24-hour light/dark cycle, providing primarily length-of-day and length-of-night information. They send light information through the *retinohypothalamic* tract (RHT) directly to the circadian *pacemaker* of the brain, (the *suprachiasmatic* nucleus of the hypothalamus). The physiological properties of these ganglion cells match known properties of the daily light entrainment (synchronization) mechanism regulating circadian rhythms.
- Photosensitive ganglion cells innervate other brain targets, such as the center of pupillary control, called the *olivary pretectal nucleus* of the midbrain. They contribute to the regulation of pupil size and other behavioral responses to ambient lighting conditions [17].
- They contribute to photic regulation and acute photic suppression by the release of the hormone *melatonin*[5] [17].
- In rats and some other animals ipRGC play a role in conscious visual perception such as perception of regular gratings, light levels, and spatial information [17].

Photoreceptive ganglion cells have been isolated in humans where, in addition to regulating the circadian rhythm, they have been shown to mediate a degree of light recognition in rod-less, cone-less individuals. Zaidi et al. [18] showed that photoreceptive ganglion cells may have some visual function in humans. The photopigment of photoreceptive ganglion cells, melanopsin, is excited by light mainly in the blue portion

[4]Melanopsin is a type of *photopigment* belonging to a larger family of light-sensitive retinal proteins called *opsins* and encoded by the gene Opn4. In the mammalian retina, the other two categories of opsins, both involved in the formation of visual images are *rhodopsin* (contained in rods) and *photopsin* (types I, II, and III) contained in cones photoreceptor cells.

[5]Melatonin is a hormone that regulates sleep-wake cycles. It is primarily released by the pineal gland and it is often used for the short-term treatment of trouble sleeping such as from jet lag or shift work.

of the visible spectrum (absorption peaks at 480 nanometers, see Fig. 1.4). In addition to responding directly to light, these cells are excited and inhibited from rods and cones by way of synaptic connections in the retina.

1.2 Pupillary Light Reflex

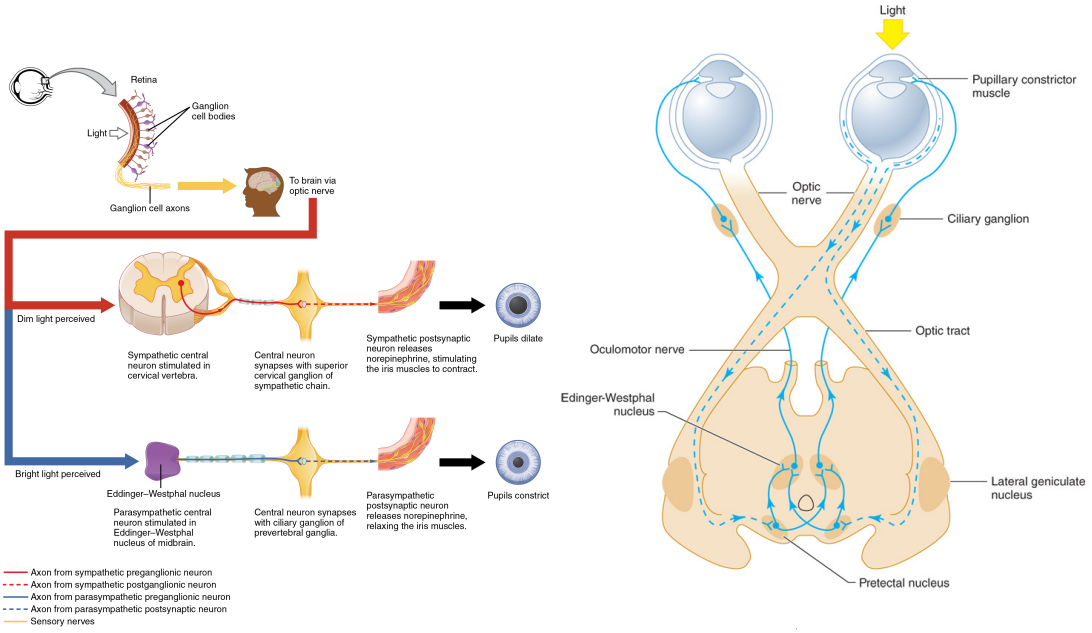
Pupillary light reflex (PLR) is a reflex that controls the diameter of the pupil in response to changes in the intensity of light incidence on the retina. There are visual photo-transduction and nonvisual ones. The mechanism that regulates this reflex is of fundamental importance for the objective of this research work because involves reactions, and neural and chemical processes that are strictly connected to health impairments due to light flicker. PLR reflex is *autonomic*[6], cranial (that includes nerves inside the brain and thus non-spinal nerve), parasympathetic-mediated (one of the two divisions of the autonomic nervous system). As one may presume, if one eye is excited by a light stimulus, also the dimension of the other pupil will be in influence, even in resting conditions without stimulus [19]. The PLR is not a reaction related only to light that shines on eyes, though this effect involves specific parts of the nervous system and some important internal reactions. By looking at Figure 1.5b the light that travels in the eye firstly impacts the surface constituted by the photoreceptors-layers, localized in the lowest part of the retina of the eye. The light stimulus perceived by photoreceptors is then converted into an electrical signal by ganglion cells. This signal is then sent through sensory fibers inside the optic nerve (the second cranial nerve) to the brain. Here is processed by the *pretectal nuclei* inside the central system, in the midbrain. Hera some axons synapse are connected to neurons in the *Eginger-Westphal nucleus*, a parasympathetic pre-ganglion nucleus that innervates the iris muscle and the ciliary muscle. The signal by crossing this part of the nervous system then continues through the motor fibers to the muscle in the iris that constricts the pupil. This leads to the neuronal projection that belongs to the *oculomotor nerve* (the third cranial nerve): we refer to pupil constriction as a parasympathetic response.

As described in the next section 1.2.1, the pupil is the round black circle at the center of the iris of the eye, through which light passes, the size is determined by the antagonist activity of two smooth iris muscles: the *sphincter muscle* and the *dilator muscle*. Looking more closely at the main nuclei and brain parts involved, it is necessary to describe the *axonal* projections of the reflex. As introduced the first cells involved are the retinal ganglion cell of the eye, which receives inputs from rods and cones, that perform the photo-transduction. The axon projects in the pretectal nucleus, located in the midbrain, and here innervates two outputs directed to both sides of the brain, one for each side: the first one is directed to the Edinger-Westphal nucleus, located in the *ipsilateral* side of the midbrain, where synapses with the ciliary ganglion are located; the second one is directed to the *contro-lateral* portion of the body. The nerve fiber that projects from the ciliary ganglion is directed to the homolateral muscle of the iris. This cranial light reflex arc results in pupil constriction. Looking at Figure 1.6 is easy to understand the complete pathway.

1.2.1 The iris muscle plant

The pupil is a hole located in the center of the iris of the eye that allows light to strike the retina. The size of the human pupil is an important parameter in different studies in Vision, Neurology, and Ophthalmology as well as in other areas such as Psychology, Psychiatry. In the present study, pupil diameter is monitored in order to evaluate annoyance or other possible visual impairments caused by light flicker. As introduced before, the pupil response is influenced not only by the light level but by a multitude of different conditions, such as focus distance, emotional status, brain activity, drugs, or clinical pathologies.

[6]The autonomic nervous system is a control system that acts largely unconsciously and regulates bodily functions such as the heart rate, digestion, respiratory rate, pupillary response, urination, and sexual arousal.



(a) Pupillary light reflex pathway (b) Neuronal path of the PLR

Figure 1.5: Representation of pathways in the pupillary light reflex.

The pupil size is directly controlled by two muscles: the iris *sphincter* muscle and the iris *dilator* muscle. These two muscles are also termed radial (external) and circular (internal) muscles. As shown in Figure 1.6, a balanced combination of contraction and relaxation of these two muscles allows pupil size control. Pupil constriction is due to the increased tension in the sphincter or radial muscle. The papillary constrictor muscle is circularly arranged and is innervated by the parasympathetic nervous system, and the motor nucleus called the *Edinger-Westphal nucleus*, located in the midbrain. Pupil dilatation in instead controlled by dilator muscles or radial muscle, which runs radially in the iris and therefore fits as a dilator. The papillary dilator muscle is radially arranged and is innervated by the sympathetic nervous system. Thanks to iris muscles, pupil diameter can vary from about 5 mm in the dark condition (10^{-5} cd/m^2) and from 2 to 3 mm in very bright light conditions (100 $cd/m^2 or 18$ W/m^2) [20].

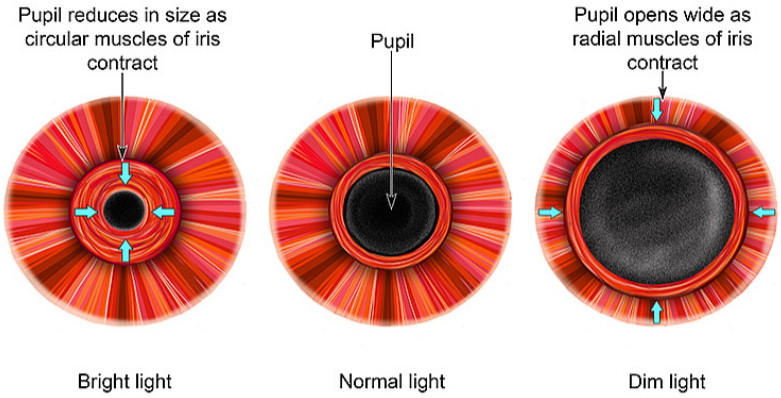


Figure 1.6: Pupil iris muscle plant

1.2.2 Accomodation

The accommodation is a reflex action of the eye that allows focusing operations. When we change the focus from a near object to a distant object (and vice versa), we have changes in visual s *vergence*[7], eye's lens shape (accommodation) and pupil size. Accommodation is dependent on the optic nerve (afferent limb of reflex), superior centers (*inter-neuron*) and [8] (efferent limb of reflex). The change in the shape of the lens is controlled by the *ciliary muscles* inside the eye. A contraction of the ciliary muscles alters the focal distance of the eye, that allow later images to be focused on the retina; this process is known as accommodation. The reflex, controlled by the parasympathetic nervous system, involves three responses: pupil constriction, lens compression or dilatation, and eyes convergence. A near object (for example, a computer screen) appears large in the field of vision, and the eye receives light from wide angles. The accommodation action can be simply described by an optical point of view: when we move focus from a distant object to a near object, the eyes will then converge. This action makes the ciliary muscle to constricts, making the eye's lens thicker and shortening its focal length. The pupil will constrict in order to prevent strongly diverging light rays to hit the periphery of the cornea and the lens, so avoiding the formation of a blurred image. [19]

1.2.3 Rod, Cone, and Melanopsin contributions to human pupil

The mechanisms of rod, cone, and melanopsin contributions to the pupil control pathway in humans are not well understood. Barrionuevo et al. [21] determined the relative contributions of rods, cones, and melanopsin to phasic pupil response using temporal sinusoidal stimulation over a large light adaptation range, spanning in both mesopic and photopic light levels to alter differentially the sensitivity of the inner and outer retinal photoreceptors. The result presented by Barrionuevo is obtained by applying the *Silent Substitution*. The silent substitution concept was suggested by Rushton et al. as a way of investigating the contribution of specific photoreceptor types to vision [22]. A silent substitution stimulus consists of two alternating stimuli, of which wavelengths and radiance are chosen such that they present steady modulated excitation in one photoreceptor type, while others are maintained constant (see. Sec 2.2). In principle, this procedure prevents modulation of the photo-transduction cascade in the silenced photoreceptor type. As reported in [21], three kinds of sinusoidal photoreceptor modulations were generated using silent substitution: rod stimuli with rod excitation modulated while maintaining constant cone excitations; cone stimuli with in-phase temporal modulation of the L-, M-, and S-cone excitations at the same contrast, so only cone luminance was modulated with a constant cone chromaticity while maintaining constant rod excitation at zero contrast. The result is presented in Figure 1.7.

[7] A vergence is the simultaneous movement of both eyes in opposite directions to obtain or maintain single binocular vision.
[8] oculomotor nerve

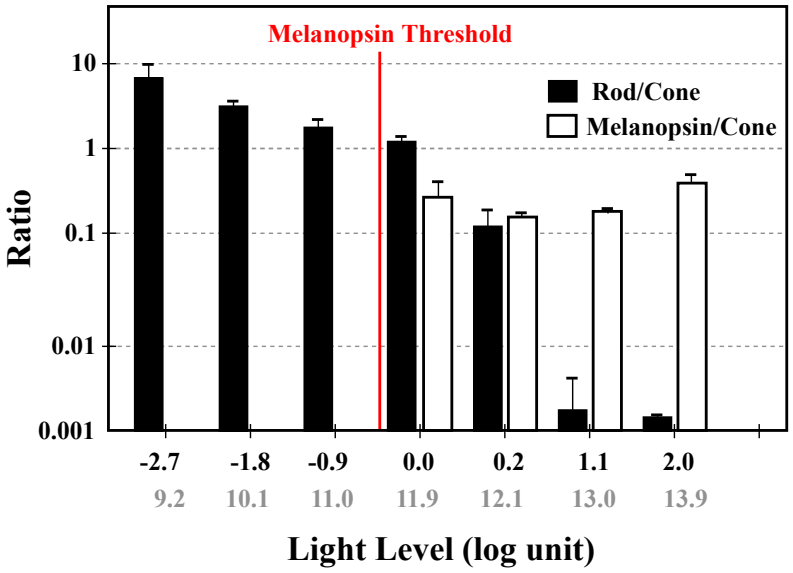


Figure 1.7: The relative amplitudes of rods and melanopsin contribution with respect to cones in all the light levels determined by Barrionuevo et al. [21].

The results showed that the contributions of rods, cones, and melanopsin were combined as a vector sum of their inputs. For lower light levels, rods dominate the response with no activation of melanopsin. For higher light levels, cones dominate the response with a significant melanopsin contribution and insignificant rod contribution. These findings are of crucial importance to determining illumination conditions when employing the Silent Substitution technique, especially when photopic vision range is considered, i.e. rod contribution can be neglected if proper background illumination level is kept over the significant contribution threshold.

1.3 Model For The Human Pupillary

1.3.1 Introduction

The *pupillary light reflex* (PLR) is the mechanism that controls changes in the size of the pupil in response to variations in illumination. As previously mentioned (see Section 1.2), the pupil is the opening in the center of the iris as it's main function is to control the amount of light that enters the eye, by dilating or constricting it in response to changes in the lighting environment. This process ensures optimal illumination of the retina and allows for human vision to function over a wide range of environmental lighting conditions.

In addition to regulating the amount of light that enters the eye, the pupillary light reflex has other important functions. For example, it can also affect the depth of field of the eye, which is the range of distances over which objects appear in focus. By changing the size of the pupil, the eye can adjust its depth of field to better focus on objects at different distances. The pupillary light reflex also plays a role in the regulation of the body's biological clock, or circadian rhythm, which helps to synchronize daily physiological processes with the 24-hour day-night cycle. PLR also involves many important intracranial and neural pathways, as constriction and dilation phases of the pupil are a function of both parasympathetic and sympathetic divisions of the autonomic nervous system. [23]

Several studies have been conducted over the past decades on the PLR and many mathematical models have been proposed and validated with experimental data. Starting in the '20s, Reeves [24] and lately

Moon and Spencer [25] successfully modeled steady-state pupil size as a function of log-light intensity. Lately, some dynamic models of PLR have been proposed by Sun [26], Stark [27], and more recently from Pamplona [28] and Privitera. [29] Fun et al. have successfully modeled, with superior results, PLR under specific light stimulation [30].

Using a control theory-based approach, the pupil oculomotor-nervous system can be considered as a simple black box with one input and one output: light stimuli, i.e. input, with a wide range of characteristics, can be easily applied to the eyes while the pupil size, i.e. output, variations can be measured effortlessly and non-invasively. The easy acquisition of PLR data allows many types of quantitative experiments to be conducted without causing unwanted stress on human subjects. The combination of all these elements makes the PLR analysis of great interest in many clinical procedures [31].

During this Ph.D. program, a physiological model suitable to describe the pupil oculomotor system exposed to short-light flashes is investigated and practically tested on human subjects (see. Sec 1.3). The model presented later in Sec. 1.3.2 consists of one second-order differential equation and, potentially, allows extracting the autonomic nervous inputs and the dynamic characteristics of the pupil oculomotor system from PLR Data.

1.3.2 Muscle Plant Model

According to the control theory, PLR can be modeled as a single-input single-output dynamic system. As discussed in the literature [32], this simple bio-mechanical system is characterized by many non-linearities as it involves different types of photoreceptors, as well as different neuroanatomical pathways, and thus its description in terms of closed-form equations is difficult.

Since the iris-muscle plant is essential throughout the control process, our model analyzes in detail this plant with reference to a bio-mechanical equivalence. In this context, PLR can be observed in response to well-defined transient light stimulation. In fact, under this type of stimulation [30, 33], it is possible to model the pupil response by considering, as the main contribution, the mechanical properties of the iris-muscle plant.

From the mechanical point of view, the iris movement is governed by three forces: passive elastic forces, viscous resistance forces, and active forces generated by parasympathetic and sympathetic modulation. In particular, the sphincter and dilator muscles control pupil size. As schematically shown in Figure 1.8, the action of these two muscles can be modeled as two antagonist viscous-elastic elements.

The viscous-elastic model described in detail by Hirata et al. [33, 34] was used as starting point for this work. In this model, the parasympathetic $E_s(t)$ and sympathetic $E_d(t)$ nervous activities, which directly innervate the sphincter and dilator muscles, are considered as the inputs of the control system. The muscles activities are then expressed with three main functions: passive elastic forces (subscript $_p$), viscous resistance forces (subscript $_v$), and active tensor forces(subscript $_a$) according to the following equations; [33] here parameters with subscript $_s$ state for sphincter muscles, while parameters with subscript $_d$ refer to the dilator. Moreover, static and dynamic components are marked with overline $\bar{}$ and a circumflex $\hat{}$ symbols, respectively.

Passive Elastic Forces:

$$P_p = \begin{cases} a(z - l_0)^4 + b(z - l_0)^2, & (z \geq l_0) \\ 0, & (z < l_0) \end{cases} \tag{1.1}$$

where z is the muscle length, a and b are two constants, and l_0 is the muscle length at rest.

Viscous Resistance Forces:

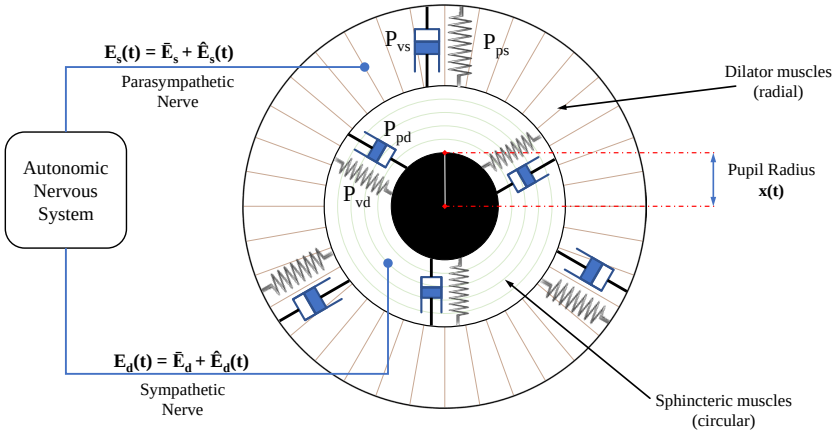


Figure 1.8: Schematic diagram of the human pupillary muscle plant. $E_s(t)$ and $E_d(t)$ are the parasympathetic and sympathetic nervous activities, respectively. $\bar{E}$ and $\hat{E}$ are the DC and AC components of the inputs, respectively. The radial, i.e. dilator, and circular, i.e. sphincter, muscles are mechanically described by a spring and dump couple, where P_{vs} and P_{vd} are the viscous components, while P_{ps} and P_{pd} are the elastic ones.

$$P_v = \begin{cases} D_+ \frac{dz}{dt}, & (\frac{dz}{dt} \geq 0) \\ D_- \frac{dz}{dt}, & (\frac{dz}{dt} < 0) \end{cases} \tag{1.2}$$

where $\frac{dz}{dt}$ is the muscle length variation velocity. D_+ and D_- are two viscous coefficients of resistance during the stretch and release phases of the muscle, respectively.

Active Tensor Forces:

$$P_a = \left(\bar{E} + \hat{g}(t)\right) \cdot p_a(z) \tag{1.3}$$

$$p_a(z) = \begin{cases} P_0 - c(z - L_0)^2, & (P_0 \geq c(z - L_0)^2) \\ 0, & (P_0 < c(z - L_0)^2) \end{cases} \tag{1.4}$$

$$\frac{d^2\hat{g}(t)}{dt^2} + (2\alpha + \beta)\frac{d\hat{g}(t)}{dt} + \alpha(\alpha + \beta)\hat{g}(t) = \beta\hat{E}(t - t_D) \tag{1.5}$$

where c is a constant, L_0 is the length of the muscle at which the maximum tension P_0 is generated. $p_a(z)$ and $\hat{g}(t)$ are muscle length-dependent and input-dependent components of the dynamic active tension, respectively. α and β are the negative and positive time constants of the tensor isometric response, respectively. $\hat{E}$ and $\bar{E}$ are the AC and DC input components coming from the autonomic nervous system. The delay time of the nervous response $\hat{E}$ is described by the time interval t_D. The two model inputs, i.e. parasympathetic and sympathetic nervous activities, are expressed as follows:

$$\begin{aligned} E_s(t) &= \bar{E}_s + \hat{E}_s,\ E_s(t) \geq 0 \\ E_d(t) &= \bar{E}_d + \hat{E}_d,\ E_d(t) \geq 0 \end{aligned} \tag{1.6}$$

The reciprocal relation for both nervous activities at equilibrium must be also considered; thus the static input nervous activities must be balanced as follow:

$$\bar{E}_d = 1 - \bar{E}_s, 0 \leq \ \bar{E}_s \leq 1 \tag{1.7}$$

In conclusion, opposite tensions and forces of the one-dimensional structure muscle configuration have been combined:

$$m \cdot \frac{d^2x}{dt^2} = P_{pd} + P_{ad} - P_{ps} - P_{as} - P_{vd} - P_{vs} \tag{1.8}$$

where m is the total mass of the moving muscles and x is the pupil radius. As $x(t)$ is considered as the model output, sphincter and dilator muscle length of Equations 1.1 and 1.4 have been adjusted accordingly. According to Usui et al. [33], sphincter and dilator muscle length can be described for this model as:

$$\begin{aligned} z_d &= x_{max} - x \\ z_s &= x \end{aligned} \tag{1.9}$$

where z_d and z_s are dilator and sphincter muscle length, respectively, whereas x_{max} is the pupil radius at brain death. The model and all the derived functions, together with all the parameters that describe the two muscles' behavior were implemented in the Matlab-Simulink© environment. In Section 7.1, the autonomic nervous inputs and all the muscle parameters have been extracted from PLR Data.

Chapter 2

Color Vision

Color vision is a fundamental aspect of human perception that allows us to perceive and differentiate various colors in our environment. The study of color vision, also known as colorimetry, is an interdisciplinary field that draws on knowledge from physics, physiology, psychology, and computer science. During this Ph.D. work, a significant amount of research activities involved the use of light stimuli on the human eye. To fully comprehend this, it is essential to understand the fundamental principles of color vision, including how colors are perceived and quantified using current metrics. Whit this scope, this chapter aims to provide a quick overview of the current state of knowledge in the field of color vision research.

In addition, the technical side of color measurement and reproduction will be examined, such as the use of color-matching functions and the RGB color space. Finally, we will introduce the state-of-the-art theoretical background behind the *Silent Substitution Techniques* and its application to visual research.

2.1 Basics of Colorimetry

Colorimetry is the science of color measurement, that finds a numerical correspondence to the subjective responses to light stimuli [35]. The study began in the early nineteenth century with the hypothesis of the trichromatic nature of humans' color vision. When in 1931 the CIE (Commission Internationale de l'Eclairage) formalized a system of color specification based on three values X, Y, Z (called tristimulus values), and colorimetry based on trichromatic color vision became a reality [36].

2.1.1 Color Matching Functions

Color matching functions (CMFs) are mathematical functions that describe the relationship between the spectral power distribution of a light source and the tristimulus values (a set of three values representing the amounts of red, green, and blue) that are needed to match that light source to a specified reference source. These functions are used to quantify and match colors and are defined by the International Commission on Illumination (CIE) as part of their colorimetry system. The color matching functions are typically represented as three separate functions, one for each primary color (red, green, and blue), and are used in various applications such as color reproduction, color measurement, and colorimetry. Color Matching Function can be derived from cone fundamentals (see. Sec. 1.1.2), which describe the sensitivity of the three types of cone cells in the human retina (L, M, and S cones) to different wavelengths of light. These functions together are used to understand how the human visual system processes color information and how it is affected by factors such as age, disease, and genetic variations.

Moreover, since the distribution of photoreceptors, in particular of the cones in the retina is slightly different among different subjects (see. Fig. 1.3), the calculation of the tristimulus values, i.e. CFMs, strictly

depends on the field of view of considered. To face this problem, the CIE defined some standards for a generic observer, which can be summarized as the following:

- CIE 1931 2° Standard Observer [37]: the average human's chromatic response is calculated within a 2° arc into the fovea, where the majority of the cones are supposed to be (see. Sec 1.1.2);
- CIE 1964 10° Standard Observer [38]: this study, presented lately to cover a larger field of view color representation, where the CMFs have been estimated as perceived by stimulating the observer with a 10° angle from the fovea instead of 2°. This is a more modern standard although less used.

The most common CMFs have been computed as a linear transformation of the cone fundamentals of Stockman & Sharpe (2000) [39, 40] endorsed by the CIE as the CIE (2006) physiologically-relevant LMS fundamental color matching functions as can be appreciated in Figure 2.1.

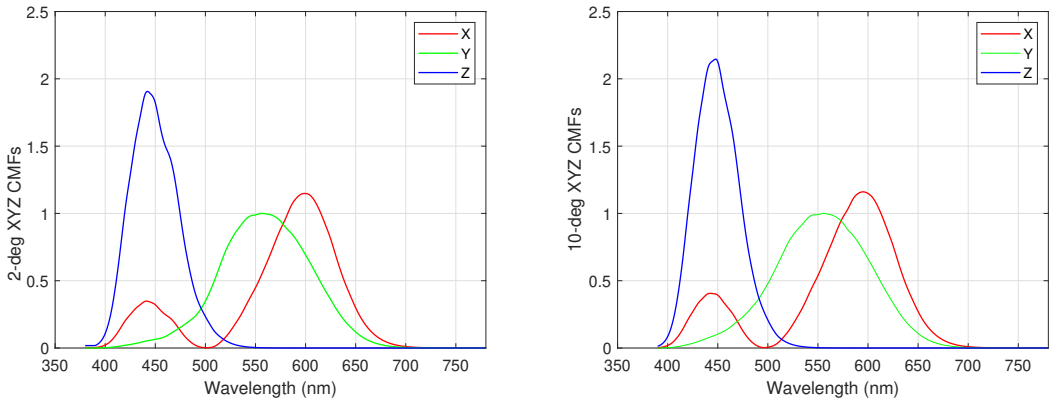


Figure 2.1: (a) 2-deg XYZ and (b) 10-deg Color Matching Functions transformed from the CIE (2006) 2-deg and 10-deg LMS cone fundamentals. Data from the Color & Vision Research Laboratoryhttp://www.cvrl.org/ and normalized to green.

2.1.2 XYZ and RGB Color Spaces

The XYZ color space, also known as the CIE XYZ color space, is a device-independent color space that was created by the International Commission on Illumination (CIE) as a way to represent colors in a manner that is perceptually uniform and independent of the specific properties of the display device or lighting conditions [41].

The CIE XYZ color space is based on the tristimulus values of a color, which are calculated based on the amounts of three primary colors (X, Y, and Z) that are needed to match the color being specified. These primary colors were chosen by the CIE to be representative of the average human color vision.

It is important to note that the CIE XYZ color space is a mathematical model of human color vision [42], and as such, it is not a perceptual color space. However, it serves as a foundation for other color spaces such as LAB and LCH which are perceptually uniform and can be used to predict the perceived difference between two colors [43].

The XYZ tristimulus values, defining a three-dimensional space can be calculated as follows:

$$X = k \int_{\lambda} P_{\lambda} \cdot \bar{x}(\lambda) d\lambda \tag{2.1}$$

$$Y = k \int_{\lambda} P_{\lambda} \cdot \bar{y}(\lambda) d\lambda \tag{2.2}$$

$$Z = k \int_{\lambda} P_{\lambda} \cdot \bar{z}(\lambda) d\lambda \tag{2.3}$$

Where k is a constant, P_{λ} is the spectral power distribution of the lighting source, $\bar{x}(\lambda)$, $\bar{y}(\lambda)$, $\bar{z}(\lambda)$ are the color matching functions (see Fig. 2.1) and the integral is over the wavelengths visible range ($\approx 380 - 780$ nm). From the tristimulus values X, Y, and Z it is possible to obtain the *chromaticity coordinates* of a specific color x, y, and z through the following equations:

$$x = \frac{X}{X + Y + Z} \tag{2.4}$$

$$y = \frac{Y}{X + Y + Z} \tag{2.5}$$

$$z = \frac{Z}{X + Y + Z} \tag{2.6}$$

Because $x + y + z = 1$, it is sufficient to use x and y values only. It is common to specify a color by its luminance (γ) and its x and y chromaticity coordinates (x, y, γ) [44].

When talking about trichromatic humans' vision, another valid numerical representation is constituted as its three main components Red, Green, and Blue, defining the *RGB triple* or *RGB Color Space*. The latter can be converted to the XYZ tristimulus values through a linear transformation, from which RGB coordinates can be computed, on the basis of the xyz chromaticity coordinates, thanks to the following relations:

$$\begin{pmatrix} X \\ Y \\ Z \end{pmatrix} = \begin{pmatrix} 0.4124 & 0.3576 & 0.1805 \\ 0.2126 & 0.7152 & 0.0722 \\ 0.0193 & 0.1192 & 0.9505 \end{pmatrix} \cdot \begin{pmatrix} R \\ G \\ B \end{pmatrix} \tag{2.7}$$

Thus, in order to obtain the RGB coordinates, it is possible to use the inverse transform:

$$\begin{pmatrix} R \\ G \\ B \end{pmatrix} = \begin{pmatrix} 0.4124 & 0.3576 & 0.1805 \\ 0.2126 & 0.7152 & 0.0722 \\ 0.0193 & 0.1192 & 0.9505 \end{pmatrix}^{-1} \cdot \begin{pmatrix} X \\ Y \\ Z \end{pmatrix} \tag{2.8}$$

Or,

$$\begin{pmatrix} R \\ G \\ B \end{pmatrix} = \begin{pmatrix} 3.2406 & -1.5372 & -0.4986 \\ -0.9689 & 1.8758 & 0.0415 \\ 0.0557 & -0.2040 & 1.0570 \end{pmatrix} \cdot \begin{pmatrix} X \\ Y \\ Z \end{pmatrix} \tag{2.9}$$

In order to obtain a linear representation of the RGB coordinates expressed with respect to the standard RGB color space, that allows to go back and forth from XYZ to RGB coordinates, the gamma-correction [45] must be applied to the RGB values. The correction procedure is reported for simplicity only for the Red coordinate but is the same for both the Green and Blue ones.

If $R \leq 0.04045$:

$$R_{linear} = \frac{R}{12.92} \tag{2.10}$$

otherwise:

$$R_{linear} = \left(\frac{R + 0.055}{1.055} \right)^{2.4} \tag{2.11}$$

Since the color matching functions $\bar{x}(\lambda)$, $\bar{y}(\lambda)$, $\bar{z}(\lambda)$, like $\bar{r}(\lambda)$, $\bar{g}(\lambda)$, $\bar{b}(\lambda)$ represent the tristimulus values of spectral colors, then they can be substituted to the X, Y, Z and R, G, B values and the following calculations are valid for both [46]:

$$x = \frac{0.4124r + 0.3576g + 0.1805b}{0.6443r + 1.192g + 1.2032b} \tag{2.12}$$

$$y = \frac{0.2126r + 0.7152g + 0.0722b}{0.6443r + 1.192g + 1.2032b} \tag{2.13}$$

$$z = \frac{0.0193r + 0.1192g + 0.9505b}{0.6443r + 1.192g + 1.2032b} \tag{2.14}$$

For the r, g, b the computation steps are similar and the results can be appreciated in the following:

$$r = \frac{3.2406x - 1.5372y - 0.4986z}{2.3274x + 0.1346y + 0.5999z} \tag{2.15}$$

$$g = \frac{-0.9689x + 1.8758y + 0.0415z}{2.3274x + 0.1346y + 0.5999z} \tag{2.16}$$

$$b = \frac{0.0557x - 0.2040y + 1.0570z}{2.3274x + 0.1346y + 0.5999z} \tag{2.17}$$

The three-dimensional space defined by the chromaticity coordinates is represented in Figure 2.2.

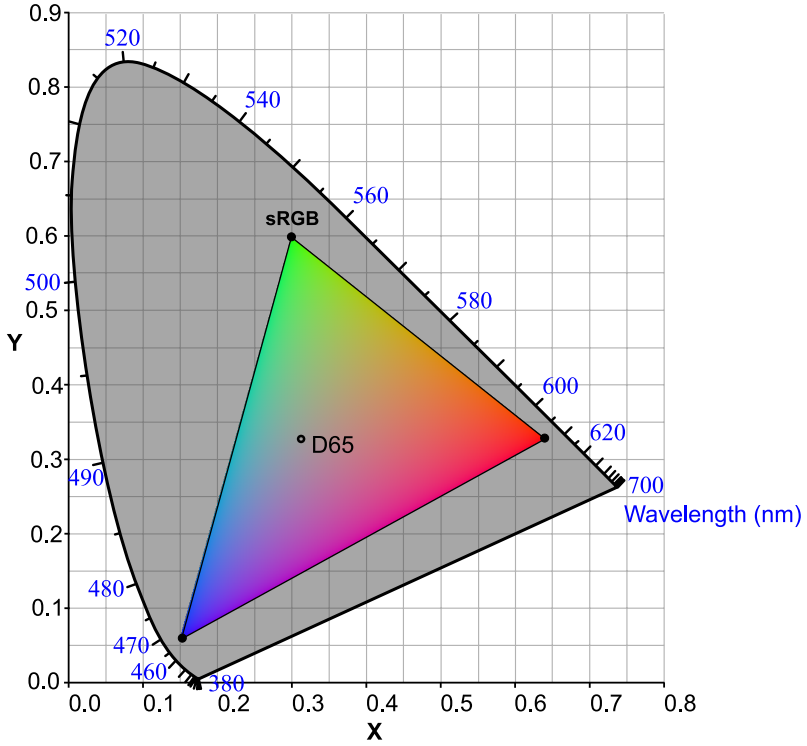
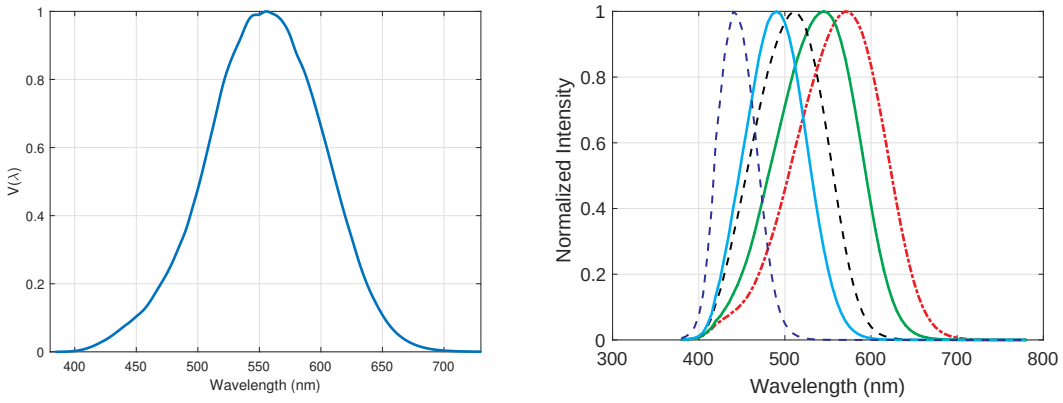


Figure 2.2: Color space defined by the CIE in 1931. The triangle defines the color space standard for RGB coordinates [47]

2.2 Silent Substitution Technique

As introduced before in Section 1.1.2, the photoreceptors constituting the retina, namely rods, cones (Long, Medium, and Short-wavelength sensitive), and ipRGCs present different behaviors to different wavelengths of light stimuli [48]. Indeed, they are responsible for both image-forming (mainly rods and cones) and other non-image-forming functions (ipRGCs) [49]. All of them thus contribute to essential functions of the human visual system [49], as well as other behavioral and physiological responses to light in the environment as they express different proteins, namely *opsins* [50]. Rods express *rhodopsin*, cones express three different types of *photopsin* for the three different wavelength-sensitive classes, and

ipRGCs express *melanopsin*. The opsins are therefore responsible for the light-sensitivity of each photopigment [50] and report different peak wavelengths sensitivities [51, 52]. In Figure 2.3b, the cyanopic (S-cones), melanopic (ipRGCs), rhodopic (rods), chloropic (M-cones), and erythropic (L-cones) Standard CIE[1] normalized sensitivity curves are shown, from left to right, respectively [53].



(a) (b)

Figure 2.3: a) Shows the CIE 10-degrees physiologically relevant or photopic luminous efficiency function. While b) shows the CIE 10-degree normalized photoreceptors sensitivity curves together with ipRGCs cells sensitivities. From left to right, cyanopic, melanopic, rhodopic, chloropic, and erythropic sensitivities [53].

To determine the wavelength of light, i.e. its color, the visual system relies on comparing the responses of the different classes of photoreceptors with distinct spectral sensitivities as illustrated in Figure 2.3. Therefore, by comparing the relative activation of different photoreceptor types, the brain is able to construct a representation of the spectral content of the incoming light. It is worth noting that despite the peaks of the photoreceptor's sensitivity curves being spectrally distinct and far away from each other, it is reasonable to consider them as partially overlapping Gaussian distributions [54].

While combining the response of different photoreceptors can result in a well defined spectral information, Rushton et al. [22] introduced *the principle of univariance* as a fundamental concept in vision science that introduce the fact that a single photoreceptor is unable to distinguish between different lighting wavelengths. In other words, the response of a photoreceptor depends only on the total amount of light that it absorbs, not on the specific wavelength(s). This makes individual photoreceptors response *color-blind* as it weights the input light by means of its spectral sensitivity only [22, 54]. Actually, given these unique photoreceptors properties, it is possible to combine different light spectral distributions to stimulate only one photoreceptor while keeping the activation of all the others unchanged. Indeed, in this way, the effect on that specific photoreceptor can be estimated [55]. In the next section, the details concerning this technique namely, *silent substitution*, will be presented along with standard equations and definitions.

2.2.1 Silent substitution methodology

The silent substitution, first investigated at the beginning of 1900 century, has seen first experimentation only half a century later [56]. The technique is based on the selective stimulation of one or more photoreceptor classes while maintaining the excitation of the others unchanged. This method has been widely used in the last years of neuro-physiological research mainly for addressing the different features

[1] S026:2018

of melanopsin-based receptors, cones, and rods. Its main attributes are excellently described by Spitchan et al. [54] and resumed below:

- **Number of primaries**
  The performed studies always had at least 4 or 5 different light sources in order to assess the selective stimulation of the five photopigment types [57].
- **Light stimuli spectral properties**
  This feature of the light stimuli is of primary importance in order to obtain a certain level of contrast over the studied class of photoreceptors [58–61].
- **Viewing geometry**
  The most employed ones are either a Ganzfeld[2] or a Maxwellian[3] one. More details about Viewing Geometry will be presented later in Sec. 3.3
- **Field size**
  This is associated with the optical modules that are employed in the measurement device. This feature obviously sets a limit over the retinal regions that can be studied.
- **Background light**
  This is essential in order to set a photopic condition where thus rods are assumed to be silenced due to their saturation.
- **Temporal properties of photoreceptor classes**
  An alternative silencing technique could be performed in the time domain by means of exploiting the different receptors' temporal properties. For example, melanopsin is way slower than the other receptor classes.
- **Retinal regions**
  As reported before in this section, different retinal regions correspond to different photoreceptor distributions meaning that moving toward the peripheral region cone density drops off very quickly as *Figure 1.3* shows. This retinal feature can be exploited for performing silent substitution without the need to have multiple numbers of primaries or certain modulation types. Once ensured to be in photopic condition, rods are assumed to be saturated and thus silenced, and, more, exciting the peripheral retina means that mostly ipRGCs are reachable. In particular, the blind retinal spot[4] is employable for stimulating melanopsin in the ipRGC axons [62].

The implementation of a system able to perform this type of stimulation is not straightforward since there are different associated challenges such as retinal inhomogeneities, individual cone spectral sensitivity differences, different melanopsin states, rod intrusion, human eye optical scattering, and device uncertainty.

Besides that, given a specific intensity spectral distribution of the light stimuli, each photoreceptor's stimulation level can be recovered by means of their equivalent illuminance, namely cyanopic, melanopic, rhodopic, chloropic, and erythropic illuminance. Lucas et al. referred to this quantity as *equivalent α-opic illuminance* E_α (α-lux), where α can be one of the five aforementioned photo-sensitives cells [51].

Therefore, E_α can be expressed as follows:

$$E_\alpha = K_m \cdot \int E_{e,\lambda}(\lambda) \cdot N_\alpha(\lambda) d\lambda \cdot \int V(\lambda) d\lambda \tag{2.18}$$

[2]The stimulus is a homogeneous field in an integrating sphere [54].
[3]The source is imaged on the pupil entrance [54].
[4]A large oval area where light is not received due to the absence of rods and cones.

Where λ is the radiation wavelength, $K_m = 683.000\, lm/W$ is the maximum spectral luminous efficacy[5], $V(\lambda)$ is the normalized spectral luminous efficacy function for the photopic vision (see. Fig. 2.3a), $E_{e,\lambda}$ is the spectral power distribution of the light source (W/m^2) and $N_\alpha(\lambda)$ is the α photoreceptor sensitivity curve considered, with unity-area normalization. As $intV(\lambda)d\lambda = 106.857$ and choosing to define $\int N_\alpha(\lambda)d\lambda = 1$, equation 2.18 can be simplified to an equivalent form for photopic lux, as follows:

$$E_\alpha = 72983.25 \cdot \int E_{e,\lambda}(\lambda) \cdot N_\alpha(\lambda)d\lambda \cdot \int V(\lambda)d\lambda \tag{2.19}$$

The aforementioned statement makes the selection of the primary light sources' peak wavelength, i.e. spectral conformation of any possible $E_{e,\lambda}$, a crucial part in the employment of Silent Substitution [58]. Therefore, when a pair of colors or two different light distributions $E_{A,\lambda}(\lambda)$ and $E_{B,\lambda}(\lambda)$ is considered, each photo-sensitive cell is stimulated with of a determined amount or contrast when these colors are alternated [54, 63]. In this case, the commonly used Michelson Contrast (C_M) and Weber Contrast (C_W), can be computed as follows [64]:

$$C_M = \frac{E_{\alpha-max} - E_{\alpha-min}}{E_{\alpha-max} + E_{\alpha-min}} \qquad C_W = \frac{E_{\alpha-max} - E_{\alpha-min}}{E_{\alpha-min}} \tag{2.20}$$

Where $E_{\alpha-max}$ and $E_{\alpha-min}$ are the maximum and minimum equivalent $\alpha-opic$ illuminances given by the two considered spectral distributions $E_{A,\lambda}(\lambda)$ and $E_{B,\lambda}(\lambda)$ with respect to the specific α photopigment considered. Higher contrast between the two selected colors implies a higher activation of a given photopigment, therefore an increased contribution of its specific effect on the observed phenomena, i.e. PLR or ERGs responses.

2.2.2 System Optimization

As previously described, the Silent Substitution technique foresees the combination of different primary intensities to achieve a *target* stimulation level in terms of contrast for each photosensitive cell. Now, let us examine how the theory can be applied to effectively find combinations of different light stimuli to selectively stimulate a specific photoreceptor while keeping the activation of all the others constant.

Let's consider the simplest case scenario, i.e. a system with four different primaries: Blue, Green, Yellow, and Red as this is the minimum number of primaries required to achieve silent stimulation on the there class of cones and ipRGCs. The light intensity of each primary, in terms of radiant flux (W), it's most likely to be proportional to the LED's forward current I_F and therefore to the Duty Cycle (DC $\in [0-100\%)$ used to drive the specific source [65, 66]. If the system is properly calibrated, i.e. the spectral distribution of each light source is known, and compensation for the non-linear relationship between the DC and Light Intensity is corrected, it is possible to analytically compute the spectral power distribution of the four light sources in (W/m^2) combined, i.e. $E_{e,\lambda}(\lambda)$ (see Eq. 2.18), for each possible DC value.

If the contribution of Rods is neglected, thus considering only photopic illumination conditions, it is possible to approximate the input-output relation of our four-primaries light source system (RGBY) as a linear set of equations. Therefore, the conversion from the four Duty Cycle (DC) values (i.e. Red, Green, Yellow, and Blue intensities, in this case) and the four corresponding $\alpha-opic$ stimulations levels in (α-lux) can be determined by 16 real coefficients, namely $K_{i,j}$, with the following equation:

$$\begin{bmatrix} E_{cyan} \\ E_{mel} \\ E_{chlor} \\ E_{eryth} \end{bmatrix} = \begin{bmatrix} K_{1,1} & K_{1,2} & K_{1,3} & K_{1,4} \\ K_{2,1} & K_{2,2} & K_{2,3} & K_{2,4} \\ K_{3,1} & K_{3,2} & K_{3,3} & K_{3,4} \\ K_{4,1} & K_{4,2} & K_{4,3} & K_{4,4} \end{bmatrix} \times \begin{bmatrix} R_{DC} \\ G_{DC} \\ B_{DC} \\ Y_{DC} \end{bmatrix} \tag{2.21}$$

[5] CIE S017:2020 -17-21-092

Where $R_{DC}, G_{DC}, B_{DC}, Y_{DC}$ are the light ratios, i.e. duty cycle values [0,100%] of Red, Green, Blue, and Yellow LEDs and $E_{cyan}, E_{mel}, E_{chlor}, E_{eryth}$ are the equivalent α-opic illuminance for Cyan-opic (S-cones), Melan-opic (ipRGCs), Chlor-opic (M-cones), and Erythr-opic (L-cones), respectively. For any pair of colors, namely **A** and **B**, i.e. eight pairs of DC values, it is possible to compute the stimulation levels of each photopigment with the above equation. Subsequentially, the Michelson Contrast (C_M) for any given photopigment activation level delivered by switching from the two given colors **A** and **B** can be calculated with Eq. 2.2.1 for each one of the photopigment activation levels. Finally, an optimization algorithm, e.g. Generalized Reduced Gradient [67] (GRG), can be used to find the best combination of DC values to achieve a *target* contrast on a specific photopigment while silencing the others.

Chapter 3

Optical Notions

3.1 Optical Elements

3.1.1 Lenses

An optical lens is a device that manipulates the propagation of light through the application of refraction. Light passing through a medium with different refractive indices, such as air and glass, will bend at the interface between the two media. An optical lens takes advantage of this phenomenon by carefully shaping the surfaces of one or more pieces of transparent material, typically glass or plastic, to control the way in which light is refracted as it passes through the lens. The shape and curvature of the lens surfaces determine its *optical power*, which is measured in *diopters* and is defined as the reciprocal of the *focal length* in meters. The focal length, in turn, is the distance between the lens and the point where light rays that are parallel to the optical axis converge. The *aperture* of the lens, which is the diameter of the *aperture stop*, controls the amount of light that can pass through the lens and affects the *depth of field*. Figure 3.1 the basic optic ray tracing diagram of a converging thin lens. A first approximated description of the lens'

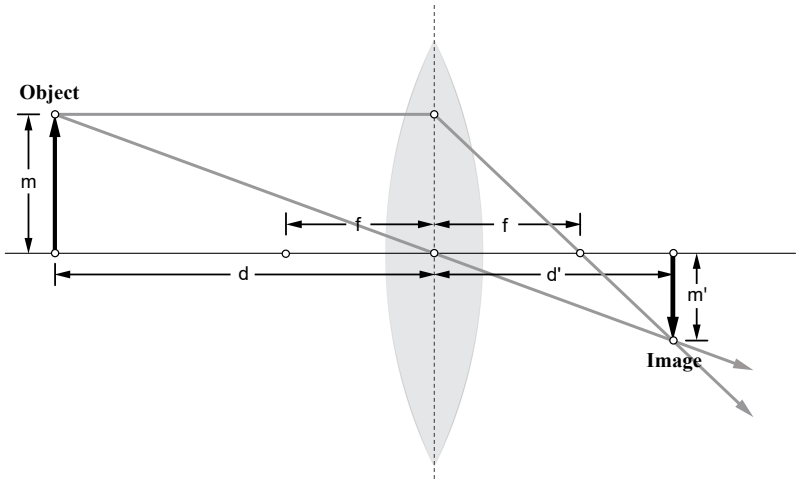


Figure 3.1: Thin Lens ray tracing diagram

behavior can be obtained by neglecting its thickness: in this way, it is possible to find a simple relation between object distance, image distance, and focal length as reported in the following Equation 3.1.

$$\begin{cases} \frac{1}{f} = \frac{1}{d} + \frac{1}{d'} \\ \\ M = \frac{m'}{m} \end{cases} \tag{3.1}$$

Where f is the focal distance, d is the distance of the object from the lens, d' is the distance of the real image from the lens, m is the size of the object, m' is the size of the image and M is the total magnification

Real Thick Lenses

Thick lenses, also known as thick optical elements, are lenses that have a non-negligible thickness compared to their curvature radius, i.e. to their focal distance. Modeling the behavior of light passing through such lenses requires taking into account the refraction phenomena that occur on their curved surfaces. However, *Gaussian optics* [68–70], a mathematical model of geometric optics, can still be used to analyze and design thick lenses by defining their principal planes.

More specifically, a thick lens can be represented by two principal planes [71]: the rear and front principal planes. These planes represent the locations where a forward axial ray arriving from the right or left appears to refract. By replacing a thick lens with these two principle planes and an *effective focal length* (EFL), it is possible to apply thin lens retracing to the thick lens. Figure 3.2 shows the main optical elements when considering a thick lens.

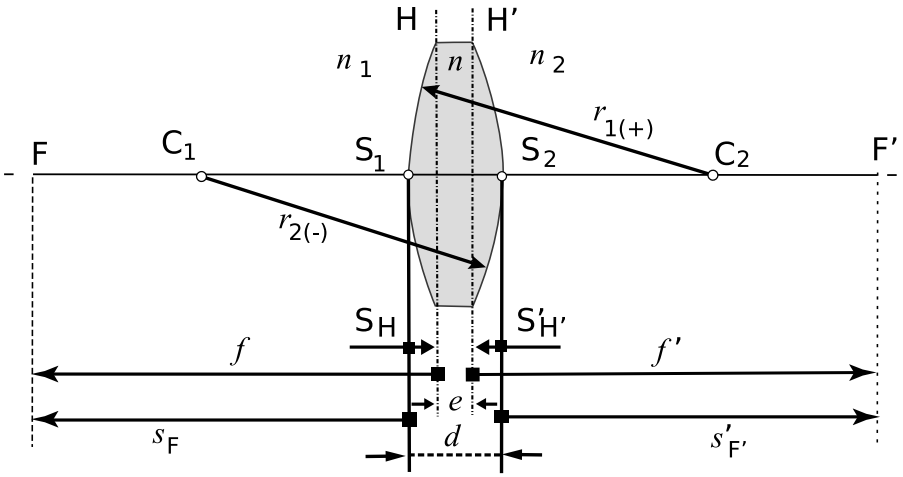


Figure 3.2: A diagram of a thick lens, with annotations for key parameters including the thickness of the lens at the center ($\boldsymbol{d}$), the thickness of the lens at the edge ($\boldsymbol{e}$), the radius of curvature of the first surface ($\boldsymbol{r_1}$), the radius of curvature of the second surface ($\boldsymbol{r_2}$), the primary principal plane ($\boldsymbol{H}$), the secondary principal plane ($\boldsymbol{H'}$), the front focal point ($\boldsymbol{F}$), the back focal point ($\boldsymbol{F'}$), the vertex of the first optical surface ($\boldsymbol{S_1}$), the vertex of the second optical surface ($\boldsymbol{S_2}$), the distance from the vertex of the first optical surface to the primary principal plane ($\boldsymbol{S_H}$), the distance from the vertex of the second optical surface to the secondary principal plane ($\boldsymbol{S'_{H'}}$), the distance from the surface of the first optical surface to the front focal point ($\boldsymbol{S_F}$), the distance from the vertex of the second optical surface to the back focal point ($\boldsymbol{S'_{F'}}$), the center of a hypothetical sphere whose radius ($\boldsymbol{r_2}$) is always perpendicular to the surface ($\boldsymbol{C_1}$), the center of a hypothetical sphere whose radius ($\boldsymbol{r_1}$) is always perpendicular to the surface ($\boldsymbol{C_2}$), the effective front focal length ($\boldsymbol{f}$), and the effective back focal length ($\boldsymbol{f'}$).

It is important to note that in general, the back focal distance and front focal distance of a thick lens are different from its EFL. Whenever the design of a new optical prototype is encountered, especially for a

compact design, the EFL, in terms of front focal distance and back focal distance should be carefully taken into account. The EFL of a thick lens can be calculated using the following equation:

$$\frac{1}{f} = (n-1)\left[\frac{1}{r_1} - \frac{1}{r_2} + \frac{(n-1)\cdot d}{n\cdot r_1 \cdot r_2}\right] \tag{3.2}$$

where n represents the refractive index of the lens material, r_1 and r_2 represent the radii of curvature of the lens surfaces, and d represents the thickness of the lens. It is worth mentioning that, while the Gaussian optics model provides a good approximation of the behavior of light in thick lenses, it is not completely accurate and other more sophisticated models exist such as *paraxial optics* [72] and *wave optics* [73]. These models are commonly used to study and design thick lenses in various fields such as microscopy, imaging, and optical communication.
When the design of an optical system that employs lenses, as lately shown in Part II, it is necessary to take into account all the above statements concerning thick lenses, such as EFL, as well as other implications as described in the next Section 3.1.1.

Aberrations

Geometric optics is a simple way of describing some features of optic systems: when thick lenses are considered and *paraxial approximation*[1] is no longer valid, the deviations found are called *aberrations* [74, 75]. Aberrations in optics refer to the deviation of the performance of an optical system from the ideal. In other words, aberrations are defects or distortions that occur in an optical system, such as a lens or mirror, that result in a less-than-perfect image. There are several types of aberrations that can occur in an optical system, including spherical aberration, chromatic aberration, and coma. Aberrations can be corrected by using special optical designs and materials, or by using multiple lenses or mirrors. Some aberrations can also be corrected digitally with image processing techniques. In the following paragraph, the most common aberrations along with some correction techniques are presented.

Spherical aberrations

Spherical aberration [76,77] is an optical aberration that occurs when a lens is not able to focus all parallel incoming light rays to a single point. This is due to the spherical shape of the lens, which causes light rays entering the lens at different distances from the optical axis to converge to different points. As a result, the overall image produced by the lens is blurred and out of focus. This effect is more pronounced towards the edge of the lens, where the angle of incidence of the light rays is greater.

To reduce spherical aberrations, as shown in Figure 3.3(b) *aspherical lenses* [78] are often used. These lenses are designed with a surface profile that is not a portion of a sphere or cylinder, but rather a more complex profile that is optimized to minimize spherical aberrations. Another solution is to use a diaphragm, which acts as a physical stop and prevents marginal rays from entering the system.

The human eye can also suffer from spherical aberration [76,77] due to the curved shape of the cornea and lens not being able to focus all parallel light rays to a single point. However, the human eye has mechanisms in place such as accommodation and the ciliary muscle 1.2.1 that help to reduce spherical aberration and maintain clear vision.

Chromatical aberration

n optics, the refractive index of a material is dependent on the wavelength of light, this property is known as dispersion. This can cause a phenomenon, also shown in Figure 3.4a, called *chromatic aberration* [79],

[1] In geometric optics, the paraxial approximation is a small-angle approximation used in Gaussian optics and ray tracing of light through an optical system. A paraxial ray is a ray that makes a small angle ($\boldsymbol{\theta}$) to the optical axis of the system and lies close to the axis throughout the system. $\boldsymbol{\sin\theta \approx \theta}$, $\boldsymbol{\tan\theta \approx \theta}$ and $\boldsymbol{\cos\theta \approx 1}$.

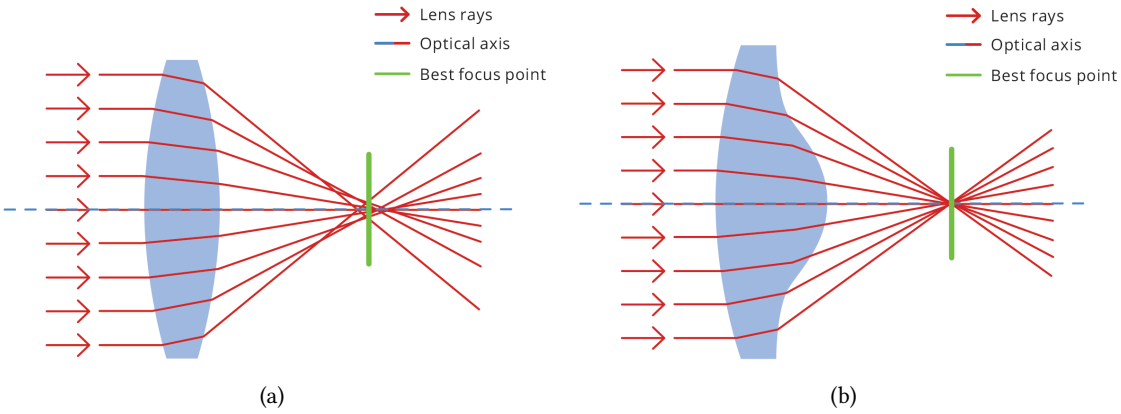


Figure 3.3: (a) shows spherical aberration. (b) shows the behaviour of aspherical lens,

where white light entering a lens is split into its spectral components, each wavelength takes a slightly different path through the lens, which causes each color to be focused at a slightly different point, leading to a loss of sharpness in the image. Chromatic aberration is more pronounced at the edges of the lens.

A solution to reduce chromatic aberration is to use an *achromatic doublet* [80], which is a combination of two lenses made of different materials with different dispersion properties that help to correct the chromatic aberration. Another solution is to use monochrome light, as it eliminates the need to correct for chromatic aberration. Chromatic aberration can occur in two different types: longitudinal, where the focal length of the lens changes with wavelength, and lateral, where the position of the focal spot changes with wavelength. As reported in Figures 3.4a,3.4b chromatic aberrations are classified into two types: longitudinal and lateral, and it is determined by whether or not the entering parallel rays are parallel to the optic axis.

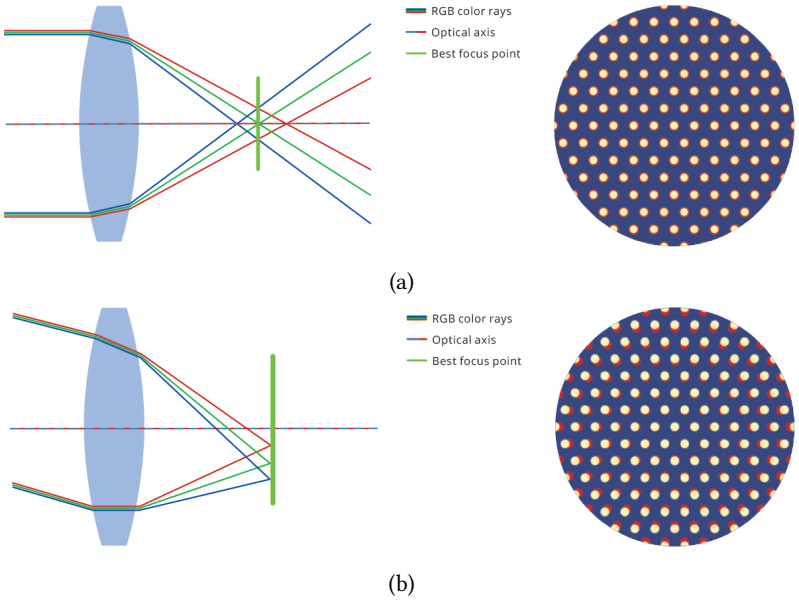


Figure 3.4: (a) Longitudinal chromatic aberration. (b) Latitudinal chromatic aberration

When designing an optical system that has the function to stimulate the eyes with different wavelengths, chromatic aberrations should be taken into account, especially when using a focused stimulation with a Maxwellian-View optical system (see. Sec 3.3.1).

Astigmatism

Astigmatism [81] is an optical aberration that occurs when an optical lens does not have the same curvature in all directions. This causes a difference in focus for light rays entering the lens in different directions, as shown in Figure 3.5 resulting in a blur in one direction and a clear image in the other direction. The blur can manifest as circles becoming elongated or distorted in one direction, and this effect is dependent on the orientation of the image with respect to the optical axis. The blur can be corrected by using lenses with a specific power distribution, or by using multiple lenses to correct the aberration.

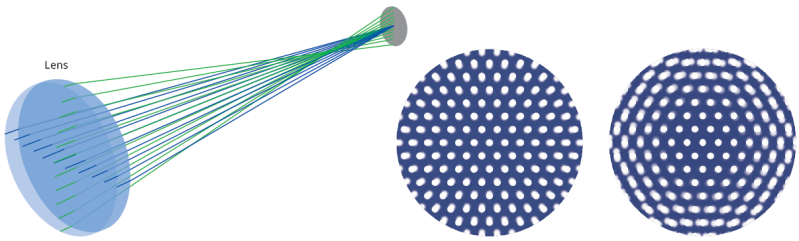


Figure 3.5: Astigmatism

Coma

Coma aberration occurs when parallel rays entering the lens at a certain angle [82, 83] are brought to focus at different positions, depending on their distance from the optical axis [84]. This happens because principal planes are effectively planar only for paraxial rays, while in general, they are curved surfaces. As shown in Figure 3.6, a circle in the object plane will appear in the image as a comet-shaped element, which gives the name to this aberration.

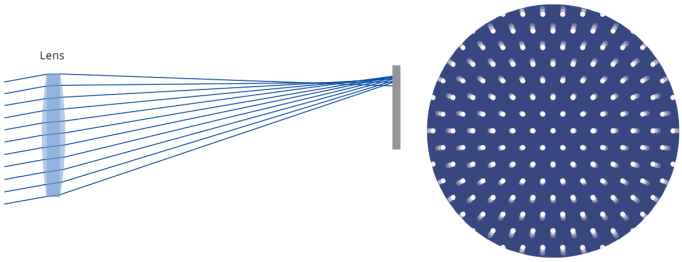


Figure 3.6: Coma aberration

Field Curvature

Field curvature [85, 86] aberration is an optical aberration that occurs when a lens does not produce a planar image from a planar object. This is due to the fact that parallel light rays entering the lens from different directions do not focus on a single plane, but rather on a curved surface. This results in the image appearing distorted or curved. In Figure 3.7 thee is an example of a diagram that shows the concept of field curvature aberration.

In ophthalmic instrumentation, field curvature aberration can be observed in instruments such as fundus cameras [87], which are used to capture images of the retina. Due to the curved shape of the retina, the image captured by the instrument may appear distorted or curved, resulting in a loss of resolution and image quality. To reduce field curvature aberration in ophthalmic instrumentation, special lens designs, and optical correction techniques can be used to ensure that the light rays entering the lens are focused on a single plane.

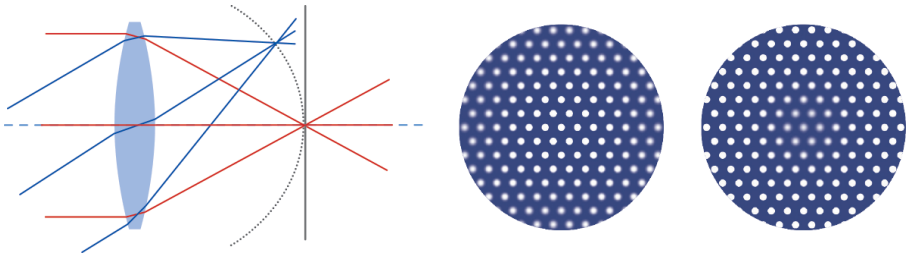


Figure 3.7: Field curvature

Distorsion

Distortion [88] is an optical aberration that occurs when the magnification of an image is affected by the distance of the object from the optical axis [89]. This type of aberration is known as radial distortion and, as illustrated in Figure 3.8 it can manifest in two different forms: barrel and pincushion distortion.

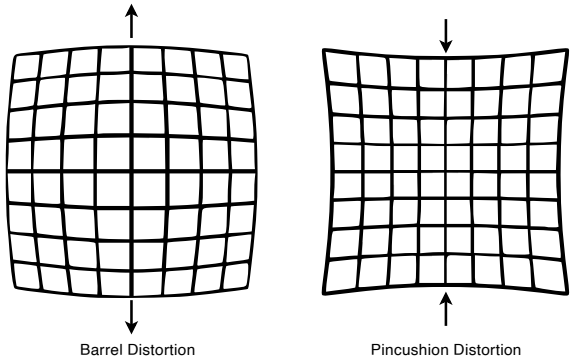


Figure 3.8: Typical Distortion on a square images

Barrel distortion is characterized by an increasing magnification with the distance from the optical axis, giving the appearance of an image being "pushed out" around a central point. This type of distortion is often found in wide-angle lenses. On the other hand, Pincushion distortion is characterized by a decreasing magnification with the distance from the optical axis, giving the appearance of an image being "pulled in" towards a central point, this type of distortion is often found in telephoto lenses. In ophthalmic instrumentation, distortion can be a problem when using cameras such as CMOS cameras which are widely used for eye imaging. Distortion can cause a loss of resolution and image quality, making it difficult to accurately diagnose certain eye conditions. To reduce distortion in ophthalmic instrumentation, special lens designs, and optical correction techniques can be used to ensure that the image captured is as accurate as possible. It's worth noting that distortion can be corrected with software by applying an inverse distortion correction algorithm, which is commonly used in digital image processing techniques [90]. This method has been widely studied in the literature, for example in [91] and [92].

3.1.2 Other optical elements

Dichroic Flat Mirrors

A dichroic mirror [93] (or dual-band mirror, dual-wavelength mirror, dichroic reflector) is a mirror that has significantly different reflection or transmission properties at two different wavelength regions of some often not so large width. These mirrors can be used to selectively reflect or transmit specific wavelengths of light, making them useful in a wide range of applications such as spectroscopy, microscopy, and color separation [93]. In order to achieve the desired performance, the quality of the substrate material and the

possible reflections from the back side need to be carefully considered. To mitigate these issues, an anti-reflection coating is often applied to the backside of the mirror to reduce reflections [94]. Additionally, a slight wedge form of the substrate can often eliminate the effects of residual reflection.

Prisms

Prisms [95] are solid glass optical elements that are ground and polished into specific geometric shapes that have specific optical properties. They are commonly used to change the direction of light by refracting and reflecting it. Prisms can be used to invert, rotate, or deviate a beam of light, and they can be used to separate light into its constituent colors, this phenomenon is called dispersion, and is the basis of prism spectroscopy.

The simplest prism is a triangular block of glass with two faces at right angles to each other and one face at an angle of 45 degrees. This type of prism is known as a right-angle prism, and it deflects a beam of light through a right angle. It is commonly used to change the direction of a beam of light or to deviate a beam of light by a specific angle.

Prisms can be made from various types of glass, including BK7, fused silica, and calcium fluoride, each of these materials has different properties that make them suitable for different applications. For example, BK7 [96] is a commonly used glass for prisms due to its low cost and high transmission, but fused silica has a lower thermal expansion and a higher damage threshold, making it suitable for high-power laser applications.

Prisms can be used in a wide range of applications such as laser systems, optical communication, and spectroscopy. They are also commonly used in ophthalmology, as they can be used to correct certain types of vision disorders such as double vision.

3.2 Basics of Light Systems

Illumination is one of the most critical components when designing an ophthalmic device where accurate image acquisition or state of art light stimulation of the human visual system must be achieved. The selection of the appropriate lighting component is the first thing to ensure that the developed system performs its tasks accordingly to the theoretical approach, thus of course excluding some levels of approximation, without being harmful or dangerous for the subjects involved.

As the above statements represent the basis of an optical system, it's clear that improper illumination will potentially result in wrongly collected data, measurement mismatches with other research, and potential safety risks. This is why the choice of the type of lighting components is of primary importance [97]. The choice of the proper illumination system focuses on many different parameters, including:

- Light source type;
- Total optical output power;
- Lighting geometry;
- Wavelength and Light Coherency;
- Surface property of the illuminated material (absorption and reflectivity);
- Safety considerations if humans or animals are involved;
- Cost and market availability;

3.2.1 Types of Illumination Source

Illumination sources play a crucial role in ophthalmic instrumentation, as they provide the light needed to capture images of the eye. Different types of illumination sources are used depending on the specific application, each with its own set of advantages and disadvantages. One common type of illumination source is the *halogen lamp* [98]. These lamps produce a bright, white light and have a long lifespan, making them well-suited for ophthalmic instrumentation. However, they also produce a significant amount of heat, which can be a problem in certain applications. LEDs (*light-emitting diodes*) [99] are becoming increasingly popular in ophthalmic instrumentation due to their low power consumption, low costs, long lifespan, and high efficiency. They can be used in a variety of applications, including fundus cameras, optical coherence tomography (OCT), and visual field analyzers. Another type of illumination source is the *xenon lamp*, which is known for its high intensity, short pulse duration, and broad spectrum [100,101]. Xenon lamps are commonly used in imaging systems such as (OCT) and *laser-scanning ophthalmoscopy* (LSO). A fourth type of illumination source is the *laser*, which is often used for microsurgery, diagnosis, and therapy in ophthalmology [102]. They offer a high level of precision, excellent coherence and monochromaticity, and small spot size. All the above types of light sources differ from each other mainly for the wavelength emission spectra, that is usually characterized by the *peak wavelength of emission* and *emission bandwidth*. Typical emission spectra of common light sources are shown in Figure 3.9.

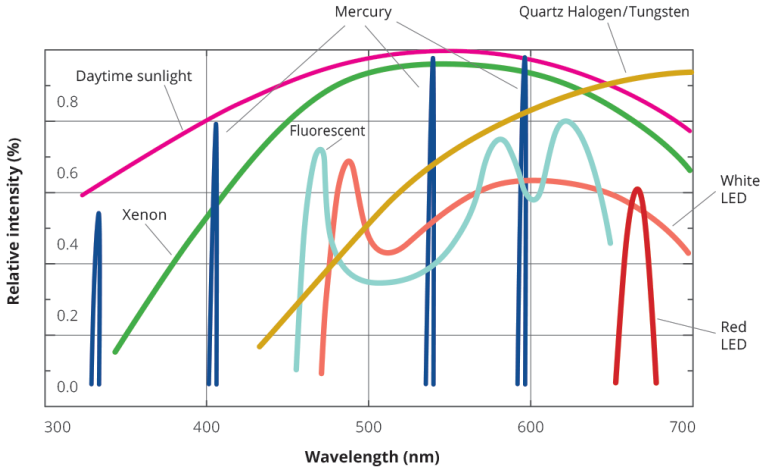


Figure 3.9: Emission spectra of different light sources

Light Emitting Diodes

A LED is a semiconductor device that emits light when an electric current flows through it. The brightness of an LED can be basically controlled by adjusting the intensity of the current flowing through it, and it is typically linear in proportion to the current.

The light emission in an LED is a result of the recombination of electrons and holes within the semiconductor material. The electrons and holes are contained within *energy bands*, known as the conduction band and valence band, respectively. The energy gap between these bands, known as the *bandgap*, determines the energy of the photons (light particles) that the LED emits. This energy, in turn, determines the wavelength of the emitted light and thus the color of the light. Different semiconductor materials with different bandgaps produce different colors of light [99].

LEDs are particularly useful in ophthalmic instrumentation due to their reliability, long lifespan, high efficiency, and low power consumption [103]. Furthermore, due to their distinct operating principles, LEDs can be engineered to emit light across a broad range of wavelengths, particularly in the visible light

spectral range. As previously mentioned, this is accomplished by utilizing different semiconductor materials, or by adjusting the structure of the LED, allowing for the precise manipulation of the bandgap energy and subsequent emission wavelength. This feature is particularly useful, enabling the use of specific wavelengths for specific applications, thus making LEDs to be widely used in various ophthalmic techniques, such as fundus cameras, optical coherence tomography (OCT), and visual field analyzers [104].

3.2.2 Photometry and radiometry

Electromagnetic radiation's physical properties are characterized by radiometric units, therefore light can be described in terms of physical quantities (e.g. *radiant flux*). Depending on the types of the selected light source, the specifications might be given by the manufacturer using any of the following radiometric quantities: *power* (also called radiant flux and measured in watts (W)), *irradiance* (measured in W/m^2), *radiant intensity* (measured in watts per steradian (W/sr)), and *radiance* (measured in W/m^2·sr). However, the radiometric units are irrelevant when it comes to light perception by a human being. The light intensity of an optical source perceived by the human eye is a photometric quantity and the luminous intensity is measured in units of candela (cd), which is an International System of Units (SI) base unit.

The corresponding photometric quantities, which are based on the SI unit for luminous intensity are listed in Table 3.1 below. These values are weighted by a spectral luminous efficiency function, V (λ) (Figure 2.3a) which describes the human eye's sensitivity to light at different wavelengths in daylight. As a result, candelas provide information about the perceived brightness of a source, while power, irradiance, radiant intensity, and radiance provide information about the absolute brightness of a source.

Table 3.1: Unit of Measures for common Radiometric and Photometric quantities

Radiometric Quantity	**Radiometric**	**Photometric Quantity**	**Photometric**
Radiant Power (Radiant flux)	W (watt)	Luminous Power (Luminous Flux)	lm = cd · sr (lumen = candela · steradian)
Irradiance	W/m^2 (watt/meter^2)	Illuminance	lx = cd · sr/m^2 = lm/m^2 (lux = candela · steradian/meter^2 = lumen/meter ^{2})
Radiant Intensity	W/sr (watt/steradian)	Luminous Intensity	cd (candela)
Radiance	W/m^2 · sr (watt/meter^2 · steradian)	Luminance	cd/m^2 = lm/m^2 · sr = nit (candela/meter^2 = lumen/meter^2 · steradian = nit)

Based on the candela, three other photometric quantities are also commonly used to specify power measurements for LEDs: luminance (measured in cd/m^2, which is also sometimes referred to as a Nit), luminous flux, whose SI unit is the lumen (lm), and illuminance whose SI unit is the lux (lx). To convert between radiometric and photometric units, one needs to know the photopic spectral luminous efficiency curve V(λ), which gives the spectral response of the human eye to various wavelengths of light (see Fig. 2.3a). The original curve, which was adopted by the Commission on Illumination (CIE) as the standard in 1924, is still used today, even though modifications have been suggested [105]. Empirical data shows that the curve has a maximum value of unity at 555 nm, which is the wavelength of light at which the human eye is most sensitive, and trails off to levels below 10^{-5} for wavelengths below 370 nm and above 780 nm.

Conversion from radiometric to photometric units becomes more complex if the light source is not monochromatic. In this case, the mathematical quantity of interest is

$$\Phi_V = K_m \cdot \int_{\lambda=380}^{\lambda=780} \Phi_E(\lambda) \cdot V(\lambda) d\lambda \tag{3.3}$$

Where, Θ_V is the luminous flux in lumens, Km is a scaling factor equal to ≈ 683 lumens per watt, $\Theta_E(\lambda)$ is the spectral power in watts per nanometer, and $V(\lambda)$ is the photopic spectral luminous efficiency function (see Fig. 2.3a). Note that the integration is only carried out over the wavelengths for which V(λ) is non-zero (i.e. λ = 380 - 780nm). Since $V(\lambda)$ is given by a table of empirical values, it is best to do the integration numerically.

3.3 Viewing Geometry

In this section, we will briefly provide an overview of the various optical stimulation systems used in scientific research for generating light stimulation. These systems are classified into two categories: *nonimage-forming* and *image-forming* arrangements.

The *nonimage-forming* arrangements include the Maxwellian view system and the Ganzfeld stimulator, which are widely used in scientific research for studying visual perception, visual adaptation, and visually evoked potentials. The Newtonian view system which is similar to the Maxwellian view system, but it simulates light from a theoretically infinitely distant source.

The *image-forming* arrangements include off-the-shelf devices and the recent emergence of multi-primary displays, which allow for the inclusion of more primary colors and the generation of stimulation for independent and combined photoreceptor and post-receptoral excitations.

Additionally, this section also highlights some limitations of these systems that researchers need to consider, such as limitations related to color gamut, sampling frequency, light range, and spatial resolution. These factors can have important implications in research practice and should be taken into account when selecting and using these systems.

Newtonian-View or natural view A Newtonian view [106] is an optical setup that consists of a bright light source, such as a tungsten bulb or a light-emitting diode (LED), that is placed at a large distance, typically between 50 cm to several meters from the observer as shown in Figure 3.10a. One of the advantages of the Newtonian view is that it provides a more realistic simulation of natural light conditions. This can be useful for studying visual perception and visual adaptation under conditions that are more alike to those encountered in everyday life [107]. However, one of the disadvantages of the Newtonian view is that it is usually more complex and expensive, as it requires more powerful light sources due to its low efficiency compared to other optical setups. Additionally, it is more challenging to control the stimulus intensity, as the amount of light that shines on the retina, is feedback regulated by the pupil size, thus can affect the amplitude of the response obtained using this setup [108].

Maxwellian-View In the Maxwellian view [109] the light pattern is projected onto the fundus in a so-called retinal projection. The arrangement is configured in such a way that the exit pupil of the optical system is placed directly on the entrance pupil of the eye as if the pattern is placed at the conjugate plane of the retina. This allows to maximize the efficiency of the light stimulation, and if the system is well designed as explained later in Sec. 3.3.1, to stimulate the eye in *open-loop*.

Ganzfeld-View A ganzfeld stimulator [110] is an optical device that is used to produce a uniform and diffuse light field over the entire visual field and it is typically used to study the visual perception of the human eye. As illustrated in Figure 3.11, the device consists of a dome or bowl-shaped reflector, usually referenced as an *integrating sphere*, that is placed very close to the eye, which is illuminated by a light that comes out from the dome-aperture. This creates a homogeneous and isotropic field of light that fills the entire visual field. The ganzfeld stimulator is widely used in various research fields such as

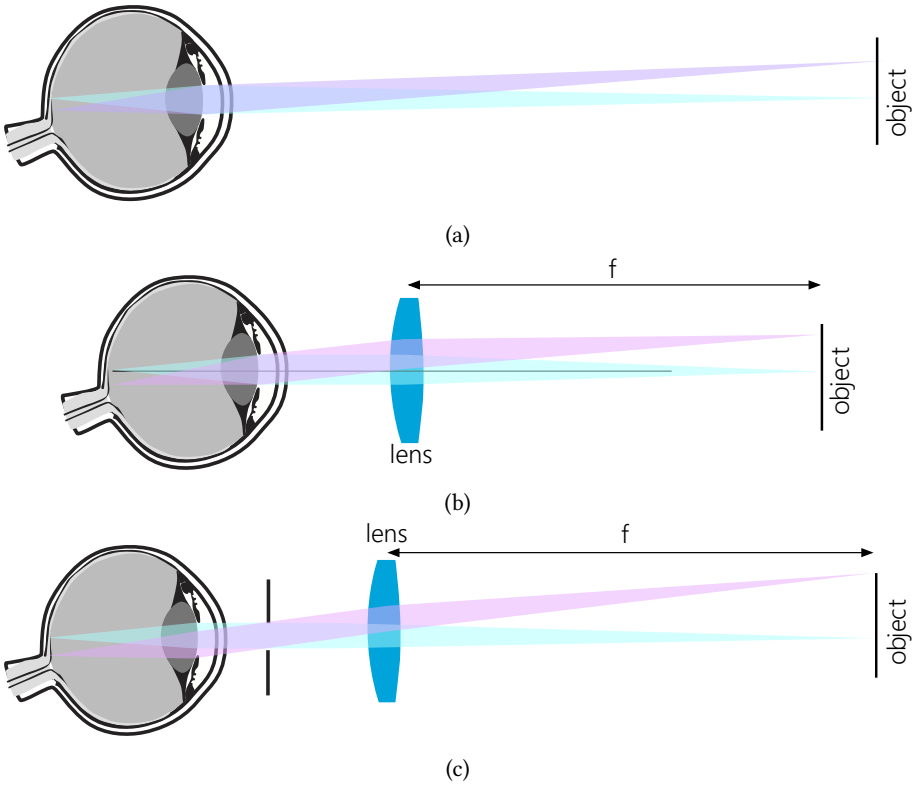


Figure 3.10: Newtonian View configurations. (a) The object is placed at a very large distance from the eye. (b) A lens is added, and the object is placed on the focus of the lens to be observed from an infinite distance. (c) An artificial pupil can be used with the system to regulate the amount of light entering the eye. This is still considered a Newtonian setup, but the inclusion of the artificial pupil causes vignetting for a large field of views. Therefore, the size of the artificial pupil must be smaller than that of the actual pupil of the eye.

visual physiology, psychophysics, and neuroscience for studying visual perception, visual adaptation, and visually evoked potentials.

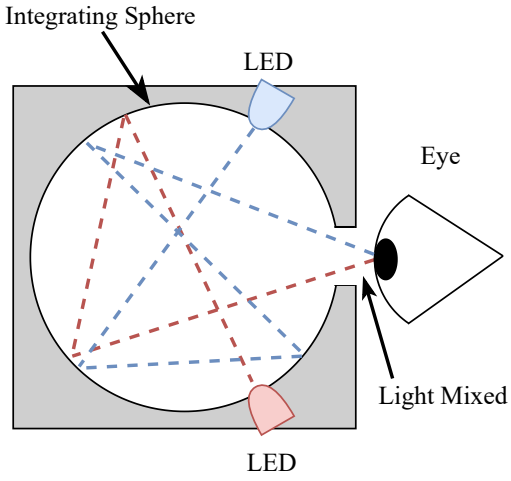


Figure 3.11: Ganzfeld-View. An integrating sphere is used to mix the light from different sources. The stimulus is presented with a large field of view or can be reduced with an artificial pupil.

3.3.1 Maxwellian View

In ophthalmology, a Maxwellian-view optical configuration uses a combination of stop-apertures and lenses such as to provide a wide field of view and superior control on retinal illuminance (see Sec. 3.3.2). It is called Maxwellian view because it is named after *James Clerk Maxwell*, who proposed this design. The basic elements of a Maxwellian view usually include the following optical components:

- A condenser lens: This lens is located near the light source and is used to collimate the light beam;
- A diaphragm or an additional aperture stop can be used to reduce the collimated beam size, as to improve beam quality and aberrations, at the cost of reduced field of view;
- A dichroic mirror or beam splitter: This mirror could be located after the condenser lens and can be used to redirect some of the light away from the source optical path, such as the eyepiece or a camera;
- An objective lens: This lens is located near the convex mirror and is used to correct for distortion and other aberrations that may be introduced by the mirrors;
- An eyepiece or camera: This component is located at the end of the device and is used to observe or record the image of the eye bulb or the retina.

One of the systems described later in Part II is based on the principle of the Maxwellian view, as shown in Figure 3.12. As shown in the Figure, a light source is located on the focus plane of the collimator lens that is used to collimate light rays. A diaphragm is then used after the collimator, while the focal point of lens **L** is located exactly on the entrance pupil of the eye, and approximately 3 mm behind the corneal vertex [111]. Therefore, if the light source is small enough, i.e. approximated to a point source, then the amount of light entering the eye will be independent of pupil size as long as the light spot is smaller than the pupil diameter. However, there are some approximations that have to be considered [109]:

- The eye is taken to be perfectly transparent;
- No distinction between the plane of the eye's entrance pupil and anterior principal plane: the error introduced is negligible;
- If the light source is an imaged in the pupil, the eye is assumed to be accommodated for the object plane which is not necessarily at infinity;
- Paraxial approximation is considered to be valid or aberration effect (see Sec. 3.1.1 are negligible).

Among the advantages, this method allows for reducing or in some cases avoiding light aberrations 3.1.1. Furthermore, retinal illuminance is considered to be uniform and easily determined as explained in the following Section.

3.3.2 Retinal illuminance

As we illustrated in the previous section, through proper Maxwellian optics, the amount of light striking the retina is not affected by the pupil diameter. Therefore, an important parameter to know when evaluating the radiant power of a Maxwellian-View optical system, also for safety reasons, is therefore the area of the retina illuminated. In Figure 3.13

To quantify the area of retinal exposure, the full angle in radians is measured from the pupil, roughly at the first nodal point of the eye, as shown in Figure 3.13. Taking d_r as the extent of this area and f_e as the eye's focal length (typical $f_e = 1.7cm$).

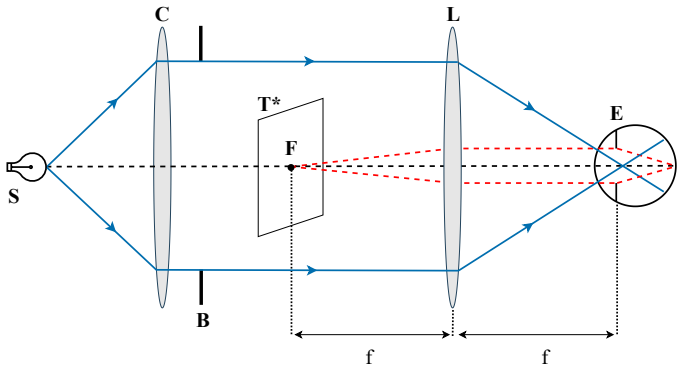


Figure 3.12: Maxwellian view system (**S**, source of light; **C**, collimator; **B**, diaphragm; **T***, the optional target can be placed in the focal plane of lens **L**, i.e. fundus image is formed on the retina **L**; **F**, the first focal point of lens **L** and conjugate of the retina of an un-accommodated eye; **E**, the center of the entrance pupil of the eye and conjugate of **S**.

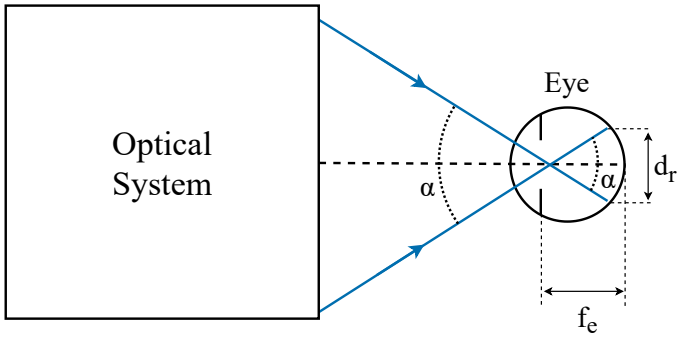


Figure 3.13: Maxwellian Illumination

$$\alpha = 2\left(\tan\frac{d_r}{2\cdot f_e}\right)^{-1} = \frac{d_r}{f_e} \tag{3.4}$$

The right term of 3.4 is correct for paraxial approximation, resulting in only a 5% error at 45°. Subsequentially, the retinal exposed area A can be calculated as follows:

$$A = \frac{\pi}{4}(f_e \cdot \alpha)^2 \tag{3.5}$$

In Maxwellian illumination, the light beam enters the eye with a known angle α through the pupil, therefore the *retinal irradiance* or *flux density* E_e (W/m^2, see Table 3.1) is equivalent to the total *radiant power* or *radiant flux* entering the pupil Φ_E in Watts, divided by the exposed retinal area found in 3.5, where τ is the transmission of the ocular media. [112]

$$E_e = \frac{4}{\pi(f_e \cdot \alpha)^2} \cdot \Phi_E \cdot \tau \tag{3.6}$$

Furthermore, as long as the intensity distributions is homogeneous over the entire α, it is possible to calculate the *radiance* ($W \cdot m^-2 \cdot sr^-1$, see Table 3.1) by simply considering the solid angle Ω (sr) subtended by the cone with apex angle α as follows:

$$\begin{cases} L_{e,\Omega} = \frac{E_e}{\Omega} \\ \Omega = 2\pi \cdot (1 - cos\ (\frac{\alpha}{2})) = 4\pi \cdot sin^2\alpha \end{cases} \tag{3.7}$$

Finally, as previously mentioned in Sec. 3.2.2, if the spectral distribution of the light source per unit wavelength is known, it is possible to convert both retinal irradiance E_e and the radiance $L_{e,\Omega}$ in the equivalent *illuminance* (E_V lux or lumen/sq.meter) and *luminance* (L_V candela/sq.meter) with the equation 3.3.

In the eventuality that the light flux entering in the eye is limited by the pupil size, another photometric unit can be used in this case, i.e. the *Troland*. The Troland (*Td*) is a unit expressing retinal illuminance that takes into account the area of the pupil. It is defined as the amount of light that falls on a unit area (1 square millimeter) of the retina when the pupil is dilated to a diameter of 1 millimeter and the illuminance of the incident light is 1 candela per square meter (cd/m^2). In other words, one troland is equal to one lux of light entering the eye through a pupil with an area of 1 square millimeter. The unit is named after Leonard T. Troland, an American psychologist who contributed to the study of visual perception [113].

Chapter 4

Opthalmic Technologies

In this final chapter, an overview of the state-of-the-art ophthalmic techniques investigated during this research work is presented. The chapter is organized into three sections:

- **Visual-Based Techniques**: This section provides a detailed examination of visual-based image analysis methods and the utilization of Artificial Intelligence to improve the effectiveness of common ophthalmic techniques.
- **Pupillometry**: This section highlights the usefulness of pupillometry as a tool for investigating and understanding the human visual system, as well as its application in clinical procedures. The metrological background of the methodology for measuring and observing the form of the human pupil, along with possible sources of error and common problems, is discussed.
- **Contactless PACG Prevention**: The final section addresses the use of contactless techniques for the prevention of Primary Angle Closure Glaucoma (PACG), one of the most common forms of Glaucoma. The advantages and limitations of these methods are discussed, as well as the potential for their effective use in everyday clinical practice.

Across the board, this chapter provides a comprehensive examination of the current state-of-the-art in ophthalmic technologies and their potential for use in clinical practice.

4.1 Visual-Based Techniques

Visual-based techniques refers to any method or approach that utilizes visual information, typically in the form of images or videos, to analyze, interpret or assist non-expert users to make decisions. These techniques are commonly used in the field of computer vision, machine learning, and image processing, and can be applied to various domains such as medical imaging, security, surveillance, and autonomous systems. Examples of visual-based techniques include image segmentation, object detection, feature extraction, and pattern recognition.

Nowadays, a popular research field is the integration of vision-based solutions into the instrumentation and measuring industry [114]. *Artificial Intelligence* (AI) can be implemented in different methods and extensions, and as shown in Figure 4.1, this field of study includes many "subcategories", depending on the specific way of implementation.

Indeed, AI applied to *Computer Vision* [115], in terms of *Machine Learning* (ML) [116], *Deep Learning* (DL) [117] and *Expert Systems* (ES) [118], can be effectively exploited to improve the performance of traditional instrumentation systems [119].

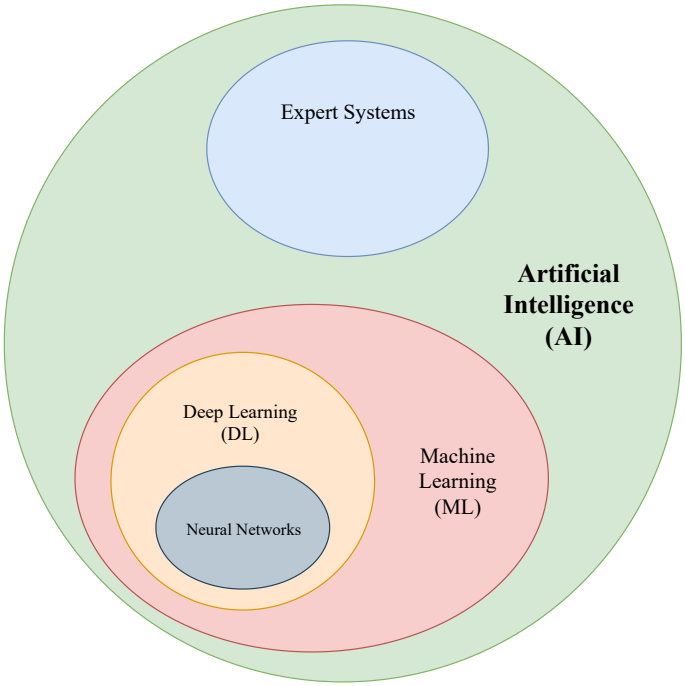


Figure 4.1: Artificial Intelligence Subcategories

More specifically, the use of AI has become a common practice in biomedical imaging [120, 121] as well as in ocular data analysis [122, 123], and ophthalmic image analysis [124–126]. Indeed, the use of image acquisition devices, such as digital cameras, in ophthalmic imaging instrumentation has introduced several improvements, especially for the diagnostic and for objective detection of the progression of a number of pathologies [127]. The aforementioned ophthalmic procedures and systems comprise, among others, slit lamp microscopy [128], optical coherence tomography (OCT) [129], funduscopy [130], pupillometry [131] as well as laser eye treatment for the correction of myopia, hyperopia, glaucoma [132], or cataract surgery [133].

Therefore, Visual-based techniques, intended as a combination of AI subcategories can be used to extract meaningful information from visual data and can be applied to various applications such as medical diagnosis, facial recognition, and object tracking. Regarding ophthalmic instrumentation, these techniques can be used to analyze and interpret digital images of the eye, thus enabling early detection and diagnosis of specific disease.

4.1.1 Expert Systems

Expert systems (ES) [134] are computer programs that mimic the decision-making abilities of a human expert within a specific field. As graphically represented in Figure 4.2, ES foresees the combination of information and notions, forming the*knowledge base*, to solve specific problems through a so-called *inference engine* with the aim of helping *Non-Expert users* to make decisions when queried with specific tasks or problems. The inference engine is the component that is responsible for inferring new knowledge or drawing conclusions starting from the information stored in the system's knowledge base. The specific algorithms and methods used by the inference engine can vary depending on the expert system, but they typically involve some form of rule-based expressions, logical deduction, or probability-based reasoning.

For example, an expert system for medical imaging may use a combination of image processing techniques and pattern recognition algorithms to extract useful information from X-ray or CT images and

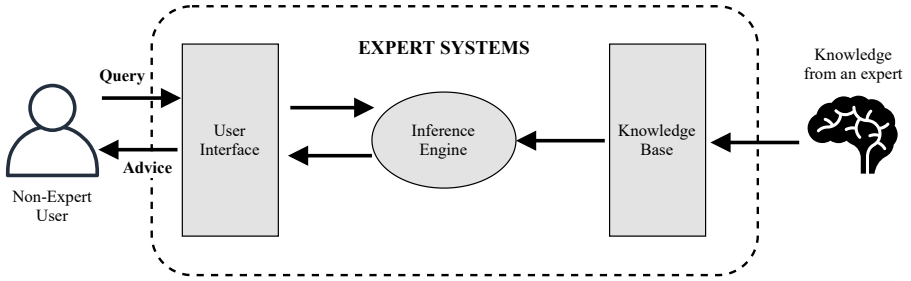


Figure 4.2: Expert Systems

help medical experts to identify abnormalities such as tumors or fractures. As another example, ES can be used in agriculture to analyze satellite images of crops and identify areas of disease or pest infestation, or in industrial imaging, to inspect products for defects at very high speed or to analyze traffic cameras to detect and identify vehicles.

Overall, expert systems can play a valuable role in ophthalmic instrumentation by providing accurate, efficient, and consistent diagnosis and treatment recommendations, ultimately improving patient outcomes.

4.1.2 Machine Learning

Machine learning (ML) is a method of teaching computers to learn from data, without being explicitly programmed [135–137]. ML foresees the application of algorithms and statistical models to allow systems to improve their performance over time. Machine learning can be classified into three types: supervised [138], unsupervised [139], and reinforcement learning [140]. *Supervised learning* is one of the most common types of machine learning used in image classification. A labeled dataset, consisting of input images and corresponding output labels, is used to train an algorithm in supervised learning. The algorithm's goal is to learn a function that maps input images to output labels so that it can accurately classify new, previously unseen images.

There are several types of classifiers that can be used in image classification, including: *K-nearest neighbors* (KNN) algorithm [141], which classifies new images based on the majority class of the k-nearest training examples. *Support vector machines* (SVMs) [142], try to find a hyperplane that maximally separates the different classes in the feature space. Another important aspect of machine learning is *optimization*. The goal of optimization is to find the best set of parameters for the classifier so that it can achieve the highest accuracy on the training dataset. There are several types of optimization algorithms, such as *gradient descent* [143], *stochastic gradient descent* [144], and *Adam* [145], just to name a few. Each one of them uses different strategies for updating the parameters of the classifier in order to minimize the objective function.

In general, machine learning techniques have shown to be very promising in ophthalmology, by providing a high level of accuracy in detecting and diagnosing eye diseases, and also by being able to analyze a large amount of data in a short time.

Deep-Learning

Deep learning [146] is a subset of machine learning that is inspired by the structure and function of the human brain, specifically the neural networks that make up brain connections. Neural networks consist of layers of interconnected nodes, or neurons, which are used to process and analyze data.

One of the most popular types of neural networks for image analysis is the Convolutional Neural Network (CNN) [147]. CNN's are particularly well-suited for image classification tasks due to their ability

to extract features from the input image and reduce the dimensionality of the feature maps through the use of convolutional and pooling layers. The extracted features are then passed through fully connected layers, which make the final classification decisions.

The training process for a CNN involves presenting the model with a large dataset of labeled images and adjusting the model's parameters to minimize the error between the predicted labels and the true labels. This process is typically performed using a variant of *stochastic gradient descent* (SGD) [144], which is an optimization algorithm that updates the model's parameters in the direction that reduces the error. The models learn to extract relevant features from the images and to use these features to classify the images into different classes, such as healthy or not. The model is usually then fine-tuned on a specific task to get very high accuracies. Popular CNN architectures for image classification include AlexNet, VGGNet, GoogleNet, and ResNet. These architectures have been widely used in the field of image classification and have shown to be effective in achieving high accuracy rates [148]. After training, the CNN can be used to classify new images. The model can also be used to extract features from the images that can be used for further analysis or diagnosis or to help trained medical personnel perform a specific procedure.

In addition to classification, CNNs can also be used for other tasks. As an example, in ophthalmology, CNNs can be used for image segmentation, which involves identifying specific structures or regions in an image. This can be used to segment the retina, the optic nerve head, or the macula, which is important for diagnosis and treatment planning. Overall, CNNs are a powerful tool for image classification and analysis in ophthalmology and can help in the early detection and monitoring of eye diseases.

It is worth noting that CNNs are not the only deep learning algorithm that can be used for image classification, other algorithms such as Recurrent Neural Networks (RNNs) [149] and Generative Adversarial Networks (GANs) [150] also show potential in image analysis. However, as we will discuss later in the last part of this work (see Part III), CNN remains one of the most popular and easy to use used deep learning algorithms for image classification tasks.

4.2 Pupillometry

Pupillometry is a technique that involves measuring the size and reactivity of the pupil in response to various stimuli [151, 152]. It can be used to study a wide range of visual impairments and pathologies, as well as for research investigations in a number of different clinical fields. Some examples include:

- **Ocular diseases:** Pupillometry can be used to diagnose and monitor various ocular diseases such as glaucoma [153], which often leads to a change in the size and shape of the pupil and how it responds in reaction to light. It can also be used to monitor the progression of retinal diseases such as diabetic retinopathy [154] and age-related macular degeneration [155].
- **Neurological disorders [156]:** Pupillometry can also be used to evaluate neurological disorders such as concussion, traumatic brain injury [157], and neurodegenerative diseases such as Parkinson's disease [158]. In such cases, it can provide an indication of the integrity of the visual pathways and the status of the autonomic nervous system [159].
- **Cognitive research:** Studying cognitive functions such as attention, memory, and decision-making is also possible with PLR analysis [160]. In such cases, it can provide an objective measure of cognitive load and cognitive effort.
- **Clinical research and testing:** Pupillometry can be used in various forms of clinical research, such as testing new drugs [161] or treatment strategies for visual impairments or providing additional information for the diagnosis of different pathologies.

- **Flicker annoyance estimation:** By measuring the amplitude and frequency of the pupillary response to flicker stimuli, it is possible to estimate the level of flicker annoyance experienced by an individual [162]. This can be useful in the evaluation of flicker-induced visual fatigue and the design of lighting systems that minimize flicker annoyance [163].

Overall, pupillometry can be considered a non-invasive and objective method that provides valuable information about the visual system and the overall health of the individual. It is increasingly being used as an adjunctive tool in the diagnosis and management of a variety of visual impairments, neurological disorders, and other medical conditions. In the following Section, the theoretical background of pupil measurement, along with some common sources of errors and how pupil dimension can be determined with mathematical representation.

4.2.1 Measurement of the human pupil

One of the investigations carried out throughout this research activity involved the responsiveness of the human pupil to various types of stimulation. This section discusses the state of the art in pupil size measuring, as well as some key points. According to the literature, the following are the main characteristics to consider:

- Form of the human pupil;
- Possible source of measurement errors.

The form of human pupil

The diagnostic value of the iris and pupil's responses to stimuli, their relative diameters, and others, account for a large portion of their clinical significance. Details of the pupil's form and location within the iris are a couple of its features that haven't gotten a lot of attention. Deviations from circularity and *emphconcentricity* must be due to structural and/or innervational anisotropies. Significant variations from circularity have been seen in several disorders, and it has been tentatively hypothesized that as children age, their ability to exhibit circularity may decline (Loewenfeld, 1979) [164]. However, Kristek (1965) [165] seems to have been the only person to attempt to define pupil shape. He did this by measuring the longest and shortest diameters and classifying the pupil as elliptical. Almost all dynamic investigations of the pupil solely measure the horizontal diameter or area; even studies of different pupil diameters (*emphanisocoria*) have only accomplished this type of investigation. Moreover, other studies [20] reported that pupil placement may have effects on the eye's optics in addition to structural ones. Ultimate findings show that no fully round pupils exist, as may be expected. Individuals display consistency in their pupil shape, which changes consistently under various lighting circumstances. In both light and dark environments, there are broader patterns in the positioning of the pupils. [20]

Among all the findings shown in the literature since the present day, all demonstrate that pupil shape is an individual trait, with significant consistency present for each subject but with certain shared characteristics: (a) In the dark, the average shape is slightly elliptical with a major axis near vertical, whereas, in the light, the average shape is more nearly circular with a major axis near horizontal; (b) With age, pupil size decreases. Non-circularity was observed to grow somewhat with age, and the increase was roughly the same in the dark.

Wyatt described the geometrical form of the human pupil margin as a circular Fourier series in polar coordinates with the pupil center taken as the origin:

$$R(\theta) = r_{ave} + \sum_{2}^{N} r_n \cdot cos \cdot n(\theta - \psi_n) \tag{4.1}$$

Where:
$R(\theta)$-distance from the pupil center as a function of polar angle θ;
r_n -is the amplitude of the nth harmonic;
r_{ave} -average radius;
ψ_n -phase angle for nth harmonic;

In the characterization of the pupil shape, a crucial point is the determination of the coordinate system. Circular shapes are naturally represented in polar coordinates. Firstly, the center of the geometrical form related to the polar coordinate system must be defined. An example of the four stages that build the digitized pupil is shown in Fig. 4.3 with the Fourier representation shown in Fig. 4.3(C). It is useful to represent the circular Fourier series by magnifying the non-circular components by an arbitrary factor for easy viewing and comparison. In the Figure, a factor of 5 was used.

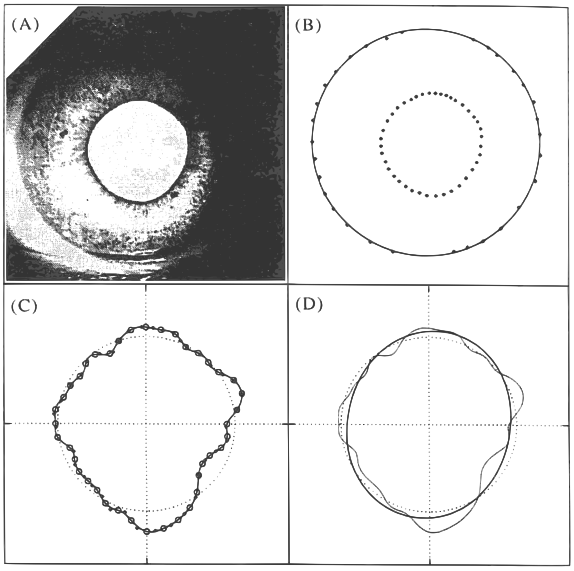


Figure 4.3: Four steps in the analysis of pupil shape. (A) The slit-lamp photograph. (B) Digitization of the pupil margin and limbus. A circle has been fitted to the limbus points. (C) Analysis of pupil shape. The diamonds are the pupil margin points digitized in (B); the circles are a data set at equal angular intervals, obtained by interpolation from the diamonds. The solid line is the 20-term Fourier representation of the shape. The dotted circle is the average radius. In (C) and (D), the non-circular components of shape have been magnified 5 x. (D) The best-fit ellipse to the shape in (C); the shape and the average-radius circle are also shown. [20]

Founding from this [20] and other research states that the average normalized shape of the pupils among different subjects was found to be primarily elliptical, with a contribution of 0.96 by an ellipse in dark condition, while under the light condition, the average shape was found to be nearly circular. Moreover, the diameter of the pupils was found to decrease with age, with a slope of about $-0.02mm/yr$. The non-circularity of the pupils was found to be similar in both the dark and light conditions, with values of 0.0176 ± 0.0062 and 0.0166 ± 0.0041, respectively. These findings provide important information about the shape and size of the pupils under different lighting conditions and how these may change with age.

Sources of Errors

When performing a measurement it is important to know the possible sources of uncertainty. During the development of the system lately presented in Chapter 5, a deep analysis was carried out in the literature of

previous attempts to measure the pupil. This section shows the main sources of uncertainty in estimating pupil size by means of digital image acquisition. The first conclusion shows that measuring an absolute value of pupil size is somewhat non-trivial. Some sources of uncertainty can not be known a priori and this involves to a not negligible measurement error. Starting from this consideration, it is convenient to compare the pupil with reference to its size in certain light conditions: for example, to a well-described adaptation condition. As a result, by using the pupil's relative size the uncertainties in measurement can be more easily evaluated and the results obtained can be compared among different subjects.

Influence of corneal geometry on the pupil image As in most cases, the pupil of the eye is observed through the first elements of the human-eye physiological structure (see Sec. 1). The cornea is the anterior surface of the eye and is the major refractive element of the human eye. The influence of the corneal shape should not be neglected in measurements of pupil size. Szczęsna et al. [166], described the influence of the corneal geometry on the diameter of the pupil and on the magnification and position of the image of the pupil. The cornea contributes to two-thirds of the total optical power. This is mainly due to the great difference between the refractive index of air and an average refractive index of the cornea (n_c = 1.377). The ray tracing shown in Figure 4.4 simply shows how the pupil image is formed when a camera is placed in front of the eye. For the drawing, an infinitely thin cornea is considered, and the corneal topography was approximated by the elongated ellipsoid.

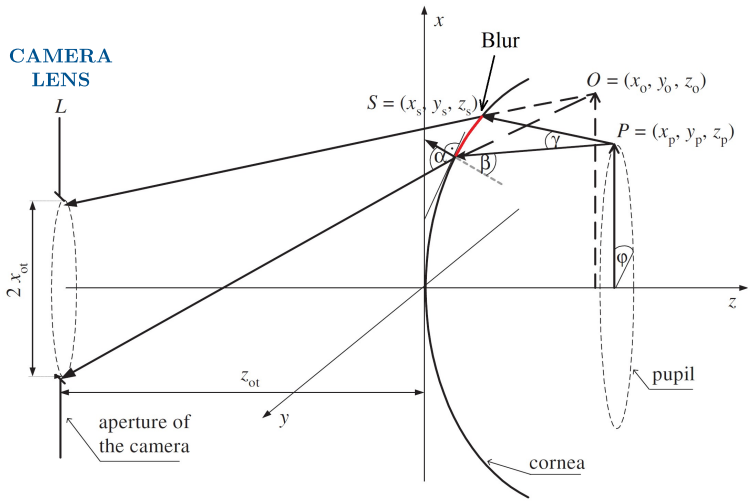


Figure 4.4: Influence of corneal geometry on pupil estimation

The effects of the cornea on the pupil image observed from outside are principally two:

- Magnification, which according to Szczęsna can go from 6,5% to 15%;
- Blur, which refers to the visual effect of an image or object appearing out of focus or with a lack of sharpness.

Szczęsna et al. performed a deep analysis of the linear magnification of the pupil as a function of the central corneal curvature, the radius of the real pupil. The magnification of the pupil image has an average of about 10% and increases with the decrease of radius of curvature R_0 and eccentricity ϵ of the corneal profile and decreases for the largest pupil X_p. Linear magnification can't always be estimated because is strictly related to the form of the subject eye and to the position of the real pupil, which is not known in advance. The main parameters that affect pupil magnifications are corneal eccentricity ϵ, the radius of the real pupil R_0, and the distance of the real pupil from the corneal apex z_p that varies among populations.

The image of the pupil is always blurred, which limits the sharp observation of the pupil. The greatest influence on the blur of the pupil image was the aperture and the distance of the optical system used for observation from the corneal apex. To reduce the blur of the pupil a high distance from the cornea Z_{ot} and a small aperture of the camera X_{ot} are both required. In our system, the distance of the camera from the cornea was about 75 mm and the aperture X_{ot} of 2.25 mm. Although in our system the optical distance between the used camera and the cornea is reduced, observing the experimental results of Szczęna the pupil blur is kept low thanks to the reduced aperture of the used camera. Based on the Szczęna et al. numerical estimations, the overall blur of the system achieved is less than 0.1 mm. In the worst case, with a completely narrowed pupil, the diameter is as low as 2 mm. Thus, give a blur percentage lower than 5%. Despite that, it does not matter which is the quality of the optical system used for observations, the pupil image will always be blurred and not sharp. [166]

Dynamic thresholding In order to perform pupil recognition from a digitally acquired image, the most common and easy technique is to use *thresholding* [167]. Image thresholding is a fundamental method of *image segmentation* [1], which is used to create binary images from grayscale or color images. An 8-bit grayscale image is usually represented by a 2D array of pixels, each of which can have a value between 0 and 255, where 0 represents black and 255 represents white. Therefore, the value of each pixel represents its intensity or gray level [168]. The simplest thresholding methods involve replacing each pixel in an image with a black pixel if the image intensity $I_{i,j}$ is less than a fixed constant T, or a white pixel if the image intensity is greater than T. There are several types of thresholding techniques, including:

- **Global thresholding:** A single threshold value is applied to the entire image, resulting in a binary image where all pixels above the threshold are white and all pixels below are black.
- **Adaptive thresholding:** A threshold value is determined locally for each pixel based on its neighboring pixels. This technique is useful for images with uneven lighting or contrast.
- **Otsu's thresholding:** This is a type of global thresholding that automatically determines the threshold value by maximizing the separation between the foreground and background pixel intensities.

The performance of thresholding on the human pupil is highly dependent on the lighting conditions [169]. Different lighting conditions can lead to overall darker or brighter pupils, which in turn affects the thresholding level T that should be used. As an example, if a threshold level T that is too high is chosen, some pixels around the outer edges of the pupil that are actually part of the iris may be dark enough to be recognized as part of the pupil. This results in a thresholded image in which the pupil is larger than the real pupil. Conversely, if a threshold level that is too low is chosen, some pixels that make up the outer edge of the pupil may be too bright and would be detected as part of the iris. This results in a thresholded image in which the pupil is smaller than the real pupil.

To overcome these challenges, the contrast between the pupil and the iris can be increased by using specific types of illumination such as infrared light. Additionally, proper focus detection on the pupil's edge can also be employed to improve the accuracy of pupil recognition. [170].

[1] Image segmentation is the process of partitioning an image into multiple segments or regions, each of which corresponds to a different object or part of the scene. The goal of image segmentation is to simplify and/or change the representation of an image into something that is more meaningful and easier to analyze. Image segmentation techniques can be based on pixel intensity, color, texture, and shape information, and can be performed using a variety of algorithms, including thresholding, clustering, and machine learning-based methods.

Radius of an ellipse As described in the section 4.2.1 the human pupil can be in most cases modeled with an ellipse, i.e. a curve surrounding two focal points. From a mathematical perspective, the ellipse is built such that the sum of the two distances from every point on the curve to the two focal points is constant. As such, it is a generalization of a circle, which is a special type of ellipse having both focal points at the same location. The elongation of an ellipse is represented by its *eccentricity*, which, for an ellipse, can be any number from 0 (the limiting case of a circle) to arbitrarily close to but less than 1. An example of the main geometric parts of an ellipse is reported in Figure 4.5.

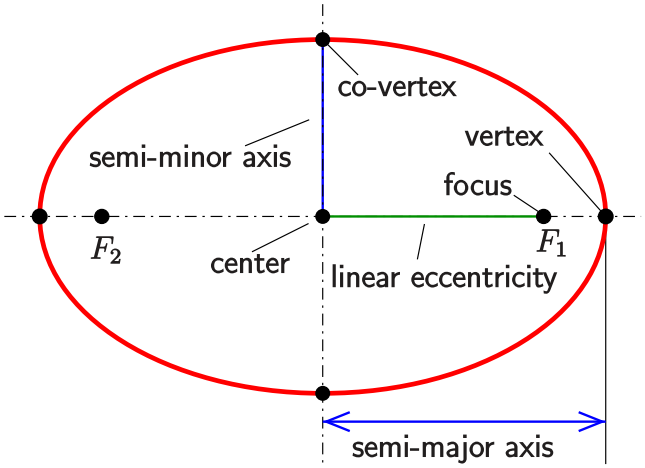


Figure 4.5: Ellipse geometry

In the realized system, pupil dimension was estimated by fitting an ellipse on the pupil's contour of the sampled image. Once the best-fit ellipse is found for a specific frame, a numerical estimation of the size of the pupil is performed. The *python* algorithm, performing the ellipse fitting, returns the values of the semi-major axis ***a*** and the semi-minor axis ***b*** of the ellipse (see Fig. 4.5). numerical estimation of pupil size. From the literature, many equations can be used to calculate the size of the ellipse:

Equi-area radius:

$$\begin{aligned} A_{ellipse} &= \pi \cdot a \cdot b \\ A_{circle} &= \pi \cdot r^2 \\ r_{eq_area} &= \sqrt{a \cdot b} \end{aligned} \tag{4.2}$$

Root Mean Square

$$R_{RMS} = \sqrt{\frac{a^2 + b^2}{2}} \tag{4.3}$$

Authalic radius

$$R_{auth} = \frac{2 \cdot a + b}{3} \tag{4.4}$$

These three equations can be used to obtain a numerical estimation of the pupil dimension. However, some discrepancies can rise up when the ellipse considered has a high eccentricity, thus $a >> b$. The graph in Figure 4.6 highlights this problem.

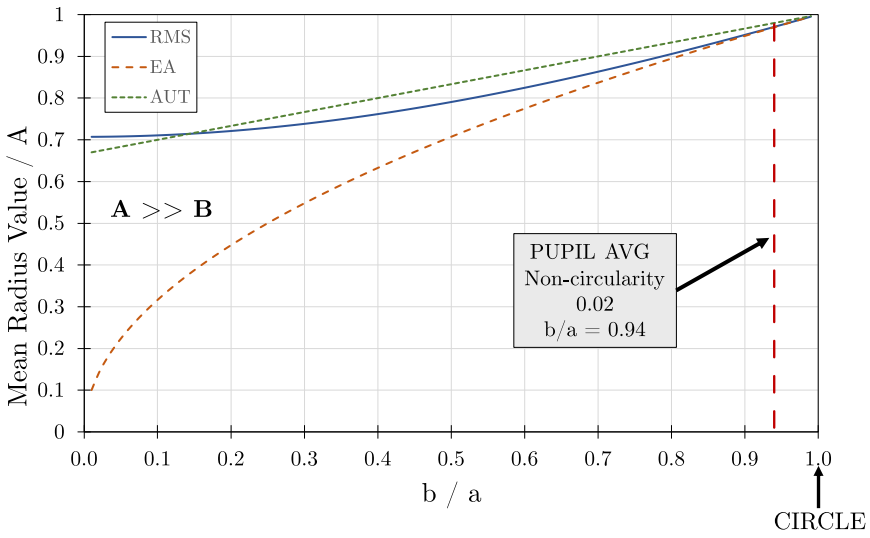


Figure 4.6: Radius Equation for an Ellipse

Wyatt in [20] reported that the average pupil non-circularity is 0.02, which means a ratio b/a of 0.94 (a/b / 1.06). As shown in the graph, for that kind of non-circularity the three equations give almost the same numerical estimation. For the worst case scenario, thus a non-circularity in the order of 0,025 (b/a ratio of 0,925), we have a discrepancy between the different formulas of 0.146% between RMS and Equi-area, 1.177 % between RMS and Authalic and 1.323 % between Equi-area and Authalic. Numerical results of different equations give a smaller contribution to pupil size estimations, so all three can be used for our purpose.

4.3 Primary Angle Closure Glaucoma

Glaucoma is a debilitating optic neuropathy characterized by progressive degeneration of the retinal ganglion cell layer, making it one of the leading causes of bilateral blindness worldwide. The disease is typically classified into two types: chronic open-angle glaucoma and *primary angle-closure glaucoma* (PACG) [171]. According to a study by Javed et al. [172], PACG affects approximately 20% of all glaucoma patients, but it is more prevalent in certain regions of the world. Both types of glaucoma are linked to elevated intraocular pressure, however, in the case of PACG, the pressure rises usually as a result of contact between the iris and the *trabecular meshwork*, thus blocking the outflow of *aqueous humor* from the anterior chamber (as illustrated in Figure 4.7) [173]. This can lead to very high intraocular pressure, even surpassing 30 mmHg (normal healthy pressure levels typically range between 12-21 mmHg) [174], causing symptoms such as nausea, vomiting, and ocular pain [175].

The insidious nature of glaucoma lies in its asymptomatic nature, with patients often only realizing they have the disease when significant loss of visual field has already occurred. In severe cases, such as with PACG, emergency surgical intervention may be necessary.

We already highlighted how PACG is a common cause of bilateral blindness across the world, which might be avoided if specific diagnostic tools could identify patients who would benefit from preventative therapies in the early stages of the disease [176]. As a result, early detection and prevention are crucial in managing this chronic condition [177].

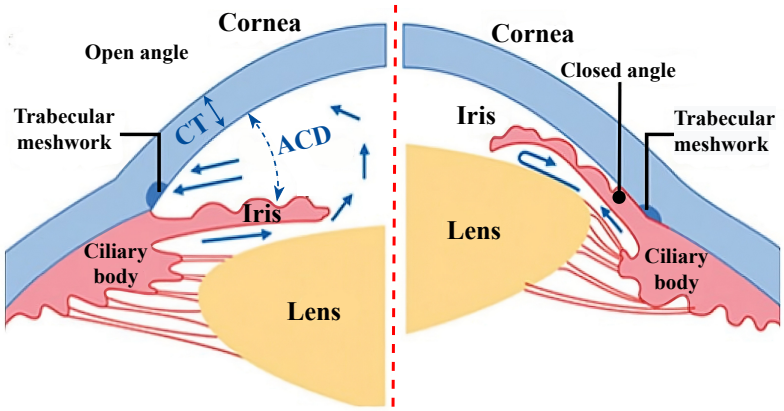


Figure 4.7: A schematic diagram of the anterior eye in open-angle (left) and the closed angel (right) glaucoma, showing how the displacement of the lens and the iris obstructs the fluid outflow across the *Trabecular Meshwork* (TM) in the case of closed-angle glaucoma [173]. In the Figure, ***CT*** stands for *Corneal Thickness* and ***ACD*** for *Anterior Chamber Depth*.

4.3.1 Prevention

Primary Angle Closure Glaucoma is one of the major causes of bilateral blindness worldwide, and, as said before, prevention is essential, in order to understand if a patient is predisposed to PACG and if the glaucoma is in progress. Prevention of PACG starts with monitoring the *Anterior Chamber Angle* (ACA) [178] condition, an operation that can be processed through different techniques, among which the reference one is called gonioscopy. This technique needs a slit lamp, as an illumination source, and a particular instrument called goniolens, the most used is the Goldmann goniolens [179]. The goniolens is a truncated-cone-like device able to reflect the light from the iridocorneal angle in the observer's direction, through mirrors placed into the device. Figure 4.8 give an explicative illustration of the working principle. The observer can evaluate the width of the ACA by evaluating the number of ocular structures visible, i.e. the larger the number of structures the wider the angle.

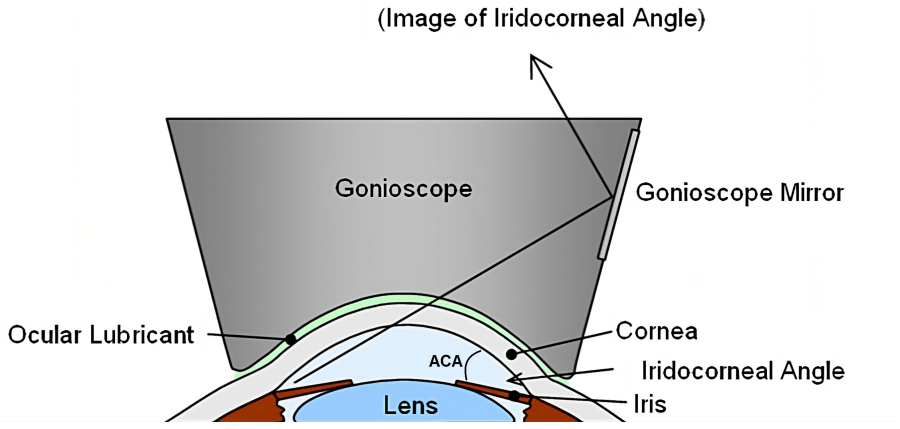


Figure 4.8: Goldmann Goniolens

Gonioscopy is a widely accepted method for evaluating the anterior chamber angle (ACA) of the eye. However, it has certain limitations that have stimulated the development of alternative techniques. One of the primary limitations of gonioscopy is its invasiveness, as it requires the use of goniolens to be placed

on the surface of the eye. Additionally, this technique requires suitably trained healthcare professionals, and the findings may vary with the amount of light or with mechanical compression during the eye examination. In recent years, alternative techniques have been developed to address these limitations, such as Ultrasound *BioMicroscopy* (UBM) [180] and anterior segment OCT (AS-OCT) [181]. Unfortunately, due to the costs and the level of experience required for their use, these techniques are not suitable for large-scale population-based studies or screening in routine clinical practice for PACG.

Among others, the *Van Herick* (VH) technique [182], named after his inventor, proved to be since early study a valid qualitative method for ACA estimation, which is less invasive and does not require the same level of expertise as gonioscopy [183].

4.3.2 Van Herick Technique

William Van Herick et al. in 1969 [182] proposed a simple and quick technique for the ACA evaluation, which exploits the correlation between the thickness of the cornea and the thick *Anterior Chamber* (AC). The working principle of the VH technique is based on the visual comparison between the peripheral anterior chamber depth and the thickness of the cornea. Such information can be obtained with a *slit-lamp biomicroscope* [2]. As illustrated in Figure 4.9 the process proposed by Van Herick requires a slit lamp, which must be placed to obtain a perfect 60° angle between the lamp and the optical axis of the eye. The narrow beam of the lamp must be aligned with the *limbus*, which is the junction between the sclera and cornea [3].

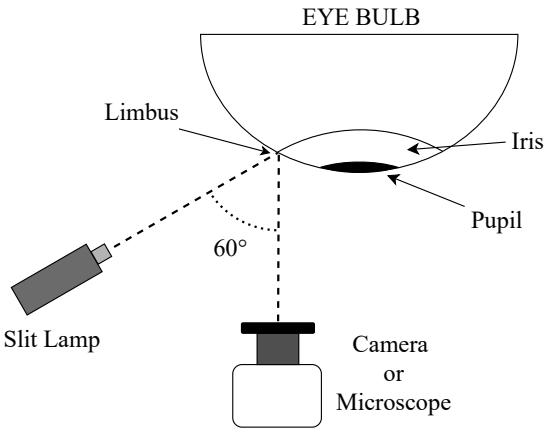


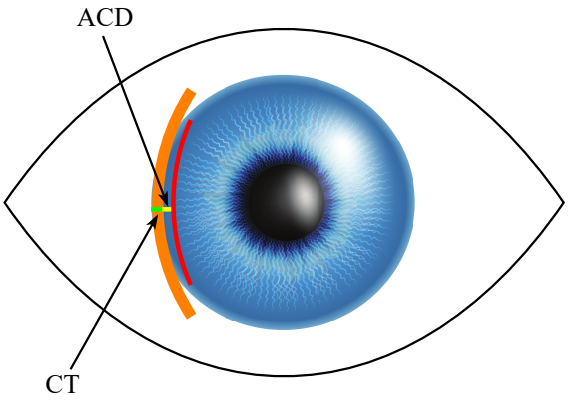
Figure 4.9: Optical scheme used for Van Herick manoeuvre

As previously mentioned, the technique exploits the difference in refractive index among air, cornea, and anterior chamber to accomplish the measurement. Indeed, the slit projected on the limbus is refracted because of the difference in index between air and cornea. As illustrated in Figures 4.10a and 4.10b, the resulting image is a slit projected onto the surface of the cornea (orange line) and its width, which is indeed the *corneal thickness* (**CT**), is used as a reference for the grading of the angle. The *anterior chamber depth*

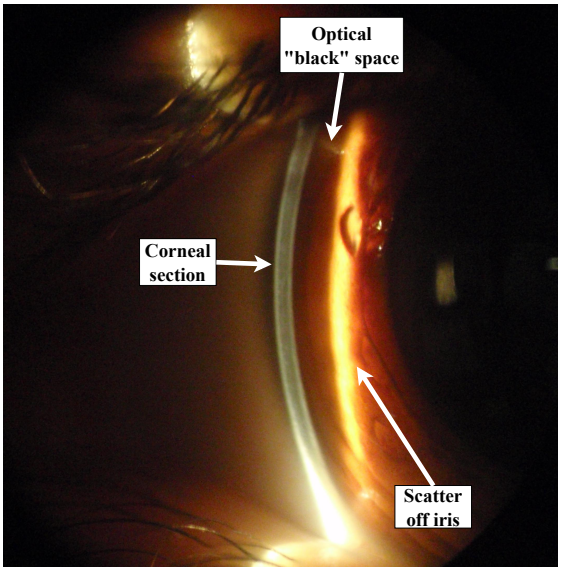
[2] A slit lamp is a device used in ophthalmology and optometry to examine the anterior and posterior segments of the eye. It consists of a high-intensity light source that can be focused into a thin, illuminated "slit", which is then directed onto the eye. The examiner can then view the eye at different magnifications and angles, allowing for detailed examination of the cornea, iris, lens, and other structures of the eye.

[3] The limbus is the border between the cornea and the sclera (the white of the eye) in the human eye. It is a circular structure located at the junction of the cornea and the sclera, and it serves as a transition zone between the two tissues. The limbus is important for maintaining the structural integrity of the cornea and for providing a barrier to prevent the invasion of conjunctival cells into the cornea.

(**ACD**) can be evaluated by observing the "dark" region between the corneal slit line (on the left) and his reflection (red line on the right) on the iris surface. The wider the space, highlighted by the yellow line in Fig. 4.10a, with respect to the corneal thickness, the wider the ACA would be [184].



(a)



(b)

Figure 4.10: The Van Herick method to evaluate ACA. (a) Graphical representation of the diffraction of the slit lamp line that strikes the limbus imaged from a frontal view of the eye. (b) A real example of the diffraction of the line inside the anterior chamber. *Corneal section* slit line impinging on the limbus shows the *corneal thickness* (CT), while the optical dark space before the scattered line on the iris indicates the *Anterior Chamber Depth* (ACD).

More precisely, the anterior chamber drainage angle is evaluated as the ratio (ACD/CT) between the peripheral anterior chamber depth and the limbal-corneal thickness, as observed in from the microscope section placed in front of the eye (see. Fig.4.9). As reported in Table 4.1, when the Van Herick grading is expressed as a ratio, i.e. the measured ACD/CT, four grades from "1" (closed-angle) to "4" (angle wide open and incapable of closure) are used [182, 185].

GRADE	ACD/CT	CLOSURE RISK
4	>0.75	Closure impossible
3	0.45 - 0.75	Closure unlikely
2	0.25 - 0.45	Closure possible
1	<0.25	Closure likely

Table 4.1: Van Herick grading scheme.

Van Herick Limitations

The VH technique is a quick and easy way to estimate anterior chamber depth, but has some drawbacks that could affect the grading: (i) uncertainty in finding the exact position of the limbus, (ii) uncertainty in optical triangulation configuration, and (iii) uncertainty in the visual estimation of the ratio ACD/CT [186]. Therefore, the measurement for the VH test can be carried out only by suitably trained and skilled healthcare professionals or technicians.
Despite the VH technique being considered to be a simple and non-invasive method for PACG preventive diagnosis, it manifests several limitations and therefore it is still considered a qualitative technique and not a reference one. Foremost, as previously mentioned, the measurement may depend on the practitioner's experience. Statistical analyses indicate that physicians exhibit a high level of agreement (80%) in determining grade 1 and 4 Anterior Chamber Angle (ACA) measurements, which is considered a favorable outcome. Conversely, agreement in determining grade 2 and 3 ACA measurements is relatively low (approximately 50%), which poses a significant challenge as these grades are prone to confusion. This is of particular concern as a grade 2 ACA is associated with an increased risk of Anterior Chamber closure and subsequent development of Primary Angle Closure Glaucoma (PACG) [172]. Besides, limitations in VH measurements include the interdependence of Corneal Thickness (CT) and Anterior Chamber Depth (ACD), which can result in similar ratios being obtained in different clinical scenarios (e.g. a thin CT with deep ACD versus a thick CT with shallow ACD) [183, 187]. This can lead to misdiagnosis in cases of open and closed-angle eyes. Furthermore, the minimum ACA measurement can be obtained from either the temporal or nasal angles, highlighting the importance of evaluating both angles for accurate diagnosis [187]. Additionally, the measurement is dependent on the distance from the limbus and the curvature radius of the eye, which can vary among patients and can lead to corrupted measurements if not taken into account properly [188].

Technique Improvement

In the last few years, several improvements have been proposed among which are the change of grading and the possibility of an automatic algorithm to evaluate the ACA grade. The idea of changing the grading scale comes from the possibility of improving the sensitivity of the measurement, and so to avoid cases in which the diagnosis is of an open angle when the ACA is quite close. The augmented scale is a seven-point scale, according to the grades given as a percentage given by the ratio between CT and ACD. The seven categories are: 0%, 5%, 15%, 25%, 40%, 75%, and 100%. Studies demonstrate that with this scale the sensitivity is improved, mostly for low grades, and useful to monitor the eventual progress of the ACA closing. However, in order to use this new grading system, it is required a good level of training from the opticians [185]. The last improvement proposed is referred to as an automatic evaluation of the ACA grade. In general, the system presented still requires an operator who sets the slit lamp in the right position to collect the eye images.

As will be illustrated in the last part (see. Chapter 8), a combination of Visual-Based Techniques (see. Sec. 4.1) can be exploited to objectively evaluate the VH grade by training a CNN network with known

ACA classified patients [189, 189]. This work starts from this point, so the idea is to improve the Van Herick technique by adding AI techniques that can potentially able to objectively evaluate the VH grades and therefore measure from a metrological point of view the ratio between CT and ACD.

Part II

Materials and Methods

Introduction

In the first Part I of this study, the physiological aspects of the human visual system, including the basic principles of ocular anatomy and functions have been examined. This medical introduction served as a foundation for understanding the mechanisms of the human eye's color perception and the standardized systems used to represent it. Additionally, we delved into the concept of Silent Substitution techniques, which involve the stimulation of specific types of photoreceptors, allowing access to deeper insights into the control of the pupillary light reflex. This led to an examination of the underlying neural mechanisms, which have significant implications for diagnostic techniques across a range of pathologies.

Subsequently, basic optical concepts such as lenses, light sources, units of light measurement, and viewing geometries were discussed to provide a background for understanding the proper design of advanced ophthalmic instruments. This included crucial technical considerations, such as the choice of optical elements and the proper adoption of such viewing geometries, thus concerning advantages and disadvantages.

Finally, in the last chapter, the ophthalmic technologies investigated during this study have been presented, which include visual-based artificial intelligence techniques, pupillometry, and diagnostic techniques for primary angle closure glaucoma. These aforementioned technologies aim at improving the diagnostic accuracy and reliability of common eye diseases.

This part is further divided into two main chapters:

- **PLR Measurement Intrumentation**
- **Automatic ACA Measurement Instrument**

The first one focuses on the technical aspects of pupillometer instruments and the second one on the description of an instrument for the objective and automatic measurement of the Anterior Chamber Angle (ACA). The motivation behind this study is to develop accurate and reliable measurement systems for pupillometry and ACA estimation, which are important diagnostic tools in the field of ophthalmology.

In the first section of this chapter, we will provide a detailed description of the technical aspects, components, and design of the pupillometry system. Specifically, we will discuss the hardware, software, and optical design of the system, as well as the methods used for data acquisition and analysis. We will also provide a state-of-the-art review of the current commercially available pupillometry devices developed by other researchers.

In the second Chapter of this Part, we will provide a detailed description of the technical aspects, components, and design of the contactless ACA measurement system that exploits the Van Herick technique. Specifically, we will discuss the hardware, software, and optical design of the system, as well as the methods used for data acquisition and analysis. We will also provide a state-of-the-art review of the current methods used for ACA estimation devices developed by other researchers.

It is important to note that, the technical details discussed in this Part are essential for understanding the methods used in this study, as well as for understanding the results lately presented in Part III. Furthermore, through the description of the techniques and ad-hoc engineering, we aim to demonstrate the significant advancement of the proposed systems as well as being an example and useful guideline for future researchers. The potential of this investigation aims to improve diagnostic accuracy and reliability in the field of ophthalmology.

Chapter 5

PLR Measurement Intrumentation

As stated in the introduction of this second Part of the manuscript, in this chapter entitled PLR Measurement Intrumentation, a technical description as well as the realization process of a pupillometer instrument, thus including some possible concrete implementation of the different elements, are presented.

A pupillometer typically consists of the following macro-blocks:

- **Light Sources:** This is used to illuminate the eye and create a reflex in the pupil, which is then measured. The light source can be a small incandescent lamp, a light-emitting diode (LED), or a combination of lasers to name a few.
- **Optical Elements:** Optical elements can be additionally used to manipulate light stimulation optical properties, improve the quality of acquired images, or make the system more compact and portable. Optical elements can include, lenses, mirrors, prisms, optical fibers, or optical filters.
- **Acquisition Device:** In modern pupillometer devices, a digital camera is typically used to acquire images or videos of the eye. From these, measuring the size of the pupil can be performed in real-time or in post-elaboration by analyzing saved files.
- **Hardware:** As in any electronic instrumentation, proper hardware design plays a crucial role. Pupillometer systems usually require hardware to provide a correct and stable power supply to all electronic components. Moreover, complex and advanced circuitry may be required to precisely drive LEDs light output, while providing excellent timing and synchronization capabilities.
- **Mounting and Component Housing:** These elements define how the system is mounted with respect to patients. As with many ophthalmic instruments, designing a pupillometer also includes implementing an alignment mechanism, which is essential for allowing to the instrument to adapt to different physical conformations, such as different head and eye shapes. Additionally, the physical enclosure that houses the components of the pupillometer must be designed to protect the components from dust, moisture, and other environmental factors.
- **Software:** The implementation of different programming languages is quite common for research and complex systems. Optoelectronics instrumentation usually includes many stages of software algorithms and routines. Starting from lower-level programmings languages such as *Assembly or # C*, which may be used for different types of microcontrollers units, followed by higher-level programming for image acquisition and image processing routines using *Python or MatLAB* and ending with a customizable user interface that can be implemented by using NI LabVIEW or QT [1].

[1] https://www.qt.io/

A well-designed user interface (UI) is very important for allowing the correct and fast acquisition of eye images and proper system configuration. UI's are generally used by non-expert users to control the device and adjust settings such as the light intensity or the camera focus and alignment. Moreover, correct graphical presentation of the results, such as the size of the pupil over time, averages, and filtering is another important aspect. The display can be a screen, a printer, or a data storage device. The software can also include algorithms for image acquisition, image processing, and data analysis.

5.1 Related Works

5.1.1 Instrumentation for the Human Pupil Measurement: State of the Art

As introduced in Section 4.2, pupillometry is a non-invasive technique used to measure changes in pupil size in response to light stimuli. In recent years, a growing number of researchers have proposed various types of pupillometer devices to improve the accuracy and reliability of pupillometry measurements.

Generally speaking, there are three main types of pupillometer devices design:

- Hand-held pupillometers as depicted in Figure 5.1
- Head-Mounted Pupillometers: with the benefit of decoupling from the patient's head movement, it usually involves a more complicated design.
- Fixed-pupillometers: this is the more common approach as it is easier to design and adapt to different head and face conformations. Fixed designs involve optical benches and chin-rest or tooth bars to stabilize the patient's head.



Figure 5.1: NeurOptics Hand-Held Pupillometer

Moreover, the most common type of pupillometer device foresees the utilization of infrared light to illuminate the eye while visible light is used to induce *miosis*, i.e. pupil constrictions. Moreover, these devices typically use a high-resolution infrared camera and dedicated software algorithms to measure the size of the pupil. Examples of commercially available infrared pupillometer devices include the NeurOptics NPi-200 HandHeld Pupillometer [190], and the Fixed Design Nidek MP-3 [191]. Other examples of commercially available video pupillometer devices include the EyeLink[2] 1000 and the EyeLink II [192].

[2]SR Research Ltd., Mississauga, Ontario, Canada

As we discussed in the first Chapter (see Sec 4.2), pupillometer instruments are widely used in the ophthalmology field to measure human pupils and are a good way to detect diseases like:

- Optic nerves disorders such as glaucoma and optic neuritis
- Retinal disorders such as age-related macular degeneration and retinitis pigmentosa
- Neurological disorders such as Parkinson's disease and multiple sclerosis can affect the function of the pupils
- Problems with specific medications, such as *anticholinergics* that can cause dilated pupils or decreased pupillary response to light
- Anisocoria, that is a condition in which the size of the pupils is unequal

Other researchers, as shown in Figure 5.2, successfully measured PLR in healthy patients, in order to demonstrate the advantages of binocular mobile devices with respect to traditional pupillometers [193].

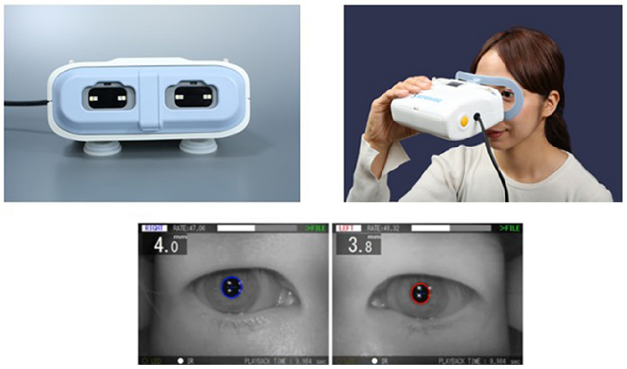


Figure 5.2: Hitomiru®binocular pupillometer

Additionally, some researchers have proposed the use of smartphone-based pupillometer devices [194], which use the camera of a smartphone to capture an image of the eye and measure the size of the pupil. These devices typically use mobile apps such as the PupilScreen [195] and the Pupillometer app [196].

The pupillometry field has seen a growing number of different types of pupillometer devices proposed by researchers, each with its own unique features and capabilities. Some of the most common types include infrared pupillometer, video pupillometer (used for tracking), and smartphone-based pupillometer devices. Technology advancements are improving the accuracy and reliability of pupillometry measurements and more is expected to come in the future, thus enabling these types of instruments to be used for a variety of applications in ophthalmology, neurology, and psychiatry.

5.1.2 Pupil Tracking

Many studies concerning eye imaging published in the last few decades are mostly focused on vision-based techniques aiming to fulfill complex tasks, such as eye tracking [197], gaze estimation [198], pupil, and iris recognition [199,200]. With this goal in mind, numerous researchers worked toward the collection of a large number of datasets, and in some cases, helped make those datasets available to the public. Unfortunately, it should be noted that for each specific task and dataset, the eye images can be characterized by a number of different factors, including the viewing angle and framed field, head position, eye color, and light circumstances as well as eye state (*i.e.* open, half closed or fully closed), skin texture, ethnicity and age of involved subjects and the visual state of health.

According to the research conducted by Winkler *et al.* [201], the bulk of eye-tracking datasets gathered between 2004 and 2012 had an average viewing distance of 70 cm, with frames recorded in a laboratory environment using a chin rest, a biting bar, or head-mounted devices to limit the patients head movement. Other datasets, instead, include face and eyes images collected in natural environments [202] or with commercially available devices such as smartphones [203], thus to solve most common eye gaze estimation during everyday tasks, such as driving [204], reading [205] or browsing the internet [206]. Other studies include images for the detection of natural blinks [207, 208], some of them with the aim to improve gaze estimation [209].

Differently, datasets used for pupil localization and iris recognition only frame partially subject's faces, as most of them exploit custom-made head-mounted devices to acquire eye images from a closer viewing angle [210,211]. Recently, the work published by Omelina *et al.* [212] reviewed tens of datasets concerning iris recognition tasks. Although many of these datasets are now freely available online, none of them was appropriate for our specific purpose due to the lack of mandatory annotations or labels, as well as the specificity of the images we required in our test case, which aim at improving the acquisition quality of a *Pupillary Light Reflex* instrument.

Several works that tackled the task of pupil detection, eye localization, or face recognition have been introduced and improved over the years. Timm *et al.* [213] suggested a method to localize the eye center by means of gradients. Others approach aimed to further investigate this task. An algorithm based on a k-means histogram segmentation proposed by Swirski was able to achieve 50 fps on a desktop CPU with a 5 px error on highly off-axis images [214]. Others [215], tried to improve the efficiency of the localization problem on BioID face database [216] with a combination of Haar features and efficient SVM, thus reaching 10 fps and 90% accuracy ($e^3 \leq 0.1$) on a 3.0 GHz desktop CPU. Lately, the research group of Kacete, proposed a Hough randomized regression tree obtaining an overall 97.9% accuracy with $e \leq 0.10$ at around 30 fps on a desktop CPU.

Following that, numerous different forms of Deep Learning algorithms, notably Convolutional Neural Networks (CNN) [197,217–219], were proposed by researchers to obtain greater localization accuracy over more heterogeneous datasets, all performing around 90% depending on normalized error threshold e, at the cost of increased computational complexity. Indeed, the best results were reached with *DeepEye* [218] with 87% detection rate with 5 px error while performing around 32 fps with the employment of an Nvidia Tesla K40 high-end GPU. More recently, the combination of Deep Learning and Expert System algorithm presented by Khean [220], showed 100% accuracy with $e < 0.1$ over popular datasets Talking-Face [221], BioID [216] and GI4E [222], thus without reporting any real-time metrics. In Table 5.1, we summarize the most effective Vison-Based face and eye recognition techniques presented in the last 10 years.

Besides that, different techniques, such as pseudo-depth mapping from RGB images [224] or implementation of a two-stage training process with anomalous data samples [225] have been investigated to furtherly increase image recognition accuracy and generalization capabilities of commonly used CNN architectures. While many studies have been carried out to improve face and eye detection, or pupil tracking with vision-based techniques, it is worth noting, that most investigations focused on the achievement of lower localization error, *i.e.* higher detection rates and accuracy, at the cost of higher computational complexity. Moreover, our findings show that there is a lack of performance comparison for the majority of the aforementioned approaches on different platforms. In our opinion, this is a key aspect that can assess the scalability of such systems for more simple, effective, and efficient solutions.

[3]This measure was introduced by Jesorsky et al. and is defined as: $e \leq \frac{1}{d} max(e_l, e_r)$, where e_l, e_r are the Euclidean distances between the estimated and the correct left and right eye centers, and d is the distance between the correct eye centers.

[4]Average displacement between predicted gaze point and real gaze point on smartphone screen

Table 5.1: Summary table of related methods available in the literature for similar tasks about eye status classification.

Task	Data	Methodology	FPS	Accuracy (error)	Architecture	Ref.
Eyes Center Localization	BioID [216]	Gradients	-	93.4 % $e \leq 0.1$	-	[213]
Pupil Edge Localization	IR Eye Images	Haar feature, k-means segmentation	50	87 % $e \leq 5px$	Quad-Core 2.8 GHz	[214]
Eyes Center Localization	BioID	Haar Features and eSVM	10	90 % $e \leq 0.1$	Pentium 4 3.0 GHz	[215]
Eyes Center Localization	BioID	Hough randomized Regression tree	30	98 % $e \leq 0.1$	Intel i7 2.7 GHz	[223]
Gaze Tracking	GazeCapture	Deep CNN	10-15	error [4] $\sim$ 1 cm	ARM 1.85 GHz	[197]
Pupil Localization	IR Eye Images	CNN with ASPP blocks	32	87 % $e \leq 5px$	Nvidia Tesla K40	[218]
Pupil Localization	BioID and GI4E [222]	ES and DL	-	100 % $e \leq 0.1$	-	[220]

5.2 System Design

In this section, the engineering of a pupillometer instrument is presented together with component details, design choices, useful recommendations, and technical notes. Following the layout previously explained in the introduction of this Chapter 5, all the main elements of a Maxwellian-View-based pupillometer are here presented and discussed. Among the different geometrical view optics that can be adopted for the realization of a device for eye stimulation (see Sec. 3.3), the Maxwellian-View seems to be the most compelling option, as the type of stimulation offers superior control of the light intensity and if properly designed, allows for open-loop pupil response analysis, i.e. light intensity on the retina is not influenced by pupil size.

Figure 5.3 illustrates the Maxwellian-View design that is furtherly described in the following sections.

5.2.1 Light Sources

Visible LEDs

Comprehension of how we see light requires an understanding of light sources and their effects on photoreceptors in the retina. Evéquoz et al. [58] suggested a way to find the theoretical levels of light that cause the lowest and biggest expression of a single photoreceptor while keeping other photoreceptors stimulated constantly. The aforementioned goal can be achieved only when the number of light sources is at least equal to the number of photoreceptors for best contrast.

To generate visible light four LEDs types with different peak emission wavelengths (RGBY illumination, namely red, green, blue, and yellow) have been used. In Table 5.2 the main specifications of the selected LEDs are reported.

As can be seen in the Table, we opted for High-Brightness standard 5 mm package, trough hole single color LEDs from Roithner Lasertechnik[5]. The relatively low Full-Width Emission Angle[6] has been chosen,

[5]Roithner Lasertechnik GmbH, Wiedner Hauptstraβe 76, A-1040 Vienna, Austria

[6]The full-width half-maximum (FWHM) emission angle, also known as the viewing angle, of a LED, is a measure of how wide the angle of light emission is from the LED. It is typically measured in degrees and it describes the angle at which the intensity of the light emitted by the LED is half of its maximum intensity.

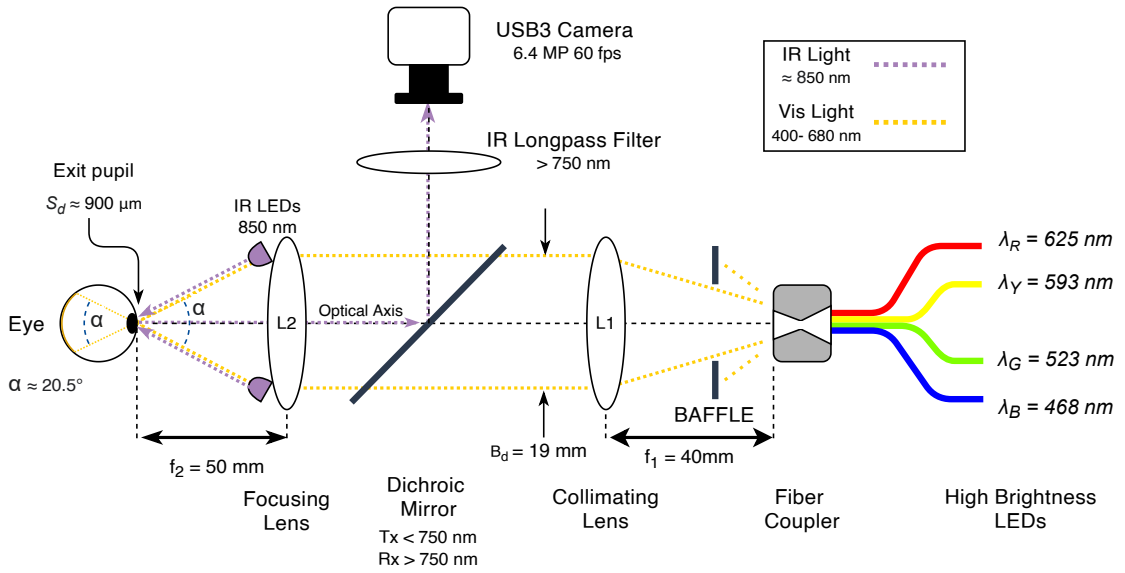


Figure 5.3: Optical diagram of the Maxwellian-View monocular pupillometer. Four fiber-coupled high-brightness LED sources are used to stimulate the eye. In order to obtain a Maxwellian-like optical system, two lenses L_1 and L_2 have been used. A dichroic mirror, a high-pass optical filter, and a USB high-resolution camera allow the recording of direct pupil response under 850 nm infrared illumination.

Table 5.2: Specifications of selected Roithner LEDs used for eye stimulation

Color	LED Code	Price Single Euro	Package Size ϕ	Emission Angle Full Width	Nominal Luminosity I = 50 mA	Continuous Forward Current	Peak Wavelength
Blue	B56L5111P	1.51	5 mm	15 °	25000 mcd	50 mA	470 nm
Green	G58A5111P	2.55	5 mm	15 °	100000 mcd	50 mA	525 nm
Yellow	Y5CA5111P	1.78	5 mm	15 °	55000 mcd	70 mA	590 nm
Red	R5CA5111P	1.78	5 mm	15 °	55000 mcd	70 mA	629 nm

as highlighted in the following sections, to reduce loss with fiber optic coupling. Furthermore, the driving techniques and circuitry are described in Section 5.2.4.

Infrared LEDs

Capturing images of the eye where it is important to enhance the contrast of the pupil edge while avoiding any stimulation of the photosensitive cells, can be achieved by using infrared light as a light source for the acquisition device. This is because the pupil does not react to infrared wavelengths (with a wavelength greater than 750 nm), allowing for a clear image of the pupil with maximum contrast. By using infrared light, it is possible to obtain high-quality images of the pupil without causing any discomfort or potentially harming the eye. As shown in Figure 5.4, a total of 8 SMD Near Infra-Red LEDs 850 nm ($\pm 15nm$) (OSRAM[7] TOPLED®, SFH 4253-R) [226, 227]have been used and circularly disposed around lens **L2** (see Fig. 5.3).

The IR LEDs have been placed after lens **L2** (see. Figure 5.3), thus avoiding unwanted reflections on the lens glass and on the dichroic mirror. More details evidencing how the light emitted by the LED is properly reflected using a hot mirror and prism to enable imaging of the eye with high contrast and resolution are presented in the following sections.

[7]OSRAM International GmbH, Leibnizstr. 4 93055 Regensburg Germany

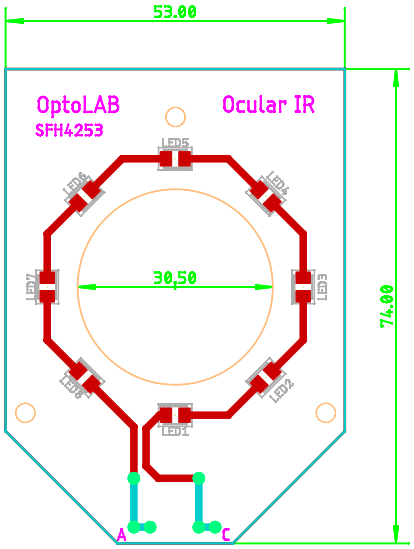


Figure 5.4: Infrared LEDs placement on a printed circuit board. The 39.5 mm diameter hole is for the housing of lens **L2**. While **A** and **C** are the anode and cathode connections for the LEDs series, respectively.

Optical Fibers

In ophthalmology, the use of fiber optic cables enables light to be transmitted into the eye in a controlled and precise manner, also allowing for optimal visualization of the interior of the eye during various procedures, such as retinal, cataract, and glaucoma surgery. Fiber optic illuminants are also used in various diagnostic instruments, such as ophthalmoscopes and slit lamps, to examine the eye and diagnose various eye conditions. The use of fiber optics in ophthalmic instruments has significantly improved the accuracy, safety, and effectiveness of ophthalmic procedures and examinations as they allow for moving light energy from the source (LEDs) to specific *optical path*, as in the case examined.

Fiber optics can be distinguished between [228]:

- **End Emitting**: optical fibers that conduct energy without many losses, composed of glass or synthetic material PMMA;
- **Side Emitting**: optical fibers characterized by relevant losses on side surfaces, made of PMMA.

In the optical scheme depicted in Figure 5.3, four fiber optics segments are used to collect the light from the four distinct LED sources and converge them into one, single end-emitting fiber. More specifically, a 1 mm core FSN-1000 end-emitting optical fiber without sheath[8], characterized by a *numerical aperture*[9] (NA) of 0.51 has been used for each LED bulb.

The numerical aperture (NA) of a fiber optic cable refers to the range of angles at which light can enter the fiber and be transmitted without significant loss. For single-mode fibers, the NA typically falls within a range of 0.05-0.4, which means that these fibers are designed to transmit a single mode of light with high precision over long distances [229].

In contrast, multimode fibers are designed to transmit multiple modes of light simultaneously, and therefore require a larger core diameter and higher NA. While the range of NAs for multimode fibers can

[8]Fort fibre ottiche s.r.l. - via Walter Tobagi 5 24035 Curno (BG), Italy

[9]The numerical aperture (NA) of an optical fiber is a measure of the cone angle of the light that can be accepted by the fiber. It is a dimensionless number that is related to the maximum angle of incidence at which light can enter the fiber without being completely reflected at the fiber's surface (called the acceptance angle). A larger NA means a wider acceptance angle and a higher ability to collect light, which leads to a higher signal-to-noise ratio in the transmitted signal.

vary depending on the specific type of fiber, it is generally true that multimode fibers have higher NAs than some single-mode fibers, with values typically exceeding 0.3.

Having a high NA can provide some advantages, such as better light coupling efficiency and higher bandwidth. However, it can also introduce challenges such as increased modal dispersion, which can cause signal distortion and reduce overall performance. Additionally, high-NA fibers can be more difficult and expensive to manufacture than low-NA fibers, and may require specialized equipment and techniques for installation and maintenance.

Overall, the NA of fiber is an important factor to consider when selecting a fiber optic cable for a specific application, and a range of factors should be considered in addition to NA, such as core diameter, cladding material, and transmission wavelength, among others. It's important that the end of the fiber, here considered for simplicity as a point source of light with determined NA, is located near the focal point of the collimator lens, in order to avoid huge magnification, which could make the Maxwellian optic inapplicable. Furthermore, rays coming out of the collimator would not be parallel and this will cause subsequent aberrations in the converging lens near the pupil. Light is emitted from multimode fibers as a wide cone of light. The angular amplitude of the cone rays is usually linked to the fiber's Numerical Aperture (NA). The general relation in the air is:

$$NA = \sin \frac{\theta_{max}}{2} \tag{5.1}$$

In our case, since each fiber is coupled with one LED the total angular amplitude obtained is $\theta_{max} = 61.3°$

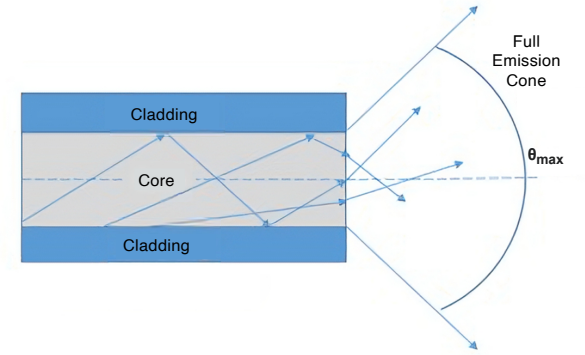


Figure 5.5: Optical fiber emission angle

Illumination Structure

As we explained in the previous Section, the selected fiber source cannot be considered an ideal point source. This makes it important to obtain a spot that is as small as possible, in order to respect Maxwellian optics when focusing rays into the pupil. To avoid or at least limit bending losses, there is a support structure for the fiber coupling, as we can see in Fig 5.6. On the right side, there is the coupling between the fibers and the four LEDs, on the left side we have the *custom light combiner* and the single fiber exit.

As illustrated in the first chapter 1.2.1 the pupil diameter can be about 1.8mm after a high-brightness luminous stimulus. Therefore, in order to comply with Maxwellian optics, it is necessary to ensure that the spot of light in the pupil is smaller than the pupil's smallest diameter. This means that the design of the light source is a critical aspect of the optical design. To achieve the best possible illumination path, a starting point is to couple the four LEDs (RGBY) with four optical fibers, with a diameter of 1mm each. If

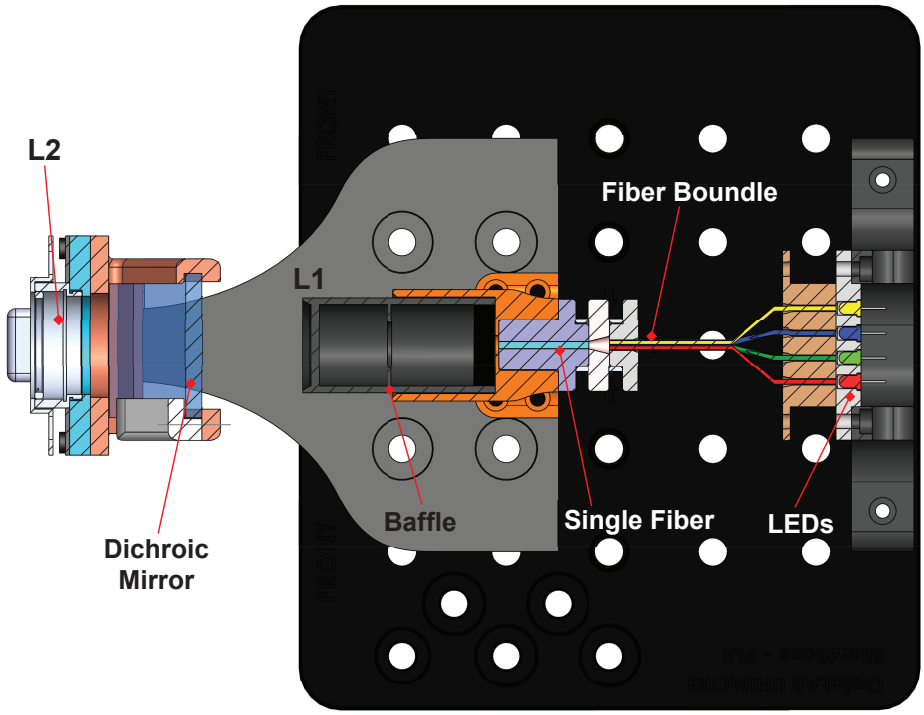


Figure 5.6: Illumination Assembly on SolidWorks, slice plane is parallel to the eye's optical axis.

the four fiber together is considered, the light spot at the end of this fiber coupling can be considered to be a square with a side of 2mm. Therefore, a simple design has been adopted to combine the four different fiber optics to obtain a single fiber output. To achieve this, a particular design of the fiber bundle has been studied and shown in Figure 5.7.

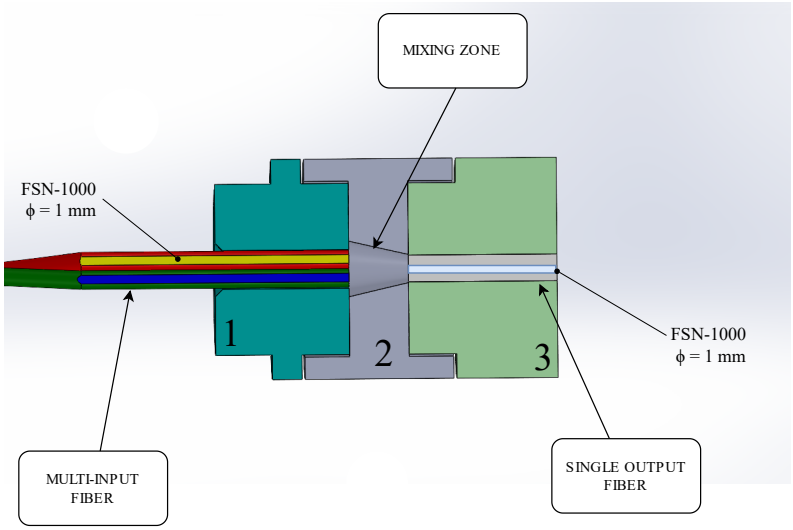


Figure 5.7: Design of the fiber coupling. As input, four 1 mm core fibers (FSN-1000) are bundled together in **1** cavity with clear epoxy. Inside the connector's **2** cavity light is mixed in the air. White cavity walls provide reduced loss. Output cavity **3** is provided with a single 1 mm core FSN-1000 fiber for further light mixing. In this case, the longer the output fiber the more uniform the mixing will be at the end.

The bundle is divided into three parts, with the middle part being in charge of the mixing of rays

among the single output fiber. However, this coupling has the drawback of very high-efficiency loss and non-uniform light mixing. Therefore, many efforts have been made to limit light losses by having a very polished finish on the external sections of the optical fibers.

In the next Sections, a description of main optical elements, i.e. the selected lenses **L1** and **L2** as well as the dichroic mirror are briefly presented.

5.2.2 Optical Elements

Collimator Lens - L1

A collimator lens can be used to converge divergent rays of a source into a parallel beam of light rays. As illustrated in Figure 5.3, in the considered design a *collimating lens*, namely **L1**, has been used to collect and collimate light rays coming from the single optical fiber, where the light collected from the different source is mixed. However, the **#f** or **NA** of the lens must match the numerical aperture (NA) of the optical fiber being used. For fibers with a high NA (≥ 0.38), standard collimators may not be able to effectively align the rays into a parallel beam, resulting in significant power loss. This is illustrated in Figure 5.8 where the use of a standard collimator with a high NA optical fiber results in the loss of highly divergent rays.



(a) (b)

Figure 5.8: (A) High NA fiber connected to low NA Collimator Lens, (B) High NA fiber connected to high NA Collimator Lens

The representation of Figure 5.8b is only valid for an ideal point-like source, but in reality, as in the analyzed case, the core diameter of an optical fiber has a finite size. Therefore, it is important to consider the influence of object size on ray tracing. To demonstrate this, a simple Zemax[10] simulation was conducted. The simulation consisted of a paraxial lens with a focal length of 28mm, a clear aperture of 40mm (NA=0.7), and an object with a size of 4mm located at the focal point of the lens. The layout of Figure 5.9 illustrates that rays starting from off-axis points do not emerge parallel to the axis, but rather exhibit slight divergence with an angle α, given by the following equation:

$$\alpha = 2 \cdot \arctan(\frac{y_{height}}{EFL}) \tag{5.2}$$

Where y_{height} is the width of the source and EFL is the effective focal length of the collimating lens. As shown in Equation 5.2, the divergence angle of the output beam increases as the height of the object, represented by y_{height}, increases or the focal length of the lens, represented by EFL, decreases. This means that smaller fibers will result in a smaller divergence angle, whereas larger core fibers will generate a larger divergence angle. In order to reduce the divergence of the output beam and maintain a high NA, it is necessary to use lenses with higher optical power and larger diameters. Unfortunately, this will also result in an increase in the output beam diameter, as depicted in Figure 5.10.

[10] ANSYS, Inc., 2600 Ansys Drive, Canonsburg, PA 15317, United States

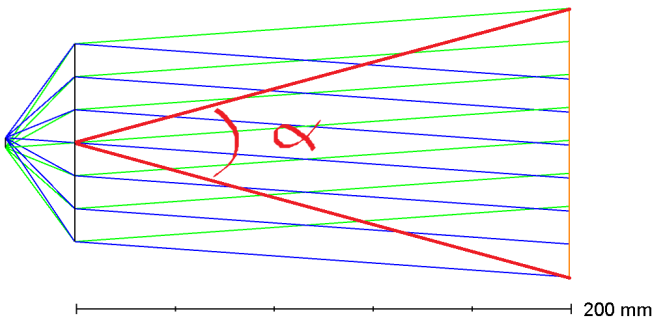
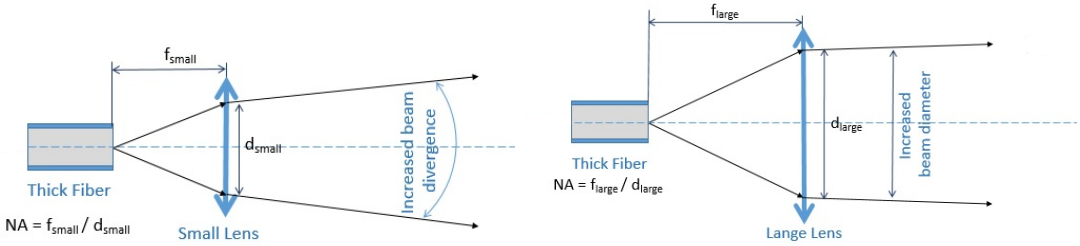


Figure 5.9: Effect of non-infinitesimal point source dimension



(a) (b)

Figure 5.10: Correct layout of collimator

As we highlighted before, when light is transmitted through an optical fiber, it is typically in the form of a diverging beam with a relatively large numerical aperture (NA). A *condenser lens*[11] can be used to collimate this beam and convert it into a parallel beam with a lower NA. Condenser lenses are commonly used in optical systems for a variety of reasons, including their ability to focus and direct light, control the angle and intensity of illumination, and improve the resolution and contrast of images. Some of the specific advantages of condenser lenses compared to other types of lenses include:

- High numerical aperture (NA): Condenser lenses can have high NA values, which allow them to collect and focus light from a wide range of angles. This can improve the resolution and contrast of images by reducing blur and increasing the amount of light that is directed onto the sample.
- Large aperture size: Condenser lenses can have large aperture sizes, which allow them to collect and focus more light onto the sample. This can be particularly useful when working with low-light samples or when trying to achieve a particular level of brightness or contrast in the image.
- Flexibility: Condenser lenses are often designed with adjustable features, such as aperture size and position, which allows the user to fine-tune the illumination and achieve the desired imaging results. They are also relatively compact and easy to integrate into optical systems.
- Compatibility with other optical components: Condenser lenses are compatible with a wide range of other optical features, such as objectives, filters, and cameras, which makes them versatile and useful in a variety of applications.

[11] A condenser lens is a type of lens that is used to focus and direct light onto a specific object or surface. The primary function of a condenser lens is to increase the intensity of light, which is accomplished by collecting and focusing light rays from a wide area onto a smaller area. The lens system is typically made up of two or more lenses that work together to focus and collimate the light.

Table 5.3: 45° AOI, 35.0mm Square, Hot Mirror Specifications

Features	Value
Angle of Incidence (°)	45
Coating	Hot Mirror, 45°
Substrate	BOROFLOAT®
Dimensions (mm)	35.0 x 35.0
Surface Quality	80-50
Thickness (mm)	3.30
Thickness Tolerance (mm)	±0.2
Type	Dichroic Filter
Dimensional Tolerance (mm)	+0.0/-0.2
Coating Specification	Tavg 85\% @ 400 - 690nm Ravg 95\% @ 750 - 1125nm
AR	Ravg 1\% @ 400 - 700nm
Wavelength Range (nm)	400 - 1125
Surface Flatness (P-V)	4 - 6λ
Coating Type	Dielectric

If we consider condenser lenses and remember the NA of the optical fiber ($NA = 0.51$), the best choice is the lens with a NA >= 0.51.

Dichroic Mirror

As explained in Sec. 3.1.2 this component is used to separate the *stimulation path* from the *acqusition path* as it transmits one portion of the optical spectrum, while reflecting other portions. High-Performance Hot Mirrors feature a multi-layer dielectric coating optimized for greater than 85% transmission of visible light and greater than 95% reflection of IR wavelengths [230]. For the system described by Figure 5.3, the goal is to transmit to the infrared-sensitive camera only the portion of the optical spectrum with wavelength $\lambda \geq 750nm$. The optical elements that enable this are called *hot mirrors* that are best suited for reflecting a long wavelength while transmitting visible light with high efficiency and high spectral separation. A configuration with an incident angle of $45°$ as depicted in Figure 5.11 has been selected, while the technical specifications of the selected mirror are reported in Table 5.3

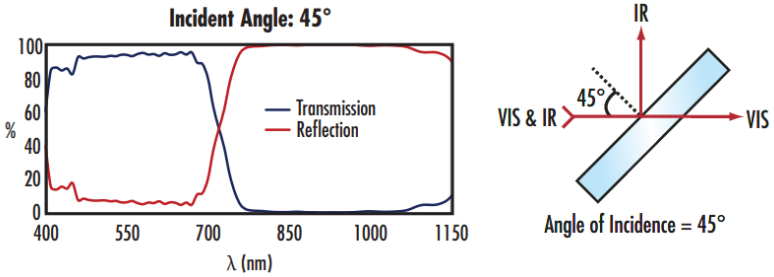


Figure 5.11: On the left, transmission, and reflection are in the function of wavelength. On the right, the working principle diagram is shown.

Aspheric Condenser Lens - L2

Finally, as depicted in Figure 5.3 the last optical element here considered is the Lens **L2**, which is used to focus the collimated light rays into the subject entrance pupil. For this purpose, an *Aspheric Condenser Lens* with a focal length ($f = 50mm$) has been used. Typically, a condenser lens modifies a divergent beam from a point source into a parallel beam, while aspheric means that this lens is corrected for spherical aberration (loss of focus for marginal rays: this feature is really important because the human pupil is located near to the focus and we want to have as much light as possible entering in the pupil. For our prototype, a plano-convex lens with a clear aperture of 24mm has been selected. When looking at the technical parameter, the f/# number, known as the ratio between the effective focal length and the aperture diameter must be taken into account as it determines the quality of the image:

- $f/\#$ **high**: we have an optic system with low brightness;
- $f/\#$ **low**: there are problems with lens aberrations like spherical or chromatic aberrations (see Sec. 3.1.1).

However, the f/# can be modified in search of the best compromise between image quality and brightness by working on the aperture of the system: that's the aim of variable diaphragms. Another important parameter to look at is the *Numerical Aperture* (NA). As previously described, a higher NA indicates that the lens can gather more light and focus it into a smaller spot. The NA is also related to the depth of field and the ability of the lens to resolve fine details. It is typically given as a dimensionless number between 0 and 1 but can be greater than 1 for lenses that use internal reflection to increase the acceptance angle.

5.2.3 Acquisition Device

The camera is the key point of the process of image acquisition. The choice of the camera and the objective must be made considering the following points:

1. **Resolution:** The resolution of the camera, in terms of the number of pixels, defines how many details we can distinguish when analyzing pupil images, as in optimal illumination circumstances, a higher resolution corresponds to a higher sensitivity to small pupil size changes. Despite higher resolutions sound always as "nice to have", an increasing number of pixels also usually reflects, smaller pixels areas and therefore reduced light sensitivity, and lower frame rates since interface bandwidth is usually limited and higher computational costs, as images and video captured at higher resolution need more processing power and more disk space;

2. **Sensor Type:** The type of sensor used in a camera can greatly affect image quality, and there are several different types of sensors used in digital cameras. The two main types of sensors are CCD (*charge-coupled device*) and CMOS (*complementary metal-oxide-semiconductor*). CCD sensors are typically used in high-end cameras and produce high-quality images, but they consume more power than CMOS sensors. CMOS sensors are more common and are used in most consumer cameras and smartphones. They are more power efficient and also cheaper than CCDs.

3. **Frame Rates:** This is another important aspect when choosing the camera. Frame rates higher than 30 are usually recommended when analyzing pupillary light reflex [231, 232]. Increasing the FPS captured translates to a higher temporal resolution of recorded PLR at the cost of reduced exposure time, i.e. darker images;

4. **FOV:** When selecting the objective lens for the camera, the *Field of View*, usually expressed as the focal length of the lens itself, must be first considered. The FOV is therefore determined by the

distance of the camera for the object and the size of the area to be framed in the picture. Additionally, lens and sensor format compatibility, as well as lens quality (expressed in MP), aperture, and size must be considered.

5. **Interface:** The camera interface, thus including Max Bandwidth and connector type must be taken into account. Popular interfaces that offer high bandwidth with standard connectors are USB3 and Ethernet.

6. **I/O:** Input-Output connectors should be also considered if additional low-level control on the acquisition process is needed. As an example, an external hardware trigger is usually one of the most common features offered by I/O additional connectors.

   All the above considerations led to the choice of a CMOS, board-level camera with S-Mount optics and SONY IMX178 sensor depicted in Figure 5.12, in particular, the camera developed by Matrix Vision (MATRIX VISION GmbH Talstraβe 16 71570 Oppenweiler, Germany).

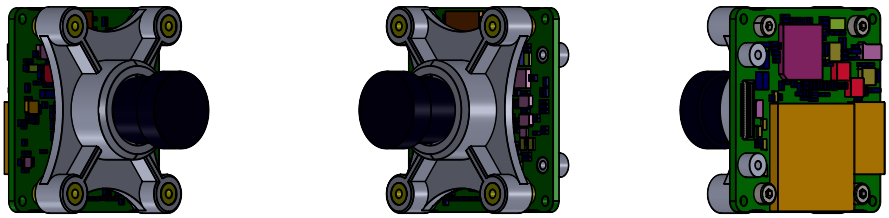


Figure 5.12: 3D view of the board level CMOS camera

The Sony IMX178 is a CMOS image sensor that was released in 2013. It has a sensor size of 1/1.8 inch and a resolution of 6.4 megapixels, which means that it can capture images with high levels of detail. In terms of dynamic range, the IMX178 has a rating of 70.9 dB. This means that it can capture a wide range of tones, from bright highlights to deep shadows. This makes it ideal for applications where you need to capture details in both bright and dark areas of an image. The sensitivity of the IMX178 is also impressive. It has a sensitivity of 2000 mV/Lux-sec for color images, and 2800 mV/Lux-sec for monochrome images. This means that it can capture high-quality images even in low-light conditions. Overall, the Sony IMX178 is a high-quality image sensor that offers a range of impressive features. Its high resolution, small pixel size, wide dynamic range, and high sensitivity make it a popular choice for a variety of applications, including machine vision, surveillance, and industrial imaging.

Table 5.4: On the left: mvBlueFOX3-3M Series – Camera board-level specifications. On the right: Edmund Optics - S-Mount - F10.1 mm lens specifications.

Camera		Objective Lens	
Feature	**Specification**	**Feature**	**Specification**
Sensor	IMX178 (1/1,8" rolling shutter CMOS - 2.4 µm pixel size)	Length (mm) & Diameter (mm)	13.40 L 15.0 D
Chroma	Monochromatic	Filter Thread	M12 x 0.50
Image formats	Mono8 .. Mono16; Bayer8...Bayer16, RGB, YUV	Horizontal Field of View	36°
FPS (Streaming)	59.0	Resolution, On-Axis	81 lp/mm @ 20% Contrast
Lens holder	S-Mount, 13 mm length	Resolution, 0.7 Field	54 lp/mm @ 20% Contrast
Optical filter	without filter without protective glass	Resolution, Full Field	64 lp/mm @ 20% Contrast
Housing	without housing	Type	M12 Imaging Lens
Inputs / Outputs	standard I/O, 12 pin Hirose	Focal Length FL (mm)	10.10
Version	USB3 Vision industrial camera	Maximum Sensor Format	1/2"
Interface	USB 2.0 / 3.0	Working Distance (mm)	400 - \infty
Digital inputs	4x PNP non-isolated	Mount	M12 x 0.5 (S-Mount)
Digital outputs	4x PNP non-isolated	Aperture (f/#)	f/2.8
Dimension	37 x 37 x 4.5 mm	Distortion (%)	-0.57 @ Full Field
Operating voltage Ub	4.45...5.25 VDC	IR Cut Filter	No

5.2.4 Hardware

In this Section, a brief overview of the hardware components, thus including the Microcontroller unit and the driving circuitry is presented. Figure 5.13 illustrates the logic control that enables setting and personalizing the light stimulation with 1 ms time resolution and 18-bit intensity resolution for each LED color.

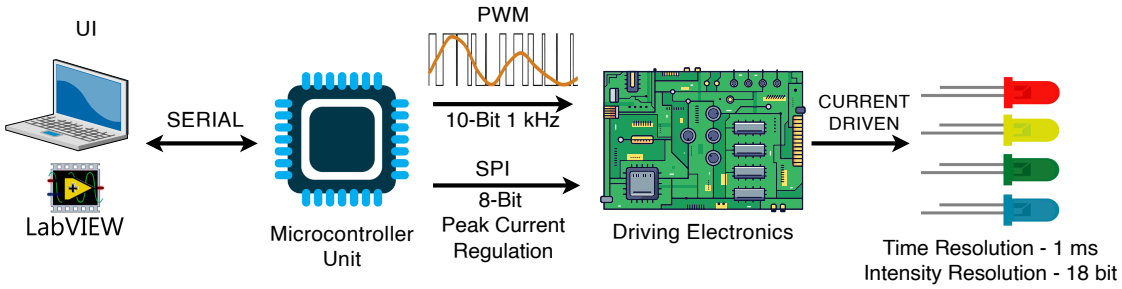


Figure 5.13: Pupillometer control block diagram

In the following, a brief description of the microcontroller unit employed and of the electronic circuit that allows driving the LED sources are presented.

Micro-controller unit

A microcontroller has been used in the presented measurement systems as the core that enables low-level control of the electronics, such as light control and acquisition synchronization. Overall, here we discuss

some of the key reasons for using a microcontroller in a general measurement system:

1. **Data acquisition:** A microcontroller can collect data from various sensors and other sources, providing accurate and reliable data acquisition.
2. **Data processing:** The microcontroller can process the data collected from sensors to provide useful information that can be analyzed and acted upon.
3. **Control:** The microcontroller can control the operation of the measurement system, including controlling the sensors, displays, and other components.
4. **Communication:** The microcontroller can facilitate communication between the measurement system and other devices or systems, such as a computer or a remote server.

As in the case of our pupillometer system, the *Atmel-based* board [233] depicted in Figure 5.14 has been employed. It embeds SAM3X8E ARM Cortex-M3 microcontroller (32-bit architecture) produced by Microchip Technology[12]. Additional information can be found in the relative datasheet [234].

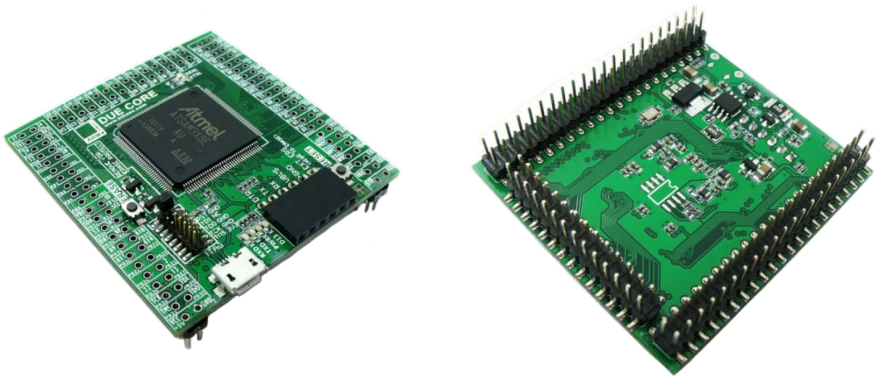


Figure 5.14: Core Due Microcontroller Board.

In the considered system, the microcontroller is in charge of the following tasks:

- Handling the low-level Serial-Communication between the User Interface (developed in LabView, see. Sec. 5.2.5) and the system electronics components (see Fig. 5.13).
- Generation of PWM (*Pulse Width Modulation*) signals to control the LEDs **ON** and **OFF** state in order to properly yield the desired light stimulation;
- Synchronization of camera frame acquisition with a dedicated hardware TTL digital signal;
- Optional synchronization of external acquisition devices, such as another light stimulator or a ERGs (electroretinogram) recording device.

PWM [13] (*Pulse Width Modulation*) can be used to control the intensity of an LED light by varying the duty cycle (DC) of the signal that is used to drive the LED. By adjusting the duty cycle of the PWM signal, the intensity of the LED light can be smoothly and continuously varied from fully off to fully on, or any level in between, providing a flexible and efficient way to control the brightness of LED lights. For the LED light current control, a proper frequency should be used in order to maximize light intensity

[12] Microchip Technology Inc., 2355 West Chandler Blvd, Chandler, Arizona, USA 85224-6199, (480) 792-7200

[13] A PWM (pulse-width modulation) signal is a type of digital signal that uses a series of pulses to control the amount of power delivered to an electrical device. The duty cycle, which is the ratio of the pulse width to the period of the signal, is used to adjust the power level. PWM signals are commonly used for precise control of motors, lights, and other power regulation tasks.

Table 5.5: CORE DUE Specifications

Feature	Specification
Microcontroller	AT91SAM3X8E LQFP-144
Operation Voltage	3.3V
Input voltage	5V
Total connector pins	44 + 44 + 28 = 116Pins
Flash	2 x 256 Kbytes
SRAM	64 + 32 Kbytes
Clock Speed	84 MHz
Number of PIOs	103
NAND Flash Controller (NFC)	Yes
SHDN Pin	Yes
EMAC	MII/RMII
External Bus Interface	16-bit data / 8 chip selects / 23-bit address
Central DMA	6
12-bit ADC	16 ch
12-bit DAC	2 ch
32-bit Timer	9 ch
PDC Channels	17
USART/UART	3 / 2 (USART3 in UART mode)
HSMCI	1 slot, 8 bits
Board dimension	54 x 58mm

accuracy and time resolution of the delivered stimuli. Before deciding to use a 32-bit microcontroller board, the ATmega 2560 (8-bit microcontroller) was employed [235]. Unfortunately, with ATmega 2560 minimal color flickering occurred, due to the limited capabilities of the microcontroller, i.e. low modulation frequency available for the PWM.

Using the 32-bit based board, which besides the more advanced and performing microcontroller is equipped with an 84 MHz clock frequency, the LED's color light intensity can be precisely set with $\pm 0.1\%$ ($R_{DC} = \frac{1}{1000}$) duty cycle resolution with a modulation frequency of $f_{PWM} = 1\ kHz$. In this way, no color flickering will be perceived by the subject. Moreover, **ON** and **OFF** states can be controlled with $t_r = 1\ ms$ time resolution. This has been achieved by configuring an internal *TIMER* that runs at $f_t = 1\ MHz$ frequency, i.e. $1\ \mu s$ time resolution[14]. Further specifications of the micro-controller board used are reported in Table 5.5.

Led Driving Circuitry

The development of the control electronics has been designed starting from the following statements:

- The easiest way to control any LED-based device is through the regulation of the forward current since, as introduced in Sec. 3.2.1, solid state sources benefit from an almost linear relationship between forward current and output optical power. Using the previously described programmable micro-controller, that outputs *pulse width modulation* PWM signals is therefore the most convenient and easy way to control LEDs' forward current;

- As introduced in the first Chapter 1, the human eye allows us to see through an incredible range of different light levels. This implies that a properly designed system should allow for a wide range of different light-intensity stimulations to be performed. Acting only on the duty cycle, even with the newest and fastest uC units, does not allow us to reach a such wide range of control on the source intensity resolution. Therefore, further development of improved driving techniques must be considered. As presented in this section, the modification of simple driving schemes with a digital potentiometer allowed us to furtherly extend the light intensity, i.e. driving current resolution, by adding additional 8-bit (256) intensity steps.

[14]The equation used to obtain DC resolution given the clock frequency and PWM frequency is: $R_{DC} = \frac{f_t}{f_{PWM}} = \frac{1}{1000}$

These requirements have made the choice of components the most critical part of the realization of the circuit.

First of all, the choice of the led driver fell on the CAT4238 from On Semiconductor [236]. The CAT4238 is an efficient (over 87 %), boost-led driver, with the capability to power up to 10 LEDs in series with a maximum current of 100 mA. In our case, the described circuit is used for each primary, which is constituted by a single LED. Moreover, the driver allows adjustable output LED current and PWM modulation up to 1 kHz. The chip is available in a tiny SOT23 package (2.8 mm w - 2.9 mm l - 1 mm h), perfect for space-critical applications. The reference schematic reported in the datasheet is shown in Figure 5.15.

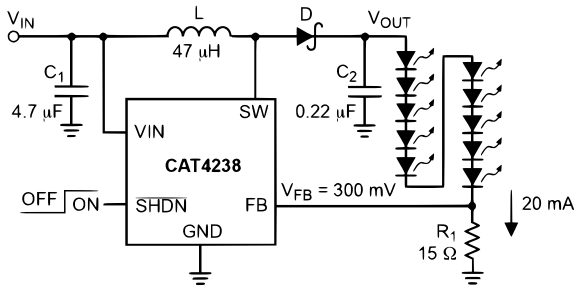


Figure 5.15: CAT4238 typical application circuit

As can be noted in the Figure the reference LED's current is simply given by the formula $I_D = V_{FB}/R_1$. It can be inferred that by changing the R_1 value it is possible to tune the LED output current, i.e. output light intensity during the **ON** state. Unfortunately, the only way to achieve that result with digital control is to operate on the feedback node where R_1 is connected to the ground. Here, a variable voltage node is introduced to dynamically set the LED's current through digital communication. Therefore, by changing the voltage at R_1 ground end between 0 and 300 mV it is possible to arbitrarily set the I_D. As a consequence, the I_D max is obtained when the R1 is tied between V_{FB} and ground. In the realized circuit, R_1 can be set for each color as it regulates the maximum current that can flow through each LED. The variable voltage was then obtained by the conditioning circuit shown in Figure 5.16.

The variable voltage V_x is generated starting from a 900 mV voltage reference ISL2108 from Renesas Electronics (Datasheet [237]) and a digitally programmable resistive divider, realized with a digital potentiometer, the AD8403 (Datasheet [238]). The AD8403 provides a quad-channel, 8-bit (256-position), digitally controlled variable resistor (VR) device. These devices perform the same electronic adjustment function as a mechanical potentiometer or variable resistor. The device is digitally programmable through SPI [15] interface. The resistance between pin A1 and pin B1 is fixed to 10 kOhm, while the W1 wiper position can be programmed with a standard microcontroller provided with SPI interface protocol. Each chip can be connected in a cascade to be serially programmed. For the system described here, a total of 4 digital potentiometers are required, thus can be achieved with only a single chip.

It is worth noting that, the ISL2108 provides a precise and stable voltage reference that is of fundamental importance for the constant current generation. Any variation in this voltage is directly reflected in LED current variation, thus in unwanted variations in output light intensity. By adding resistance R_{P1}, the voltage at pin A1 is then fixed to be slightly above 300 mV. By programming the AD8403 with a digital value in a range from 0 to 255, the voltage at the W1 wiper pin can go from 0 to 315 mV respectively. A voltage W1 equal to 0V gives the maximum LED current, that is $I_D = V_{FB}/R_1$. Setting W1 voltage higher than 300 mV gives no current on LEDs, since $V_{FB} - V_X < 0$. The output buffer (Av=1) stage is

[15] The Serial Peripheral Interface (SPI) is a synchronous serial communication interface specification used for short-distance communication, primarily in embedded systems. SPI devices communicate in full duplex mode using a master-slave architecture with a single master. The master device originates the frame for reading and writing. Multiple slave devices are supported through selection with individual slave select (SS) lines.

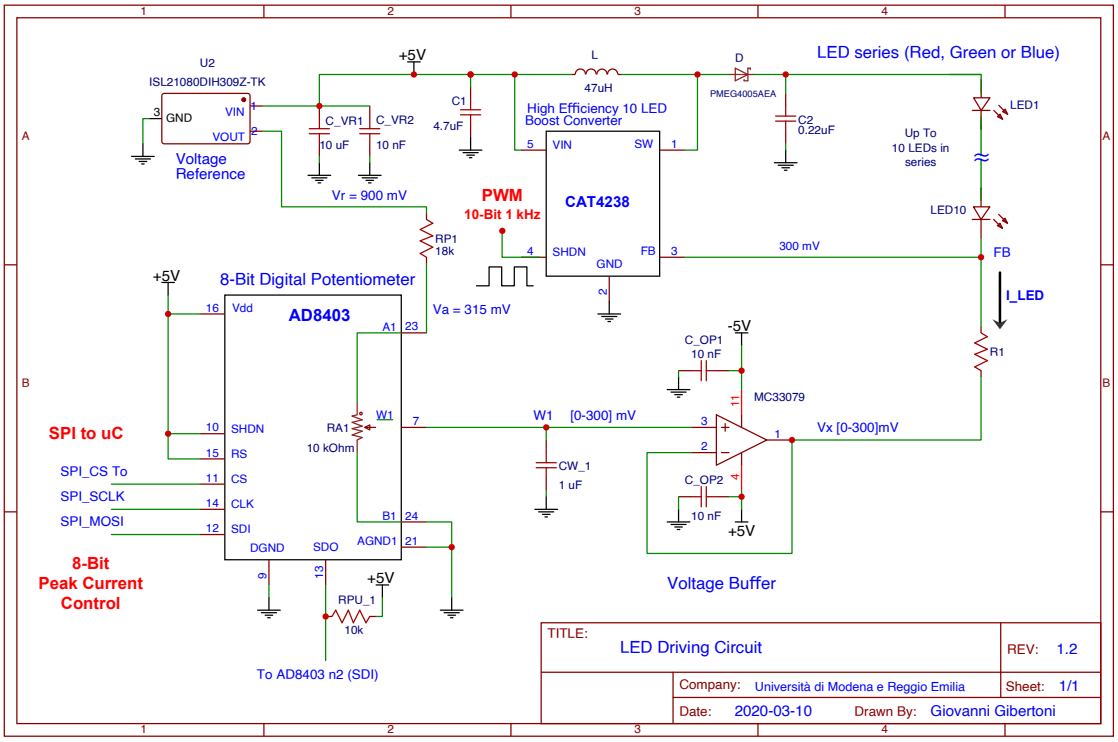


Figure 5.16: Schematic of the LED driving circuitry realized. The schematic can be used to drive up to 10 LEDs in series. In our case, the above circuit is used for each primary, which is constituted by a single LED. A single PWM signal can be used to turn **ON** or **OFF** the less or to modulate the intensity with a 10-bit resolution. An SPI interface is also used to set the 8-Bit digital potentiometer, thus giving an additional 8-Bit resolution on the current peak intensity.

added to avoid the breakdown of the digital potentiometer since it can only support an absolute maximum current of $\pm$ 5 mA between W1 and B1. For the buffer stage, the selection of the amplifier is also critical. A low noise, low offset, low output impedance amplifier that is capable to sink the entire I_D is required. Unfortunately, with a single supply, the output stage of any operational amplifier, even Rail-To-Rail ones, is limited to a few dozen of mV when sinking high currents. For that reason, the choice of dual supply was the only alternative to obtain Vx output signal swiping between 0 and 300 mV. Considering all these requirements, the choice for the operational amplifier fell on the SOIC14 Low Noise Quad Operational Amplifier MC33079 provided by On-Semiconductor [239].

As can be seen by looking at Figure 5.16, the LED current can be further modulated with a PWM signal that can go up to 1 kHz switching frequency. The digital control also allows controlling the timing, i.e. **ON** state and **OFF** state of each LED source. Therefore, by proper modulation of the PWM digital signal through Duty Cycle[16] (DC) variations, it is possible to further regulate the LED intensity.

5.2.5 Software

As in almost any modern electronic system, a software component has been developed for this pupillometer system. The main parts and functions of the realized logic as well as the programming language used

[16]The duty cycle is the ratio of the time that a signal is active or "on" to the total time of one period of the signal. It is often expressed as a percentage or decimal fraction. The duty cycle is used to describe the amount of time a signal spends in a particular state, such as high or low, and is commonly used in electronic circuits, including power converters, pulse-width modulation (PWM) circuits, and oscillator circuits.

are the following:

- Logic functioning of the microcontroller - *#C code*
- Pupil Identification Algorithm - *Python Language*
- User Interface to control the system and data recording - *NI LabVIEW*

In the next subsections, a brief description of a basic pupil detection algorithm and the user interface (UI) is provided.

Basic Pupil Identification Algorithm

One of the major routines here described is related to the algorithm used for pupil recognition and size estimation. *Python*[17] programming language has been chosen as it presents numerous packages and libraries for high-level object-oriented solutions for image processing. Among many free available frameworks, one of the most popular ones, used in deep learning and computer vision applications, is OpenCV. OpenCV (Open source computer vision) is a library of programming functions mainly aimed at real-time computer vision. The library is cross-platform and free for use under the open-source BSD license. The full library description can be found here [240]. OpenCV has a modular structure, which means that the package includes several shared or static libraries. The following modules are available:

1. Core functionality (*core*) - a compact module defining basic data structures, including the dense multi-dimensional array Mat and basic functions used by all other modules.
2. Image Processing (*imgproc*) - an image processing module that includes linear and non-linear image filtering, geometrical image transformations (resize, affine, and perspective warping), color space conversion, histograms, and so on.
3. Video Analysis (*video*) - a video analysis module that includes motion estimation, background subtraction, and object tracking algorithms.
4. Camera Calibration and 3D Reconstruction (*calib3d*) - basic multiple-view geometry algorithms, single and stereo camera calibration, object pose estimation, stereo correspondence algorithms, and elements of 3D reconstruction.
5. Object Detection (*objdetect*) - detection of objects and instances of the predefined classes (for example, faces, eyes, mugs, people, cars, and so on).
6. High-level GUI (*highgui*) - an easy-to-use interface to simple UI capabilities.
7. Video I/O (*videoIO*) - an easy-to-use interface to video capturing and video codecs.

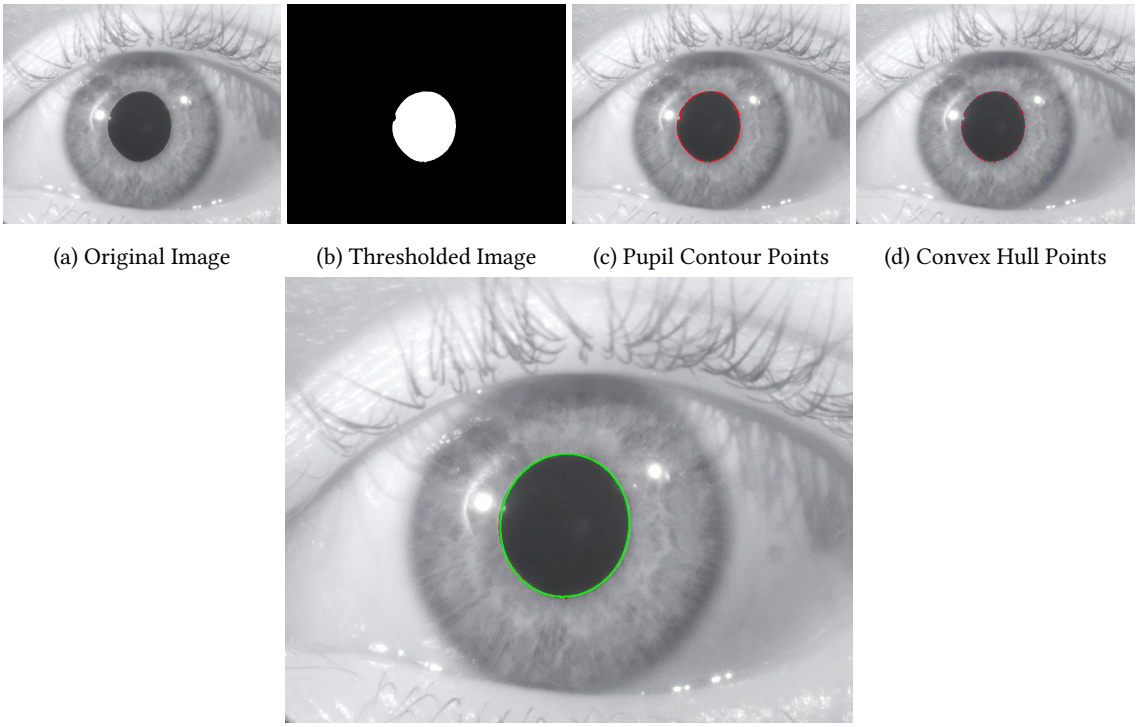
OpenCV thus allows easy manipulation of images. Captured frames are treated as pixel arrays in the CV environment, thus making pixel-to-pixel operations easier. Therefore, captured frames must be converted to OpenCV-compatible objects. Such frame acquisition is performed inside by the Camera through the LabVIEW UI (see Sec. 5.2.5).

[17] Python is a high-level, interpreted programming language that is widely used for general-purpose programming, web development, data analysis, artificial intelligence, and scientific computing. It was first released in 1991 by Guido van Rossum and has since become one of the most popular programming languages in use today. Python is known for its simplicity, ease of use, and readability, which makes it an ideal language for beginners to learn to program. Its syntax is designed to be easily understood, with fewer lines of code needed to accomplish a task than many other programming languages. Python is an interpreted language, which means that it does not need to be compiled before it is run. This makes development faster and easier, as changes to code can be tested immediately without needing to wait for compilation.

Once the frame is acquired, some operations must be performed on the image to obtain pupil size.

In the following, a basic and simple pupil detection method is presented. Despite many other techniques and methods that have been presented to detect pupils in noisy and low-quality images, the following can be used with well-contrasted pupil images, thus being light in terms of computational cost.

The main steps are shown in Figure 5.17.



(a) Original Image (b) Thresholded Image (c) Pupil Contour Points (d) Convex Hull Points

(e) Fitted Ellipse

Figure 5.17: Automatic pupil recognition steps

Moreover, the function which describes each elaboration step are here summarized:

1. Most recent frame is opened and an 'Original' NumPy RGB array is produced 5.17a;
2. The *Original* Image is then converted into grayscale (8-bit);
3. From the grayscale image, *thresholding* is performed. This operation requires accurately setting a threshold value. Each pixel of the grayscale image has int own gray value on a scale that goes from 0 (black) to 255 (white). Applying a threshold of, for example, 100 means that all the pixels with gray values under 100 are set to 0 (black) in the thresholded image, while all pixels with gray values over 100 are set to 255 in the thresholded image. Thus a binary, black-and-white image is produced with thresholding. As explained in Section 4.2.1 this step is very critical for pupil detection. In an ideal case, the thresholded image must be composed of a black spot constituting the pupil with a white background 5.17b;
4. From the original image, OpenCV allows finding geometrical shapes inside the binary image. For each shape detected the function returns a set of points constituting his edge. Such sets of the point are called contours. For contours to be founded, these shapes must be uniform and contiguous sets of pixels.

5. Among the found contours, by looking for those that have a geometrical shape similar to a circle and with dimensions comparable to those of the pupil of the eye. From there one contour must be founded inside the whole picture that corresponds to the pupil 5.17c;

6. IR eye illumination can introduce light reflex, due to corneal reflection, represented as a white spot in the picture. When this white spot falls exactly on the edge of the pupil the acquisition of the shape of the pupil can be altered. In picture 5.17c one of these spots can be clearly visible. As a consequence, a recess in the contours of the pupil is produced. This problem can be overcome by using the Convex Hull[18]. The result sets of print are shown in Figure 5.17d.

7. Finally, from the sets of points, obtained an ellipse can be fitted 5.17e. The parameters of the ellipse are then saved and sent to LabView User Interface for further analysis.

The steps just described are repeated frame after frame until the record is active for a specific test.

Another feature that has been adopted is the *dynamic cropping* of the analyzed images. Therefore, in order to reduce the number of pixels analyzed for each frame, once the pupil outer perimeter is found the *region of interest* (ROI) coordinates, i.e. the bounding box enclosing the detected pupil, are stored to crop subsequent frames. When the next frame is analyzed in that region to improve the frame rate. If the pupil moves toward the edge of the cropped image, the cropping area is shifted, trying to follow the pupil. The results look like the pupil is 'encapsulated' in a small portion of the picture analyzed. In the eventuality that the pupil's ROI is lost, which can happen for blinking or exceptional movement by the patient, the ROI area is broadened to the whole frame, thus allowing fast re-detection of pupil position.

Device User Interface

The user interface has been developed with LabVIEW, trying to make it as much user-friendly as possible. In the following, an explanation of the main parts of the interface is provided. In the VI there are the following main parts:

- **Test**: it is possible to open the serial communication controller board with the embedded microcontroller. Moreover, it is possible to set the following:
  - One single color (18-bit resolution with 256000 intensity levels - $> 95\%$ linearity calibrated);
  - A synthetic sinusoidal modulation on single or multiple primaries (up to 100 Hz);
  - A *test* of a couple of alternating colors with different predefined frequencies and duty cycles (1 ms time resolution);
  - A full configuration with 20 sub-periods (2 switching colors each). Each sub-period can be set with two colors: a background and a superimposed peak with 1 ms precision, i.e. up to 1kHz switching frequency. The configuration will be written to the microcontroller and arbitrarily executed with the possibility of *smart-pausing* between sub-periods.

  Additionally, it is possible to manually start a *free-run* or *triggered* acquisition and control the IR LEDs intensity (1-100%).

- **Light Graphs**: it is possible to control in real-time the plots related to the LED output spectra and photoreceptors' individual equivalent illuminance levels ($\alpha - lux$). In particular, the merged spectra obtained by computations in LabVIEW are reported. Moreover, it is possible to check the

[18] In mathematics, the convex hull of a set X of points in the Euclidean plane or in a Euclidean space is the smallest convex set that contains X. For instance, when X is a bounded subset of the plane, the convex hull may be visualized as the shape enclosed by a rubber band stretched around X

quantum efficiency of the reference power meter and perform a light calibration. The relative luminous efficacy, the color matching functions (related to the XYZ coordinates), and the sensitivity of the photoreceptor are also shown in the graphs section. Additionally, all the light specifications, including photometric and radiometric values, geometrical optics, and estimated perceived color can also be monitored;

- **Pupil Preview**: at any time it is possible to control the pupil diameter size (both in mm and in pixels) and the alignment of the system to make adjustments before each test. It is also possible to control all the settings of the camera, thus including *gain*, *exposure time*, resolution, and region of interest.
- **Pupil Graph**: finally, while performing a test, it is possible to monitor in real-time the pupil measurement vs time.

5.2.6 Mounting and Component Housing

Additive Manufacturing (AM) has gained significant attention in recent years, particularly for the production of functional prototypes. This approach is particularly useful for projects that are subject to a significant number of variables and potential imperfections that may require modifications to the original design created using Computer-Aided Design (CAD) tools such as SolidWorks®[19]. However, it is important to note that the choice of production method can greatly affect the design of the parts, as AM is fundamentally different from traditional production techniques that are based on subtractive manufacturing.

The use of AM also presents several challenges. Firstly, the process and material selection are more closely interrelated than in conventional processes, which means that the quality of the final product is not solely dependent on the precision of the machine. For example, even an expensive Fused Deposition Modeling (FDM) machine may not produce a satisfactory result if the filament is not used in the recommended operating conditions. Additionally, the machine itself may require the setting of single task variables such as different calibrations and working conditions to prevent defects such as warping and or deformation that will affect the proper coupling between parts.

Another important aspect to consider is the influence of variables such as orientation or support structures on the surface roughness and appearance of the final product. In our project, we aim to identify which parts require more precision and, based on this information, decide on the appropriate set-up variables for the machine, such as the orientation of the part on the build plate. Overall, it is important to keep in mind that the strength and structural rigidity of the final product can be challenging to guarantee when using AM techniques.

5.3 Realized Prototypes

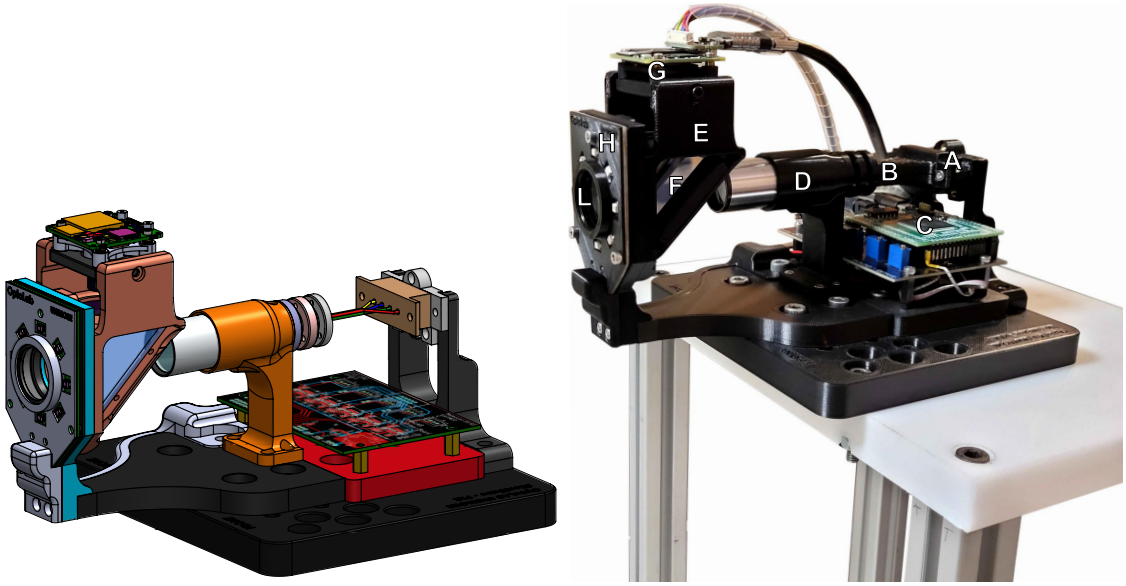
In the previous section, some basic block and design concepts that have been faced during the development of pupillometer devices were presented. Following on, the design and specification of the realized devices that have been used for research and investigation, lately presented in Chapter 7, are here briefly presented.

[19]Dassault Systèmes, 10 rue Marcel Dassault, 78140 Vélizy-Villacoublay, France

5.3.1 Maxwellian Monocular Pupillometer

The realized monocular pupillometer consists of a double-lens optical system including four fiber-coupled LEDs sources to achieve a Maxwellian-View-like optical system [109, 241]. A schematic diagram of the realized device is depicted below in Figure 5.3

Figure 5.18 shows a picture of the device positioned in front of the ophthalmic chin rest.



(a) (b)

Figure 5.18: View Maxwellian-View monocular pupillometer instrument. Figure a) shows the 3D CAD design of the optomechanical components for housing the optics, camera, and circuitry that have been custom realized with additive 3D printing. b) Shows the real device.

Four high brightness LEDs sources (**A**)[20] with peak wavelength (FWHM[21]) of 625 nm (14.5 nm), 593 nm (12.7 nm), 523 nm (29.7 nm), and 468 nm (19.6 nm) have been used to stimulate the eye. The four LEDs, with output full-width viewing angle not higher than $30°$, have been coupled with four plastic fibers (**B**) with 1 mm core (NA = 0.51). Moreover, for each LED, a constant current boost LED driver (**C**) has been used to control the output light intensity (see Sec. 5.2.4), where digital intensity modulation has been implemented with PWM signals($0\% - 100\% \pm 0.1\%$), while peak current is adjusted by using an 8-bit digital potentiometer. An Atmel SAM3X8E ARM Cortex-M3 80 MHz 32bit *Micro Controller Unit* (MCU) has been used to generate all four high-resolution PWM signals. Lens L1 (**D**) ($f_1 = 40mm$, $D_1 = 2.54cm$) has been used to collimate the light towards lens L2 (**L**) ($f_2 = 50mm$, $D_2 = 2.54cm$) that focuses the output beam to the eye pupil plane, obtaining an exit pupil of $\approx 1,2\ mm$ diameter with a full-width viewing angle $\theta = 54°$. The eye image was acquired thanks to the illumination performed by eight 850 nm infrared (IR) LEDs circularly arranged (**H**), while the dichroic mirror (**F**) [22] has been used to reflect the pupil image to the compact high-resolution USB3 Camera[23] **G**). The IR High-Pass Filter (**E**)($\lambda_c = 750nm$) has been additionally used and positioned in front of the camera objective to filter out unwanted visible light.

A laptop computer running a specifically developed Python code allows for capturing high-resolution

[20] Wurth Elektronik and Kingbright
[21] The full width at half maximum (FWHM)
[22] DMSP750B, Thorlabs © Newton, New Jersey, U.S.
[23] BF3-3M-0064ZG-1Y0020 mvBlueFOX3-3M- Matrix Vision GmbH Oppenweiler, Germany GE

6.4 Mpx monochromatic images at 60 fps. The camera is hardware triggered by the MCU to synchronously acquire frames with light stimulation. Finally, an interface designed with NI LabView allows to control and configure the type of stimulation.

5.3.2 Maxwellian Binocular Pupillometer

Lately, the monocular Maxwellian optical design presented in Section 5.3.1 has been modified to develop a binocular version. Binocular pupillometers allow testing many other combinations of visual stimuli, such as contro-lateral stimulations or allowing for the recording of both pupil responses at the same time, thus allowing for the detection of discrepancies between left and right visual pathways. In this section, we briefly describe our approach to the development of such a binocular solution.

Design Concept

All the components have to be contained in a closed structure to avoid that outside light could affect image acquisition. The design of the visor is really challenging because it should satisfy some requirements:

- Good ergonomics (avoid that all the weight is supported by the nose);
- Precise realization of the connections with optic components;

The precise alignment and coupling of various optical components are crucial for the proper functioning of the visor. Specifically, any deviation in the planarity of the sliding surfaces can lead to a malfunction of the mechanism. Additionally, maintaining a consistent distance between the human pupil and the first converging lens is essential for achieving optimal image focus. To address this issue, the use of rubber pads as spacers on the visor's contact points with the face can be employed to adjust the pupil distance.

In the design and construction of the visor, a balance must be struck between utilizing additive manufacturing techniques for streamlined assembly, and the need for adaptability in the prototype phase. Initially, the visor may be fabricated as a single piece to minimize assembly complexity, but this may also limit the ability to make adjustments to the optical configuration. Ultimately, a modular design consisting of three distinct parts, as depicted in Figure 5.19, has been realized as the most suitable approach for this prototype project.

Schematic Diagram

Starting from the optical design of the monocular version described in Section 5.3.1 and as depicted in Figure 5.3, some changes have been introduced in this proposed binocular version. The first thought concerned the acquisition of both eyes with the same camera, thus allowing to simplify the further processing of acquired images. The solution found is illustrated in Figure 5.20.

As can be noted, the optical scheme of the light stimulation path is unchanged from the Monocular version previously introduced. The Maxwellian view is realized through the use of two lenses, a collimator lens, thus making parallel rays from the single fiber output light beam, and a converging lens to focus the light beams in a tiny spot on the pupil plane. Again, the optical fiber output and the eye's pupil must be placed and aligned with the collimator and converging lenses' effective focal distances (EFL), respectively. It is worth remembering that, as explained in Section 3.1.1 the EFL takes into account the physical size of the lens and the location of the object being imaged.

Two dichroic mirror [242], previously used to bend infrared rays by 90° in the monocular version, have been adopted here to bend both IR paths (illustrated in purple in Figure 5.20) toward a gold plated optical prism. The function of the prism, furtherly described in the next section, allows the combination of the

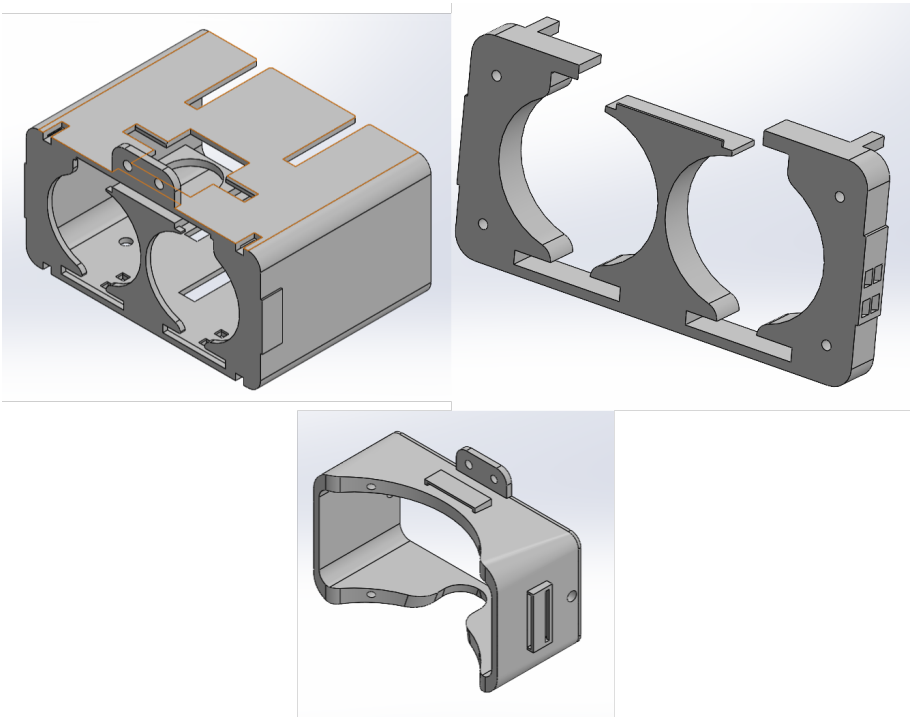


Figure 5.19: Binocular pupillometer's different parts. The optomechanical components for housing the optics, camera, and circuitry have been custom realized with additive printing.

two paths into a single one by bending right and left IR paths (X-axis, opposite direction) upwards toward the Z-axis. By placing the camera

Prism

As we introduced in the State of The Art Chapter 3.1.2 optical prisms, allow changing the orientation of the optical rays. To achieve the task presented in the previous section, a 90° specialty mirror [243] from Edmund Optics[24] has been used. These specialty mirrors are constructed from right-angle prisms with a mirror coating on the two legs and an uncoated hypotenuse [244]. The mirrored surfaces form a precise 90° angle, ideal for splitting an image from a single imaging lens onto two different cameras, or for combining two images onto a single camera as in our case.

For this application, we have chosen a 20 mm Prism made of NBK7 with a gold coating, which can guarantee, as further detailed in Figure 5.21 more than 98% reflection at $90degrees$ over its Wavelength range (750nm-1100nm, i.e. over the whole *near infrared range* NIR) [245]. It's important to note that surfaces that will reflect light rays have to respect strong geometric tolerances: planarity is measured in fractions of a reference wavelength, in this case, 632nm. So, a $\lambda/8$ will have a maximum peak-to-valley deviation of 79 nm.

Image acquisition

One of the goals of designing the optical scheme shown in the previous section was to obtain an image of both eyes in the same frame, as illustrated by Figure 5.22.

Considering the optical scheme showed in Figure 5.20, Record both pupils with the same camera while keeping the alignment with the Maxwellian stimulation is a very hard challenge, especially when con-

[24]Edmund Optics Inc., 101 East Gloucester Pike, Barrington, NJ 08007-1380 USA

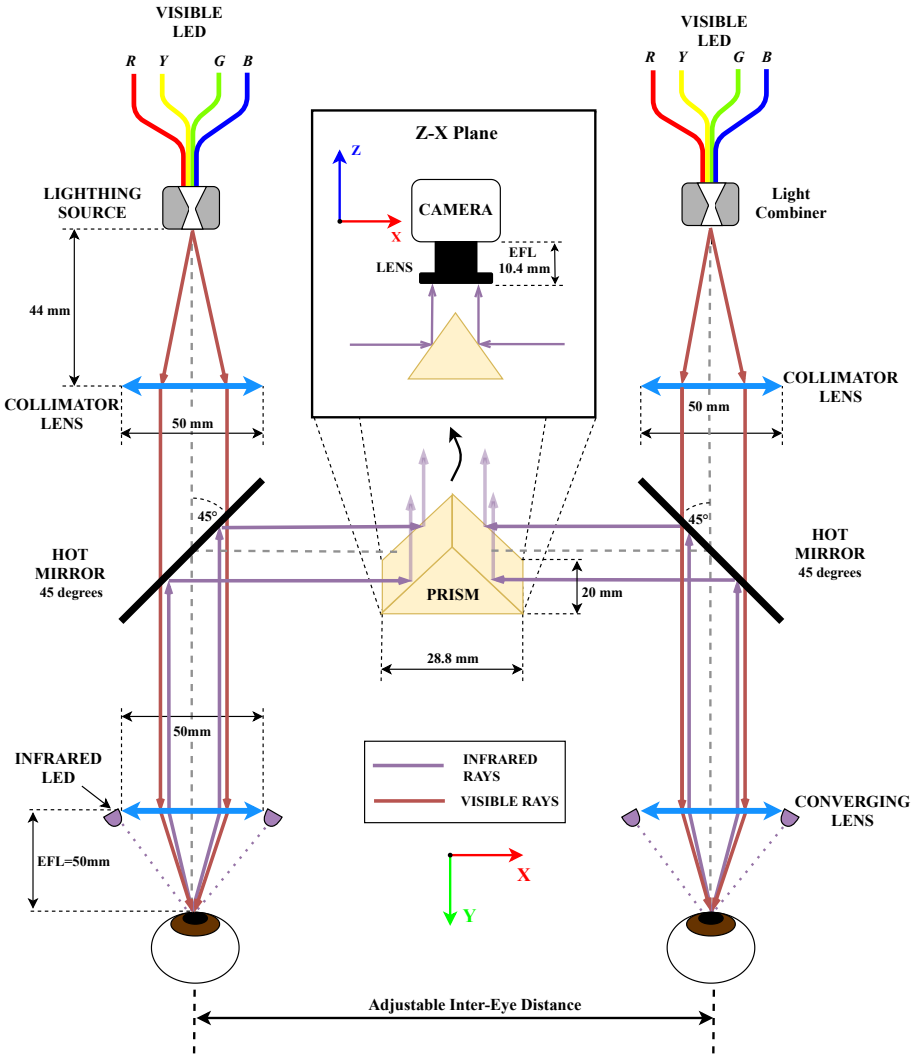
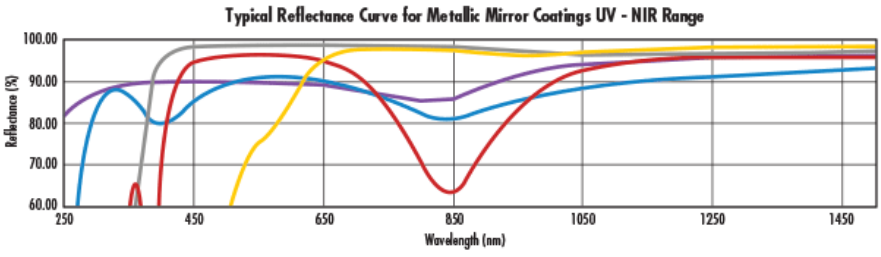


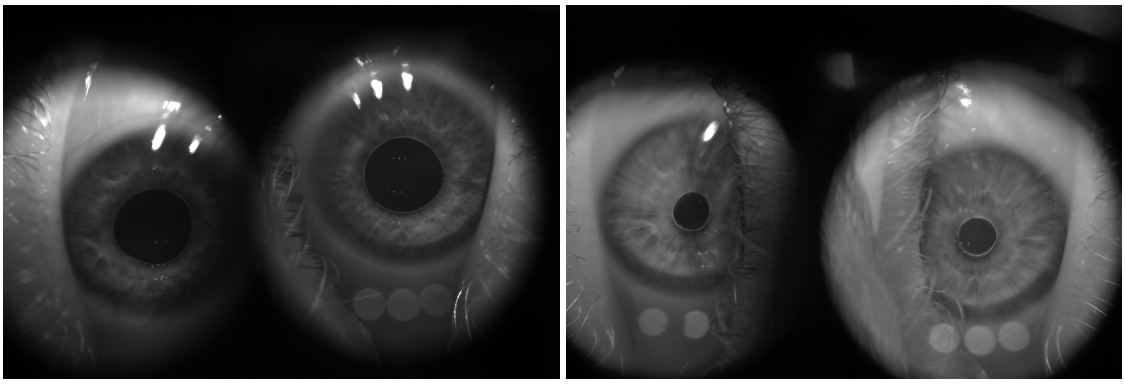
Figure 5.20: Optical diagram of the binocular pupillometer design.



Protected Aluminum		Enhanced Aluminum		UV Enhanced Aluminum		Protected Gold		Protected Silver	
Range (µm)	% Reflection	Range (µm)	% Reflection	Range (µm)	% Reflection	Range (µm)	% Reflection	Range (µm)	% Reflection
0.4 - 0.7	85	0.45 - 0.65	95	0.25 - 0.45	89	0.7 - 2.0	96	0.45 - 2.0	98
0.4 - 2.0	90	–	–	0.25 - 0.70	85	2.0 - 10.0	96	2.0 - 10.0	98

Figure 5.21: Technical Characteristics of Optic Prism

sidering the huge amount of different morphology of human faces, thus including inter-ocular distances, that can vary among subjects in a range from 50 mm to 75 mm if only considering adult subjects. [246]. Despite that, using only one camera comes with many advantages, such as making the synchronization of



(a) (b)

Figure 5.22: Dual acquisition with a single camera. (a) Pupils dilated and (b) pupils constricted when stimulated with visible light.

dual acquisition much easier and more precise, thus reducing the development costs of the final prototype and computational loads on the processing unit.

Final Design - Drawbacks and future works

Besides a binocular device introduces many advantages and enables more advanced and complete PLR stimulations, The realized binocular device is graphically shown with a 3D rendering in Figure 5.23.

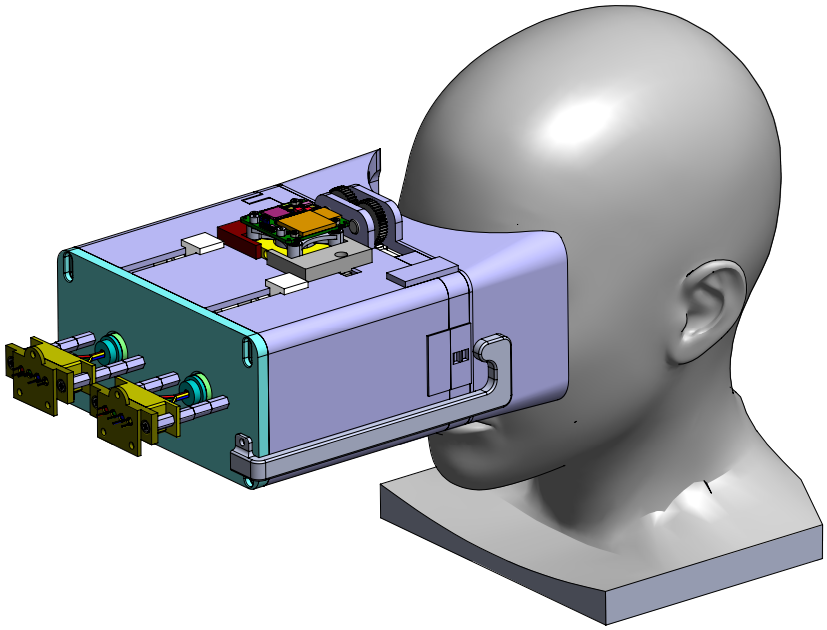


Figure 5.23: 3D rendering of the realized binocular pupillometer device

By analyzing the problems during the measurement phase, a series of improvements are deducted:

- The first improvement should be related to the introduction of an additional double-convex converging lens adjustment mechanism that allows changing its straight distance from the subject pupil,

thus accounting for different face physiognomy that can result in out-of-focus images.

- The stimulation path should be modified: with the current horizontal dimension, the compactness of the device is compromised. So, an interesting idea would be thinking about periscopic-like optical path illumination.
- Reduction in the number of device pieces, in order to decrease errors during the assembly phase. Furthermore, this would help when moving from the prototyping phase to the production of the device.
- **Pupil position**: since the simultaneous recording of both eyes implies perfect alignment between stimulation and acquisition optical paths, the pupil position has a great influence on the quality and accuracy of the recorded responses. As previously illustrated, as operating very close to the lens focus dramatically reduces the depth of focused images, a slight misalignment of the pupil in the Y direction (see. Fig. 5.20) will lead to highly blurred images. Moreover, a shift of the pupil in respect to the optical axis in the X-Z plane will introduce spherical aberrations, i.e. a deformation of the pupil's original shape and size. This could be a problem if we consider that human face physiognomy can vary significantly between subjects.
- **Fiber Coupling**: the analysis of the light spot allows us to notice that there isn't a perfect mixing of the four wavelengths. An improved mixing stage that can be realized by using a liquid fiber or an integrating sphere will further improve the uniformity of mixed color in the output beam;
- **Dimensions of the device**: the instrument has the minimum dimensions compatible with the optical and assembly constraints, but we can say that the horizontal dimension is still significant. Although the device itself is not heavy, on the extremity there are the illumination components: this extremal weight can cause the device inclination and should be reduced as much as possible.

5.4 System Performance

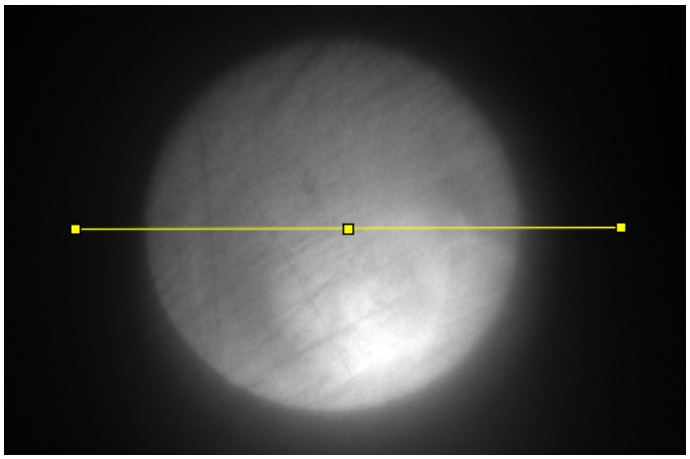
In this chapter we will talk about the results obtained with the use of the instrument: these measurements are really useful in order to understanding if the behavior of the device is similar to what we saw in the simulations. In particular, we have considered what we want to obtain with the two optical paths:

- Power and Spectral output of the light sources;
- Dimensions of the spot obtained with the illumination path;
- Resolution of the pupil's image acquired with the camera;

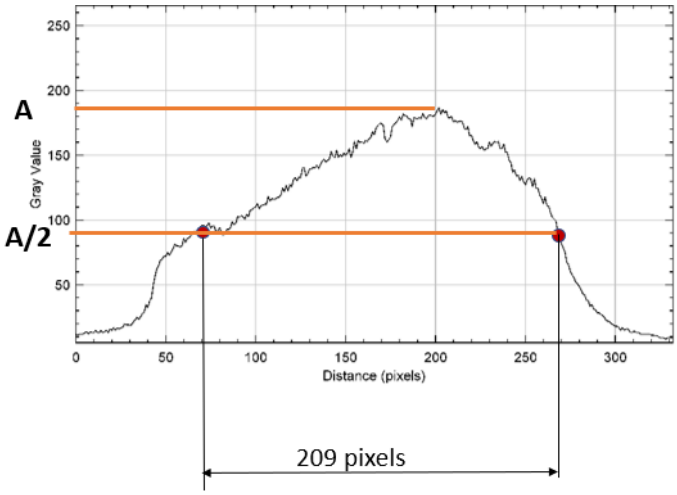
5.4.1 Exit Pupil Spot Size Measurement

In order to ensure that the Maxwellian view is properly implemented in our optical system, it is necessary to measure the spot size of the light beam at the output of the system. This can be accomplished by using a camera without an objective lens in place of the pupil's virtual plane and examining the acquired image. Therefore, the light spot from the illumination path is focused on the camera's CMOS sensor, which will provide an accurate measurement of its dimension and uniformity. In order to analyze the acquired image of the spot, specialized open-source software, such as *Image-j*[25], can be used to extract image luminosity profiles. The results of this analysis can be seen in Figure 5.24.

[25] Image-J Software Documentation



(a)



(b)

Figure 5.24: (a) Spot size image on a CMOS sensor. (b) Plot of the spot size luminosity horizontal profile at the center.

By tracing a line on the spot image, as shown in Figure 5.24a the software will plot the pixel's scale of the grays profile. As shown in Figure 5.24a the x-axis represents the dimensions of the line traced before (in pixels), the y-axis instead, shows the gray value, which ranges from 0 to 255 (8 bit). To compute the spot size it is sufficient to take the profile peak value **A**, the points whose gray value is **A/2**, and then measure the pixel distance between these points. The CMOS sensor used in this case is the *Sony ICX204AL*, that as reported in the datasheet has a single pixel dimension of $S_{px} = 4.65\mu m^2$. Therefore, the dimension of the spot size on the lens focus can be simply calculated as follows:

$$\textbf{Spot Diameter} = D \cdot S_{px} = 209 \cdot 4.65 \cdot 10^{-6} = 0.97\text{mm} \tag{5.3}$$

Where $D = 209\ px$ is the dimension of the spot size in pixels and S_{px} is the width of a single pixel on the CMOS sensor. As the human pupil has a diameter that is about 2 mm in miosis condition (fully constricted), we can declare that if the system is properly aligned and focused, the entire radiant flux emitted at the system output enters through the eye's pupil even if it's fully constricted.

5.4.2 Image acquisition: Resolution

A measure of the magnification of the acquisition path can be obtained by replacing the pupil with graph paper with squares size $L_{real} = 1mm$ (squares of 1mm x 1mm size) and analyzing the resulting image on the camera. A sample image of the graph paper acquired with the camera trough the optical system is depicted in Figure 5.25.

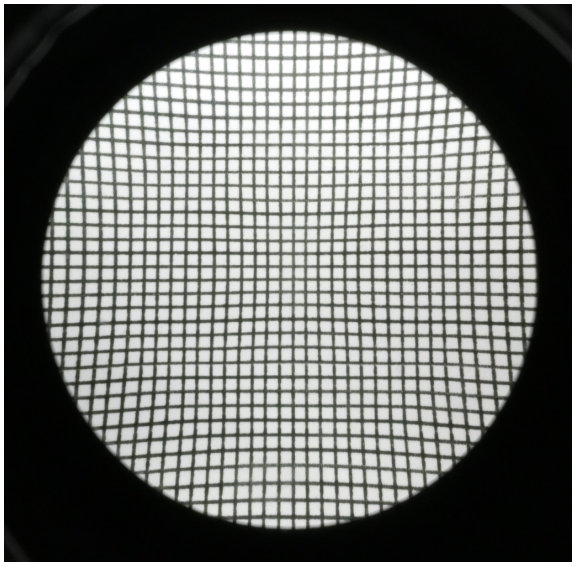


Figure 5.25: Spatial resolution reference measure. Spherical aberrations can be observed toward the external edge of the lens L2.

The measurement of the conversion ratio between the acquired size in pixels and the corresponding size on the acquisition plane can be achieved by analyzing Fig. 5.25 with the same software used for calculating spot dimensions. Moreover, as the pixel dimension on the camera sensor (IMX178 - 1/1.8", RS, CMOS) has a dimension of $S_{px} = 2.4\mu m$ by using this ratio it is possible to compute the total magnification M of the acquisition optical path. By tracing a line in the center of Figure 5.25 the resulting grayscale profile is depicted in Figure 5.26.

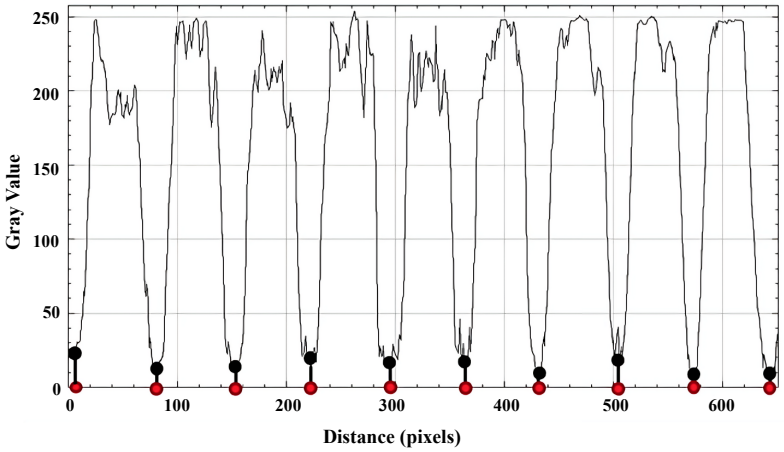


Figure 5.26: Graphical measure of the paper graph square size acquired on the camera. The average valley distances $\overline{L_{px}}$ can be observed.

Where again, a high gray scale value corresponds to white pixels, while a value close to zero corre-

sponds to black pixels. Therefore, the average square dimension on the camera sensor as seen through the lens objective and the lens L2 can be obtained as follows:

$$L_{img} = \overline{L_{px}} \cdot S_{px} = 71 \cdot 0.0024 = 170.4\mu\text{m}; \tag{5.4}$$

$$M = \frac{L_{img}}{L_{real}} = 0.1704; \tag{5.5}$$

Where $\overline{L_{px}}$ (px) is the average dimension of the square side in the image of Figure 5.25, L_{img} is the imaged square dimension in mm on the camera sensor and M is the optical magnification. The spatial resolution of the acquired images can be calculated as follows:

$$\textbf{Resolution:} \qquad R_p = \frac{L_{real}}{\overline{L_{px}}} = \frac{1000}{71} = 14\mu\text{m} \tag{5.6}$$

From the resolution it is possible to calculate the standard uncertainty u_i related to the measure of the pupil diameter:

$$\textbf{Pupil Diameter:} \qquad \begin{cases} P_d = \bar{P}_d \pm u_i \\ u_i = R_p \cdot \frac{2}{\sqrt{3}} = 4.04\mu\text{m} \end{cases} \tag{5.7}$$

5.4.3 Light Sources Characterization

A comprehensive analysis of the light sources has been conducted, taking into account both the spectral distribution and power emitted by each individual source. This section provides a detailed account of the measurement techniques employed, the mathematical formulations utilized, and the resulting outcomes. The computer-controlled instrument used in this study are the following:

- **Light Spectrometer** - Hamamatsu PMA-11 [247]
- **Radiometer** - Newport 1918R model with a 918d-UV-od3 optical head.

The measurements were carried out on LEDs under controlled environmental conditions and with each color being lit independently.

Sources Output Spectra Measurment

The analysis of the spectral emission of the sources was performed medially using a Photonic Multichannel Spectral Analyzer. The tool used is the PMA-11 produced by Hamamatsu [247]. The spectrometer has a wavelength sensitivity that ranges from 300 nm to 800 nm and a wavelength resolution lower than 3 nm. It is important to point out that the intensity provided by the instrument on the Y axis is in AU (Arbitrary Unit) and does not provide any indication of the watt power emitted by the sources. The graph below shows 5.27 the normalized spectral distribution of the three LED sources used.

In table 5.6, the measured peak value and the FWHM (Full Wavelength Half Maximum) values of the three sources are reported. Theoretical values i.e. retrieved from the datasheet can be found in Table 5.2 instead.

Output power

Another important aspect to consider for the characterization of the system concerns the maximum optical power emitted, and therefore the luminance of the sources. To obtain this information, a power meter produced by Newport was used, the 1918R model with a 918d-UV-od3 optical head.

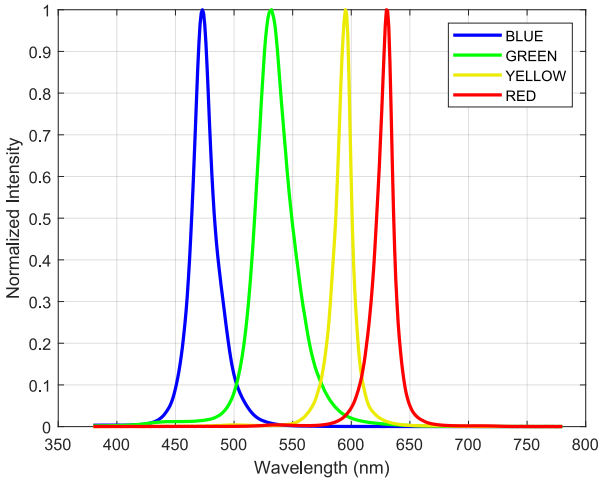


Figure 5.27: Normalized output spectra of the selected LEDs

	PEAK [nm]	FWHM [nm]	Product Code
BLUE	473	18	B56L51P
GREEN	531	30	G58A5111P
YELLOW	595	13	Y5CA5111P
RED	630	14.0	R5CA111P

Table 5.6: Sources peak level and FWHM measured with Hamamatsu PMA11 Spectrometer [248]

The current photogenerated by the diode of the optical head is given by Equation (5.8).

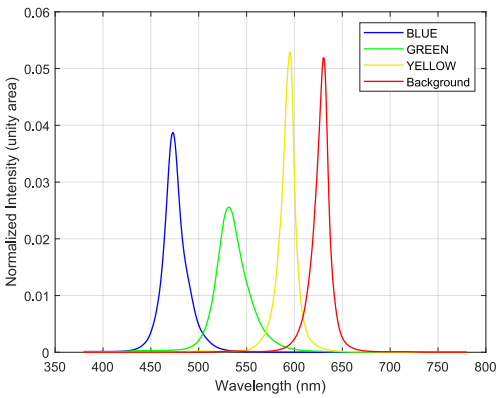
$$I_{ph} = \sum_{i=1}^{N} S_{power}(i) \cdot q_e(i) \tag{5.8}$$

Where $i = 1$ refers to λ_{min} and $i = N$ refers to λ_{max} that are the extremes related to the wavelength in which the source emits light. $S_{power}(i)$ is the amount of optical power in watts emitted by the source at the $i-th$ bins and $q_e(i)$ is the quantum efficiency in [A/W] of the photodiode at that specific wavelength range (i.e. the spectral band relative to the considered bins). To compute the total optical output power, λ_{max} and λ_{min} must be known. The quantum efficiency of the power meter is given by the manufacturer and is reported in Figure 5.28b. From the spectral distribution S_{PMA} obtained from the spectrometer (reported in Figure 5.27), it is possible to compute the power spectral density S_u for each chromatic source. Such distribution function can just be obtained by dividing each spectral value $S_{PMA}(\lambda_i)$ given in au (arbitrary unit), for the area subtended by the entire spectrum. The Equation (5.9) just describes this mathematical step.

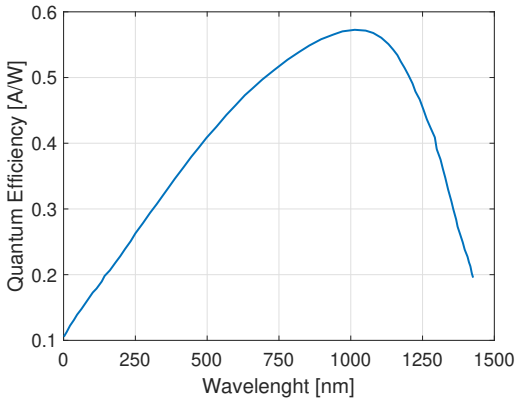
$$I_{ph} = \underbrace{\sum_{i=1}^{N} \frac{S_{PMA}(i)}{\sum_{i=1}^{N} S_{PMA}(i)}}_{\text{Power Spectral Density } S_u} \cdot q_e(i) \cdot \underbrace{\sum_{i=1}^{N} S_{power}(i)}_{\text{Source Output Power [Watts]}} \tag{5.9}$$

The obtained distribution function has a unity area value and can be multiplied by the corresponding q_e to obtain the so-called mean quantum efficiency $\bar{q_e}$ of the given light source. The Equation (5.10) gives the result.

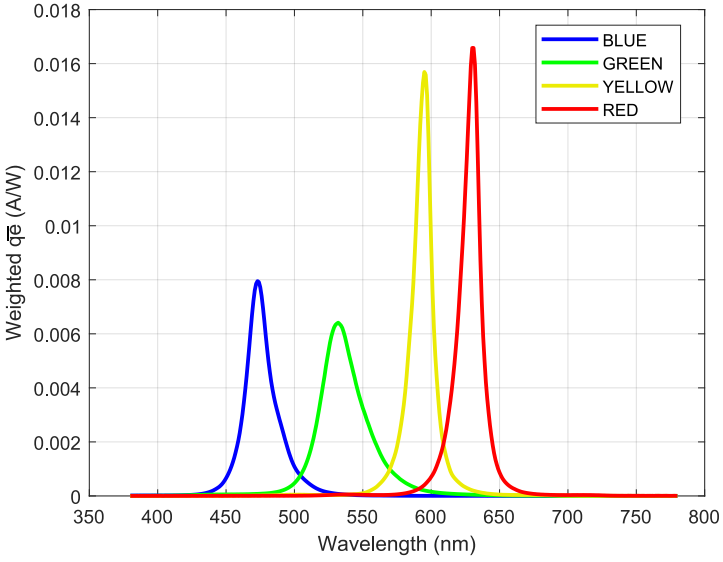
$$I_{ph} = \underbrace{\frac{\sum_{i=1}^{N} S_{PMA}(i) \cdot q_e(i)}{\sum_{i}^{N} S_{PMA}(i)}}_{\text{mean quantum efficiency } \bar{q_e}} \cdot \sum_{i=1}^{N} S_{power}(i) \tag{5.10}$$



(a) Unity Area Spectra S_u



(b) NewPort QE



(c) Mean Quantum Efficiency $\bar{q_e}$

Figure 5.28: Source output spectral power analysis. Blue, green, yellow, and red lines are for blue, green, yellow, and red LED sources respectively.

The three spectral density functions obtained are shown in Figure 5.28a, while the three convolution products functions $\bar{q_e}$=$q_e \cdot S_u$ are reported in Figure 5.28c. Finally, the total optical output power can be obtained by dividing the photocurrent I_{ph} measured with the power meter by the area subtended by the mean quantum efficiency of a given source.

$$\sum_{i=1}^{N} S_{power}(i) = \frac{I_{ph}}{\bar{q_e}} \tag{5.11}$$

To obtain the output power for a given source at a particular current setting, we placed the Newport power meter's optical head on the optical axis, where the pupil should be placed. The photogenerated current I_{ph} for each LEDs at different current settings was then acquired. Finally, given the quantum efficiency q_e and the spectral distribution of the three sources, a Matlab environment was used to compute the output power in watts for each I_{ph} acquired.

Output luminance

The optical output power given in Watts can be used to compute the luminance of the system. From the luminance, safety levels can also be computed for a given pupil condition. Luminance is the luminous intensity per unit area of light traveling in a given direction. It describes the amount of light that passes through a particular area, and falls within a given solid angle Ω. The SI unit for luminance is candela per square meter (cd/m2). The candela (cd) is the base unit of luminous intensity: that is the luminous power per unit solid angle emitted by a point light source in a particular direction. Luminous intensity is given in lumen per steradian (lum/str), thus the contribution of each wavelength is weighted by the standard luminosity function (a model of the sensitivity of the human eye to different wavelengths). Accordingly, to compute the output luminance of a given source the physical quantities must be known: firstly, the amount of light power impinging on the photodiode sensible area (given in W/m^2), the Photopic Luminous Efficacy at the sources peak wavelength (given in lum/W) and the solid angle Ω of the light sources. The first two terms are known; the emitted power in W is given by the Newport power meter, while the photopic luminous efficacy, can be found in literature [249].

The third parameter that is necessary to compute the output luminance is the solid angle Ω. This last value is obtained using the theory explained in Section 3.3.2.

Accordingly, to the optical scheme depicted in Figure 5.3 and to the background theory reported in Section 3.3.2, the solid angle of the light cone can be obtained by the following Equation:

$$\begin{cases} \alpha = 2 \cdot arctan\left(\frac{B_d - S_d}{2 f_{L2}}\right) \\ \Omega = 2 \cdot \pi \cdot \left(1 - cos\left(\frac{\alpha}{2}\right)\right) = 99.4\, msr \end{cases} \tag{5.12}$$

Where, B_d is the collimated beam diameter, S_d is the spot size diameter, f_{L2} is the lens $L2$ focal length (see Figure 5.3), and α is the beam full-width angle. This Ω value is common to all the LED sources used. This is because the α value depends only on the collimated beam diameter and on the focal length of the lens L2. Finally, the luminance for a given source can be calculated by:

$$Luminance \quad (I_{ph}) = \frac{I_{ph}(A)}{\bar{q_e}\left(\frac{A}{W}\right)} \cdot \frac{1}{S_{Area}(m^2)} \cdot V_\lambda \left[\frac{lum}{W}\right] \cdot \frac{1}{\Omega(sr)} \tag{5.13}$$

Where:

I_{ph}	-photogenerated current in (A)
$\bar{q_e}$	-Area of the Mean Quantum Efficiency of the given source(A/W);
S_{Area}	-The Optical Head's sensor area, equal to 1 cm^2
V_λ	-Photopic Conversion coefficients (lum/W);
Ω	-Solid Angle (sr);

Safety considerations

Different kinds of damage can be produced by intense light irradiation of the retina. These types of damage can be separated into changes that are induced by photochemical or thermal effects in the tissue. Photochemical damage occurs mainly with intense irradiation of a few seconds or longer whereas thermal effects appear to prevail at irradiation times in the 1 ms to 1000 ms range. The distinction between photochemical and thermal damage is very difficult because both types of injury appear as disorders in the retinal pigment epithelium and the outer segments of the photoreceptors. In our case, since the power levels are limited and the exposure times are long, we focused on the possibility of incurring photochemical damage with the use of high-brightness LED sources focused on the retina. The safety calculations were performed using tools made by François Delori of the University of Harvard (Boston), called the

Ocular Light Calculator (OcLC). The 'OcLC' covers exposure safety computations according to the ANSI Z136.1 (2014) and ANSI Z80.36 (2016) [250]. This calculator allows for rapid calculation of safe levels for exposures by lasers and broadband sources with emphasis on ophthalmic devices and on experimental devices. The calculator also evaluates illuminance and bleaching levels, performs various conversions routinely used in photometry, and allows the computation of the optical density of various ocular pigments. The International Standard used as a reference gives guidance for evaluating the photobiological safety of lamps and lamp systems including luminaries. Specifically, it specifies the exposure limits, reference measurement technique, and classification scheme for the evaluation and control of photobiological hazards from all electrically powered incoherent broadband sources of optical radiation, including LEDs but excluding lasers, in the wavelength range from 200 nm through 3000 nm [251]. The following conditions are considered in safety evaluation:

- Output spectral distribution of light sources are considered to be Gaussian with the peak wavelength and FWHM reported in table 5.6;
- Solid angle calculated in Section 5.4.3 is considered;
- An immobilized pupil of 7 mm diameter was considered. That means that the subject is forced to fix light sources and that its pupil is in *Mydriasis*[26] The condition considered is likely to be the worst-case condition for ophthalmic instruments safety assessment.
- Level of power in watts/m^2 considered are the highest measured with the power meter during all the tests.
- Constant light output was considered;

In Table 5.7, values of maximum emitted power and maximum time of exposure allowed from the standard are reported.

Table 5.7: Safety exposure limits for maximum optical power.

Color	**Peak** $\lambda(nm)$	**FWHM (nm)**	Ω **(msr)**	**Peak Retinal Irradiance** ($\mu W/cm^2$)	**Maximum Exposure Time for Photochemical Damage**	**Maximum Exposure Time for Thermal Damage**
BLUE	473	18	99.4	44.61	8.3 h	Inf
GREEN	531	30	99.4	13.29	8.3 h	Inf
YELLOW	595	13	99.4	1.61	8.3 h	Inf
RED	630	14	99.4	27.80	8.3 h	Inf

The table shows that any of the light can cause photochemical damage, even after a long exposure time and worst case scenario. Photochemical damage has been widely studied because it can cause retinal damage within the intensity range of natural light. Photochemical lesions are primarily located in the outer layers at the central region of the retina. Two classes of photochemical damage have been recognized: Class I damage, which is characterized by the rhodopsin action spectrum, is believed to be mediated by visual pigments, with the primary lesions located in the photoreceptors; whereas Class II damage is generally confined to the retinal pigment epithelium. The action spectrum peaks in the short wavelength region, providing the basis for the concept of blue light hazard. Vision loss due to photochemical damage is typically reversible, lasting for as short as one month to over one year. The fundus changes are variable and usually bilateral, mild cases often show no alteration, and moderate to severe cases show a

[26] Mydriasis is the dilation of the pupil, usually having a non-physiological cause, or sometimes a physiological pupillary response. Non-physiological causes of Mydriasis include disease, trauma, or the use of drugs.

foveal yellow spot on the first days after exposure. After a few days, it is replaced by a reddish dot often surrounded by pigment. Although it is frequently claimed that the retina is burned by looking at the Sun, retinal damage appears to occur primarily due to photochemical injury rather than thermal injury [252].

Chapter 6

Automatic ACA Measurement Instrument

6.1 Related Works - Van Herick Grading

As introduced in the State of Art Section 4.3, the Van Herick technique is a very promising approach for non-invasive *anterior chamber angle* (ACA) measurement [253]. Despite its advantages with respect to other methods, some specific limitations of the Van Herick maneuver have narrowed its usage. In recent years, many studies have been carried out to improve the objectiveness and accuracy of the VH grading technique [254, 255]. Foster et al. [256] proposed a new grading scale system to improve the sensitivity of the evaluation. According to this work, the new scale reduces the possibility of wrongly diagnosing "open-angle" cases with a close-angle condition. Moreover, Sihota et. al [257] introduced a modified grading system. However, in order to use these new grading systems, the opticians are required to have acquired a good level of training.

To overcome the intrinsic subjectivity of this approach, an automatic measurement of the ACA could be performed. Theeraworn et al. [258, 259] present a Support Vector Machine algorithm able to extract the measurement of the ACA from slit-lamp images. This approach is auspicious, but it still requires the presence of an operator that correctly sets the slit lamp and performs the maneuver. In fact, the algorithm just extracts the information from the images. Other automatic procedures have been proposed over the years. However, such works foresee the usage of other techniques such as gonioscopy [260] or OCT [261], even exploiting Machine Learning techniques. In the first case, the technique is invasive while in the second the procedure requires an OCT machine, which is expensive, and thus not suitable for continuous screening. Moreover, Shimizu *et al.* have recently presented a portable device that can be equipped on a smartphone, whose aim is to replicate slit-lamp microscope system behavior in a cheaper and more compact design [262]. However, the analysis of the collected image is still subjective and relies on expert medical opticians' evaluation.

Differently, the goal of this research activity conducted during my Ph.D. is focused on the development of an instrument that automatically and objectively performs the VH procedure in a cheap, compact, and portable fashion. In the following chapter, the design and technical aspects of a new system, that will be used to perform ACA measurement through an automated execution of the Van Herick procedure (see Sec. 4.3.2), is presented. The proposed system will be used along with Vision-Based techniques (see Sec. 4.1), which indeed exploits Machine Learning techniques for image classification. Machine Learning techniques, in literature, have been widely applied to VBM systems [263], especially CNN–based ones. Indeed, CNN's revealed their suitability for VBM systems in many different applications [264]. For exam-

ple, the authors [265] proposed a CNN-based system for railway network inspection. Differently, [266] presented a method for head pose estimation in vehicles, demonstrating high versatility in the application of CNNs. Furthermore, an interesting review paper [267] summarizes the most widespread Deep Learning (DL) techniques for Image Classification, with regard to ophthalmic applications. They identified several CNN network models that proved to be promising such as, among others, AlexNet [268], GoogleNet, [269] and ResNet [270]. These networks showed the best results in the ImageNet Large Scale Visual Recognition Challenge [271] and are all based on Convolutional Layers. Later, in Sections 8.2 and 8.3, two research conducted on human subjects, are presented to show preliminary results obtained with this technique.

6.2 System Design

In this section, a detailed description of a fully working prototype that reproduce the Van Herick technique in a fully automatic way is reported. The device, which presents exploits new technology to enable the objective estimation of the VH grade, is being tested at IRCCS Fondazione G.B. Bietti Rome, Italy from expert medical personnel. The goal is to build a large dataset with the images acquired with this automatic technique. Some preliminary results are therefore presented later in Chapter 8, where Artificial Intelligent algorithms are being tested to replicate the evaluation of trained opticians.

In the following sections, an overview of the optical diagram, of the components that are behind the working principle of the device and the realized prototype are fully described.

6.2.1 System Optical Diagram

As explained in the state of the art (see. Sec. 4.3.2), the Van Herick procedure used to measure the ACA must be accomplished with specific alignment constraints [253]. It has been shown by Leung et al. [272] that both illumination and observation angles affect the ACA openness assessment. As a consequence, particular attention was paid during the realization of the optical setup for such an experimental evaluation. Therefore, a modified schematic diagram of the optical setup used to perform the Van Herick measurement, previously described in Section "Van Herick Technique", is shown in Fig. 6.1.

The measurement setup has been maintained as close as possible to the original optical setup, except for the substitution of a Digital Light Projector instead of the traditional slit-lamp and a CMOS Embedded camera instead of a microscope.

6.2.2 General Description

The optical setup consists of two main devices. Firstly, a digital CMOS camera Basler Dart (daA1600-60uc S-Mount, Basler© AG, Ahrensburg, Germany) has been choosen to replace the traditional microscope, and therefore positioned in front of the patient's eye, aligned with its optical axis. A 16 mm focal length S-Mount lens[1] is used in the optical setup. This objective hab been chosen as it is not-expensive, light and companct and allow both a wide viewing angle and very low working distance. Secondly, a LED-based *Digital Light Projector* DLP [2] was used as the illumination unit, instead of the traditional slit light. The DLP relies on modern micro-mirror technology to project structured light onto a specific target (see further details later in Sec.6.2.2). The illumination unit of the DLP was placed at a 60-degree rotation angle with respect to the eye and camera optical axis as shown in Fig. 6.1. Moreover, the DLP has been configured to emit a uniform red slit light that scans the whole surface of the eye under examination, as to maximize the contrast whit all type of differently colored irises. Thus, during the measurement procedure, the emitted

[1](Evetar Lens M12B1618IRM12 F1.8)
[2](DLP2010EVM-LC, Texas Instruments©, Dallas, Texas, U.S.)

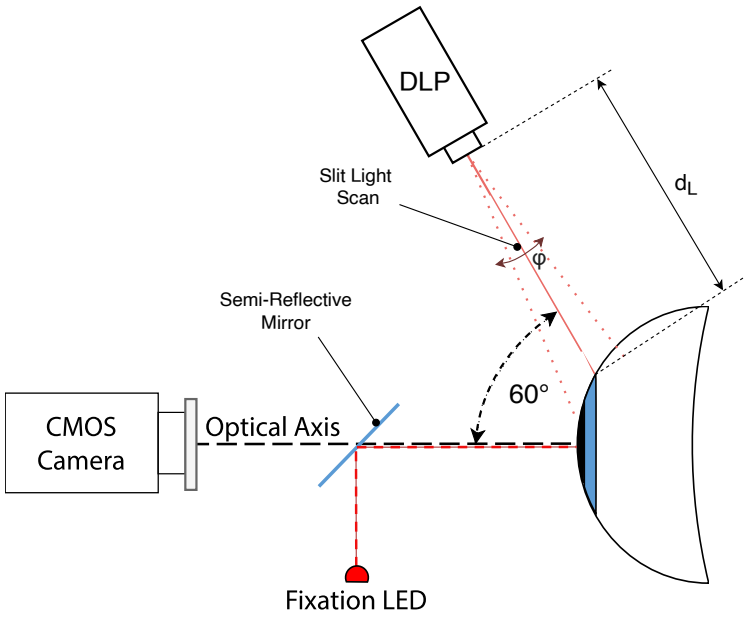


Figure 6.1: Optical Scheme of the modified ACA measurement setup, top view. The original VH measurement setup, as described in Section Van Herick Technique, has been modified where the traditional slit lamp has been replaced with a *Digital Light Projector* (DLP) from Texas Instruments, while the microscope has been replaced with a CMOS USB3 Camera, which is aligned with the eye's optical axis. A small LED and a semi reflective mirror, has been used as a fixation target for the patient.

slit light scans the eye from the external corner of the sclera towards the nose. Reference picture will be later presented in the results chapter (see Fig. 8.9). This scan takes place during the acquisition of the frame with the digital CMOS camera. A fixation target, i.e. a small light pointer, was placed on the eye-camera optical axis, through a 45° semi-reflecting mirror, to help the patient to look straight ahead. The patient's head is then placed on a chin rest to guarantee steadiness and alignment with the optical setup. A single measurement procedure has been designed to perform two entire scans of the eye in 4 seconds, allowing for a total of 120 raw pictures to be collected at 30 fps. The entire system is connected to a Windows® based embedded computer (Lattepanda Alpha 864s) with an Intel® Core™ m3-8100Y processor unit. The computer runs a Python-based graphics user interface (GUI) that is in charge of peripheral control (Camera and DLP) as well as real-time image processing (see. Sec. 6.2.4). Moreover, as we are going to show later in Section 8.2 the set of images acquired by the camera is then analyzed by a Machine Learning algorithm, aiming at the identification of correct images for the classification of Van Herick Grade.

Camera

The selection of the camera for this application is again of crucial importance for obtaining high-quality eye pictures. It is worth underlying that all the statements depicted for Pupillary Light Reflex devices in Section 5.2.3 are valid also in this case.

By looking on all the possible valid choices, the camera from Dart Series daA1600-60uc (S-Mount) produced by Basler[3] depicted in Figure 6.2 has been selected.

This choice proved to be ideal due to its versatility and capabilities. Overall, Basler Cameras meet the requirements of numerous computer vision applications and leave nothing to be desired in terms of

[3]Basler AG, An der Strusbek 60-62 22926 Ahrensburg, DE

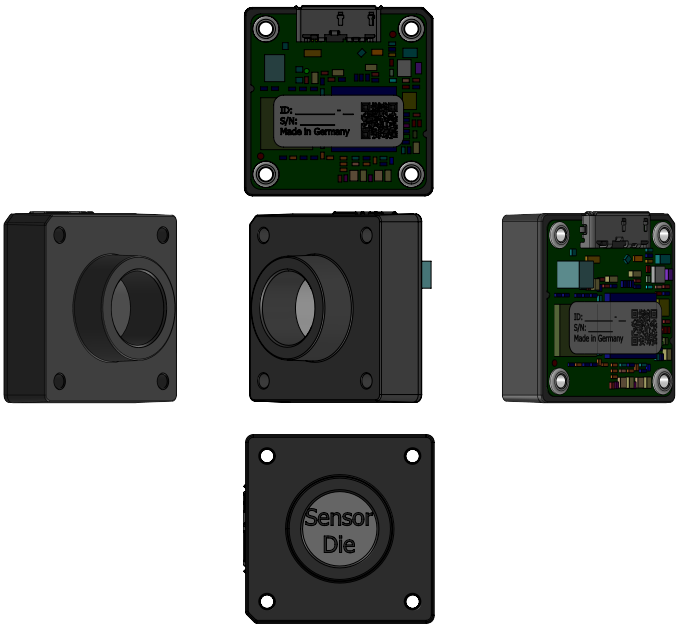


Figure 6.2: Basler Camera Dart Series - daA1600-60uc S-Mount

design as they offer various mounting options in combination with different sensors, making them highly flexible for different setups.

The Dart Series camera, with a small form factor, low weight, and low power consumption makes it ideal for applications with challenging installation conditions. Additionally, its board-level design allows for flexibility in system setup, and it is available as a bare board, S, and CS-Mount. This camera also offers high-speed USB 3.0 and BCON for MIPI interfaces, and it is available with various sensors for resolutions between VGA and 13 MP, with frame rates of up to 525 fps. Moreover, this Dart version offers outstanding image quality and an unbeatable price/performance. The detailed specifications of the camera are summarized in Table 6.1.

Table 6.1: Basler Camera Specification

CAMERA Basler dart1600-60uc	
Power Source	USB (5V)
Interface	USB 3.0 Micro-B connector
Sensor	EV76C570 (CMOS)
Pixel Depth	8 bits
Resolution	1600 px X 1200 px
Frame Rate	60 fps
Shutter	Global Shutter
Mono/Color	Color
Sync Options	Hardware/Software Trigger o Free-Run
Consumo di Potenza	1.3W

Digital Light Projector

Digital light projector (DLP), first developed by Texas Instruments in 1987, is a type of video projector that uses a *Digital Micromirror Device* (DMD) to project an image onto a screen or surface. The DMD chip is

divided into thousands of tiny pixels, and each pixel corresponds to a micromirror. The mirrors are tilted at different angles to either reflect light onto the screen or to an absorbing element, creating the pixels of the projected image. An example of the working principle of a DMD-based projector is shown in Figure

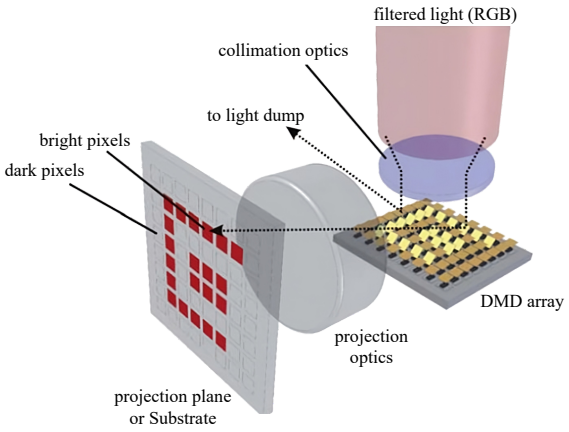


Figure 6.3: Working principle of a DMD-based light projector

The DMD chip is controlled by an external circuit, which sends signals to the individual micromirrors to tilt them at precise angles. This allows for high-resolution images and contrasts on many types of different sources. Therefore, DLP projectors have several advantages over other types of projectors:

- High contrast ratio, which results in deeper blacks and more vivid colors.
- Excellent color accuracy, making them a popular choice for professional use in industries such as photography, graphic design, and video production.
- Fast response time, allows for the display of fast-moving images without blurring, making them a good choice for gaming and sports broadcasting.
- Long lifespan for the lamp, reducing maintenance and replacement needs.
- Energy efficiency, which can help lower operating costs and reduce environmental impact.
- High resolution, suitable for displaying detailed images such as photographs or architectural drawings. Compact and lightweight design, making them easy to transport and set up in different locations.
- Affordability, making them a good option for prototypes and qualitative research.

The DLP2010 Evaluation Board depicted in Figure 6.4 has been chosen for this purpose.

6.2.3 Realized Prototype

The realized instrument is depicted in Figure 6.5. This instrument has been realized as the first working prototype to be tested with trained medical personnel at IRCCS Fondazione G.B. Bietti Rome, Italy.

The instrument is moreover composed of the following parts:

1. **Optical Motorized Table:** the optical table allows to adjustment of instrument height (Z-axis in the picture) with respect to the patient's sitting position. This allows setting the instrument in the most comfortable position for all types of patients.

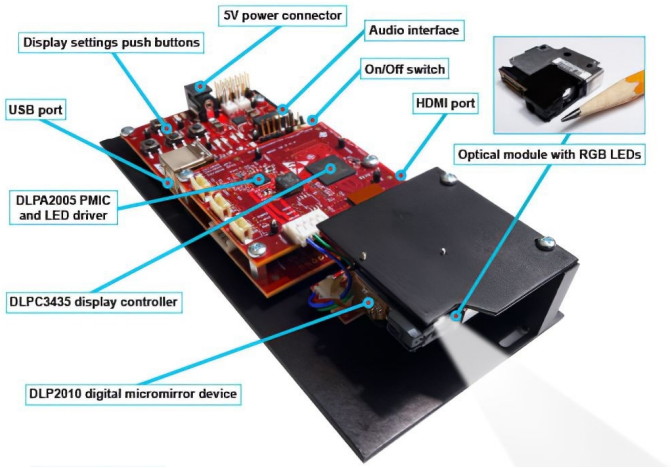


Figure 6.4: The DLP 2010 development board by Texas Instrument

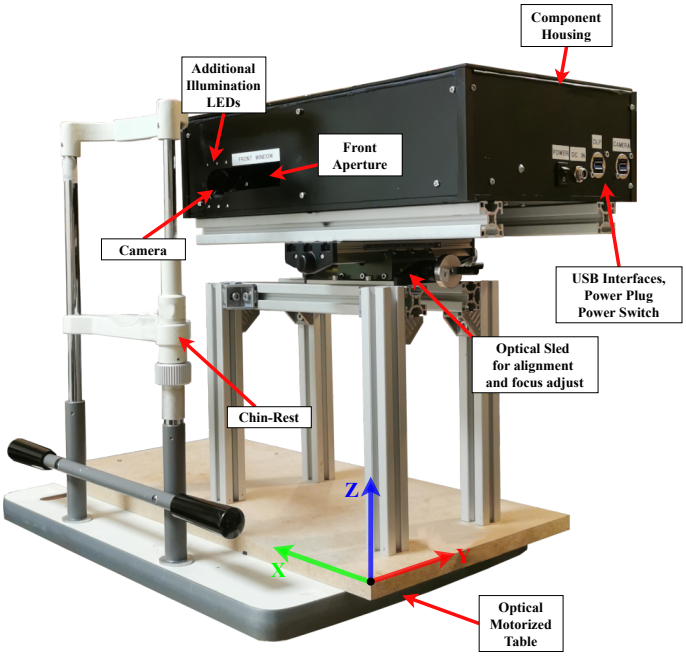


Figure 6.5: Realized Instrument for Automatic Anterior Chamber Angle Width.

2. **Chin-Rest:** an optical chin-rest is commonly used in various scientific experiments in the field of optics and vision science, to support and stabilize the head of the participant. It is typically a small and adjustable piece of equipment that can be mounted to the optical motorized table that can be adjusted (typically the height of the chin) to meet different face physiognomies. This allows for more accurate and precise measurements of the participant's eye, as the head movement can introduce errors in the results.

3. **Physical Structure:** The structure of the system has been realized with custom-cut aluminum (30mmx30mm) square Bosch[4] profiles, making the structure solid and sturdy.

4. **Optical Sled:** An optical sled made by Proxxon[5] allows for X-axis and Y-axis adjustment (with

[4]Robert Bosch GmbH, Robert-Bosch-Platz 1, 70839 Gerlingen-Schillerhöhe, Germany
[5]PROXXON GmbH Industriepark Region Trier, Dieselstraβe 3 - 7, 54343 Föhren Germany

rotating wheels) of the entire system mounted on top.

5. **Component Housing:** The component housing has been custom-made with polymethyl methacrylate (PMMA) sheets. Inside, all the comments, his including the camera, the digital light projector, and the embedded computer are protected from the external environment. A front window, as shown in Figure 6.6, allows for eye illumination performed by the DLP and image acquisition by the camera. On the side, an I/O interface is equipped with USB 3.0 ports for peripherals, a power button, and a 19V DC power plug.

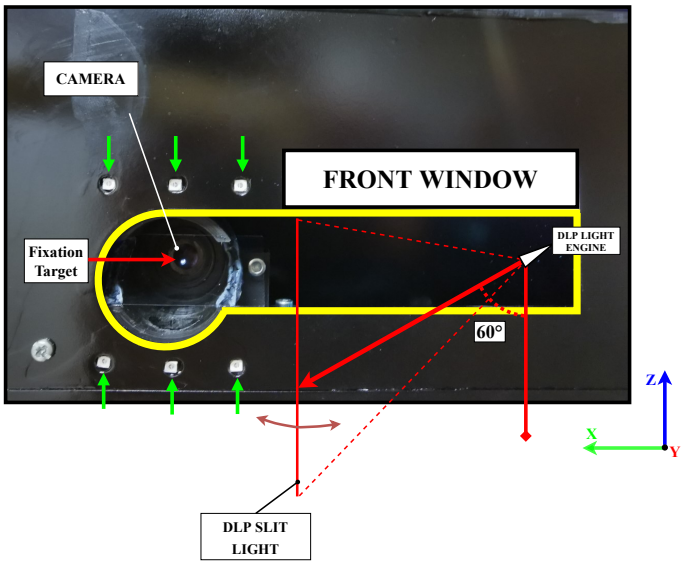


Figure 6.6: Front window aperture on the component housing is highlighted in yellow. The white fixation target, reflected with a 90° angle in respect to the LED source, is in front of the camera lens, aligned with eye optical axis (Y-axis direction). The patients right eye therefore will be aligned in front of the camera. The slit line of light, that extends vertically on the Z-axis, is delivered by the DLP light source at a nominal 60° angle in respect to the eye's optical axis. Green arrows indicates blue light illumination LEDs, useful during the alignment phase.

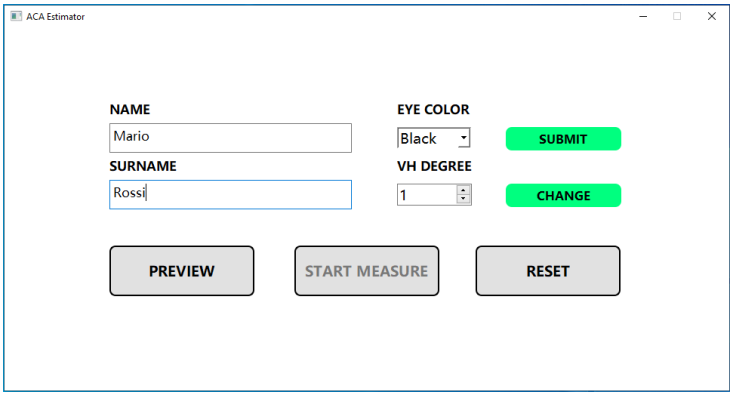
6.2.4 Software

User Interface

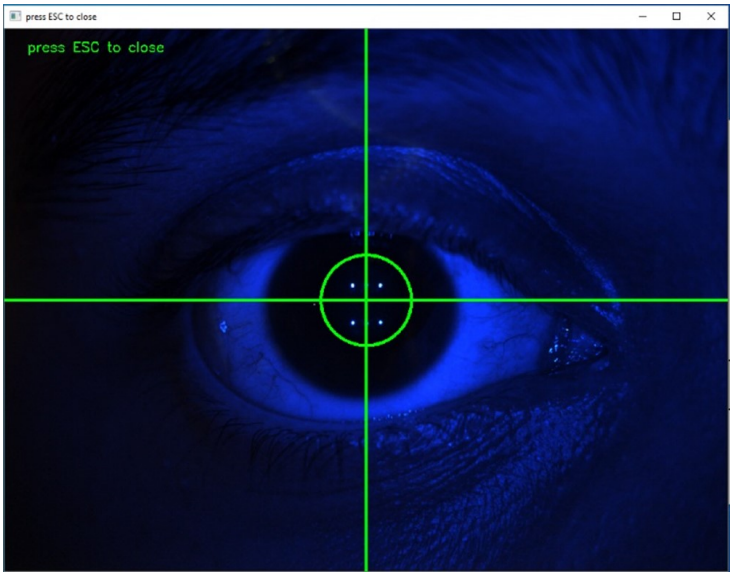
Designing a simple user interface for ophthalmic instrumentation is crucial for the efficient, accurate, and accessible use of the instrument. Ease of use, minimizing user errors, reducing the need for extensive training and education, accessibility, and patient comfort are some of the key factors that are important to consider when designing a user interface for ophthalmic instrumentation. A simple interface makes it easier for users to navigate and operate the instrument, reducing the time and effort required to complete a task. It also helps to minimize user errors by providing clear and intuitive controls and prompts. Furthermore, it makes the instrument more accessible to users with different levels of technical expertise or physical abilities and reduces the time patients need to spend on the instrument, making the experience more comfortable and less stressful.

In Figure 6.7 the simple user interface that allows for recording a measurement for a specific patient is reported. The interface, which can run on a standard Windows-based system, has been realized with Python and QT libraries. The interface is also in charge of the serial communication with the DLP and

the acquisition performed by the camera. To perform a measurement, the operator will start by fulfilling patients' information, i.e. name and surname, a simple label (black, blue, green, and brown) to identify the color of the eye (this information will be used as shown later in Section 8.2), and a label to set the VH grade (1-4) as a reference measured that should be performed with other standard techniques, as explained in previous Section 4.3.2. All this information allows for the collection of a complete database of labeled images, with additional information on eye color and Van Herick grading, determined by an optical expert. Furthermore, in Figure 6.7b, the preview windows are reported. This preview, allows the operator to align the instrument with the help of visual aids as shown in the Figure. This is of crucial importance to have optimal images, that are in focus and that respect the strict alignment requirements expected by the correct execution of the VH technique.



(a)



(b)

Figure 6.7: (a) Simple user interface (UI) to control the instrument. (b) Preview to align the camera.

Measurement Procedure After correct alignment, by clicking the *submit* button, the Python program will communicate through a serial interface (over USB) to the DLP that will start the scanning. The scanning is performed by projecting a vertical line of 1 px width on the RED channel, which will be shifted from left to right one pixel at a time, thus performing the scanning of the eye. A single scan is programmed to be executed in 2 seconds and for each measurement, two eye scans are executed for

a total of a 4 seconds measurement Keeping the measure short in terms of time, allows to reduce the patient annoyance level, thus also limiting head movement that can affect measurement quality. While executing the scan, the DLP is also programmed to set an output digital pin that triggers the acquisition on the camera. Therefore a single picture is collected whenever the line is shifted of one position. This procedure allows for superior resolution and modularity, as the speed of the scan can be set accordingly to the brightness of acquired images. Moreover, the thickness and the color of the line can be changed at will. We opted for a RED line to obtain maximum contrast with the background illumination that is set on the BLUE (as illustrated in Figure. 6.7b). By extracting the red channel from the RGB images, the contrast of the line that scans the eye can be further enhanced.

6.2.5 Safety Considerations

By using the data from the Optical Engine Reference Design for DLP2010 *Digital Micromirror Device* [273] from Texas Instruments, as reported in Table 1, an evaluation of the emitted optical power and safety of use of the DLP2010 projector used for the experimental measurements was performed. To calculate the optical power emitted by the DLP, it is necessary to know the luminous flux (Luminous Flux) in lumens of each source. The table shows the values declared by Texas of the sources used, set to maximum power (max brightness) [273]. The value of the luminous flux of each source must be multiplied by the declared duty cycle, as the sources are not continuously lit, but controlled by a PWM signal. The output luminous flux also depends on the efficiency of the optics (composed of optical transmission and geometric efficiency) that allows the projection of images, in this case on the eye. The projector's optics thus introduces an attenuation on the output power of about 30% on all three chromatic components.

Table 6.2: Characteristics of the LEDs and the power emitted through the projector optics

OPTICAL PARAMETER DLP2010			
	RED	**BLUE**	**GREEN**
Wavelength (nm)	624	455	520
Half Beam Width (nm)	20	20	100
Luminous Flux (lm)	85	31	293
Duty Cycle (%)	30	20	50
Optical Engine Efficiency[6] (%)	32.4	32.3	31.0
Photopic Conversion (lm/W)	19.1	32.8	485.0
Single source optical power (mW)	37.7	61.1	93.6
Total Power (mW)		192.4	

The table also includes the data called Photopic Conversion or Photopic Luminous Efficacy, also known as V_λ, used to convert the light flux in (*lm*) into radiated power (Watts). The values reported in the table refer to literature, in particular to the Luminous Efficacy curves reported by the International Commission on Illumination (CIE-1931) and subsequently revised [59, 275–279]. The power of each source was then obtained from the following equation:

$$P_{opt}(R,G,B) = \sum_{i=R,G,B} \frac{\Phi_{R,G,B} \cdot DC_{R,G,B} \cdot \eta_{R,G,B}}{\int V_\lambda(\lambda) \cdot \overline{E_{R,G,B}}(\lambda) d\lambda} \tag{6.1}$$

Where, $\Phi_{R,G,B}$ is the luminous flux of the specific R,G,B source, DC is the duty cycle value $[0-1]$, η is the optical engine efficacy and $\overline{E_{R,G,B}}(\lambda)$ is the normalized source spectral distribution. The integral values at the denominator are reported in Table 6.2 as the Photopic Conversion. Therefore, the total power P_{opt} in

[6] The optical engine efficiency is related to transmissions rates of optical elements used for shaping the light pattern. The optics includes, collimator lens, a dichroic, a prism, a projection lens and other components. The overall efficiency is it also related to the geometric efficiency. For a detailed analysis, check the official datasheet at [274]

Watts can be obtained as the linear sum of the powers of the three chromatic components. In our case, since the power levels are limited and the exposure times are relatively long (in the order of seconds), we focused on the possibility of incurring photochemical damage through the use of high-brightness LED sources focused on the retina, such as those coming from the projector used. Safety estimates of the sources were performed using a tool made by François Delori of the University of Hardward (Boston), called *Ocular Light Calculator* (OçLC) [280]. This tool refers to the ANSI Z136.1 (2014) and ANSI Z80.36 (2016) standards [250]. The tool allows for an estimate of safety levels for exposure to laser sources (coherent) and broadband light sources, with emphasis on ophthalmic devices and experimental devices. The standard IEC [281] considered as a reference provides a guide for the evaluation of the photobiological safety of lamps and lamp systems, including LED sources. Specifically, it provides exposure limits, reference measurement techniques, and the classification scheme for evaluating and controlling photobiological hazards related to all electrically powered broadband optical radiation sources, including LEDs but excluding lasers, in the wavelength range between 200 nm and 3000 nm.

The following considerations were adopted for the estimate of the safety of the emitted optical radiation:

- The spectral distribution of the light sources is considered Gaussian with the peak wavelength and FWHM reported in Table 1. The values of the peak wavelength and FWHM of each source refer to the official Datasheets of the sources used within the DL2010 of Texas [282, 283].
- The solid angle obtained from Lab measurements. The results are reported in Table 6.3:

Table 6.3: Measurement of the emission solid angle of a Texas Instrument DLP2010 device

	Half AngleCone Aperture (°)	**Solid Angle (msr)**
Horizontal Field of View	17.13	0.27873
Vertical Field of View	9.50	0.08617
Ratio H/V	1.778	

- For the limits on exposure, an immobilized pupil of 8 mm in diameter was considered. This consideration corresponds to the case where the subject in question is forced to directly observe the light sources without being able to look away with the pupil in a state of mydriasis (full dilation). In this condition, all the light emitted by the device analyzed is irradiated on a surface equal to or less than the pupil. Therefore, the conditions considered constitute the worst case for the evaluation of the safety of ophthalmic instruments.
- The levels of power of the luminous flux in (lm) are the maximum ones emitted by the LED sources examined [282, 283].
- The entire light radiant flux,

Under these conditions, the above-mentioned analysis tool reported that, for an optical power irradiated on the retina of $E_{e0} = 331 mW/cm^2$, equal to that resulting from the DLP2010, the maximum duration of exposure before incurring permanent photochemical damage is 15 seconds. However, even considering these conditions, it is established that the maximum duration of eye exposure in the tests carried out with the prototype examined does not exceed 5 seconds in any case.

Thereafter, a safety analysis was carried out considering the normal use of the developed prototype. The normal use conditions are similar to the previous ones (sources set to maximum power), with the exception of the distance between the eye and the sources, fixed at a minimum of $d_t = 100mm$. In this case, as illustrated in Figure 6.8 the area illuminated by the DLP2010 on a surface placed orthogonally to

the sources at the aforementioned distance d_t is equal, accordingly to the solid angle previously reported and the following equations:

$$\begin{cases} H_{dt} = 2d_t \cdot tan(\alpha_H) = 61.643\ mm \\ V_{dt} = 2d_t \cdot tan(\alpha_V) = 33.469\ mm \\ A_{dt} = H_{dt} \cdot V_{dt} = 2063\ mm^2 \end{cases} \tag{6.2}$$

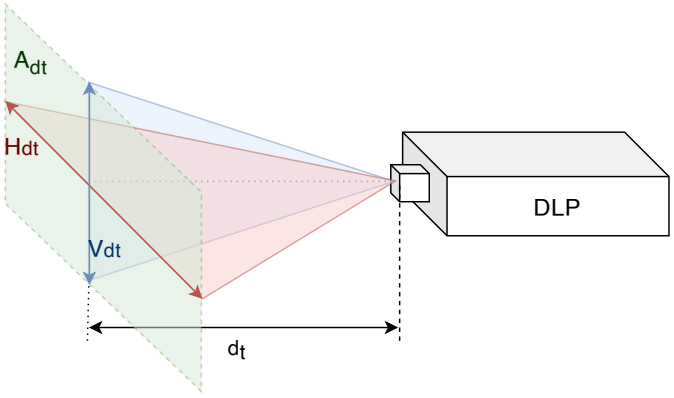


Figure 6.8: DLP Field of View Projection at a distance d_t.

Furthermore, if we consider a pupil area (in mydriasis condition) equal to $A_{p8mm} = 50.27\ mm^2$ (pupil diameter = 8 mm), the optical power incident on the retina will be only the 2.4% of the total emitted by the sources. This result was derived from the following equation:

$$P_{ret-eq} = \frac{P_{opt-tot} \cdot A_{p8mm}}{A_{d_t}} \tag{6.3}$$

By analyzing the effect of this radiation again with the work proposed by Delori et Al. [280], it is obtained that the device irradiates the retina with an optical power of $8.11 mW/cm^2$. For these power values, the maximum exposure time before incurring photo-chemical damage is 773 seconds.

Part III

Results and Discussion

Introduction

This last part describes the results and relative discussion of the experiments conducted on human subjects. As one of the main steps to be performed during the development of ophthalmic devices, the experiments presented here represent the starting point for future works and improvements of the realized measurement systems. More specifically, this part describes a "hands-on" on the instrumentation presented in Part II as well as a practical use-case of the understanding illustrated in the theoretical background (see Part I). Therefore, the results concerning in-vivo experiments are here presented.

The part is divided into the following Chapters:

- **Pupillometry:** In this Chapter 7 are presented all the experiments and relative results concerning Pupil Light reflex measurements. In particular, three experiments with and related preliminary results obtained concerning pupillometry and associated physiological effects are described.
- **Vision-Based Image Classification:** In this Chapter entitled "Vision-Based Image Classification", three research works that exploit VB techniques to improve the accuracy and objectiveness of ophthalmic instrumentation are presented.

Chapter 7

Pupillometry

In this Chapter, three experiments with and related preliminary results obtained concerning pupillometry and associated physiological effects are described. All the experiments have been performed with the techniques and instruments realized and presented in the previous Chapter 5.

The chapter, which includes three different experiments, is further divided into the following Sections:

- **Modeling of the oculomotor system**
- **Silent Substitution experiments**

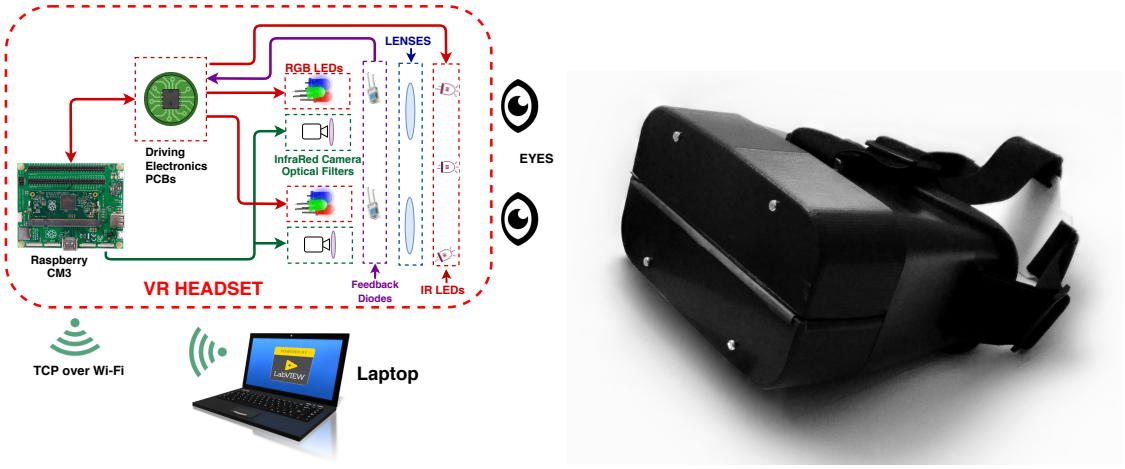
7.1 Modeling of the oculomotor system

As presented in Section 1.3, the pupil oculomotor working principle can be considered as an input-output black box system: light stimuli can be easily applied to the eyes, and pupil size can be measured effortlessly and non-invasively.

In this Section entitled "Modeling of the oculomotor system", an experimental approach to modeling short-light-flash-induced transient pupillary light reflex responses is presented and preliminary outcomes describing the model features are presented. Results confirm that the developed pupillary light reflex model is suitable to describe the pupil oculomotor system exposed to short-light flashes.

7.1.1 Instrument

The instrument shown in Figure 7.1b was realized by exploiting a modified VR (Virtual Reality) Headset. In Figure 7.1, the block diagram summarizes the main elements of the system. The pupillometer is capable of stimulating both eyes with a huge amount of different light stimuli. Four anular areas of the eye, from central to peripheral can be tested both individually and simultaneously; moreover, for each area, three different spectral components (Red, Green, and Blue) can be selected. Other parameters of light stimuli, such as frequency ($0.1 - 1000Hz \pm 0 : 1Hz$), peak intensity (256 levels), duty cycle ($\pm 1\%$) and phase shift ($\pm 1deg$) can also be set independently for each color. A set of photodiodes with spectral sensitivity adapted to the human eye are used to synchronize and record the selected light stimuli. Two infrared cameras allow real-time monitoring of pupil responses. A Raspberry Pi compute module is used to collect and elaborate pupil size in real time. The entire system can be controlled wirelessly with a laptop computer running a LabView-developed user interface. A detailed description of the device and how it was realized and characterized can be found in our previous works [66, 284].



(a) (b)

Figure 7.1: The VR pupillometer prototype. (a) shows the block diagram of the realized system. (b) shows a picture of the prototype realized by modifying a VR headset.

7.1.2 Methods

To understand autonomic nervous activities and dynamic mechanical properties characterizing the PLR, preliminary experiments were performed on human volunteers.

The experiments were performed using a custom binocular pupillometer that was developed by modifying a VR (Virtual Reality) Headset [66]. Pupil size was measured at 24 fps using two infrared cameras fixed on the VR display plane.

The experiment was performed by observing the PLR response to green short light flashes on two male human volunteers A and B aged 26 and 55 years, respectively. Using transit stimulation, the autonomic nervous innervation activities, described in Eq. 1.6, can be assumed to have the same temporal waveform of luminous flux intensities with additional time delays [33]. Figure 7.2 shows a schematic diagram of the assumed autonomic nervous activities in response to a short light pulse.

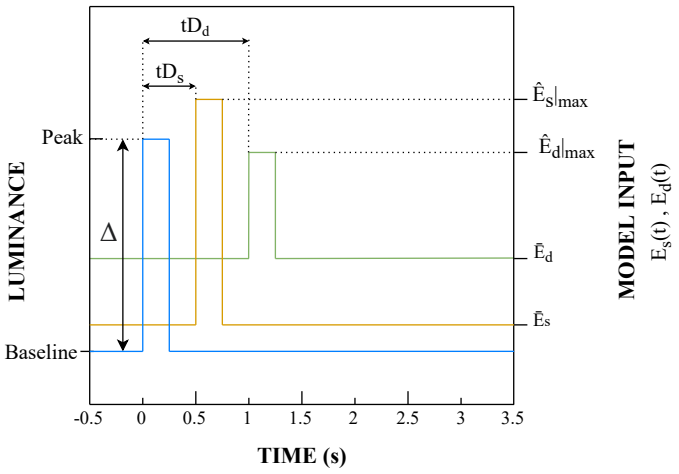


Figure 7.2: Schematic diagram of autonomic nervous activities in response to a short light flash. $E_s(t)$ and $E_d(t)$ are the parasympathetic and sympathetic nervous activities, respectively. Time $t = 0\ s$ corresponds to the rising edge of the 250 ms flash, $t_s = -0.5\ s$ is the *time-start* of the recording, while $t_f = 3.5\ s$ is the *time-finish* of the recording.

As shown in Figure 7.3, each experiment consisted of three different light stimulation phases. The first phase lasted 2 minutes with all light sources turned OFF. Luminous flux in this phase was comparable to a dark room during the daylight. This initial dark adaptation is essential to decouple the photoreceptor's excitation conditions from the external environment. In the second phase, a steady luminous flux equal to the *baseline* value was presented for 2 minutes. This phase ensured that the photoreceptors properly reached the *baseline* excitation level. In the last phase, a total of 30 flashes of 250 ms width and 5 seconds interval period were presented to the stimulated eye. The pupil response, in terms of area (mm^2), has been recorded for 4 seconds, from $t_i = -0.5\ s$ (i.e. 500 ms before the rising edge of the stimulus) to $t_f = 3.5\ s$. The light stimulus was generated by a set of green LEDs, with peak emission at 528 nm, FWHM of 27

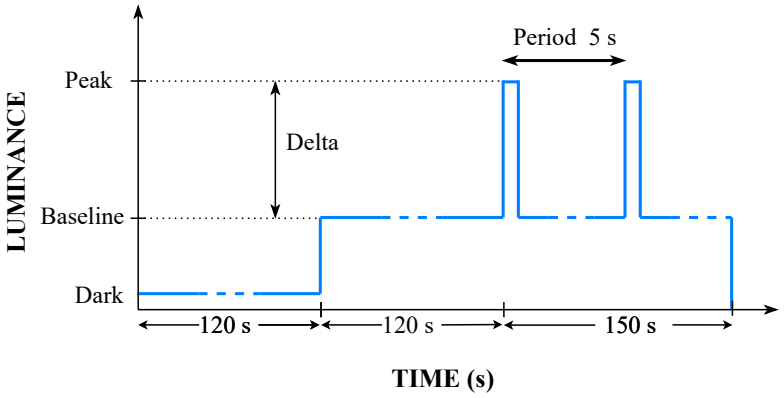


Figure 7.3: Experimental temporal phases: (i) two minutes of dark adaptation, (ii) two minutes of baseline adaptation, and (iii) 30 green flashes of 250 ms duration and with 5 seconds interval period.

nm; thanks to the LED's spatial distribution and the VR optics (for further details see Appendix 8.3.4 and our previous works [284, 285]), the stimulus illuminated uniformly the retina in a field of view (FOV) of about 45 degrees.

Three different tests were performed for each of the two volunteers stimulating the right eye. To minimize the effect of other physiological reactions that could alter the normal state of activity of the pupil, each test consisted of two sets of measurements acquired on two different days. Moreover, the measurements were carried out in a dark and noise-free environment, between 11:00 and 12:00 am. Luminous flux levels of the baseline and peak for the three experiments, obtained with the procedures and methods detailed in Appendix 8.3.4, are shown in Table 7.1. As in experiments 1 and 2, the light stimulus had ap-

	Baseline (mlm)	**Peak (mlm)**	**Delta Δ (mlm)**
Experiment 1	0.753	6.100	5.347
Experiment 2	3.900	5.900	2.000
Experiment 3	3.900	9.600	5.700

Table 7.1: Luminous flux levels of the baseline and peak for the three experiments.

proximately the same peak luminous flux but different baseline values. Experiments 2 and 3 shared the same baseline luminous flux while the last one had a higher peak luminous flux. In experiments 1 and 3, the light stimulus had almost the same amplitude, i.e. Δ. These stimuli were selected to highlight possible correlations among model parameters estimated for different autonomic nervous system excitation levels.

7.1.3 Results and Discussion

Figure 7.4 shows the average experimental response recorded during the experiments. The inverse aforementioned model was used to fit the experimental data. The obtained fitted curves are shown in the same figure.

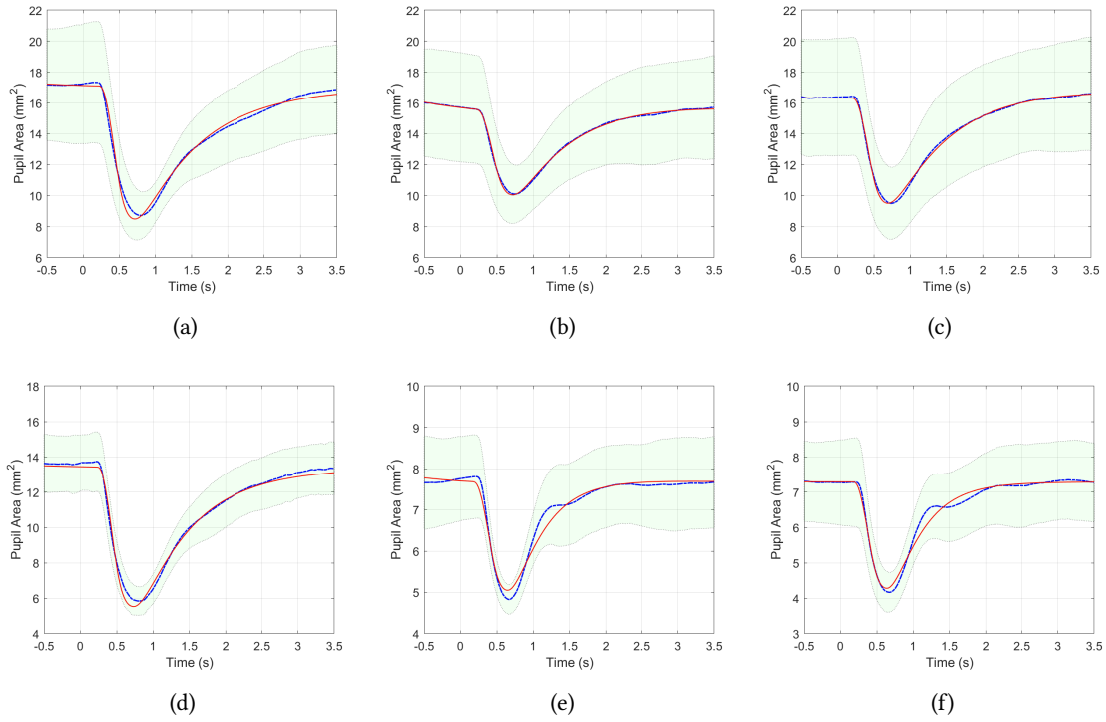


Figure 7.4: (a), (b), and (c) shows the pupil response of subject A to experiments 1, 2, and 3, respectively. (d), (e) and (f) show the pupil response of subject B to experiments 1, 2, and 3, respectively. Time $t = 0\ s$ corresponds to the rising edge of the 250 ms flash. For all the graphs, $t_s = -0.5\ s$ is the *time-start* of the recording, while $t_f = 3.5\ s$ is the *time-finish* of the recording. Blue dashed lines are the average experimental pupil response. Light green regions represent the standard deviation of the mean. Solid red lines show the best-fit results obtained from our model, previously described in Sec. **Model For The Human Pupillary**.

The PLR responses, i.e. dashed blue lines, were obtained with a boxcar average over the 30 flash responses. Temporal alignment of the responses was possible thanks to system-integrated photodiodes that generated a reference signal. As shown in Figure 7.2, light flash rising edge takes place at time instant $t = 0$ s also in graphs of Figure 7.4.

The model fitting was then computed for the PLR responses by applying some mechanical and physiological constraints. Mechanical constraints are strictly related to the nature and physical functioning of the pupillary response and are reported last column of Table 7.2. The fitting was performed by a nonlinear least square method with *trust-region-reflective* algorithm integrated in the parameter estimation toolbox provided with Simulink© R2020b. Fittings were set to minimize the sum square error of each PLR response. The estimated parameters of our model for the two subjects considering the three experiments performed are summarized in Table 7.2. Parameters not dependent on the input light stimuli, strictly related to physiological/mechanical properties of the subject eye, were estimated once for each subject. Due to the correlation to the activity of the autonomic nervous system, the input-dependant variables instead, highlighted in Table 7.2, were computed for each experiment. Looking at the estimated parameters, it

Model Parameters	SUBJECT A			SUBJECT B			Fitting Constrains
	Exp1	Exp2	Exp3	Exp1	Exp2	Exp3	
a_d	5.700			5.968			$a_d \geq 0$
a_s	4.320			4.318			$a_s \geq 0$
b_d	31.228			32.023			$b_d \geq 0$
b_s	11.775			11.686			$b_s \geq 0$
c_d	9.319			6.295			$c_d \geq 0$
c_s	128.030			127.270			$c_s \geq 0$
$\alpha_d(1/s)$	0.275			0.275			$\alpha_d \geq 0$
$\alpha_s(1/s)$	8.966			8.038			$\alpha_s \geq 0$
$\beta_d(1/s)$	5.576			5.576			$\beta_d \geq 0$
$\beta_s(1/s)$	5.024			8.331			$\beta_s \geq 0$
$D_-(mN/mm/s)$	173.450			199.970			$D_- \geq 0$
$D_+(mN/mm/s)$	120.450			103.350			$D_+ \geq 0$
$L0_d(mm)$	2.897			2.856			$L0_d > l0_d$
$l0_d(mm)$	1.392			1.832			$l0_d \geq 0$
$L0_s(mm)$	3.751			3.699			$L0_s > l0_s$
$l0_s(mm)$	2.000			1.760			$l0_s \geq 0$
$P0_d(mN)$	396.600			373.130			≥ 0
$P0_s(mN)$	1177.500			1209.700			≥ 0
$A_{max}(mm^2)$	47.051			44.914			$A_{max} \leq \pi X_{max}^2$
$A_{ini}(mm^2)$	17.217	16.046	16.331	13.515	7.778	7.296	$A_{max} \geq A_{ini} \geq \pi X_{min}^2$
$\bar{E}s(a.u.)$	0.260	0.265	0.261	0.295	0.377	0.385	$1 \geq \bar{E}s \geq 0$
$\hat{E}_d\|_{max}(a.u.)$	≈ 0	0.166	0.125	≈ 0	0.046	0.052	$\hat{E}_d \geq 0$
$\hat{E}_s\|_{max}(a.u.)$	20.136	12.161	16.573	19.810	10.661	14.588	$\hat{E}_s \geq 0$
$tD_d(s)$	0.572	0.546	0.405	0.698	0.401	0.503	$tD_d \geq tD_s$
$tD_s(s)$	0.218	0.207	0.200	0.228	0.175	0.172	$tD_s \geq 0$

Table 7.2: Fitted parameters from the model outputs in Figure 7.4. A_{max} is the estimated pupil area at brain death whereas A_{ini} represents the pupil area at the initial condition in each experiment. X_{max} and X_{min} are pupil radius maximum and minimum allowable values.

is worth noting that both subjects have similar mechanical/physical properties of the muscle plant, with minor differences in muscle lengths at rest ($l0_d$ and $l0_s$) and pupil sizes at brain death (A_{max}). Subject A presented a slightly faster sphincter contraction time (α_s) but a significantly slower sphincter release time (β_s). This is also well visible in the pupil response in Figure 7.4: a slightly steeper contraction slope but evidently a smoother and slower pupil dilation phase in respect to subject B, especially in experiments 2 and 3.

Considering the input dependant estimated parameters, the dynamic parasympathetic nervous activity, i.e. $\hat{E}_s|_{max}$, is the highest in both subjects in experiment 1 and the lowest in experiment 2, even if the peak luminous flux was roughly the same. This is probably due to a larger stimulus amplitude, i.e. Δ. Although experiment 3 exploited a stimulus amplitude similar to experiment 1, the parasympathetic nervous activity is less consistent. This is also well visible in Figures 7.8c and 7.8f, variations in the pupillary area are lower in experiment 3 for both subjects. This is probably related to the initial excitation status of the oculomotor system that approaches the saturation level for the higher baseline luminous flux used in experiment 3.

Concerning the parasympathetic static activity, i.e. Es_{stat}, the fitting results show a consistently higher value in experiments 2 and 3 for subject B. Besides, the dynamic component of sympathetic activity, ($\hat{E}_d|_{max}$), is negligible for the first experiment but is significant in the other two experiments for both

subjects. This is, again, probably related to the higher baseline excitation that, in turn, determines the initial pupil condition, i.e. A_{ini}. Regarding the nervous activity delay times, it is worth noting that the sphincter reaction time, tD_s is slightly lower if the baseline excitation level is higher, especially for subject B.
Table 7.3 reports the sum squared relative errors of the fitting as obtained by the following equation:

$$\overline{SSE} = \sum_{t=t_s}^{t_f} \left[\frac{y_t - f(t)}{y_t} \right]^2 \tag{7.1}$$

Where, y_t is the measured value of pupil area at time t, $f(t)$ is the simulated (predicted) value of the pupil area at time t, $t_s = -0.5\ s$ and $t_f = 3.5\ s$ are the *start-time* and *finish-time* of the recording, respectively.

	Sum Squared Relative Errors ($\overline{SSE}$)	
	SUBJECT A	**SUBJECT B**
Eperiment 1	0.1603	0.1490
Eperiment 2	0.0162	0.2476
Eperiment 3	0.0322	0.2381

Table 7.3: Sum squared relative errors of the model fitting for the three experiments.

These low error values prove as the analyzed physical model adequately fits the experimental data for the considered short-light-flash stimuli. The average coefficient of determination among all six experiments, i.e. R^2, is about 0.86. Low-frequency fluctuations in pupil size, commonly present in the oculomotor system of the human eye, can affect the boxcar averaging results reducing the fitting accuracy. Another variable that can affect the fitting results could be the assumptions used to model the input signal from the autonomic nervous system explained previously in Figure 7.2.

7.1.4 Conclusions

A preliminary study towards the development of a new model for the iris oculomotor system has been described. The developed model for short-light-flash-induced transient PLR proved to match acquired experimental data with a coefficient of determination, R^2 of 0.86 among two different subjects and different flash intensities. Many other experiments need to be conducted to validate and complete the model for larger sets of eye stimulations. In the near future, the definition of new methods and models for PLR analysis can pave the basis for more advanced diagnostic techniques that can be exploited to estimate optic-nervous system diseases.

7.2 Silent Substitution experiments

As we discussed in Section 1.2.3, the three classes of photoreceptors cones, rods, and *intrinsically photosensitive retinal ganglion cells* (ipRGCs) contribute to the pupillary light reflex (PLR). The Silent Substitution technique has been proposed to analyze the contribution of the individual photoreceptor to PLR. Through the usage of properly selected pairs of light stimuli, this approach allows stimulating a single class of photoreceptors while keeping the activation of all the others constant. In this way, it is possible to understand the single photoreceptors class effect on both image-forming and non-image-forming functions of the human eyes.

7.2.1 Experiment 1: PLR Induced Response of M-Cones and ipRGCs

In this Section, preliminary tests conducted on three volunteers in which the PLRs induced by melanopic and chloropic stimulation are presented. As we will discuss later in Section 7.2.1, the light-adapted pupil diameter is principally regulated by the activation level of the melanopsin-expressing ipRGCs photoreceptors, while cone-driven induced pupil responses to peak in color contrast are transitory, reverting to the light-adapted baseline pupil diameter more rapidly in respect to melanopsin counterpart.

Test Methodology

Two experiments, silencing and stimulating different photoreceptors, have been carried out in a controlled illumination environment on three volunteers (S1, S2, and S3): two males aged 27 and 30, and a 24 years old female.
As depicted in Figure 7.5, both experiments share the same timeline where a two phases stimulation is adopted.

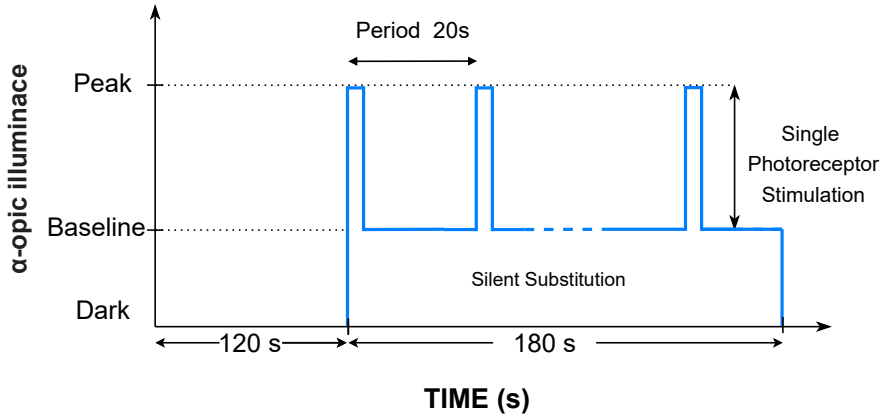
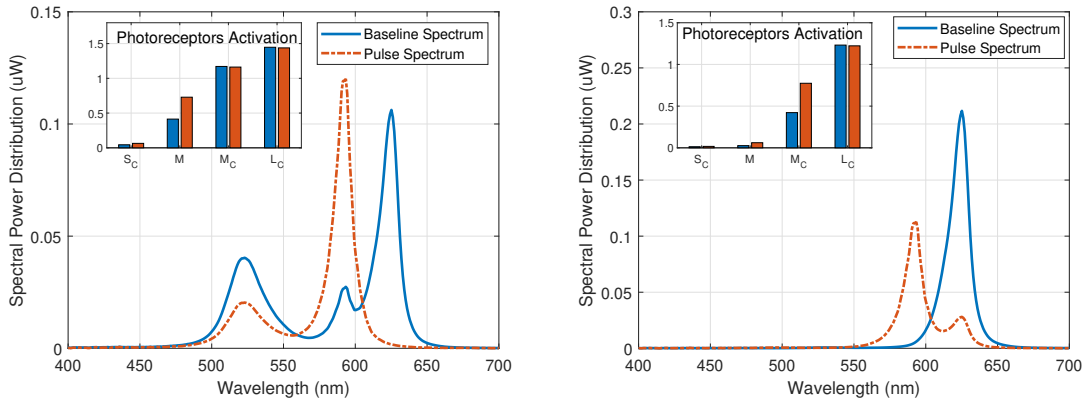


Figure 7.5: Experimental temporal phases: (i) dark adaptation in a controlled environment (2 min), (ii) single photoreceptor stimulation (3 min). During the stimulation phase, light pulses with higher equivalent illuminance for one selected photoreceptor with respect to the baseline illumination level are presented for 1 s with a repetition period of 20 s.

During the first two minutes, the subject's pupil was left to resting condition, without any direct light stimulation. This initial dark adaptation is essential to decouple the photoreceptor excitation conditions from the external environment. In the second three minutes test phase, nine one-second pulses with higher equivalent illuminance for one selected photoreceptor type were presented to the subject's eye with twenty seconds repetition period. Between each peak, a baseline stimulation is used to maintain a photopic vision keeping the rods saturated [286]. More in detail, the peak and baseline share the same level of stimulation for three photoreceptors while the fourth has been selectively stimulated. For this purpose, as shown in Figure 7.6, two properly selected colors have been used for each test. The spectral distributions, i.e. LEDs intensities combinations in terms of duty cycles DC, have been selected to obtain the highest and almost equivalent Weber contrast (Equation 2.20) in both the tests.

The conversion between LED current duty cycles (DC) and the relative output spectral distribution has been calculated by scaling the output spectral distribution measured for each LED with a spectrometer (PMA-11, Hamamatsu), with the relative output power in Watt for each DC step. The last was measured by using a calibrated optical power meter (Newport 918R model, 918d-uv-od3 optical head). Moreover, a LabVIEW interface implements the calculations that, accordingly to the standard CIES026:2018 [48] and



(a) (b)

Figure 7.6: Spectral distribution of two colors used for the melanopic stimulation (a): the blue solid line is the baseline spectrum while the orange dash-dot line spectrum is the one used for the peak. On the top left the photoreceptor's activation levels are shown, where S_c, M_c, and L_c represent the three types of cones, while M represents the ipRGCs. Spectral distribution of the output light used for the chloropic stimulation (b): the blue solid line is the baseline spectrum and the orange dash-dot line represents the peak spectrum.

to the work of Lucas et al. [51] (See Eq. 2.18), give the relative $\alpha - opic$ equivalent illuminance for any given spectral distribution.
The first test was focused on the stimulation of ipRGCs (Melanopic) while the second one was on the M-CONEs (Chloropic) stimulation. Two sessions of both experiments were carried out on each subject to cover the minimum repeatability.
For each test, in Table 7.4 the equivalent illuminance of each photoreceptor and the total photopic illuminance are reported. For the ipRGC melanopic stimulation test, the selected colors presented a Weber contrast $C_W = 76\%$, while for the M-CONEs stimulation test $C_W = 83\%$.

Table 7.4: Experiment $\alpha - opic$ equivalent illuminance and radiant power. Conditions of greatest contrast between stimulus and baseline affecting $Melanopic$ and $Chloropic$ are highlighted in red.

	ipRGC		M-CONE	
	Baseline	**Peak**	***Baseline***	**Peak**
Cyanopic ($\alpha - lux$)	0,04	0,06	0,01	0,01
Melanopic ($\alpha - lux$)	0,41	0,73	0,03	0,05
Chloropic ($\alpha - lux$)	1,17	1,16	0,42	0,77
Erythropic ($\alpha - lux$)	1,45	1,44	1,23	1,22
Radiant Power ($\mu W/cm^2$)	0,30	0,40	0,41	0,26
Photopic Illuminance (lux)	1,46	1,49	1,01	1,21

Results and Discussion

In Figure 7.7, the average PLR response to ipRGC stimulation, i.e. solid orange line, has been calculated as the boxcar average over the nine flash PLR responses in the three minutes test phase.

The temporal alignment of the responses was possible thanks to the hardware triggering of each frame

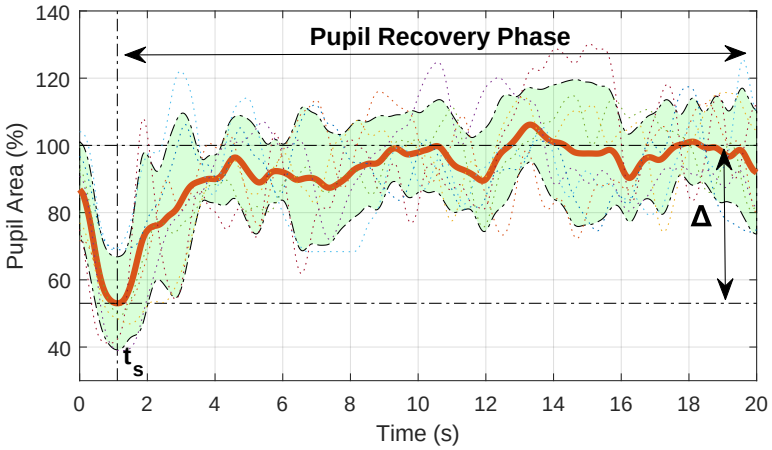


Figure 7.7: Average pupil light response to ipRGC stimulation (solid orange line). The average response is calculated as the boxcar average over the nine PLR responses (dashed lines) registered in the three minutes test phase. The light green region represents the standard deviation of the mean. The one-second pulse, with higher stimulation on ipRGC, is presented at time t = 0 s. The baseline color is maintained for the remaining nineteen seconds.

acquisition by the MCU. The pupil responses have been normalized to the 100% of the *Estimated Steady State Pupil Area* (ESSPA) corresponding to the specific baseline stimulation level. In order to be easily performed and to limit the annoyance on the subject's eye, the tests have been kept limited in terms of duration. This implies, that ESSPA has been estimated by observing the trend of the average curve from $t_e = 5s$ until the end of stimulation. Afterward, the pupil recovery phase has been selected starting from the maximum contraction point of the average ($t_s \simeq 1\ s$) until the end of the period (Figure 7.7). All the responses have been further normalized with respect to the total variation Δ from the baseline pupil area (Figure 7.7) where the maximum constriction corresponds to zero, while the ESSPA value corresponds to 100%.

The curves obtained from the experimental data are illustrated with dash-dot blue lines in Figure 7.8, where (a, b, c) correspond to the ipRGC pupil recovery phase of subjects S1, S2, and S3, respectively, and (d, e, f) to the M-CONE pupil recover phase of subjects S1, S2, and S3, respectively. The time t_s (Figure 7.7), as it depends on the PLR response delay, which is not constant [287,288] and higher than zero, will always be higher than 1 second. As a result, the obtained pupil recovery curves shown in Figure 7.8 will always last less than 19 seconds, depending on the aforementioned delay.

The pupil light response was analyzed by fitting a double-term exponential to the experimental data. The parameters τ_1 and τ_2, and K of the fitting curve in Equation 7.2 have been estimated with a nonlinear least square method. The fittings, shown with solid orange lines in Figure 7.8, were set to minimize the root mean square error (*RMSE*) for each PLR response.

$$\Delta P_A(\%) = (100 - K) \cdot \left[1 - exp\left(\frac{-t}{\tau_1}\right)\right] + K \cdot \left[1 - exp\left(\frac{-t}{\tau_2}\right)\right] \tag{7.2}$$

In Equation 7.2, the two exponential terms take into account for both fast and slow dilation components of the recovery phase of pupil area variation (ΔP_A), each one with its specific time constant τ_1 and τ_2, respectively. The K component represents the percentage contribution amount of the slow exponential components to ESSPA. The selection of specific fitting constraints, reported in Table 7.5, allowed keeping the two-time constants distinct from each other.

Table 7.6 reports the results of the PLRs analysis. In the table, the estimated parameters obtained for

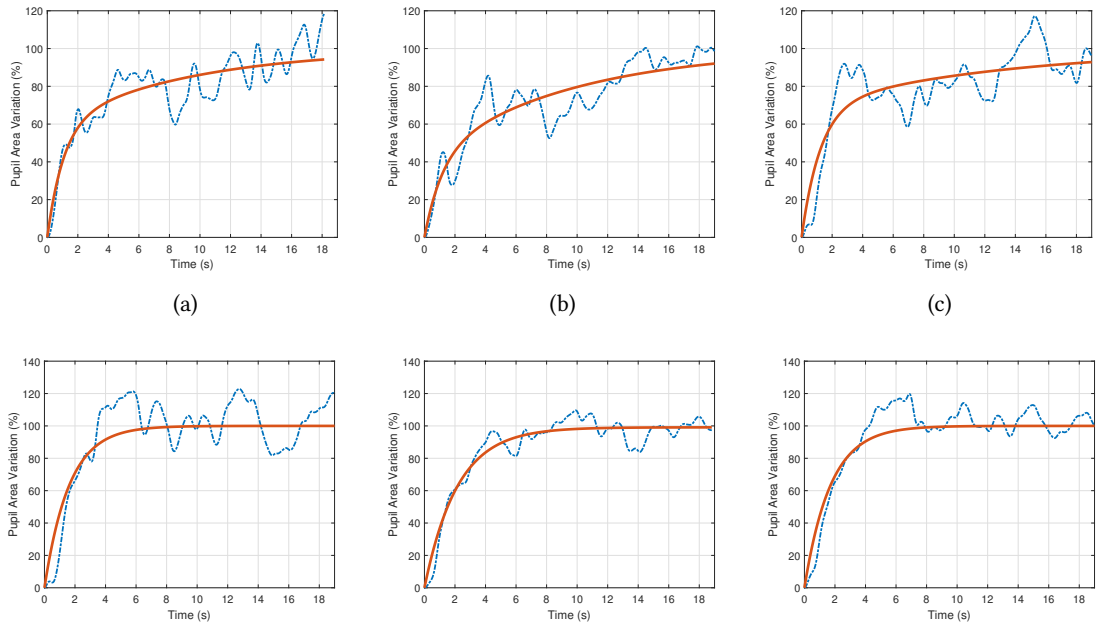


Figure 7.8: Pupil recovers from melanopic one-seconds pulse stimulation for subjects S1 (a), S2 (b) and S3 (c). Pupil recovers from a chloropic one-second pulse response for subjects S1 (d), S2 (e) and S3 (f).

Fitting Constraints		
	Lower	**Upper**
K	0	100
τ_1	0	5
τ_2	5	Inf

Table 7.5: Parameters Constraints of the double-term exponential fitting function.

the three subjects S1, S2, and S3 in both tests are summarized. The results refer to the two experimental sessions.

	Melanopic						**Chloropic**					
	S1	**S1**	**S2**	**S2**	**S3**	**S3**	**S1**	**S1**	**S2**	**S2**	**S3**	**S3**
K (%)	21,2	37,6	55,6	21,5	27,5	29,8	$\simeq$0	$\simeq$0	$\simeq$0	$\simeq$0	$\simeq$0	$\simeq$0
τ_1 (s)	1,34	1,11	1,19	1,09	1,09	1,23	3,33	1,50	1,33	2,15	1,71	1,69
τ_2 (s)	9,12	8,99	8,90	12,10	6,54	12,38	N.R.	N.R	N.R	N.R	N.R	N.R
R^2	0,95	0,81	0,81	0,72	0,81	0,72	0,86	0,71	0,71	0,93	0,76	0,86
RMSE	4,45	9,24	9,85	10,86	9,20	12,14	9,65	15,46	13,19	6,48	13,39	9,50

Table 7.6: Results of the PLRs analysis: fitting parameters τ_1 and τ_2, and K for three subjects S1, S2, and S3 refer to the two experimental sessions. The fitting Root Mean Square Error (RMSE) and coefficient of determination R-squared (R^2) describe how far apart the predicted values are from the experimental data, on average, and the link between the variability of the experimental data and the correctness of the double-exponential model, respectively

Two different trends that characterize the recovery phase from pulse stimulation of the two different photoreceptors, i.e. ipRGCs and M-CONEs, are well visible in Figure 7.8 and highlighted by the fitting parameters in Table 7.6. The ipRGCs recovery phase is always approximated with a double term exponential, where the slow K coefficient ranges from 21% to 55% (average 32.2 %) and its time constants τ_2 sets between 6.5 seconds and 12.1 seconds (average 9.67 seconds), while the fast component τ_1 is just over 1 second for all the three subjects. On the contrary, M-CONEs recovery from an equally contrasted pulse stimulation is consistently fitted with a single, overall faster, exponential term, where K factor has been always estimated near to zero, thus making the slow constant τ_2 not relevant (N.R.) for the exponential fitting. The time constant τ_1 ranges from 1.33 seconds to 3.33 seconds with an average of 1.95 seconds for the three subjects. For all the experiments, the coefficient of determination (R^2) ranges from 0.71 to 0.95 with an average of 0.804. The variability of the estimated parameters could be mainly associated with the low number of single flash responses used to calculate the average and to the presence of fluctuations in the pupil size, commonly present in the oculomotor system of the human eye. The results confirm the expectations, most likely the light-adapted pupil diameter is principally regulated by the activation level of the melanopsin-expressing ipRGCs photoreceptors [289], while the cones-driven induced pupil responses to peak in color contrast are transitory, reverting to the light-adapted baseline pupil diameter more rapidly with respect to the melanopsin counterpart. The slower temporal properties of the melanopsin pathway have been observed in many studies [290, 291] as its main contribution to pupillary light reflex resides in the regulation of the steady-state pupil size in daylight illumination. McAdams et al. [292], proved that the subject pupil responses to silent stimulation of specific photoreceptors stimulus can be approximated with a six-parameter nonlinear three-components model. The simplified two-term three-parameter exponential equation presented in Eq. 7.2 seems to agree with the more sophisticated and deeply verified models of other recently presented research. Accordingly to our findings, the obtained results for the melanopsin-directed evoked responses consistently show higher exponential values during the recovery phase [292]. Although a more extensive experimental campaign, with a greater number of patients and repeated measurements, is necessary, this simplified approach to the Silent Substitution technique proved to be a valid method for the investigation of a single type of photoreceptor's contribution to the pupillary light reflex.

Conclusions

In this first experiment, preliminary studies and performances of a simple and in-expensive Maxwellian-View optical system for Silent Substitution have been presented. The tests conducted on human volunteers with short-light-flash-induced stimulation on a single class of photoreceptors showed that this approach to the Silent Substitution technique allows us to deeply understand the contribution of ipRGCs to both image-forming and non-image-forming functions of the human visual system. Despite this, many other experiments need to be conducted in order to validate and improve this novel approach to the technique. In the near future, the definition of new test methodologies and experiments for single photoreceptor stimulation PLR could serve as a foundation for more advanced diagnostic procedures that can be used to estimate optic-nervous system disorders.

7.2.2 Experiment 2: Comparing ERG and PLR

Investigation of single-type photoreceptor contribution to pupillary light reflex.

Introduction and Goals

The Electroretinogram (ERG) [293, 294] is a measurement of the retina's overall electrical activity in response to light stimulation, while the Pupillary Light Reflex (PLR) [295, 296] is the process that mediates changes in the pupil area in response to variations in illuminance. ERG techniques, such as full-field flash ERG (ffERG), pattern ERG (PERG), and multifocal ERG (mfERG), are commonly used to evaluate the functional status of the retina and retina-related disorders in human care, veterinary procedures, and medical research [293, 297]. On the other hand, Pupillary Light Reflex (PLR) not only provides information about the retina's functional status but also provides insight into both the parasympathetic and sympathetic divisions of the autonomic nervous system, as well as intracranial and neurological connections [298]. ERG and PLR responses to diffuse flashes of light include contributions from all major classes of cones (long-(L), middle-(M), and short-(S) wavelength sensitive photopigment) and rod photoreceptors [299]. While such stimuli are effective in assessing retinal function in a non-selective, global fashion, there is also a lot of interest in recording ERG and PLR that reflect the activity of particular photoreceptor populations [61, 64]. As we previously discussed, it can be challenging to stimulate specific photoreceptors without activating others due to the overlap in photopigment spectral sensitivities [48, 300]. Therefore, the Silent Substitution technique is among the best choice to selectively stimulate specific photoreceptor populations, since it rely on the "Principle of Unvariance" [22], which asserts that the photocurrent of a specific photoreceptor is only a scalar output and cannot differentiate between changes in wavelength and changes in intensity.

In this study, we investigate the combined response of ERG and PLR with a silent stimulation technique that can lead to a new method for the examination of the health and function of the eye and the optic nerve, which can be used to diagnose and monitor eye diseases such as glaucoma, retinitis pigmentosa, and age-related macular degeneration [1].

Test Methodology

Four experiments, stimulating the two different classes of cones photoreceptors (L and S) singularly with two different contrast (C_M) while silencing the others along with ipRGCs, have been carried out on three male volunteers (S1, S2, and S3) aged 24, 34, and 55 years old. The experiments have been carried out in a controlled illumination environment, where a series of 200 ms flashes were presented with a 0.5 Hz frequency or 2 seconds period. This timing configuration has been specifically selected as a trade-off between clear ERGs and PLR responses. As we can learn from the literature the easiest way to get clear ERGs responses is by repeating many high-brightness short flashes (duration < 100 ms) [301] at 2-3 Hz interval frequency. Differently, for well-visible pupil responses, longer flashes, in the range of 500 ms or more [302, 303] with much higher interval time, i.e. in the range of seconds, are preferable. In our case, since both signals are recorded at the same time, timing values that will work for both techniques must be considered. Therefore, as the best compromise between clear and meaningful responses and test duration, the timeline depicted in Figure 7.9 has been used in all four of our experiments.

More specifically, for each experiment, we used a 2 minutes *adaptation phase (i)* with background illumination, while natural eye-blink was allowed. During this phase, only the recording of pupil size was active to evaluate the subject's specific pupil size at the background illumination level. Afterward, the stimuli were presented in a series of 10 consecutive flashes for a total of 20 seconds where no blinks were allowed since ERGs signals are extremely sensitive even to the smallest ciliary muscle movements. The *stimulation phase (ii)* is followed by a *PAUSE* interval with a variable duration comprised between 5 and 10 seconds to allow the subject to blink and rest for the next series of flashes. The 10 flashes stimulation phase with pause interval is then repeated up to 20 times, for a total of 200 averages of single burst responses. During the 20 seconds stimulation phase, the simultaneous recording of both ERG and PLR responses is

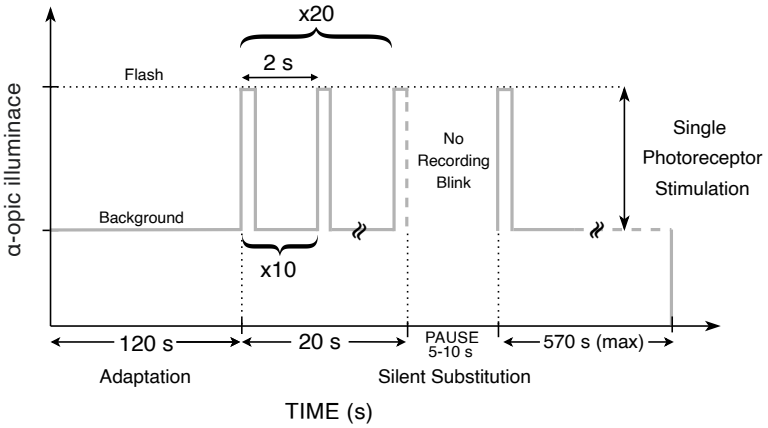


Figure 7.9: Experimental temporal phases: (i) 120 seconds of background *adaptation* in a controlled environment, (ii) single photoreceptor stimulation ($\approx$ 10 min). During the stimulation phase, 200 ms light flashes with higher equivalent illuminance for one selected photoreceptor with respect to the background illumination are presented with a interleave period of 2 seconds. Every 10 flashes (20 s) a *PAUSE* interval with a variable duration comprised between 5 and 10 s is used to allow the patient to blink.

active on the stimulated eye, while during the pause no recording is active except for the live video stream that allows for continuous adjustment of the eye alignment performed by the operator.

Accordingly to the silent substitution technique presented in Section 2.2, we optimized the LED intensity for each experiment to obtain a *target* Michelson Contrast C_M (see. Eq. 2.2.1) of 40% ($\pm 2\%$) and 70% ($\pm 2\%$) for L-CONEs (experiments #1 and #2) and S-CONES (experiments #3 and #4). Table 7.7 summarize all the specifications of the light stimuli for each experiment. The *Base* columns refer to the background stimulation level, while *Flash* columns highlight the specifications with increased stimulation on the specified photopigment.

As highlighted in the Table, the four experiments share the same viewing angle (FOV), timing, and environmental condition. The number of averages recorded for each experiment and subject was closely linked to the noise level of ERGs signals and ranged from 100 to 200 for all tests. For completeness, Figure 7.10 shows the whole spectra flux distributions (W/m^2) in the visible range used for each experiment.

Preliminary Results and Discussion

By using silent substitution, isolating the responses of L and S Cones were made possible along with measuring simultaneous PLR and ERG signals to those specific stimuli. In Section 7.2.2 we present the results described by ERGs signals while in Section 7.2.2 the results concerning PLR responses are shown.

ERG results Figures 7.11a,7.11b, and 7.11c highlight characteristics of the ERG's isolated responses for L and S cone silent stimulation at 40% and 70% C_M on the three subjects, namely S1, S2, and S3 respectively. Time t = 0 s corresponds to the beginning of the 200 ms flash for all the graphs. As previously mentioned, each curve represents the average from over 100 single flash responses. After averaging, the responses have been band-pass filtered with [1 Hz - 300 Hz] cutoff frequencies accordingly to ISCEV's last dated guide to electroretinography [301, 304] and to other reference research studies [300, 305]. Moreover, we performed smoothing with cubic spline [306], while keeping the total attenuation of the signal under 3%. Statistics of ERGs average responses from the three subjects are reported in Table 7.8.

As can be seen from the graphs, ERGs individual responses are pretty consistent for the three subjects. In particular, we can notice that the amplitudes of a-wave, b-wave, and d-wave [293], as well as for the

Table 7.7: Experiments specification. The $\alpha - opic$ stimulation levels reported as B, M, G, R are indicative for Cyan-opic (S-cones, Blue), Melan-opic (ipRGCs), Chlor-opic (M-cones, Green), and Erythr-opic (L-cones, Red), respectively.

		Experiment #1 L-CONE 40% C_M		**Experiment #2** L-CONE 70% C_M		**Experiment #3** S-CONE 40% C_M		**Experiment #4** S-CONE 70% C_M	
		Base	**Flash**	**Base**	**Flash**	**Base**	**Flash**	**Base**	**Flash**
Perceived Color		Orange	Red	Green	Red	Dark Yellow	Pink	Light Green	Pink
Wavelengths (nm)		-	-	473	473	473	-	473	437
		531	-	531	-	531	473	530	530
		595	595	595	-	-	595	-	595
		-	630	-	630	630	-	630	630
Total Radiant Flux (uW)		0.80	3.38	0.64	5.59	1.26	1.41	1.62	1.72
Luminance (cd/m2)		88.42	163.29	73.37	264.64	105.19	89.92	149.22	130.91
α-**opic illuminance** (α-**lux**)	**B**	0.07	0.09	0.39	0.71	1.34	3.08	0.56	3.06
	M	0.55	0.22	2.11	1.06	3.61	3.99	3.95	4.77
	G	2.84	2.90	3.15	4.87	4.22	3.81	5.93	5.29
	R	3.97	9.03	2.78	14.7	4.49	4.43	5.92	6.10
FOV		20.5 ° FOV							
Number of subjects		3 Males (age 23,34,53)							
Timing		200 ms flash with 2 seconds period (10 flash seq.)							
Test Condition		Afternoon – Room light – Undilated Eye							
Averages		100 to 200 recordings on the same day for each subject							

photopic negative response (PhNR) [307] are higher for the L-CONEs (dashed dark red line in Fig. 7.11) with $70\% C_M$, thus for all the three subjects (See Table 7.8). The L-CONEs $40\% C_M$ instead (solid orange line), show lower values in terms of PhNR (-4.46 μV) and *OFF-Response*, or d-wave, which is what is normal to be expected from lower intensity (i.e. lower contrasted) flashes [308]. Looking at the S-Cones responses, a different trend from L-Cones is appreciable for all three subjects. In particular, b-wave and PhNR amplitudes are lower for both S-Cones 40% and 70% contrast, especially for subject S1 (Fig. 7.11a) and S3 (Fig. 7.11c) if compared to the L-Cones counterpart. Taking a closer look, b-waves for S-Cones at 70% C_M also show to be slightly delayed (48.32 ms) if compared to the 40% ones (40.69 ms). Moreover, S-Cones shows a significantly lower amplitude (2.250 - 2.406 μV) and delayed (337 - 365 ms) d-wave (OFF-Response) if compared to L-Cones (3.745 - 12.485 μV) amplitudes and (243 - 297 ms) d-wave specifications.

Table 7.8: Average ERGs response statistics

Cones Type	**a-wave time (ms)**	**a-wave amplitude (uV)**	**b-wave time (ms)**	**b-wave amplitude (uV)**	**PhNR-wave time (ms)**	**PhNR-wave amplitude (uV)**	**d-wave time(ms)**	**d-wave amplitude (uV)**
L-CONE $70\% C_M$	16.59	-0.846	42.06	4.285	105.89	-9.378	297	12.485
L-CONE $40\% C_M$	18.94	-0.924	46.09	2.933	86.68	-4.461	243	3.745
S-CONE $70\% C_M$	19.84	-0.995	48.32	1.491	130.92	-2.949	365	2.406
S-CONE $40\% C_M$	16.57	-0.389	40.69	1.501	98.11	-3.587	337	2.250

PLR results PLR responses have been simultaneously recorded with ERG as explained in Section 7.2.2, where single flash responses have been averaged for each subject. The point-by-point averaged responses of each subject, have been furtherly normalized accordingly to the following equation:

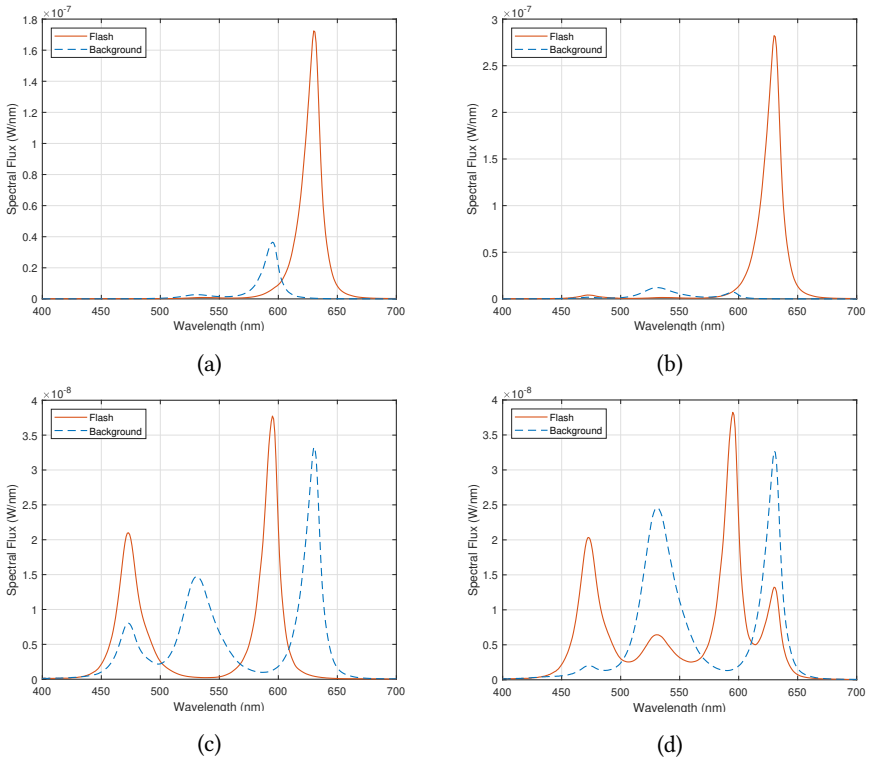


Figure 7.10: Spectral distribution of light stimuli used for the silent substitution in the four experiments. For each graph, the blue dashed line is the background spectrum while the orange solid line is the spectral flux used as a flash for each test. a) shows spectral flux for experiment **#1** with 40% contrast on L-cones (RED), b) shows the experiment **#2** with 70% contrast on L-cones, c) shows experiment **#3** with 40% contrast on S-cones (BLUE), and d) shows experiment **#4** with 70% contrast on S-cones.

$$\overline{P_D}(t) = 100 \cdot \frac{P_D(t) - min(P_D)}{P_D(t = t_0) - min(P_D)} \tag{7.3}$$

Where $\overline{P_D}(t)$ is the pupil diameter normalized value at time t, $P_D(t)$ is the pupil diameter at time t in mm, $min(P_D)$ is the minimum size of the pupil diameter in mm and $P_D(t = t_0)$ is the pupil diameter in mm a time $t = 0$, i.e. just before the beginning of the flash. This normalization technique allows us to furtherly average the responses among the three subjects, thus enhancing timing and the recovery phase as explained in our previous articles [309]. Figure 7.12 shows the average combined responses for L and S cone silent stimulation at 40% and 70% C_M among the three subjects.

As highlighted by Figure 7.12 and reported in Table 7.9, there is an appreciable difference between S-Cones (solid light-blue line and dashed blue line) and L-CONES (dashed red line and solid orange line) driven PLR recovery phase. In particular, averaged S-CONEs induced PLR response recovers at 80% for 40% C_M and 60% for the $70\%C_M$ of the initial background-adapted diameter. This result is confirmed as reported in Table 7.9, the PLR dilation time constant (see [309] for details) is around 500 ms for both L-Cones drove responses, while is 50% higher for 40% S-Cones at 764 ms and 100% higher for 70% S-Cones at over 1000 ms.

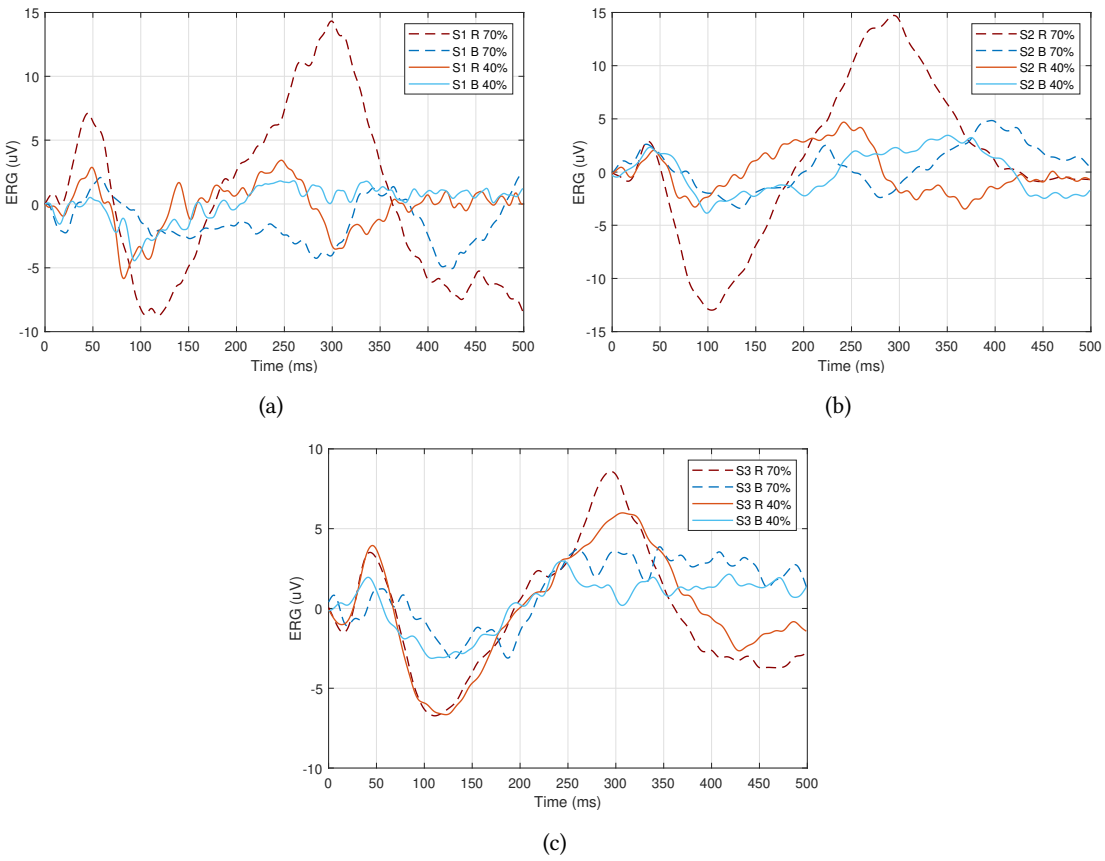


Figure 7.11: ERGs electrical response to L and S cones silent stimulation. Figures (a), (b), and (c) refers to subjects S1, S2 and S3, respectively. Dashed dark red lines (R 70%) correspond to L-Cones stimulation at 70% C_M; Solid orange lines (R 40%) to L-Cones stimulation at 40% C_M; Dashed blue lines (B 70%) to S-Cones stimulation at 70% C_M; Solid light blue lines (B 40%) to S-Cones stimulation at 40% C_M. For all graphs, time t=0 ms corresponds to the beginning of the 200 ms flash.

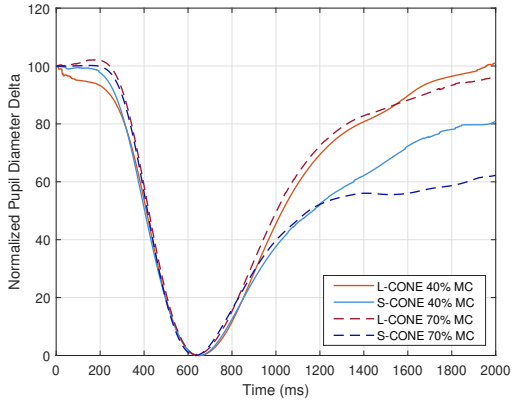


Figure 7.12: Normalized and averaged PLR response among the three subjects for 200 ms flash-driven response. Time t=0 ms corresponds to the beginning of the 200 ms flash.

Conclusions

In this study, preliminary tests were performed with a low-cost Maxwellian-View optical system for Silent Substitution where PLR and ERG signals have been simultaneously observed on human subjects. With the

Table 7.9: Average PLR waveforms values for 200 ms flashes at 40% and 70% Michelson Contrast

Cones Type	Constriction Delay (ms)	Peak Constriction Time (ms)	Constriction Time (ms)	Dilation Time Constant (ms)
L-CONEs 70% C_M	291	638	305	509
L-CONEs 40% C_M	260	652	379	500
S-CONEs 70% C_M	287	632	296	1035
S-CONEs 40% C_M	256	651	339	764

smaller field of view (20 degrees), the ERG amplitudes showed to be lower than that of a typical full-field stimulation. Nevertheless, the results are repeatable among different subjects and enable simultaneous measurement of the pupil function as well. As relevant from Figures 7.11,7.12 of Section 7.2.2, it is clear how ERG and PLR responses highlight different features of the human visual pathway as the most information from ERG is observable in the first 300 ms after delivering the flash while PLR dynamics provide useful knowledge regarding iris-muscle plant reaction and pupil recovery phase in the time range between 200-2000 ms. Overall, this approach proved to be a faster, less invasive, and more complete way of investigating and potentially detecting common optic-nervous system disorders. For future experiments, we are planning to start a measurement campaign of humans affected by mild traumatic brain injury diseases (mTBI).

Chapter 8

Vision-Based Image Classification

As we introduced in Section 4.1, *Visual-based* techniques refer to any strategy or methodology that analyzes, interprets, or assists non-expert users in making decisions by utilizing visual information. These approaches are frequently used in computer vision, machine learning, and image processing, and may be used in a variety of areas including medical imaging, security, surveillance, and autonomous systems.

Nowadays, a popular research field is the integration of vision-based solutions into the instrumentation and measuring industry [114]. Indeed, *Artificial Intelligence* (AI) applied to *Computer Vision* [115], in terms of *Machine Learning* (ML) [116], *Deep Learning* (DL) [117] and *Expert Systems* (ES) [118], can be effectively exploited to improve the performance of traditional instrumentation systems [119].

The use of digital cameras in ophthalmic imaging instruments has brought about significant advancements, particularly for the diagnosis and objective detection of various pathologies [127], thus making AI a popular tool in biomedical imaging, specifically in ocular data and ophthalmic image analysis [120–126]

In this Chapter entitled "Vision-Based Image Classification", three research works that exploit VB techniques to improve the accuracy and objectiveness of ophthalmic instrumentation are presented. In particular, this chapter presents the following research works:

- **Pupil Position Classification [310]**
- **Image Classification for ACA Objective Measure [311]**
- **Preliminary Experiment for Automatic Detection of the Van Herick Grade [312]**

8.1 Pupil Position Classification

The accuracy and the overall performances of ophthalmic instrumentation, where specific analysis of eye images is involved, can be negatively influenced by invalid or incorrect frames acquired during everyday measurements of unaware or non-collaborative human patients and non-technical operators. Therefore, in this Section, we investigate and compare the adoption of several vision-based classification algorithms belonging to different fields, *i.e.* Machine Learning, Deep Learning, and Expert Systems, in order to improve the performance of the ophthalmic instrument designed for the *Pupillary Light Reflex* measurement previously presented in Section 5.3.1. To test the implemented solutions, we collected and publicly released *PopEYE*, as one of the first datasets consisting of 15k eye images belonging to 22 different subjects acquired through the aforementioned specialized ophthalmic device. Finally, in Section 8.1.3 we discuss the experimental results in terms of classification accuracy of the eye status, as well as computational load analysis since the proposed solution is designed to be implemented in embedded boards, which have limited hardware resources in computational power and memory size.

8.1.1 PopEYE Dataset

The acquisition device used for collecting the images is briefly described in Sec. 8.1.1. More details about the acquisition setup have been discussed previously in Section 5.3.1. Moreover, the test methodology adopted and the technical procedure to acquire and manually annotate eye images are depicted in Section 8.1.1.

Acquisition Setup

The system used for this experiment is a *Maxwellian-view*-based monocular pupillometer [109] with a configurable BGRY LED-based light source and a board-level CMOS camera, used to acquire grayscale images of the human eye. As described in [65], the optical design of the instrument presents several advantages in the field of pupillometry. In particular, the two lenses stage allows precise control of the light stimulation level of the retina while avoiding the utilization of pupil dilation. The device schematic diagram is depicted in Figure 5.3; it consists of a double-lens optical system including four fiber-coupled high-brightness LED sources. Lens **L1** ($f_1 = 40mm$, $D_1 = 2.54cm$) together with a stop aperture has been used to collimate the light towards lens **L2** ($f_2 = 50mm$, $D_2 = 2.54cm$) that focuses the light beam to the eye's pupil plane, obtaining an output spot-size of $\approx 900\ \mu m$ diameter with a full-width viewing angle $\theta = 20.5°$. The proper functioning of the system, *i.e.* correct visualization of the stimulus by the subject, requires the eye to be precisely aligned to the center of the lens **L2**. Moreover, since the PLR is observed through the lens L2, an incorrect alignment of the eye, and therefore a shift between the center of the pupil with respect to the optical axis of the lens, would introduce spherical aberrations in the recorded image, which would modify the shape and size of the observed pupil, resulting to incorrect measurements.

The eye images are acquired thanks to the illumination performed by eight 850 nm infrared (IR) LEDs circularly arranged around lens **L2**, while a dichroic mirror [1] has been used to reflect the pupil image at $90°$ towards the compact high-resolution camera [2] equipped with a 10.1 mm f/2.8 lens [3], thus allowing to separate the *acquisition path* from the *stimulation path*, that is necessary for recording in-axis images of the eye. An infrared long-pass filter ($\lambda_{cutoff} = 750\ nm$) has been additionally used and positioned in front of the camera lens to filter out the visible light, making it possible to have fixed illumination of every frame even during different types of the ongoing light stimulation.
A desktop computer running a custom-developed program allows for capturing images up to 60 fps. The camera is hardware triggered by the micro-controller unit to synchronously acquire frames with light stimulation coming from the high-brightness LEDs. An interface designed with NI LabVIEW [313] allows the user to control and configure the type of stimulation and monitor in real-time the pupil response dynamics.

Acquisition Procedure

The pictures used for the investigation have been collected from both the left and right eyes of 22 subjects, 6 female and 16 male, with ages between 20 and 38 years old. The pupillometer is set to acquire continuous monochromatic 8-bit depth pictures at 50 Hz. The output frames recorded from the sensor[4] have been resized and stored as uncompressed video files with output resolution equal to 772×520 pixels (width and height, respectively).

During the acquisition, we asked the subjects to observe a circular light target of fixed light intensity, and under voice command to move the gaze in the four cardinal directions: right, down, left, and up.

[1] DMSP750B, Thorlabs © Newton, New Jersey, U.S.
[2] mvBlueFOX3-3M, Matrix Vision GmbH Oppenweiler, Germany GE
[3] Edmund Optics Inc. Barrington, NJ, USA
[4] SONY IMX178 6.4 Mpx CMOS

Moreover, we recorded the subject's natural eye blinks as well as a slowly controlled one, *i.e.* while asking them to close their eye completely and slowly open their lids. Thereafter, individual frames have been extracted from the saved video files with a temporal sub-sampling with a sample rate of 10 Hz, thus avoiding nearly equal frames from a visual point of view. Each frame has been manually labeled into one of the 6 different classes: "correct", "closed", "right", "down", "left" and "up". Sample images that illustrate each class are shown in Figure 8.1.

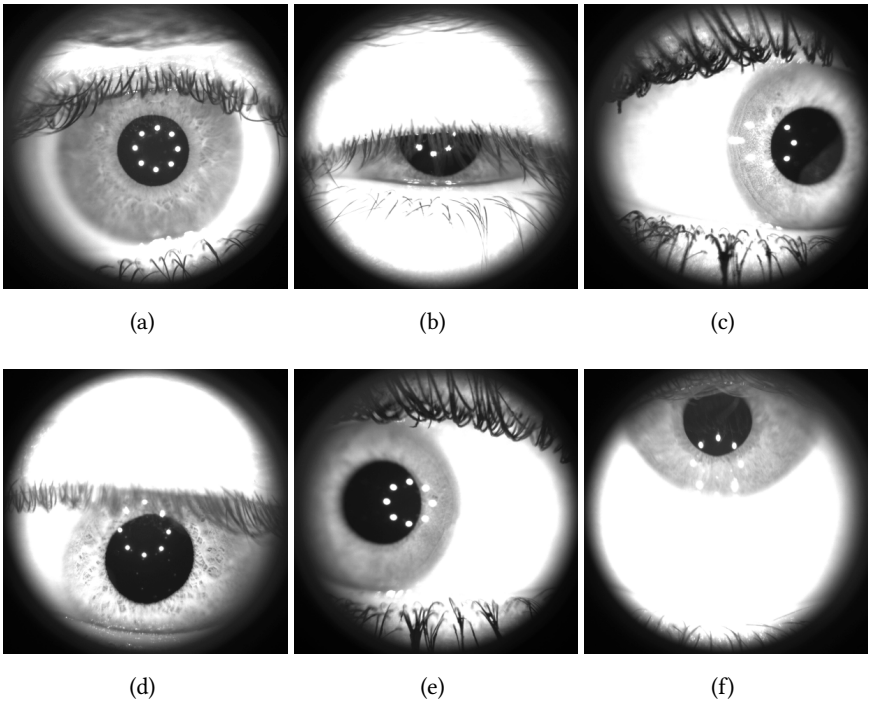


Figure 8.1: Example of images collected from different subjects of the *PopEYE* dataset. The images have been labeled in 6 different categories: a) correct b) closed c) right d) down e) left f) up. As shown, in images are well visible the pupil, the iris, the eyelashes, and, in certain cases, the eyelid.

As shown, every image contains the eyeball as seen through the lens **L2** (see Figure 5.3). The region outside the lens area is dark as it is not illuminated by the infrared LEDs. Manual classification has been carried out by the same operator, with the help of visual aids depicted on the acquired images. In particular, as shown in Figure 8.2, each frame has been cropped to a square-shaped image (520×520 pixels) and divided into 4 zones obtained by the two diagonals. Moreover, a circular area (with radius set to 69 pixels) has been added to define the *central region* to support the annotation phase. The size of the *central region* has been chosen specifically to avoid spherical aberrations of the pupil and non-uniform illumination of the retina by means of the light beam used for the stimulation. The ES algorithm described in Section 8.1.2, is used also during the annotation procedure to highlight, if possible, the position of the pupil (denoted with a blue bounding box in Figure 8.2) and its center (yellow point) to support the final labeling operation.

The operator, supported by the aforementioned fixed visual aids, evaluates the location of the center of the pupil and assigns one of the 6 labels as follows:

1. **Correct**: the center of the pupil is inside the central region (edge included) and pupil area is uncovered ($> 90\%$ is visible);

2. **Closed**: the center of the pupil is inside the central region (edge included) and the pupil area is covered by eyelids ($> 10\%$ covered) or the pupil center is outside the central region and covered by eyelids ($> 85\%$ covered) or pupil not visible or detectable by the operator;

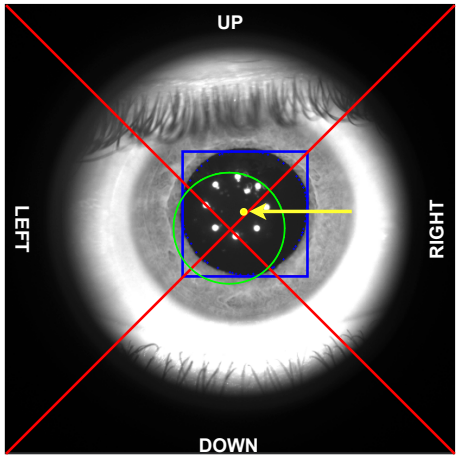


Figure 8.2: Visual aids used for the data annotation phase. The two diagonals in red define the four cardinal regions, named: *Up, Right, Down, or Left*. The green circle determines the *central region* for *"correct"* images. The ES algorithm (described in Section 8.1.2) finds and highlights the pupil bounding box (blue square) and the pupil center (yellow dot) whenever possible to support the human operator in the labeling process.

3. **Up, Right, Down or Left**: the center of the pupil is outside the central region, and the pupil area is visible or partially covered by eyelids ($> 15\%$ is visible); the final class depends on which triangle the center of the pupil falls;

For each frame, the ES algorithm automatically suggests the position of the pupil and then the label that should be assigned following the previous rules. The operator must manually confirm or change the proposed label and in the eventuality that the ES algorithm can't find the pupil or the detection is not accurate, the human operator must choose a label on its own based on the aforementioned rules. The obtained dataset, named *PopEYE*, constituted by a total of 14976 images, has been divided into classes as indicated in Table 8.1. The unbalanced data distribution represents a challenging element since it can negatively affect the training phase, especially for Machine and Deep Learning approaches [314].

Table 8.1: *PopEYE* dataset composition across the six different annotated classes.

Class	N° Images
Correct	8160
Closed	1790
Right	1336
Left	1296
Up	1379
Down	1015
TOTAL	**14976**

8.1.2 Vision-based Image Selection

In this section, we describe the vision-based algorithms used to tackle the image classification problem described in Section 8.1.1. Among others, we investigate methods belonging to Expert Systems (ES), Machine Learning (ML), and Deep Learning (DL).

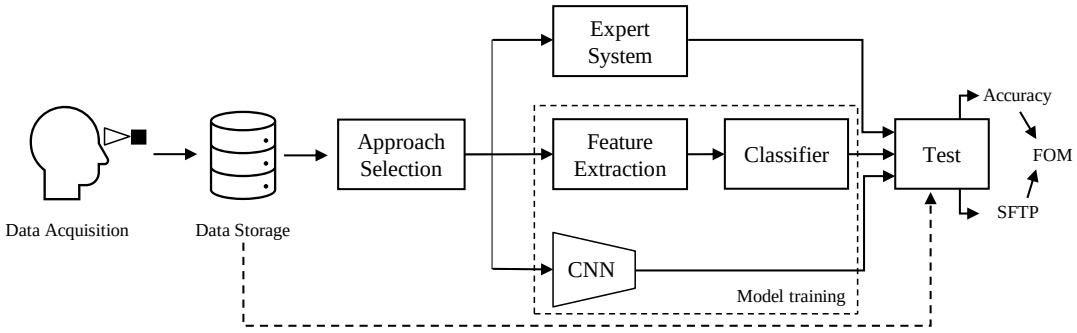


Figure 8.3: General overview of the proposed analysis. Data are acquired and stored using the device described in Section 8.1.1 and illustrated in Figure 5.3. Then, three different approaches based on Expert Systems, Machine, and Deep Learning fields, are trained and tested on that data, obtaining final accuracy and the SFPT with which is possible to compute the FOM metric (see Section 8.1.3).

Expert Systems

The large availability of open source packages, such as the *Open Source Computer Vision Library* (OpenCV[5]) or the *Python Imaging Library* (PIL[6]), offers many functions that simplify the work of solving a variety of Computer Vision and Image Processing tasks.

In our case, we aim to code an algorithm based on expert and a-priori knowledge to make the final classification, then through an approach commonly referred as "Expert System". Specifically, the proposed method is able to automatically detect, through several sequential image processing operations, the eye's pupil and its position respectively to the center of the lens **L2**, *i.e.* the optical axis of the system (see Figure 5.3). In the following, we list and analyze the steps of the proposed algorithm, graphically summarized also in Figure 8.4 to improve understanding and clarity.

1. The original gray-scale 772×520 pixels frame is cropped to a square image of 520×520 pixels, in which the large part of the black borders is removed. The crop coordinates are fixed since the black borders on the image are produced by the acquisition device and then are always in the same position.

2. In order to mask the $L2$ lens profile, as visible in the second image of Figure 8.4, a fixed threshold value set to 80 is applied. Then, if a pixel value is smaller than the threshold, it is set to 0, otherwise, it is set to a maximum value (255). Finally, the resulting image is normalized stretching minimum and maximum values to 0 and 255, respectively.

3. A filter with a *Gaussian* kernel with size 21×9 is applied to the image. The greater horizontal dimension for the kernel has been found empirically, and it is specifically used to enhance the blur on eyelashes which can possibly cover the dark pupil.

4. A second fixed threshold has been used to further remove unwanted brighter parts of the image. The threshold is chosen between the value 70 and the 5-th percentile of the gray level image. Then, the normalization applied in the second step is used a second time, stretching minimum and maximum values to 0 and 255, respectively.

5. In the resulting image, an adaptive threshold operation is applied; the neighborhood area from which select the threshold value is set to 9×9 pixels;

[5] https://opencv.org/
[6] https://pillow.readthedocs.io/en/stable

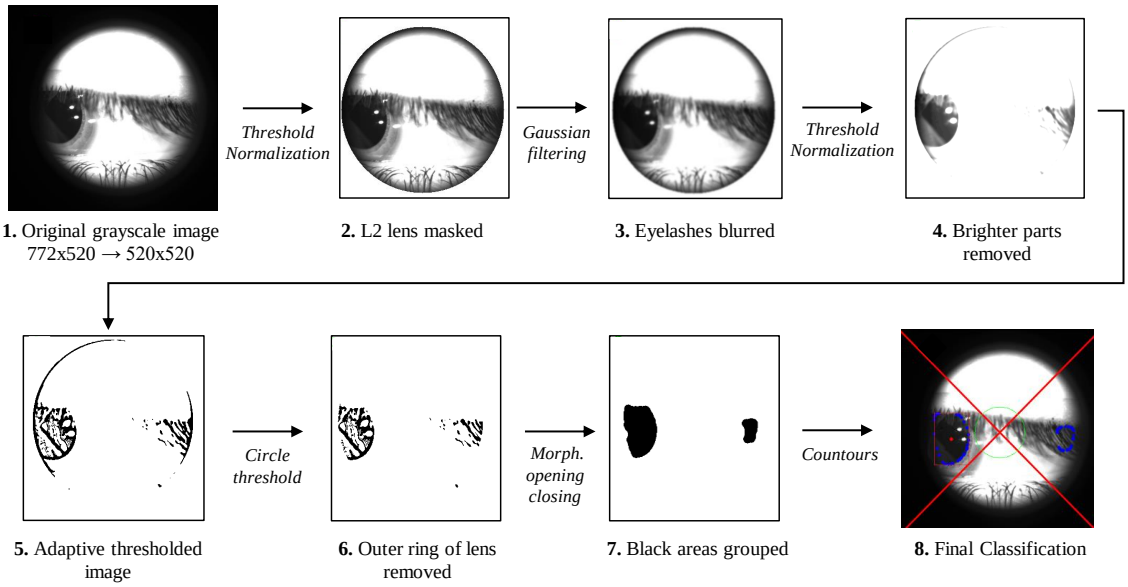


Figure 8.4: Flowchart of the image processing steps performed by the developed ES algorithm as detailed in Section 8.1.2. The final detection of the pupil is reported in the last image in which evaluating the *pupil center* (red dot) and the aspect ratio of the bounding box (red bounding box), the picture is labeled with the class "left" by the algorithm.

6. The outer ring of the detected lens edge is removed applying a threshold on pixels located at a certain distance from the image center. Also, in this case, the lens edges are in the same position, and then a fixed distance can be set.

7. The morphological opening and closing operations with an elliptical kernel with size 21×21 have been used to group small dark regions (at this point, the main dark area is the pupil, if present, and eyelash) of the image;

8. Lastly, we find the contours in the binary image. The contours found are subjected to a hull transformation and analyzed in terms of roundness, average brightness, and size. Specifically, the radius of the circumference inscribed in the bounding box computer for each contour must be in the range $[20, 150]$, and the average pixel value must be greater than 50. In this way, too-small and too-big contours and to-bright contours are discarded by the algorithm. Then, a numeric score is associated with the remaining contour, *i.e.* the most circular, darkest, and biggest contour is chosen as the best candidate. Finally, its center is used to determine the pupil's position.

It is worth underlying that all the previously hard-coded functions, thus including kernel sizes, threshold levels, and brightness or contour sizes have been empirically set for our specific test dataset. Any changes in the image's sizes, aspect ratio, exposure, or contrast will require a manual re-tuning of all these parameters.

Accordingly, to the rules outlined in Section 8.1.1, by evaluating the position and the aspect ratio of the pupil found by the algorithm, the predicted label is assigned to each frame automatically. If any pupil contours are found in the last step, the frame is labeled as *closed*.

Machine Learning

Within the *Machine Learning* field, we test a variety of classifiers in combination with two different handcrafted features applied on images, *i.e.* *Histogram of Oriented Gradient* [315] (HOG) and *Local Binary*

Patterns [316] (LBP).

Specifically, HOG features have been originally created for the task of *People Detection* [317], but they have been successfully used in a variety of different tasks [318] in the computer vision community. HOG encode the information of the edges' orientations into an image and then they can be useful in our classification task, since the visual appearance of the eye is strictly related to the position of edges. In our experiments, we produce the final HOG histogram with 8 orientations, computed on 4×4 pixels per cell and 1×1 cells per block.

Also, LBP features have been widely used in the literature and in the Computer Vision community, and in particular to have a powerful descriptor of microstructures (texture) present inside an image. For this reason, we believe that this hand-crafted feature can be effectively used in our classification task about the eye status, even though it has spatial support area and then the noise in the image can affect two single-pixel values [319]. In our experimental procedure, we empirically code the LBP feature setting the radius $R = 5$ and the number of samples points $P = 100$.

In our experimental investigation, we specifically focus on eight different classifiers, namely *Support Vector Machine* [320] (SVM), *Multi-Layer Perceptron* (MLP) [321] and *Random Forest* [322] (RF), *Decision Tree* [323], *Gaussian Naive Bayes* [324], *K-nearest neighbors* [325], *Adaptive Boosting* [326], and *Quadratic Discriminant Analysis* (QDA) [327] respectively. With these classifiers, we aim to investigate not only the final accuracy but also the computational load.

We use the SVM classifier with a *Radial Basis Function* (RBF) [328] kernel, the regularization parameter $C = 1.0$ and the kernel coefficient $\gamma = 10^{-3}$. For the MLP classifier, we adopt an architecture composed of 3 layers (1 input, 1 output, and 1 hidden layer with 100 neurons), *ReLU* [329] activation and the *Adam* [330] optimizer. With the RF ensemble classifier, we set the number of trees in the forest equal to 100, using the *Gini*'s index [331] to measure the quality of the obtained splits (used also with the Decision Tree classifier). With the Gaussian Naive Bayes, we set the smoothing value to e^{-9}, while we used the K-Nearest Neighbors with the number of neighbors equal to 3, and the weight function used in the prediction set to *uniform*. All these classifiers are tested with the aforementioned hand-crafted features in input, in addition to the case in which the input image is simply unrolled (for instance, an input image of 32×32 images is flattened in a vector of 1024 elements) and normalized by a factor of 255 (the maximum value of a given pixel), putting input data in a range of $[0, 1]$.

Deep Learning (CNN)

In the Deep Learning approach, we select and compare several different architectures of *Convolutional Neural Networks* (CNNs).

The first is *MobileNet* [332] architecture since it is a well-known architecture that combines an overall great accuracy on the reference dataset *ImageNet* [333] and a limited number of internal parameters ($4.3M$). This element leads to a limited computational load on the GPU on which the model is running and a reduced amount of training data. In our implementation, we set $\alpha = 1$, the delta multiplier to 1 and the dropout to 10^{-3} [334].

The second exploited CNN is *ResNet-50* [335], an architecture widely used for different classification and regression tasks, with good accuracy and a greater amount of parameters ($25.6M$). For similar reasons, we test also VGG neural network, one of the well-known object recognition models available in the literature. Specifically, we use the architecture with 16 layers, usually referred as VGG-16 model. Differently from *MobileNet*, these architectures can suffer from the limited availability of training data and are more complex from a computational point of view.

Among the other neural networks, we test *i.e.*, Inception-V3 [336] and EfficientNetB0 [337]. In the first case, we observe that the presence of multiple filters with different sizes at the same level can contrast

the overfitting phenomena [338], especially when a limited amount of training data are available. In the second case, EfficientNet proved to offer great accuracy in classification tasks, with an order of magnitude fewer parameters with respect to common CNNs.

In both cases, with respect to the original architecture, we change the last fully connected layer with a dense layer with 6 neurons, equal to the number of our dataset's classes. To fine-tune both neural networks, pre-trained on *ImageNet* [333], we exploit as optimizer the *Stochastic Gradient Descent* (SGD), with a learning rate equal to 10^{-3} and a momentum of 0.9. We exploit the Binary Cross Entropy (BCE) loss function, defined as follows:

$$BCE = -\frac{1}{N}\sum_{i=1}^{N} y_i \log(p(y_i)) + (1 - y_i)\log(1 - p(y_i)) \tag{8.1}$$

where y_i is the binary label of the i-th sample, N is the total number of data points and $p(y_i)$ is the predicted probability for a certain sample to belong to a specific class.

In our experiments, we exploit the *TensorFlow* [339] framework with *Keras* [340] wrapper implementations.

8.1.3 Results

In this Section, we present all the results obtained through the algorithms described in Section 8.1.2. All the approaches have been tested on the same test dataset constituted by 30% of the entire dataset, *i.e.* 750 images for each class. It is important to observe that the test dataset is balanced (simplifying the score evaluation and understanding), while the train dataset, used only with ML and DL (since ES does not require training data), is highly unbalanced and constituted as reported in Table 8.2.

Table 8.2: Train and test splitting used in *PopEYE* dataset for both ML and DL approaches.

Class	Train Images	Test Images
Correct	7410	750
Closed	1040	750
Right	586	750
Left	546	750
Up	629	750
Down	265	750
TOTAL	**10476**	**4500**

Moreover, as introduced before, one of our goals is to evaluate the computational cost of the proposed algorithms on different systems, thus investigating the eventuality of more portable and more efficient solutions. Therefore, we compared the *Single Frame Processing Time* (SFPT) among the systems described in Table 8.3. The SFPT consists of the sum of the elapsed time between the instant in which the frame is available in the RAM memory and the time instant in which the final classification is produced by the system. We observed that, in our scenario, the acquired frames are used in real-time and then the *load time*, intended as the elapsed time necessary for the system to load the frame from the local hard drive to the RAM, should be neglected. In all approaches described below, the SFPT measurement has been computed as the average on the entire *test dataset*, *i.e.* 750 frames per class for a total of 4500 images. In addition, we report also the 90th percentile of the SFPT time, in order to highlight the impact of higher prediction times due to variable loads that can affect the performance of tested systems.

Table 8.3: Hardware specification of the devices used to compute the SFPT across all experiments.

Device	Processor			Ram	GPU
	Name	N° Cores	Max Frequency		
Desktop	Intel i9-10850K	10	4.8 GHz	32 GB DDR4	NVIDIA RTX 3090
Laptop	Intel i7-7700HQ	4	3.6 GHz	32 GB DDR4	-
Raspberry 4	Cortex-A72 (ARM v8)	4	1.5 GHz	4 GB LPDDR4	-

Expert System Algorithm For the ES algorithm described in Section 8.1.2, experimental results are reported in Table 8.4.

As shown, the proposed algorithm is able to achieve over 90% accuracy using full-size input images. Unfortunately, we observe that the proposed algorithm relies on a series of values, thresholds, and hard-coded image processing procedures that strictly depend on the dataset and images acquired. These elements can limit the generalization capability of the developed algorithm, and negatively affect the speed performance, as listed in the second and third columns of Table 8.4.

Table 8.4: Accuracy and timing performance of the ES algorithm over the Desktop Computer

Input Size	Accuracy	SFPT (ms)	90th Percentile SFPT (ms)
520x520	90.2 %	10.472	11.904
260x260	89.9 %	2.160	2.480
130x130	87.8 %	1.410	1.488
65x65	82.1 %	1.564	1.984

Machine Learning-based Approaches Classification accuracy obtained with the best-performing Machine Learning-based methods in combination with different hand-crafted features is reported in Figure 8.5.

As shown, from a general point of view all the six classifiers, *i.e.* MLP, SVM, RF, Decision Tree, GaussianNB, and KN-neighbors obtain good accuracy, in the range of $[80\%, 100\%]$. The most interesting element to note here is the use of unrolled images as input, without the computation of any manual feature: in all cases, this (very) simple image feature representation is the best solution in terms of accuracy. As shown, the use of HOG feature produces better results with respect to LBP features, widely used to code the texture information in images (while HOG mainly encodes the shape). LBP feature in combination with SVM classifier achieves the worst accuracy. It is also important to note that the input size is only slightly related to the final accuracy: this is an important finding since, as reported in Fig. 8.6, large input sizes negatively affect the speed performance. Among the different ML classifiers, we also tested the Adaptive Boosting and Quadratic Discriminant Analysis classifiers. However, we have decided not to report the results relative to these two as they showed the worst performances in terms of accuracy $[< 80\%]$. In terms of speed performance, for all six classifiers and image resolutions, LBP features represent the worst scenario, followed by the HOG features. As expected, unrolled images in input have the lightest impact on the computational load since no particular operations are needed: this element, combined with the great accuracy highlighted in the previous analysis, promotes the use of MLP or SVM classifiers with unrolled images as input data as the best solution within the ML scenario.

Deep Learning-based Approaches Results obtained through a Deep Learning approach are reported in Table 8.5. As shown, almost all the tested Neural Networks achieve great accuracy even with a limited amount of training data: in this context, we observe that the use of pre-trained models is fundamental in

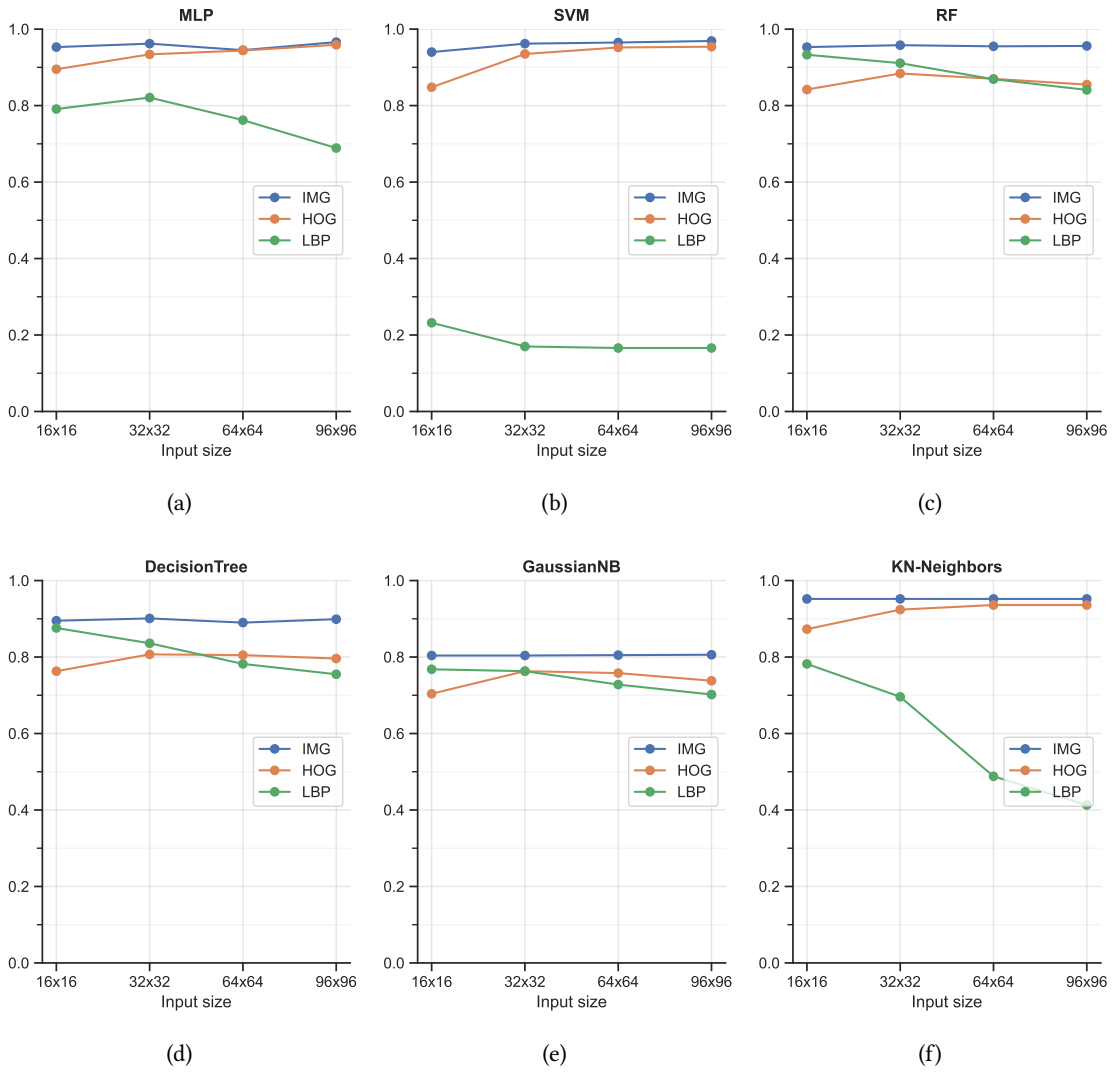


Figure 8.5: Classification accuracy of the three Machine Learning-based classifiers across different input sizes and input features: 8.5a shows the performance of the Multi-Layer Perceptron (MLP) classifier, while 8.5b shows Support Vector Machine (SVM) classifier, 8.5c Random Forest (RF), 8.5d shows Decision Tree classifier, 8.5e shows Gaussian Naive Bayes (GaussianNB) classifier, and 8.5f shows K-nearest neighbors (KN-neighbors) classifier.

order to obtain good accuracy. As was foreseeable, the approach based on deep neural networks achieves the best accuracy across all the other approaches: the ability to automatically learn features from images is a key element also in our classification task.

On the other hand, DL offers the worst speed performance, while the use of pre-trained networks forces the use of input images with 224×224 pixels resolution, and 299×299 for Inception V3. The best speed performance in terms of SFPT has been obtained with *MobileNet* (only 6 milliseconds of difference in respect to the best performing ResNet50 with the Desktop configuration as reported in Table 8.3), at the cost of a very minimal drop in terms of classification accuracy. It is interesting to notice how SFPT for different network architectures, scales accordingly to the number of parameters and images input sizes, while other factors may affect the time performances as well. It is worth underlying, that SFPTs have been calculated on the prediction of individual frames one at a time, as that's what would happen in a real-case scenario. This approach significantly impacts the workload on the GPU, as the majority of the time is

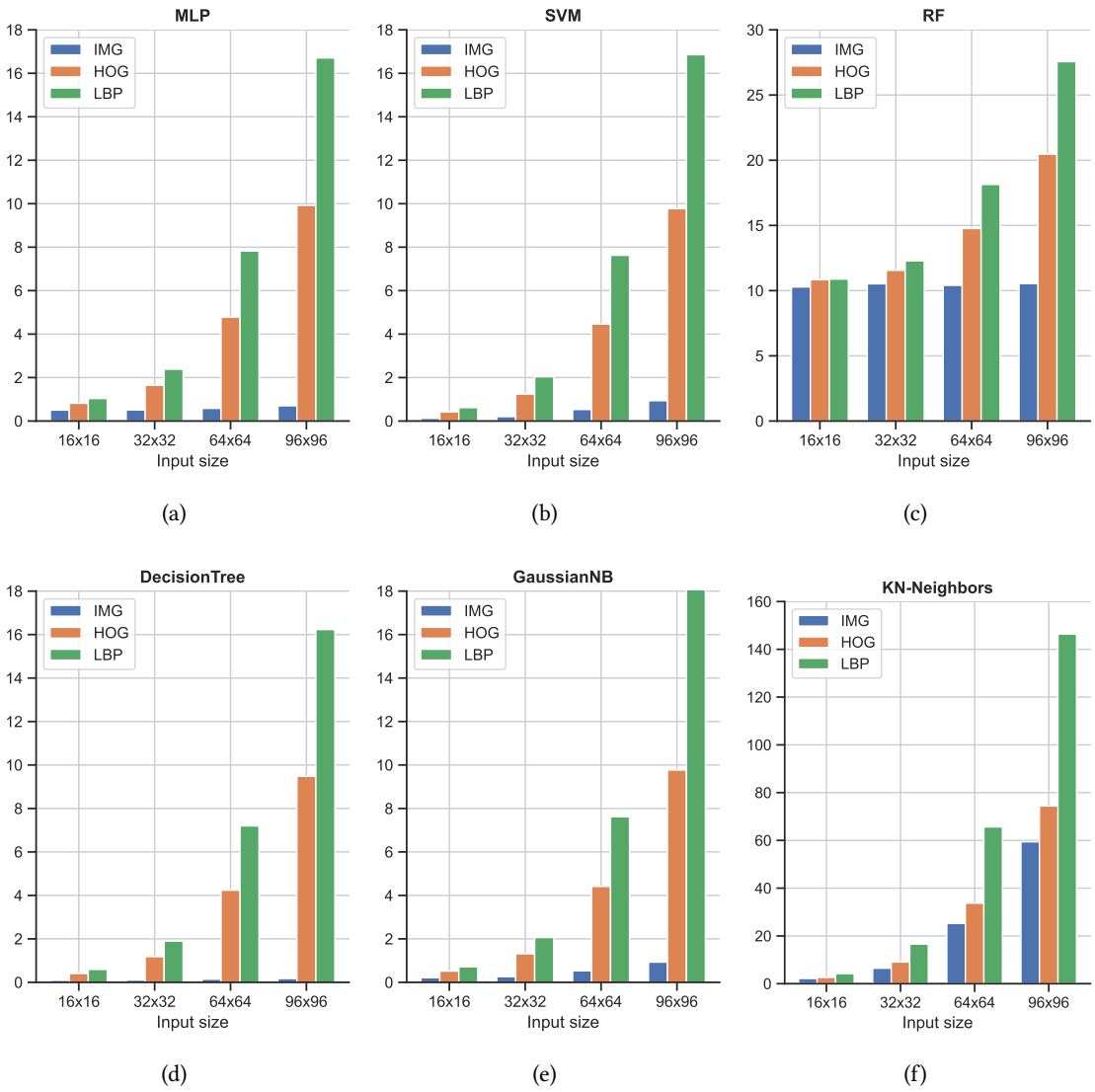


Figure 8.6: Comparison of the average *Single Frame Processing Time* (SFPT) computed as time consumed for the features extraction process plus the prediction time, of the three Machine Learning-based classifiers running on a Desktop computer. 8.6a shows Multi-Later Perceptron (MLP) classifier times, 8.6b Support Vector Machine (SVM) classifier, 8.6c Random Forest (RF), 8.6d shows Decision Tree classifier, 8.6e shows Gaussian Naive Bayes (GaussianNB) classifiers, and 8.6f shows K-nearest neighbors (KN-neighbors) classifier. Time values are expressed in milliseconds (ms).

spent transferring individual frames from RAM memory to the dedicated graphics memory on the GPU.

Final Considerations Among all the classification algorithms tested, we have reported in Table 8.6 the best combination of classification accuracy and speed performance obtained through each proposed approach.

More precisely, to compare and select the best algorithms we used Equation 8.2 as a mathematical *Figure of Merit* (FOM):

$$FOM = A^2 \cdot e^{-\left(\frac{SFPT}{\tau}\right)^2} \tag{8.2}$$

Table 8.5: Accuracy and speed performance obtained with Neural Network classifiers. Experimental results can be considered also in relation to the size and number of parameters of each neural network.

Architecture	Size (MB)	Parameters	Input Size	Accuracy	SFPT (ms)	90th Percentile SFPT (ms)
MobileNet	16	4.3 M	224×224	99.82 %	29.790	30.752
ResNet50	98	25.6 M	224×224	99.88 %	35.978	36.704
VGG-16	528	138.4 M	224×224	98.80 %	31.473	32.240
Inception V3	92	23.9 M	299×299	98.14 %	42.149	43.133
EfficientNetB0	29	5.3 M	224×224	71.81%	38.447	38.689

Table 8.6: Classification accuracy and speed performance comparison across the three investigated approaches.

Approach	Input size	Classifier	Accuracy	90th Percentile SFPT (ms) - CPU	90th Percentile SFTP (ms) - GPU	FOM
ES	130x130	pre-defined inst.	87.8%	1.488	-	0.767
ML	32x32	SVM	96.2%	0.496	-	0.925
DL	224x224	MobileNet	99.8%	38.688	30.752	0.096

The equation gives the score value $FOM \in [0, 1]$, where $A \in [0, 1]$ is the accuracy, $SFPT$ is the *Single Frame Prediction Time* in seconds, and τ is a constant[7] used to balance the equation in order to get that $FOM = 0.5$ for a 0.8 accuracy and $SFPT = 10\ ms$, that we consider as the target minimum score. Indeed, target SFPT has been set to guarantee an output frame rate higher than 50 fps to match the standard of modern pupillometer devices [231, 232], thus taking into account the additional processing time that can be needed to extract the pupil diameter value from *correct* frames. For this reason, we designed the equation to penalize the processing time with an exponential decay as the algorithm is intended to be used in *real-time*. As a consequence, a score $FOM < 0.5$ would be obtained even with $A = 1$ if the SFPT is not small enough ($SFPT_{limit} \simeq 16.75\ ms$). Moreover, the accuracy *target* score, is set to 0.8 to limit, in the first place, the amount of wrongly discarded images to ($\frac{1}{5}$ or 20%), and secondly to match the minimum average score of algorithms with a similar task [205, 217, 341].In the equation, A is squared, such as any solutions, even with the lowest $SFPT$, will give a $FOM < 0.5$ if the algorithm accuracy is lower than ($A_{limit} = \sqrt{0.5}$). Figure 8.7 shows how the *FOM* from Eq. 8.2 varies for different values of *A* and *SFPT*.

From the figure is clear why the DL algorithm shows the lowest score, since while having the highest accuracy ($A = 99.8\%$) it is also the most computationally expensive one, making it not adequate for practical implementations. Results reported in Table 8.6, suggest the ML approach with SVM classifier and a 32×32 pixels input size image is the one showing the highest score, with an average SFPT of 0.202 milliseconds and an accuracy equal to 96.2% on the desktop computer.

Finally, to further investigate whether these approaches can be employed on less power-consuming and more portable systems, we compute the SFPT on the different systems, as detailed in Table 8.3. Figure 8.8 shows the average SFPT comparison among the three devices.

As expected, the SFPT average times for all the methods considered are higher for both the laptop and the *Raspberry* board when compared to the desktop computer. It is interesting to note that ML represents the best solution for speed performance, obtaining real-time on all three tested platforms, and in particular on the embedded board.

[7] $\tau = \frac{-10 \cdot 10^{-3}}{\sqrt{ln\left(\frac{0.5}{0.8^2}\right)}} \cong 0.02013\ \ s^{-1}$

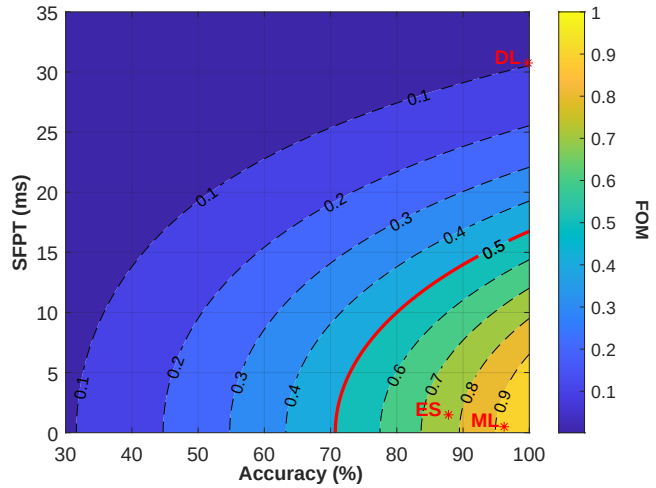


Figure 8.7: FOM heatmap for different values of A and SFPT. Red stars * indicates the score of selected approaches from each category.

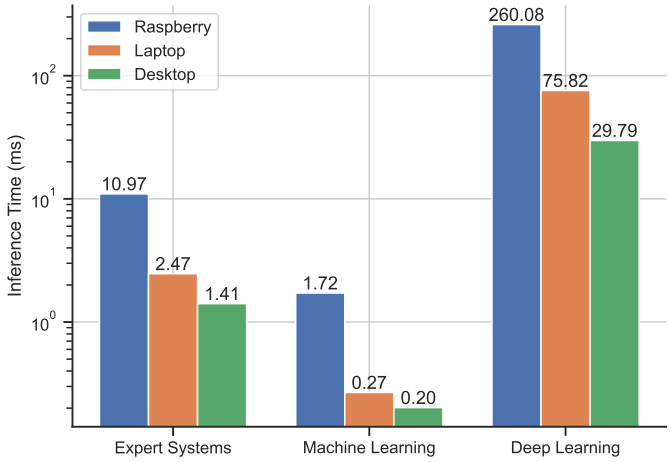


Figure 8.8: Timing performance comparison across the different platforms. Average SFTP for best solutions of ES, ML, and DL methods. Time values are expressed in milliseconds (ms).

8.1.4 Conclusion

In this first research, we have investigated the use of vision-based classification algorithms to improve the acquisition quality of a device used for the analysis of *Pupillary Light Reflex*, based on the acquisition of eye images. In particular, we have analyzed three different fields, *i.e.* Expert Systems, Machine Learning, and Deep Learning, aiming to train a classifier able to determine the status of the eye in input images. A new dataset, namely *PopEYE*, is presented and publicly released to test the investigated methods and to obtain the final results. Experimental results, in terms of classification accuracy and speed performance, reveal that the use of Machine Learning-based classifiers with unrolled images as input represents a simple, efficient and suitable solution, capable to achieve real-time performance even on the embedded board *Raspbery Pi*, with limited computational power.

8.2 Image Classification for ACA Objective Measure

8.2.1 Experimental Setup and Research Goals

The Van Herick procedure used to measure the ACA must be accomplished with specific alignment constraints [253]. It has been shown by Leung et al. [272] that both illumination and observation angles affect the ACA openness assessment. As a consequence, particular attention was paid during the realization of the optical setup for such an experimental evaluation. As presented in Section 6.2 the schematic diagram of the optical setup used to perform the Van Herick measurement is shown in Fig. 6.1. The instrument realized and presented [311, 342], composed of a Digital Light projector DLP and a digital CMOS camera, has been used to perform the VH maneuver (see Sec. 6.1) in a semi-automated fashion.

As previously mentioned, the Van Herick technique foresees the comparison of the depth of the peripheral anterior chamber with the thickness of the cornea. This measure can be derived when a narrow slit of light shines within the limbus, i.e. the edge between the cornea and the sclera. As a consequence, within the entire set of images acquired during the scan, only a few of these (referred to as *central* images) can be used to measure the ACA. Both previous and subsequent acquisitions, where the light is placed respectively on the left and on the right of the limbus, must be discarded. Indeed, since the patient eye position may change between different measurements, an a–priori image selection can not be performed. Consequently, a wider area must be scanned.

The outcome of a single measurement, that is, the dataset coming from the acquisition system consists of two scans of the entire eye, each one composed of 60 images with a $1600x1200$ px resolution. As an example, a set of images acquired during a scan is represented in Fig. 8.9.

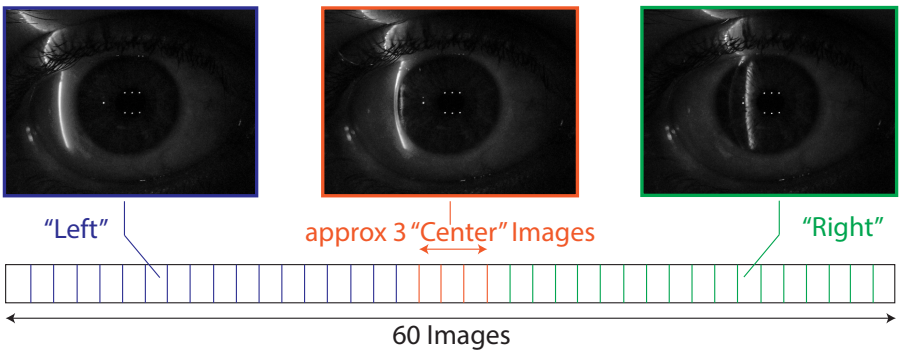


Figure 8.9: Example of a set of images acquired during a scan.

The approach we followed in this work is based on a Convolutional Neural Network (CNN), solving a three-class image classification problem. The CNN takes as inputs the images acquired by the setup and performs the classification activity by tagging the images as *left*, *central* or *right* respectively labeled with 0, 1, 2.

In the following, after a comparative analysis among different ML approaches, we identified the two CNNs that revealed most suitable to solve the classification problem. Both of them have been then specifically analyzed, through an objective approach presented in Sec. 8.2.4. As a last remark, as outlined in Section 6.1, to the best of our knowledge there are no other contributions in the literature addressing an automatic procedure to perform the Van Herick maneuver, whereas other works focus on the of ML techniques to process images acquired with the standard manual Van Herick technique. As a result, it is not possible to identify a literature baseline, with which to compare our approach.

For this reason, in this work, the behavior of the classification algorithm is evaluated by means of two different approaches:

1. We first used classical Machine Learning metrics, like accuracy, precision and recall to evaluate the network behavior and choose the best model. These tasks have been addressed in Sections 8.2.2 and 8.2.3.

2. Secondly, we have tested the developed network by means of a metrological evaluation strategy, described and presented in Section 8.2.4. It is worth observing that the test data used to carry out this last evaluation have not been used for the network training, nor for the accuracy, precision, and recall evaluations.

8.2.2 ML-based classification Technique

In the following, the Neural Network design is specifically addressed. At first, we choose the best ML techniques for the considered application, by a comparative approach. An investigation of the adopted CNNs is then proposed.

Typical metrics and ML Algorithm Comparison

Typically, a first evaluation of the network performance includes the analysis of the accuracy. This is simply calculated as the percentage of correctly labeled data (y_t) over the total observations ($y_t + y_f$):

$$accuracy(\%) = \frac{y_t}{y_t + y_f} \cdot 100. \tag{8.3}$$

Accuracy, however, becomes a not representative metric if the validation dataset is unbalanced. Among all the *central* predictions obtained by the network (Total Positive, TotP), a group of them (True Positive, TP) is well predicted while others are not (False Positive, FP). Moreover, it is possible that the network wrongly labels some *central* images as *right* or *left*, namely False Negative (FN). Given these definitions, precision and recall are defined as:

$$Recall(\%) = \frac{TP}{TP + FN} \cdot 100. \tag{8.4}$$

$$Precision(\%) = \frac{TP}{TP + FP} \cdot 100, \tag{8.5}$$

Recall indicates the network's ability to mark all the real *Central* images as *Central*. On the other hand, precision represents the network capability not to label *left* and *right* images as *central*. If the number of False Positives (i.e. left and right images marked as central) decreases, precision increases.

In general, it would be important to obtain high values of both recall and precision, but for the application considered in this work, precision is more important. Indeed, if some *left* or *right* images are wrongly interpreted as central, the measurement outcome taken from those images becomes intrinsically less accurate. Considering the aforementioned metrics, different ML techniques have been tested and evaluated to identify the most suitable one for the application at hand. As underlined in Section 6.1, image classification problems can be solved by exploiting CNN-based architectures. To this aim, several network structures have been trained, since the level of complexity of the given problem does not preclude the selection of any specific model, nor imposes an *a priori* choice of one model with respect to another. Therefore, we tested and compared the classification performance of the most commonly used CNN structures, as well as of a linear *Space Vector Machine* classifier (SVM) and of a *K-means* unsupervised classification algorithm.

In Table 8.7 the results of the performance comparison among the aforementioned techniques are reported. Namely, the performance of the different machine learning approaches over a *test data-set*, composed of 8677 non-augmented images, have been assessed in terms of validation accuracy (VAL-ACC), *center* class prediction recall (CTR-REC) and precision (CTR-PR), single frame prediction time (SFPD) and

the respective standard deviation over the whole test data set. It is worth observing that, the *test data-set* used for the comparison has not been used before during the training phase. Moreover, the total number of parameters of each CNN, regarding convolutional layers only, have been reported to give an idea of overall network complexity.

Table 8.7: Classification Method Comparison

Method	VAL-ACC	*CTR-PR*	*CTR-REC*	SFPD (ms)	σ SFPD (ms)	Parameters
AlexNet	98.82 %	86.04 %	86.04 %	29.98	3.43	6088768
VGG16	99.02 %	88.44 %	87.18 %	33.42	3.53	14713536
ResNet50	98.29 %	79.56 %	82.05 %	39.94	6.28	23581440
SVM	92.90 %	26.92 %	7.98 %	0.39	0.21	-
K-means	59.31 %	3.73 %	12.82 %	0.71	0.25	-

Among the different ML techniques, CNN's show superior performance in terms of accuracy if compared to both the linear SVM classifier and the unsupervised *k*-means approaches. It is worth noting that the SVM accuracy is quite high while the prediction of *center* images is not equally acceptable. Indeed, the linear classifier can correctly predict most of the *left* or *right* images, while confusing the central images. The same can be said for the k-means ML algorithm, but with even worst performances: In this case, the unsupervised method failed to recognize a common pattern among the presented training images, hence resulting in significantly lower performance in the validation phase.

From Table 8.7, AlexNet and VGG16 [343] are the networks providing the best performance in terms of precision and recall, and in general with respect to all the parameters. As a general consideration, the medical operator needs to review the images classified as 'central' just after the procedure, possibly repeating the measurement if the acquisition was not successful. Besides the accuracy of the classification, also the overall time taken by CNN to label all the acquired images is an important performance index. From Table 8.7 Alexnet revealed a lower complexity in terms of total parameters (last column of Table 8.7) and showed to be slightly faster than VGG16, which is however able to provide better values of precision and recall. For these reasons, both will be considered in the following analysis, and as potential candidates for implementation within the proposed VBM.

Convolutional Neural Network Design

As described in the previous section, both AlexNet [268] and VGG-16 [343] structures can be finally chosen for this application. Different Alexnet and VGG-16 settings have been tested during an extensive experimental campaign, where a trial and error methodology has been adopted. In particular, several typical parameters, such as precision and recall, have been used to optimize the training activity. Afterward, the best training configuration for our application has been chosen and it is presented in this section. Moreover, as the adopted method is a supervised ML technique, we took particular care of the labeling process. The collected images have been carefully divided into three classes, by exploiting the guidelines of expert ophthalmologists. *Relu* has been adopted, both for AlexNet and VGG-16, as it is a commonly used activation function [344], that is in charge to manage the Input-Output behavior of neurons. Moreover, in this situation, it achieves excellent performance and demonstrated to learn faster. AlexNet structure, as typical CNNs, is formed by both Convolutional and Pooling layers, where the latter are placed between each convolutional layer and the subsequent one. Specific image patterns are identified by means of a Kernel slicing on the entire layer. Afterward, a common practice consists in the usage of a pooling layer, that downsamples the input patterns, aiming to increase the robustness of the network to slight variations of the detected features. The extraction of such meaningful features is done taking the maximum from each

kernel acquisition, namely *max pooling*. Finally, the last fully connected layers and the *softmax activation* compute the probability of each image belonging to each of the 3 classes. A slight modification has been made with respect to the typical AlexNet structure: we used a bilinear interpolation algorithm to obtain resized $400x300$ px input images. It is worth noting that downsized images are used only for classification purposes, while the ACA measurement will be performed with native-resolution ones. Indeed, there are no network performance improvements when using the typical $227x227$ px AlexNet input size. Likely, an higher quality of the image is, for our purposes, more important than a fine-tuning of layers and kernel sizes. Fig. 8.10 shows the network structure we used.

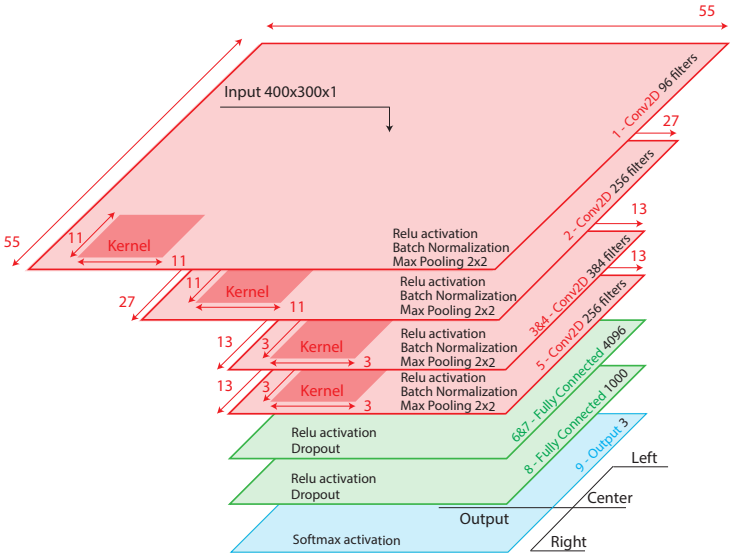


Figure 8.10: The implemented AlexNet structure.

As it is possible to see from Fig. 8.10, the dropout technique, which consists on the deactivation of some randomly chosen neurons, is used to reduce inter-dependency between fully connected layers, thus preventing overfitting. The Dropout Rate has been set to 50%.

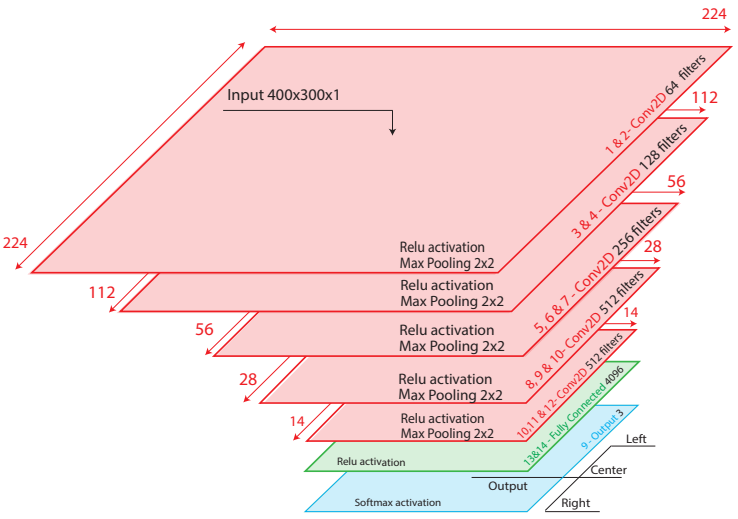


Figure 8.11: The implemented VGG-16 structure.

Analogously, Fig. 8.11 represents the VGG-16 architecture, which is basically formed by the same

components already discussed for the AlexNet one. Actually, the difference resides in the number and dimensions of the various layers.

Data preparation is a fundamental task to be done before the training stage. Hundreds of acquisitions were made and the data have been manually split into three classes to train the network. Data are normalized between 0 and 1, and then 70% of the total has been used to train the network, while the other portion is for validation purposes. One important feature of the available dataset is the low number of *central* images (i.e. those ones to be identified with the network), usually three or four out of 120 images acquired during the measurement procedure. To cover the hump, *data augmentation techniques* have been adopted. Data augmentation usually foresees the generation of modified training examples, applying different and pre-tuned image transformations, e.g. horizontal and vertical shifts, rotations, and brightness modification, only to name a few. This technique is typically used to generalize the behavior of the network, trying to generate new and meaningful examples targeted for the application. Instead, we used data augmentation also to generate more *central* images, this way giving the possibility to train the network with comparable amounts of *left*, *right*, and *central* images. The data augmentation technique has been applied to the already labeled images, to ensure that the augmented images are correctly labeled. In Table 8.8 are listed our data augmentation parameters.

Table 8.8: Data Augmentation Setup Parameters.

Horizontal Shift Range (% of the width)	$(-1\%, 1\%)$
Vertical Shift Range (% of the height)	$(-1\%, 1\%)$
Rotation Range (deg)	$(-7, 7)$
Brightness Multiplication Factor Range	$(0.5 - 1.75)$
Zoom Range (% of the picture size)	$(90\% - 110\%)$

Indeed, with little movements to the right and to the left, rotations and zooms may occur. Furthermore, different brightness levels could take place in different surrounding environments. It is worth observing that we generated more central images than the other two classes, aiming to increase the precision of the classification of the *central* images. After the data preparation stage, the prepared data set had the properties listed in Table 8.9

Table 8.9: Train Data Set Properties.

	Original	Original Training	Augmented	Total Training
Left	8537	5976	5711	11637
Central	593	416	14994	15410
Right	7877	5513	5471	10984

In Table 8.9, as said before, the original images have been split into validation and training data, respectively the 30% and 70% of the total. Afterward, only the training images have been augmented.

8.2.3 Neural Network Evaluation

The CNN *AlexNet* and *VGG-16* described in Section 8.2.2 have been implemented in Python, within the *Keras* (Tensorflow Version 2.1.0) framework and trained according to the set–up described in Table 8.10. Clearly, as the hyper-parameters have been chosen after a trial-and-error stage, the final settings can be slightly different for each CNN.

Table 8.10: CNN training settings.

	AlexNet	**VGG-16**
Optimizer	SGD	Adam
Learning Rate (LR)	10^{-2}	$2 \cdot 10^{-4}$
Epochs	75	150
Batch Number (BN)	128	332
Loss Function	SCC	SCC
Validation Data (% of original images)	30	30

At each training stage, the error gradient was calculated through the Stochastic Gradient Descent (SGD) algorithm for Alexnet, and by exploiting the Adam optimizer [345] for the VGG-16 approach. By controlling the error gradient the optimizer updated the weights so that the error decreased step by step. The next weights choice was done by evaluating the *error cost*, through a specific loss function. Given the training settings of Table 8.10, considering the n–th observation was labeled as a specific class c with probability $p_{n,c}$ and N was the total number of observations, the Sparse Categorical Crossentropy (SCC) loss function was expressed as:

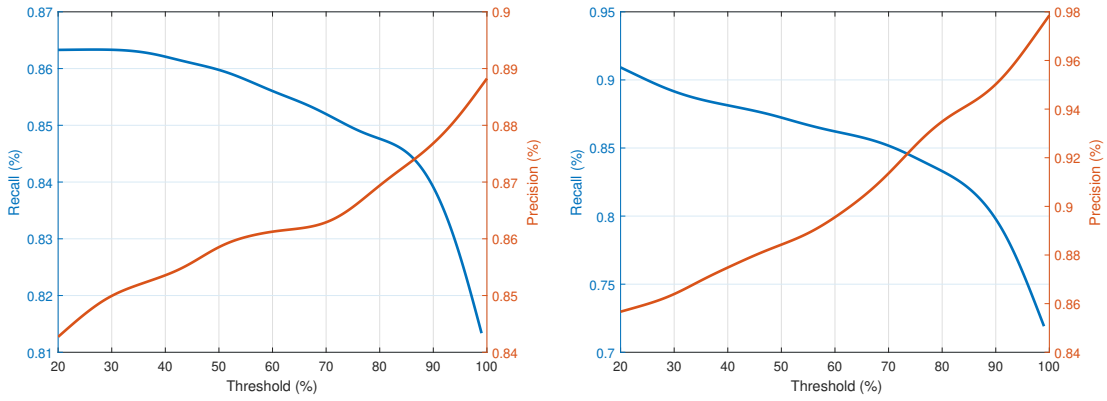
$$Loss(p_{n,c}) = -\frac{1}{N}\sum_{n=1}^{N}[log(p_{n,c})]. \tag{8.6}$$

In this context, the Learning Rate (LR), which represents how quickly the network learns, was surely a key parameter, that has been chosen after several experimental tests. Weights were updated at each step proportionally to the LR and to the calculated error. Both training and validation data have been divided into BN chunks that were individually loaded in memory to increase computational efficiency.

It is worth noting that in our test case the train dataset was used several times to feed the network, 75 and 150 Epochs for AlexNet and VGG-16, respectively. The training has been stopped when the loss and accuracy did not improve for several consecutive epochs, to avoid overfitting. Results are encouraging since it is possible to achieve high accuracy values, already presented in Table 8.7. Despite this, a more accurate analysis is needed, and a deeper evaluation is now conducted by means of different metrics. Indeed, the objective of the network is to identify images belonging to the *center* class, that has very low validation examples. For this reason, high accuracy values can be obtained also if the *central* class is not well predicted. Moreover, there is an impact of the threshold value on the precision. The threshold is defined as the probability level above which an observation is labeled as *center*. The resulting recall and precision curves obtained are shown in Fig. 8.12a and Fig. 8.12b for AlexNet and VGG-16, respectively.

An evident effect is that, as the threshold increases, recall decreases with increasing precision. Indeed, a threshold increase reflects on a lower number of total positives, i.e. $TotP = TP + FP$. The growth of the precision is a clear indication that the total positive decrease goes together with a decrease in false positives that mostly become true negatives. The recall decrease is slighter than the precision increase. This allows choosing a high value of the threshold to increase the precision of the whole network. It is worth observing that all the reasoning is made on the global number of test sequences, but high values of the threshold may involve a small number of total positives for a single data–set. For this reason, in this work the chosen threshold is 89%, allowing to achieve a precision much greater than the 80% for both the CNNs.

The trained network can be finally used to predict *central* images on the newly acquired data set. The classification algorithm can be run in the described embedded system, with additional few seconds of execution that does not increase the acquisition time, as it is performed after the scans are completed. This



(a) (b)

Figure 8.12: Precision and Recall: (a) AlexNet and (b)VGG-16

is surely an important aspect to underline, as it is demonstrated that the patient's ability to look steady toward the fixation target, is time-limited.

8.2.4 Test results

The performance of the networks and the instrument were tested by exploiting the evaluation technique presented in Section 8.2.4. The images were collected in greyscale by extracting the red channel from the original images, to emphasize the light line. In distinction, the reference image was collected in RGB to simplify iris recognition. In the following, results obtained by two different datasets are presented: i) the preliminary results with the old dataset, presented in our first work [342], and ii) the clinical results obtained with the latest dataset, collected by expert ophthalmologists at IRCCS Fondazione G.B.Bietti [311]. For both datasets written informed consent was obtained from all patients via an agreement document.

The original dataset was acquired by the authors at OptoLab, Department of Engineering "Enzo Ferrari", UNIMORE, Modena, Italy. Six different subjects have been tested five times, for a total of 60 eye scans (i.e. 30 measurements). The number of *center* images chosen by the network ranged from 3 to 5 per each measurement. The total amount of analyzed images was 125. The six subjects on which the measurements were carried out were chosen with different colors of the iris to exclude this variable as a likely possible source of error in the validation phase.

The newly acquired dataset, instead, has been collected on a total of 36 different subjects by expert ophthalmologists in a clinical environment. As before, the number of *center* images chosen by the network ranged from 3 to 5 per each measurement. The total amount of analyzed central images was 140. In this work, the preliminary results have been compared with the new ones and an analysis of the influence of the iris pigmentation on the network's performances is presented. It is also worth observing that, in the following, all the histograms reporting the resulting error between the light line and limbus position have been derived by using the AlexNet network. Those related to the use of the VGG network have not been presented, as they are not informative and the comparison between the two networks has been conducted only by analyzing the mean and standard deviation values of the considered error.

Metrological Evaluation Technique

The goodness of the CNNs performance is evaluated, from a metrological point of view, through the study of the difference in pixels between the position of the limbus and the position of the light line on

the eye surface: the lower this difference the higher the CNN accuracy. This procedure has been divided into 4 steps: i) recognition of the iris from a reference image to have a reference for the intensity profile extraction; ii) extraction of the limbus position from a reference image captured at the first instant of the measurement procedure; iii) evaluation of the line position for every image labeled as *central*; iv) computation of the difference between these two positions. It is worth observing that all the procedure is conducted in a semi-automatic way, thus revealing to be not directly applicable to identifying the center images. Indeed, the aim is to build a totally automatic VBM system.

The extraction of the limbus position is performed by considering the limbus intensity profile, that can be fitted as an error function such as the one in Eq.(8.7), where A, B, C and D are fitting parameters that change for each reference image. Then, the maximum of the fit function derivative, Eq.(8.8), is computed to represent the limbus position, X_{limbus}.

$$f(x) = A + B\frac{2}{\sqrt{\pi}}\int_0^{D(x-C)} e^{-t^2}dt \tag{8.7}$$

$$f'(x) = D \cdot B\frac{2}{\sqrt{\pi}}e^{-D^2(x-C)^2} \tag{8.8}$$

Conversely, since the light line intensity profile can not be easily fitted by a standard distribution, the X_{line} position of the light line is estimated as in [346] [347]:

$$X_{line} = \frac{\sum_i I_i x_i}{\sum_i I_i}, \tag{8.9}$$

where x_i is the single–pixel x-coordinates, while I_i is the single pixel intensity. The error between the limbus position X_{limbus} and the line position X_{line} is finally computed as:

$$E = X_{limbus} - X_{line}. \tag{8.10}$$

The value of E can be positive or negative (i.e. left or right, respectively) based on the light line position with respect to the limbus on the images selected by the neural network.

The error E measurement is evaluated through a statistical analysis with a histogram of the error occurrences, observing its center of gravity and standard deviation.

Preliminary Results

In the following, the results obtained with the dataset collected in the OptoLab Laboratory are presented. A typical reference image, from which the limbus position X_{Limbus} is extracted, is depicted in Fig. 8.13(a). In particular, a reference image is collected for each measurement. Furthermore, in Fig. 8.13(b) the limbus intensity profile, extracted in correspondence to the eye center y-coordinate, is plotted along with its fitting as an error function (orange solid line) and its derivative (light green solid line). The maximum of the derivative represents the limbus position. In Fig. 8.14 a typical *center* image used to extract light line position is shown. After retrieving the position of the Limbus X_{Limbus} and of the light line X_{Line}, exploiting Eq.8.10 the displacement E is computed.

In Fig. 8.15, the histogram of the error E occurrences, for the AlexNet network, is shown. As it is possible to see, the histogram has a Gaussian-like behavior with parameters: $\mu = 5.99$ px and $\sigma = 5.92$ px. By exploiting the same technique with the VGG-16 approach, it is possible to derive $\mu = 6.27$ px and $\sigma = 6.3$ px. Actually, VGG-16 results in a higher error and standard deviation. Despite this, as the values are greatly lower than the light line thickness, both networks can not perform better, and both errors are totally negligible.

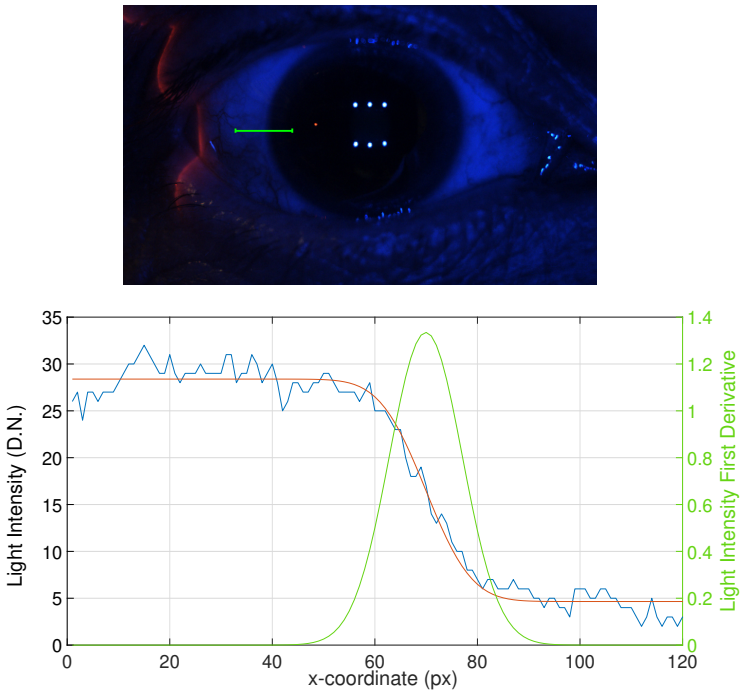


Figure 8.13: Typical reference image used to estimate the limbus position (a); the corresponding intensity profile along the y-coordinate of the eye center (•) (green line in (a)), the fitting error function (•) and, its derivative (•) (b).

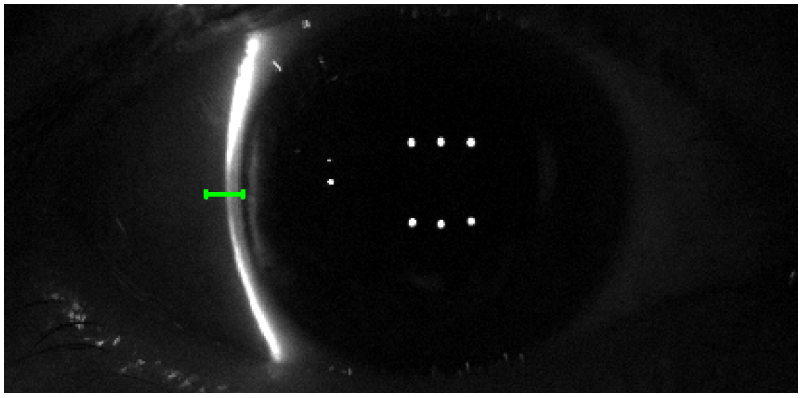


Figure 8.14: Typical *center* image used to estimate the light line position; The intensity profile of the line is extracted along the y-coordinate of the eye center (green line).

Clinical Results

To evaluate the influence of different iris pigmentation on network capability to extract *center* images, a new dataset has been collected on a total of 36 volunteers by specialized ophthalmologists. It is worth noting that, for each volunteer, a different number of measurements have been performed, as to monitor the progression of the glaucoma several measures are needed. The dataset includes eyes of four different colors: brown, blue, black, and green. The exploitation of this novel dataset, acquired by professionals, is surely of fundamental importance to analyze the accuracy of the whole system. The number of measurements comprised in this new dataset for each color is presented in Tab. 8.11. It is worth observing that, for each measurement, the number of *central* images can be different, so that the analysis was conducted by using 35 images for each iris pigmentation. More precisely, the balanced dataset has been obtained by

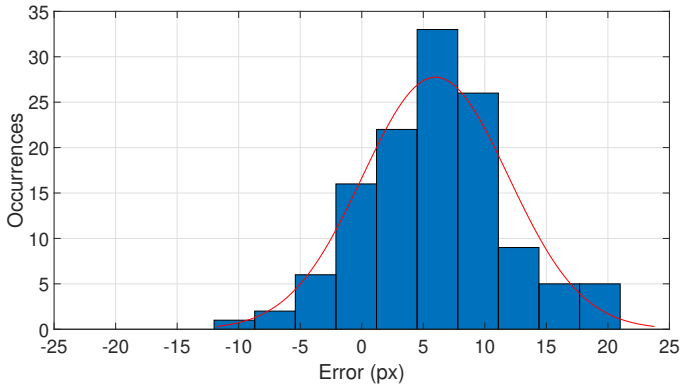


Figure 8.15: Histogram of occurrences of the error between the limbus and line position in pixel considering the preliminary dataset with the AlexNet network. The (•) line represents the Gaussian fitting of the histogram.

randomly removing a few images for some eye colors.

Table 8.11: New dataset properties.

Color	Number of Measurements
Black	14
Brown	13
Green	11
Blue	12

As before, the error between the limbus and the line position, in pixel, is evaluated. The error distribution histogram of the complete dataset, as well as the Gaussian line-fit, is depicted in Fig. 8.16, considering the AlexNet network. The mean experimental error is $\mu = 4.12$ with standard deviation $\sigma = 5.67$, as also summarized in Tab. 8.12, where a comparison with the VGG-16 network has been conducted.

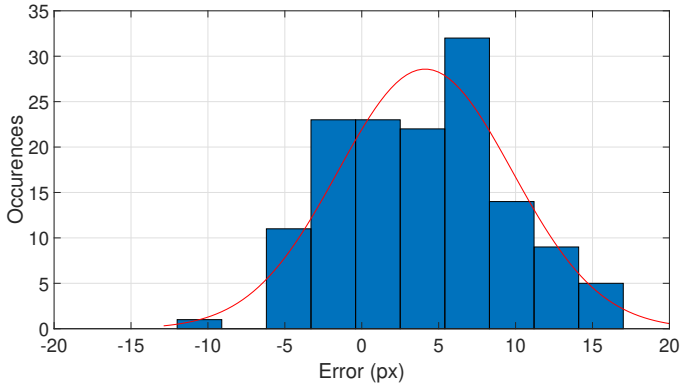


Figure 8.16: Histogram of occurrences of the error between the limbus and line position in pixel for the new dataset, exploiting the AlexNet network. The (•) line represents the Gaussian fitting of the histogram.

By comparing the results obtained from the two datasets, respectively of Fig. 8.15 and 8.16 it is possible to notice that both revealed similar standard deviations (slightly lower for the new dataset). This result is totally reasonable as the two datasets present similar number of statistical samples (slightly higher for

the new dataset). Moreover, it is possible to underline that in both situations the mean error is similar, but always positive. Indeed, we decided, by suitably labeling the training data, to instruct the network to choose central images which present the line slightly inside the iris, rather than slightly outside. Actually, when the line is somewhat inside the iris, it is still possible to see the refraction of the light, and derive the Van Herick grade. To evaluate the iris pigmentation influence the error distribution histogram for each color is extracted, as shown in Fig. 8.17, that refers to the AlexNet network. The same reasoning can be made referring to the results obtained with the VGG-16 network, presented in Tab. 8.12. Moreover, the VGG-16, as before, still results in a higher error and standard deviation. As said before, this comparison still depends on the specific hardware used (in particular the light line thickness) which makes substantially this error totally negligible.

According to Table 8.12, the best results have been obtained for black and brown eyes. Differently, green and blue eyes show a slightly higher mean error and standard deviations. This trend is reasonable since a red-colored light line is used.

Table 8.12: Mean and standard deviation of the error E between the limbus and the light line position for different iris pigmentation.

	AlexNet		VGG-16	
Color	μ (px)	σ (px)	μ (px)	σ (px)
Black	1.09	4.36	2.6	3.2
Brown	1.20	4.28	3.7	5.9
Green	6.69	5.19	6.2	5.6
Blue	7.51	5.48	7.2	6.2
Total	4.12	5.67	5.37	6.1

For this reason, the system acquires the red RGB channel from the images, to better highlight the line. This operation leads to different light line intensities, depending on the specific eye pigmentation. In Fig. 8.18 it is possible to observe the mean maximum line intensity per eye pigmentation.

The mean maximum intensity is retrieved by extracting ten contiguous horizontal line intensity profiles from ten different center images per color. The profiles have been extracted in correspondence with the eye y-center. As it is possible to see in Fig. 8.18 the brown eyes show the highest light line intensity, while the blue eyes present the lowest maximum intensity. The rationale of the aforementioned behavior is that brown eyes have a higher red component with respect to green and blue eyes. For this reason, brown eyes images are clearer, resulting in a lower mean error. Black iris represents an exception as it shows a lower mean maximum intensity while performing better in terms of mean error. In this case, the results are reasonable because black is a neutral color, thus its behavior does not depend on the specific RGB channel acquired. At the same time, black is the iris color that shows a better contrast with respect to the white color of the sclera, which probably leads to better light line recognition by the neural network.

8.2.5 Conclusions and Future Work

The use of Machine Learning techniques to extract measurement information from ophthalmic images is a very promising technique that can overcome some critical aspects of the manual Van Herick approach. After a research phase where different ML techniques have been tested, CNN networks proved to perform better in terms of precision and accuracy for our specific test case. Both Alexnet and VGG-16 structures proved to be suitable for the considered application. Indeed, AlexNet revealed to be less resource-demanding, providing slightly lower prediction times. Besides, VGG-16 is a little more accurate,

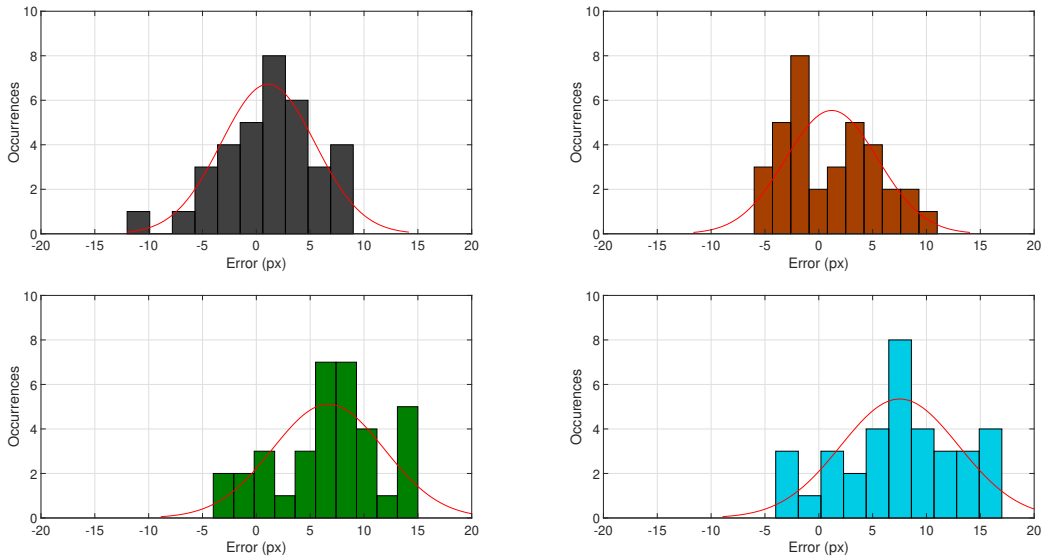


Figure 8.17: Histograms of occurrences of the error E between the limbus and the light line position for different eye pigmentation, were obtained with the AlexNet network. (a) black eyes, (b) brown eyes, (c) green eyes, and (d) blue eyes. In every Figure, the • line represents the Gaussian fitting for each histogram.

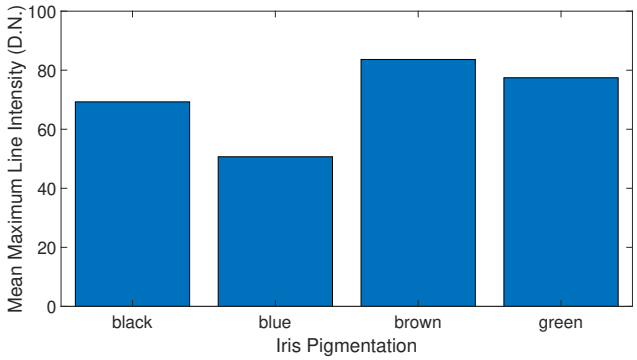


Figure 8.18: Histogram of the mean intensity of the light line for each different eye color.

and considering that due to the specific employed hardware and the fact that the analysis is made after the image collection phase, the proposed Neural Networks provide very good results in the *center* images choice while maintaining optimal computational complexity.

In this work, a new dataset has been collected by an expert ophthalmologist. This extensive measurement activity is of fundamental importance to, on the one hand, evaluate the neural network with realistic statistical samples. On the other hand, these measures have been taken in different environmental conditions with the respect to the training images. Moreover, the effect of different iris pigmentation has been observed. The presented results show low mean and standard deviation values of the error between the light line and the limbus positions. Moreover, also the maximum error observed during the experiment, i.e. $E \approx 18$ px, is visually comparable to the line width. Moreover, the trained CNN has proven to work as expected in different environmental conditions, in a realistic clinic field, and with eyes of different colors. More precisely, the detection of the line on darker irises, i.e. black and brown, reported a noticeably lower average μ error than eyes with lighter colors. For this reason, as a future improvement, the system will be automatically able to change the light line color, depending on the specific patient's iris pigmentation.

After the *center* images are identified, a Vision-Based algorithm is currently under development to measure the displacement between the slit light that hits the cornea and the refracted light inside the anterior chamber. A refined tuning of the Vision-Based system will be carried out, based on a comprehensive inter–subject experimental campaign. Moreover, the ongoing activity is aimed at a careful analysis of the measurement uncertainty.

8.3 Preliminary Experiment for Automatic Detection of the Van Herick Grade

8.3.1 Goals

As introduced in Section 4.3.2, the Van Herick technique is a widely used, qualitative method for determining the angle of the anterior chamber (ACA) in the eye. It can serve as an alternative to gonioscopy as a simple screening tool. In the previous Section studies 8.2, a Visual-Base approach has been presented to select valid images, acquired from the system presented (see. Sec. 6.2), that can be used to determine the Van Herick Grade (VHG). In order to fully automate the screening process, it is necessary to develop a method for automatically determining the VHG from the acquired images. In this experiment, it is presented the second stage for + the Anterior Chamber Angle classification, in which a deep-learning algorithm has been used to determine the VHG. More specifically, the algorithm has been tested using eye images from more than 80 patients, and the performance of three different convolutional neural networks (CNNs) have been compared.

According to this non-contact, qualitative approach (as explained in 4.3.2), the ACA width can be retrieved by comparing the Peripheral Anterior Chamber Thickness (ACD) and the thickness of the cornea (CT) [256, 348]. The width is then classified into 4 grades, i.e 1 for narrow-angle and 4 for wide-angle. The technique usually requires a slit lamp, enlightening the limbus with a 60° angle, and trained personnel to perform the maneuver. The estimation comes from the visual or digital image comparison between ACD and CT and so some uncertainty due to the operator and conditions of the maneuver (illumination, position, etc.) can be introduced [186]. Digital eye images can be analyzed according to two complementary possible approaches: i) image recognition algorithms extracting the ACD and CT measurements (i.e. Expert Systems [118]), and ii) Artificial Intelligence (AI) algorithms for the classification of the images according to the Van Herick grade (VHG). As introduced before, for this preliminary approach, only Deep Learning techniques, in particular CNNs, will be tested.

8.3.2 Methods

Eighty adult subjects, 30 males and 50 females, with ages ranging from 25 to 70 years were recruited from the *"IRCCS Fondazione G.B. Bietti per lo Studio e la Ricerca in Oftalmologia"*, and informed consent was obtained from each subject. The collected dataset has the characteristics described in Table 8.13.

Note that the subjects had also different eye pigmentation, thus allowing to train a network to be capable to generalize its functionality to a variety of eye colors. Standard Van Herick's technique was first applied to each patient's right eye by highly trained personnel and the corresponding VHG was assigned. This value was considered as the reference for the analysis of CNN's performance. Afterward, the subject was analyzed using our automatic instrument (see Sec. 6.2), and the images of the right eye generated were used for the training and verification of the CNNs. Since the instrument generated 2 to 4 images for each measurement, the total number of images considered for this study was 277; the distribution of these images in the four VHGs is shown in Table 8.14.

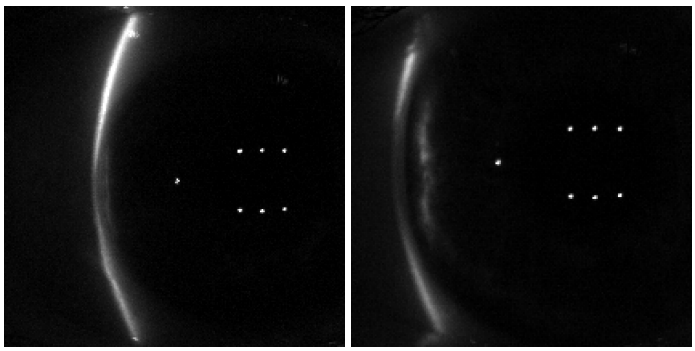
Charateristic		N° of Patients
Sex	Male	30
	Female	50
Age	<30	4
	30-50	48
	50-70	28
Eye Colour	Black	9
	Blue	15
	Brown	47
	Green	9

Table 8.13: Enrolled subjects data.

VHG	Eye Images
1	55
2	62
3	54
4	106

Table 8.14: Number of images collected for each VHG.

It is worth noting that, by remaining faithful to the real distribution of the VHGs in the population, no prior selection of the subjects were bede, thus resulting in a higher number of collected images associated with VHG = 4. As an example, in Figure 8.19 two typical images acquired by the instrument at the two extreme conditions, i.e. VHG = 1 and VHG = 4, are shown.



(a) (b)

Figure 8.19: Typical images acquired with the instrument. Figure (a) shows a typical VHG = 1 eye, in which the two line projections are quite closed, while Figure (b) shows a VHG = 4 with a wide distance between the two line projections.

Exploiting the Deep Network Designer tool of MATLAB, three different types of CNN were tested. Specifically, the tested networks were: i) AlexNet, already used for finding the most significant images in our previous work [342], ii) GoogLeNet, and iii) ResNet. All the CNNs were just pre-trained by the MATLAB tool. The validation of the networks was performed using the 40% images of the original dataset, while the remaining 60% images were augmented and used for the training of the network. Because the collected images were imbalanced towards the VHG = 4, data augmentation was performed just on the training images, thus obtaining a balanced final training dataset. Data augmentation was performed using

a Python algorithm that randomly shifted, rotated, zoomed, and changed the brightness of the original images. This operation was not performed using MATLAB, since the Deep Network Designer tool was not able to control the number of images of the augmented set. It is important to highlight that all the augmented images were used, with no post-processing and no manual selection, in order to obtain a more robust training of the networks. The final augmented dataset, used for both training and validation of the CNNs, is summarized in Table 8.15.

VHG	Training Images	Validation Images
1	4026	22
2	3996	25
3	3968	22
4	3969	43

Table 8.15: Dataset used for the training and validation of the network.

After training, the performances of the CNNs were compared in terms of the capability of correctly classifying an image according to its VHG class. The images classified by a network resulted in true-positive (TP), i.e. correctly classified, false-positive (FP), i.e. incorrectly classified in a class, and false-negative (FN), i.e. incorrectly not classified in a class. The performances of the networks were evaluated according to three metrics. Firstly, Accuracy, defined as in 8.11 for the entire dataset describes the capability of a network to correctly classify an image. Then, the Precision for a specific class C, defined as in 8.12, indicates the network capability to not label different class images to class C. Finally, Recall for a specific class C, defined as in 8.13 represents the network capability to not confuse class C images with other class images.

$$Accuracy(\%) = \frac{Correct}{Total} \cdot 100, \tag{8.11}$$

$$Precision_C(\%) = \frac{TP_C}{TP_C + FP_C} \cdot 100, \tag{8.12}$$

$$Recall_C(\%) = \frac{TP_C}{TP_C + FN_C} \cdot 100, \tag{8.13}$$

where subscript C identifies the specific VHG class.

8.3.3 Results

The results of the training of the GoogLeNet, ResNet, and AlexNet are shown, respectively, in Figures 8.20a, 8.20b, and 8.20c. In these images, the plot of the training accuracy, in blue, and the validation accuracy, in orange, are shown with respect to the number of software iterations performed to train the networks. As shown in the figure, the number of iterations is not equal for the different networks, since the training was performed until the validation accuracy stabilizes. From these plots, it is possible to observe that the ResNet network reaches a higher value of accuracy, both for training and validation. Since the training and validation accuracy grow together it is possible to exclude the possibility of overfitting. Moreover, AlexNet was the network that, depending on the *i*-th iterations, had the higher variability in accuracy; probably this result is due to the fact that this network had the simplest configuration among the tested network.

The performances of the networks were evaluated in terms of Recall and Precision by exploiting the Validation dataset. In Figures 8.21.(a), 8.21.(b) and 8.21.(c) the confusion matrix for each trained network is shown. The columns represent the reference VHG (Target) while the rows the predicted VHG (Output).

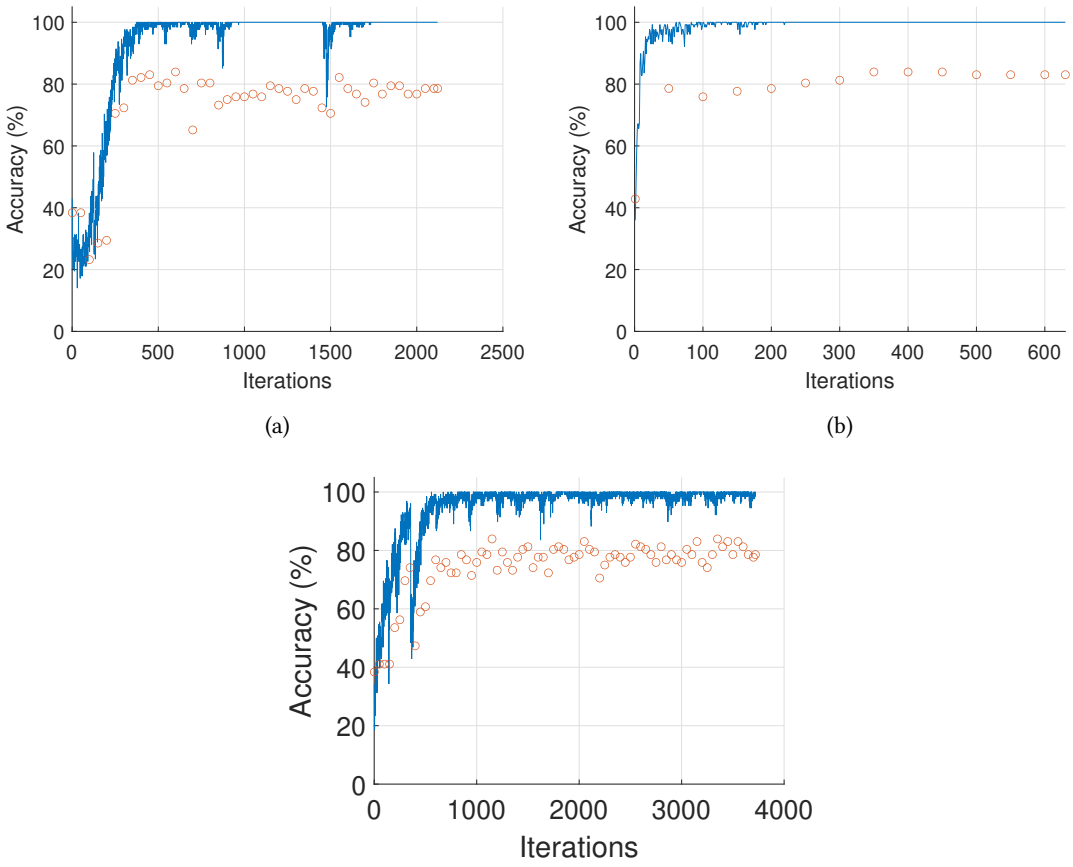


Figure 8.20: Accuracy plot of GoogLeNet (a), ResNet (b), and AlexNet (c). Training Accuracy (-) and Validation Accuracy (○)

The main diagonal represents the images that are correctly classified, while the other cells represent the images that are not correctly classified and the incorrect VHG estimated for them. The percentage in each cell is calculated with respect to the total validation image number. The last column represents the Precision, in green; the last row represents the Recall, in green. The bottom right cell shows the overall accuracy of the trained network.

8.3.4 Discussion and Conclusion

In this preliminary study, we have shown that CNNs can be used to estimate the Van Herick grade. The performances of all the tested networks are suitable for real-time estimation of Van Herick grade in portable screening instruments, without requiring a huge computational power.

All the networks have similar characteristics. The overall accuracy is in the order of 80% for each network, showing good accuracy even if the training dataset is still limited. Analyzing the obtained results, even if the networks work in a very similar way, it is possible to appreciate that ResNet has better behavior, but at the same time is the most complex network, with the highest computational cost in the training phase, among the CNNs that have been tested.

Recall results show that the probability of correctly classifying a VHG = 1 and VHG = 2 is higher than 85%. Differently, the Recall value for VHG = 4 is lower. This recall reduction could be due to the intrinsic difference in the positions of the light line projections among the images at different grades. In

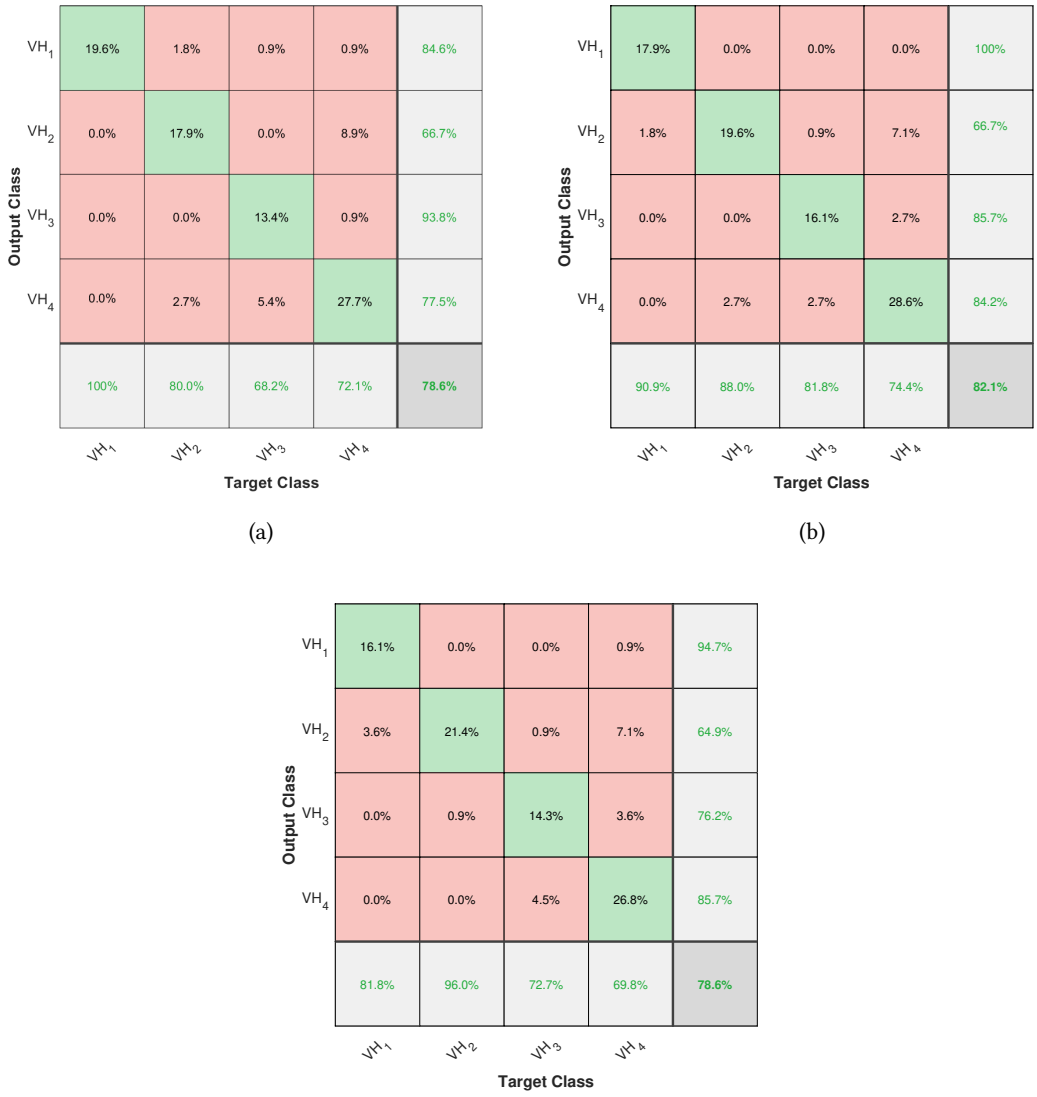


Figure 8.21: Confusion matrix for the GoogLeNet (a), ResNet (b), and AlexNet (c). The main diagonal, green cells, represents the correctly classify images. The light grey row shows the Recall data, in green. The light grey column shows the Precision data, in green. In the bottom right cell, there is the overall Accuracy data.

fact, considering the VHG = 4, a small misalignment of the light line with respect to the limbus position produces a large variety of the position of the projected line on the iris; thus VHG = 4 can be easily classified as a VHG = 3 or worst as VHG = 2. This phenomenon result also in a low value of Precision for VHG = 2, for all the tested networks, and VHG= 3, mostly for AlexNet. In fact, networks confuse VHG = 4 with the other grades increasing the number of images incorrectly classified as other grades. It is possible to observe that each network incorrectly classifies at least the 7% of VHG = 4 images as VHG = 2. Differently, for the other grades, these critical issues tend to be reduced, causing less confusion in the classification.

Much more work is still needed to develop a specific CNN for our automatic instrument. However, the

results obtained to date are encouraging and hopefully, they validation accuracy will improve by having a larger set of training images. In addition, it will be important to enhance the detection of the correct images for measurement in order to feed the VHG convolutional network with more accurate images and reduce miss-classification. Simultaneously, a deterministic approach capable of providing a measure of the distance between the projected light lines is currently under development. In this case, the effort is to reduce the computational load in order to make the algorithm implementable in a compact and portable system.

Conclusions

In this manuscript, the use of ad-hoc designed optoelectronic techniques for studying particular aspects of the human visual system and related common eye disorders has been examined. Overall, the research here discussed focused on the design, development, and characterization of the aforementioned devices, as well as their implementation for in-vivo and in-vitro experiments. The final goal was to propose some useful understanding regarding the realization of new methods that enhance the diagnostic capabilities of current ophthalmic instruments and make the prevention of common vision disorders more accessible.

Two main topics focus concerned the *Pupillary Light Reflex* measurement and the assessment of the *Anterior Chamber Angle* estimation for preventive detection of *Primary Angle Closure Glaucoma* using the Van Herick technique. Overall, some of the useful breakdowns of the investigated solutions and discussion on the presented results (see. Part III) are here summarized:

- A mathematical model for the iris oculomotor system has been tested on human subjects with short-light-flash-induced transient Pupillary Light Reflex (PLR). Overall, the proposed simulations show promising characteristics for describing the iris oculomotor system exposed to such stimuli;
- A simple and inexpensive design of a Maxwellian-View-based optical pupillometer that is capable of Silent Substitution has been described in this thesis. The preliminary tests on human volunteers with short-light-flash-induced stimulation on a single class of photoreceptors revealed that this approach to the Silent Substitution technique enables us to gain a comprehensive understanding of the contribution of ipRGCs to both image-forming and non-image-forming functions of the human visual system;
- By using the aforementioned pupillometer system as a light stimulator, PLR, and (*electroretinogram*) ERG signals have been simultaneously recorded on human subjects while silently stimulating specific photopigments; the results to 200 ms series of flashes showed to be repeatable across participants and allow for simultaneous evaluation of pupil reaction and photoreceptor's specific electrical response. From the results, it is clear how ERG and PLR responses highlight different aspects of the human visual pathway, as the majority of information from ERG is visible in the first 300 ms after delivering the flash, whereas PLR dynamics provide useful information about iris-muscle plant reaction and pupil recovery phase in the time range 200-2000 ms. Overall, this method demonstrated to be more efficient, and less invasive, as it does not require dilation due to the Maxwellian-View optics, and is a more complete way for studying and potentially detecting common optic-nervous system problems.
- The use of Visual-Based classification algorithms to enhance ophthalmic device's acquisition reliability has been also examined. Specifically, a classifier trained to identify the state of the eye in provided images, acquired with a pupillometer device has been investigated. Three different Artificial Intelligence domains, namely *Expert Systems*, *Machine Learning*, and *Deep Learning* have been examined. For this purpose, a new dataset, namely *PopEYE*, composed of over 15k images has been

collected to test the aforementioned classification methods as well as to obtain real case results on human subjects. Overall, the use of machine learning-based classifiers with unrolled images as input represents a simple, effective, and suitable solution, capable of achieving outstanding real-time performance even on embedded boards with limited computational power, also in terms of classification accuracy. The presented method reached accuracy scores higher than 96% for the detection of wrongly acquired images and an average single-frame prediction time of 0.27 ms on a standard laptop computer.

- As illustrated in Section 6.2 a new optical instrument has been presented for the objective and automated assessment of the Van Herick maneuver. Once more, machine learning methods have proven to be a very promising approach for overcoming some crucial drawbacks of the traditional Van Herick method, such as poor objectivity and the required trained medical personnel to perform the measurement. The tested deep-learning algorithms have been used for the classification of correct images for the evaluation of the anterior chamber angle. Following this, CNN networks showed to perform better in this particular test case in terms of precision and accuracy. The considered application turned out to be a good fit for both the *Alexnet* and *VGG-16* CNN's architectures. AlexNet did seem less resource-demanding, offering slightly slower prediction times on our tested machines. Besides, VGG-16 showed to be slightly more accurate with over 98% validation accuracy on the three-class classification task.
  Moreover, a collaboration with expert ophthalmologists allowed for the collection of a new dataset for this study. Moreover, a new dataset was collected by expert ophthalmologists. The extensive measurement activity proved to be crucial for evaluating the neural network with realistic statistical samples and for understanding the effect of different environmental conditions and iris pigmentation. In conclusion, a trained CNN has successfully been used in various conditions, including real-world clinical settings and on eyes of different colors. However, the detection of lines on darker irises, such as black and brown, had a lower average error than on lighter-colored eyes.

- In the first training campaign concerning automated ACA assessment we were able to accurately retrieve the correct images for the estimation of the Van Herick grade (VHG) starting from a collection of images acquired with an automatic scan of the eye. Lastly, we used the output of such an experiment to train another set of CNNs that aims to effectively estimate the Van Herick grade starting from images labeled by trained medical personnel. All tested networks achieved similar accuracy levels of around 80%, with ResNet performing the best, but also having the highest computational cost. Results show that the probability of correctly classifying a VHG = 1 and VHG = 2 is higher than 85%. However, the recall for VHG = 4 is lower, which may be due to the difficulty in correctly aligning the automated slit line with the limbus position in images at this grade. This could result in a mismatch in image classification, with at least 7% of VHG = 4 images being classified as VHG = 2.

Future Works

The realized systems have been characterized and tested for some many experiments on human individuals. The aforementioned results confirm the potential of the presented ophthalmic instruments. Despite these considerations, some future works have already been programmed and reported below:

Pupillometer device The simple, compact, and in-expensive Maxwellian-View-based monocular pupillometer showed to be a valid prototype for the Silent Substitution approach. Besides that, some improvements must be faced:

- The uniformity of the light beam can be further improved as at the current state, the utilization of the custom light combiner realized with 3D FDM techniques is not optimal and non-uniform distribution of the light over the visual field can be noticed by the patients during the experiments;
- The optical system's light efficiency and stability should be improved. The current system suffers from the low light intensity on some of the primaries, especially the yellow. Moreover, active feedback on the light control can be implemented to improve the color accuracy of delivered stimulations;
- The use of more primaries will benefit the maximum achievable contrast when the Silent Substitution technique is employed. Moreover, a more efficient and user-friendly optimization algorithm for the calculations of color pairs to achieve state of art silent stimulation should be further investigated;
- Besides a binocular version of the pupillometer device has been already investigated and presented in Sec. 5.3.2, some major changes in the design to improve the portability and effectiveness of the alignment should be carried out in the future. A binocular pupillometer will enable the investigation of more complex techniques for the preliminary detection of human visual system impairments;
- Concerning the simultaneous acquisition of ERGs and PLR silent responses, for future experiments a measurement campaign on humans affected by *mild traumatic brain injury diseases* (mTBI) will be carried out.

Visual-Based techniques for ACA objective assessment: The new system for the anterior chamber angle measurement with automatic execution of the traditional Van Herick maneuver proved to offer many potentials, especially by making this technique more objective and accessible. The following future works are still needed to fully access this goal:

- The adjustment of the line color based on the patient's iris pigmentation will improve the accuracy of detecting correct images for light-colored eyes. Moreover, a Vision-Based improved algorithm is also being developed to measure the displacement of slit light within the limbus of the eye, as well as a comprehensive study is being conducted to analyze overall measurement uncertainty;
- Further work is needed to develop a specific CNN and improve image detection for the final VH grading, thus increasing accuracy and reducing the misprediction of final grades. Additionally, a deterministic, or Expert-System based approach to perform the ACA measure in an objective and geometrical manner is also being developed. This approach will probably help to reduce the computational load and thus making the algorithm implementable with embedded and portable systems.
- Currently the system can only perform the measure on the right eye of the patients. A binocular version of the system is currently under development. In this way, the evaluation of VHG on both eyes could be performed at the same time, thus reducing measurement time and patient discomfort during the test.

Appendices

Output luminance - Measurement

In this section, the results of the characterization measurements concerning the LED's output luminance relative to the experiment explained in Section 7.1 are presented and discussed. In [285], this topic is already discussed; however, further investigations have been required in order to estimate in a rough but effective way the solid angle of the light beam that would be sensed by the human eye. Optical power datasets for the different LED rings were already available when this study has been performed. As explained in [113], optical power (or radiant flux) $[W]$ permits to assess of the physical property of light, such as the number of photons and their energy; however, the evaluation of the safety levels associated to a certain pupil stimulation condition is compulsory in the development of a prototype like the one that is described in this thesis. Safety levels can be characterized by means of luminance, a photometric quantity, that thus permits the characterization of the light perception of the human eye. Luminance can be expressed in terms of other photometric quantities:

$$L_v = \frac{\mathrm{d}^2\Phi_\mathrm{v}}{\mathrm{d}\Sigma\,\mathrm{d}\Omega_\Sigma\cos\theta_\Sigma} \tag{14}$$

Where:

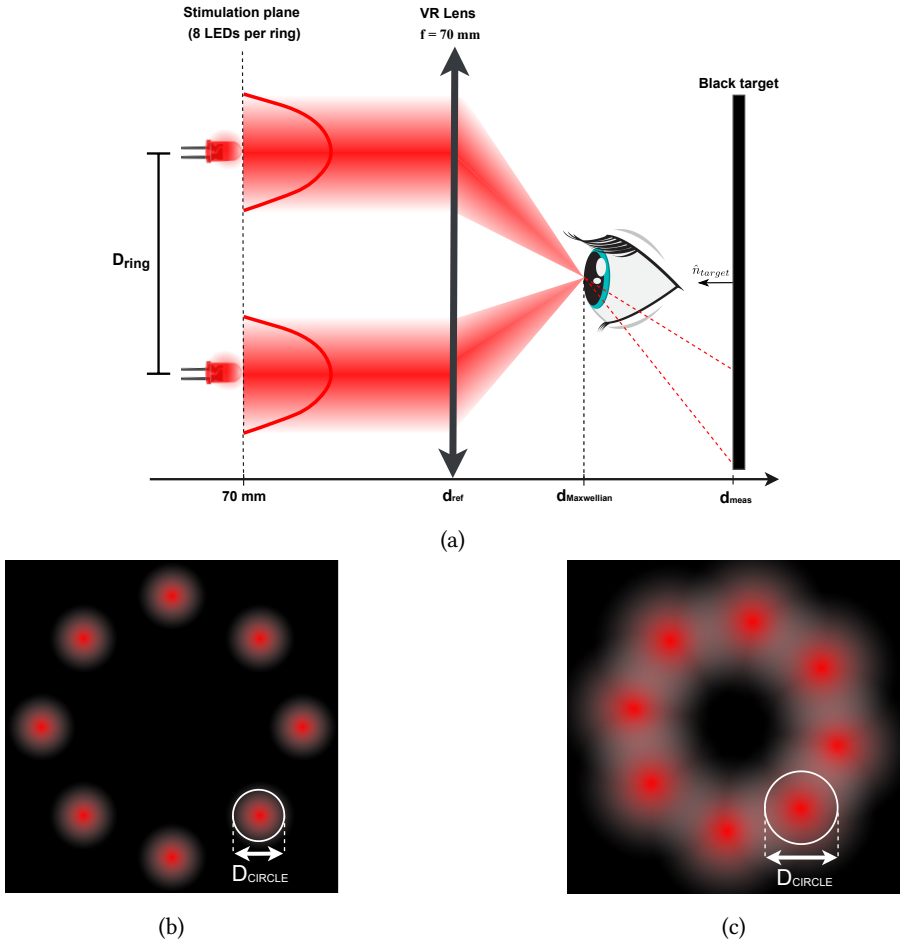
- L_v is the luminance, expressed in $[cd/m^2]$;
- $\mathrm{d}^2\Phi_\mathrm{v}$ is the luminous flux $[lm]$ that moves from the area $\mathrm{d}\Sigma$ in every direction contained inside the solid angle $\mathrm{d}\Omega_\Sigma$;
- $\mathrm{d}\Sigma$ is an infinitesimal source area portion $[m^2]$ that contains the specified point;
- $d\Omega_\Sigma$ is an infinitesimal solid angle $[sr]$ that contains the specified direction;
- θ_Σ is the angle $[deg]$ between the specified direction and the normal versor $\hat{n}_\Sigma$ to the surface $\mathrm{d}\Sigma$.

Assuming θ_Σ to be null, three physical quantities are thus required in order to compute the output luminance of the pupillometer light sources:

1. As said before, the optical power has been already measured using a power meter (Newport 1918R model, [349]) and an optical head (918d-uv-od3 model, [350]). Consecutively, power density $[W/m^2]$ datasets have been obtained.
2. The Photopic Luminous Efficacy at sources peak wavelength [lum/W] ([249]).
3. The light source solid angle $\Omega[sr]$.

Measurement setup

Figure 22 shows the conceptual scheme that has been realized in order to measure the light beam solid angle. The VR headset system exploits an optical module with two adjustable lenses in order to focus the LED sources toward the human pupil entrance, assuming a perfect Maxwellian condition. The Maxwellian view is a viewing geometry in which an image is focused on the observer human pupil ([351]). This condition is obviously dependent on the particular design implementation that is exploited when it comes to stimulation system building. In [352], it is explained that a typical Maxwellian system is composed of a converging lens that forms an image in the plane of the observer pupil entrance. If the eye is focused on the lens, the lens will appear as a disc filled with the light of uniform intensity.



(a)

(b)

(c)

Figure 22: Solid angle measurement setup: a) Conceptual schematic and b) light beams distribution.

Thus if the eye is properly positioned at a distance $d_{Maxwellian}$ from the optical module of the pupillometer, the uniform beam of light will converge at the pupil entrance and stimulate the retina. As it is described by *Figure 22*, a planar black target has been positioned at $N = 6$ different distances $\mid d_{meas,i} - d_{ref} \mid (i = 1, .., 6)$ with an angle between the light beam direction and the normal versor $\hat{n}_{target}$ to the target surface $\mathrm{d}\Sigma_{target}$ that can be approximated to be null to a first approximation. In fact, this measurement session has been performed using the first LED ring, which is needed to stimulate the central retina that has a visual angle of about $1°$ to $2°$. *Figure 22b* and *22c* show two conceptual representations of the light beams distribution over the black surface: each LED ring comprises 8 RGB sources, thus 8 colored circumferences are expected on the target surface, either separated or overlapped.

Solid angle estimation

At first, the consistency of the geometrical positioning of the target with respect to the reference plane (the VR lens plane) has been roughly proved to estimate the eccentricity of the light projection. After this first assessment, multiple measurements of the circumference diameter have been gathered in order to consequently estimate an average circumference area:

$$Area_{av,i} = \frac{\sum_{i=1}^{10} (\frac{\pi}{2} Diam_n)^2}{10} \tag{15}$$

The solid angle is thus mathematically defined as:

$$\Omega_i = \frac{Area_{av,i}}{\mid d_{meas,i} - d_{Maxwellian} \mid} \tag{16}$$

However the exact value of $d_{Maxwellian}$ is really difficult to be obtained, thus a different mathematical method for gathering the solid angle value is needed: a differential approach has been chosen. Assuming a Maxwellian viewing condition, different estimates of the solid angle measured at different distances and with the same setup will lead to the same solid angle value:

$$\Omega_j - \Omega_i \simeq 0 \tag{17}$$

In this condition, the beam converging point is assumed to be an unknown and, thus, the precedent mathematical expression can be further evolved as it is shown below:

$$f(d_{Maxwellian}) = \begin{cases} \Omega_j - \Omega_i \simeq 0 \\ \Omega_j = \frac{Area_{av,j}}{[d_{meas,j} - d_{Maxwellian}]^2} \\ \Omega_i = \frac{Area_{av,i}}{[d_{meas,i} - d_{Maxwellian}]^2} \end{cases} \tag{18}$$

After some mathematical calculations, it is possible to obtain the following second-order equation:

$$f(x) = \begin{cases} x = d_{Maxwellian} \\ ax^2 + bx + c = 0 \\ a = (Area_{av,j} - Area_{av,i}) \\ b = -2 \cdot (Area_{av,j} \cdot d_{meas,i} - Area_{av,i} \cdot d_{meas,j}) \\ c = Area_{av,j} \cdot (d_{meas,i})^2 - Area_{av,i} \cdot (d_{meas,j})^2 \end{cases} \tag{19}$$

Results description

One of the two solutions of this system permits gathering Ω_i by means of (16). This approach has been repeated three times: each session has permitted gathering a solid angle estimate. Once collected, their mean value and type-A uncertainty have been computed, obtaining the following result:

$$\Omega_{est} = \Omega_{av} \pm \Omega_{std,dev} = (0.4065 \pm 0.08) sr \tag{20}$$

The resultant uncertainty (approximately 20% of the estimated mean value) is pretty high due to the instruments that have been used in order to measure the area of the circumference. Below are shown the luminance results.

The table results are sorted by color and LabView intensity settings: these have been obtained by means of dividing the already available illuminance $[lux]$ datasets by the gathered solid angle. Consecutively, the linearity relation between the output luminance and the imposed $I_{LabView}$ is shown for the first ring of the right eye. In *Document [285]*, it is described that the LED driving circuitries have been prototyped in order to let the user impose equiluminant stimuli through the LabView UI by mean of, simply, imposing equal $I_{LabView}$. It can be seen, however, that this condition is not totally achieved since the curve associated with BLUE stimuli differs from the other: this is easily correctable by means of further modifying the driving circuit implementation. Moreover, for higher $I_{LabView}$ values, the RED and GREEN start to separate each other; this is most probably due to the increased current levels flowing through the LEDs that enhance the non-linearity components affecting the relationship between the output luminance and the current itself. In order to get a better understanding of the order of magnitude of the obtained results, *Table 17* is reported. This resumes the luminance values of typical settings and light sources that belong to our daily lives. The characterized prototype has been realized in order to mainly work in the photopic region, thus with luminance levels higher than $5cd/m^2$. The pupillometer can span from really tenuous luminance values, on the boundary in between the mesopic and photopic conditions, up to intense ones, such as a typical LCD monitor or even more.

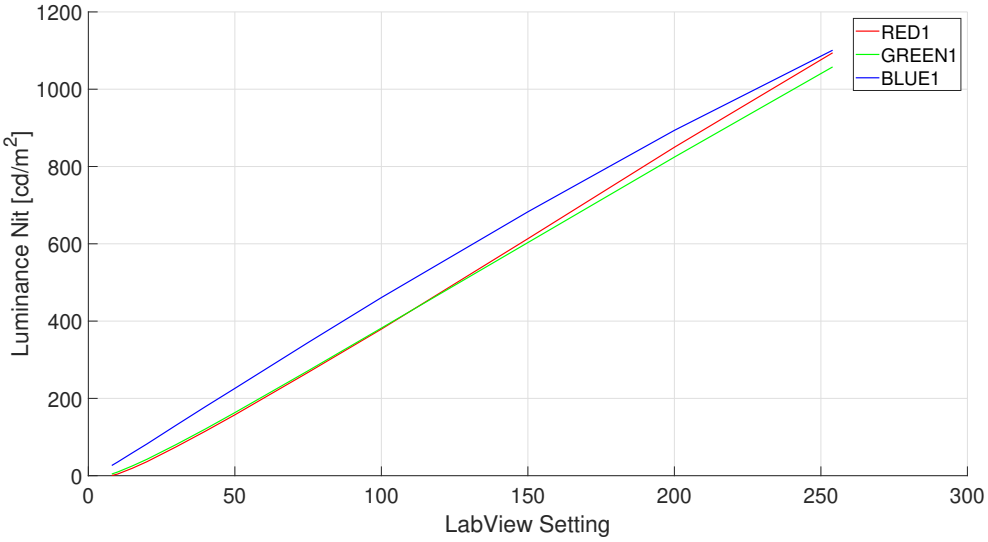


Figure 23: Output luminance result inherent the RGB light of the first LED crown.

LabView Setting	Right 1			Right 2			Right 3		
	R1	G1	B1	R2	G2	B2	R3	G3	B3
20	36	42	82	32	36	59	26	22	35
100	379	381	460	308	331	387	256	265	306
180	752	733	798	604	632	693	504	516	562
254	1094	1057	1100	883	905	956	736	746	784

LabView Setting	Right 4			Left 1			Left 4		
	R4	G4	B4	R5	G5	B5	R8	G8	B8
20	22	24	32	45	36	42	19	26	30
100	198	211	240	355	363	422	204	224	247
180	391	405	437	686	703	747	405	427	451
254	566	581	604	996	1009	1038	590	611	630

Table 16: Output luminance results. All the reported data are expressed in $[cd/m^2]$.

Factor (cd/m^2)	Value	Item
0		Ideal Black body [353]
10^(-6)	1 ucd/m^2	Absolute threshold of vision [353]
10^(-4)	400 ucd/m^2	Darkest sky [354]
10^(-3)	1 mcd/m^2	Night Sky [354]
	5 mcd/m^2	Approximate scotopic/mesopic threshold [355]
10^(0)	2 cd /m^2	Floodlit buildings, monuments, and fountains
	5 cd/m^2	**Approximate mesopic/photopic threshold [355]**
10^1	**25 cd/m^2**	**Typical photographic scene at sunrise or sunset [356]**
10^2	**250 cd/m^2**	**Peak luminance of a typical LCD monitor [357]**
10^3	2 kcd/m^2	Average cloud sky [354]
	2.5 kcd/m^2	Moon Surface [354]
	7 kcd/m^2	Average clear sky [353] [354]
10^4	12 kcd/m^2	Fluorescent lamp [354]
	75 kcd/m^2	Low pressure sodium-vapor lamp [354]
10^5	600 kcd/m^2	Solar disk at horizon [358]
10^6	7 Mcd/m^2	Filament of a clear incandescent lamp [357]
10^8	100 Mcd/m^2	Possible retinal damage [353]
10^9	1,6 Gcd/m^2	Solar disk at noon [354]

Table 17: Luminance order of magnitude concerning typical settings and light sources.

Publication List

Published

Journals

- **G. Gibertoni**, G. Borghi, and L. Rovati, "Vision-based Eye Image Selection for Ophthalmic Measurement Systems", Sensors, vol. 23(1), 386, **Jan 2023**, Link
- T. Fedullo, D. Cassanelli, **G. Gibertoni**, *Assessment of a Vision-Based Technique for an Automatic Van Herick Measurement System*, IEEE Transactions on Instrumentation and Measurement, vol. 71, pp. 1–11, **Aug 2022**, Link
- **G. Gibertoni**, N. Lenzini, L. Ferrari, and L. Rovati, *Design and Performance of a Near-Infrared Spectroscopy Measurement System for In-Field Alfalfa Moisture Measurement*, Photonics, vol. 9, no. 3, Art. no. 3, **Mar. 2022**, Link

Conferences

- T. Fedullo, E. Masetti, **G. Gibertoni**, F. Tramarin, and L. Rovati, *On the Use of an Hyperspectral Imaging Vision Based Measurement System and Machine Learning for Iris Pigmentation Grading*, in 2022 IEEE International Instrumentation and Measurement Technology Conference (I2MTC), **May 2022**, pp. 1–6. Link
- D. Cassanelli, T. Fedullo, **G. Gibertoni** et al., *Training of an artificial intelligence algorithm for automatic detection of the Van Herick grade*, in Ophthalmic Technologies XXXII, **Mar. 2022**, vol. 11941, pp. 35–41. Link
- **G. Gibertoni**, V. D. Pinto, S. Cattini, F. Tramarin, M. Geiser, and L. Rovati, *A simple Maxwellian optical system to investigate the photoreceptors contribution to pupillary light reflex*, in Ophthalmic Technologies XXXII, **Mar. 2022**, vol. 11941, pp. 52–60. Link
- T. Fedullo, D. Cassanelli, **G. Gibertoni** et al., *A Machine Learning Approach for a Vision-Based Van-Herick Measurement System*, in 2021 IEEE International Instrumentation and Measurement Technology Conference (I2MTC), **May 2021**, pp. 1–6. Link
- D. Cassanelli, **G. Gibertoni**, S. Cattini et al., *A new screening system for the estimation of ocular anterior chamber angle width*, in Ophthalmic Technologies XXXI, **Mar. 2021**, vol. 11623, pp. 101–105. Link
- **G. Gibertoni**, S. Cattini, and L. Rovati, *Towards the development of a new model for the oculomotor system*, in Ophthalmic Technologies XXXI, **Mar. 2021**, vol. 11623, pp. 93–100. Link

- **Gibertoni G.**, S. Cattini, and L. Rovati, *Design and realization of a binocular pupillometer for RGB flicker annoyance estimation*, XXXVI National Congress of Electrical and Electronic Measurements, **Sept 2019** GMEE, Perugia, Italy

Accepted

- **G. Gibertoni**, A.B. Pothiadia Irungovel, S. Viswanathan, and L. Rovati, *Silent stimulation of Cones: a comparison between the ERG and PLR responses*, Ophthalmic Technologies XXXIII

Master Thesis Co-Advisor

- M. Botrugno, **G. Gibertoni**, E. Masetti, L. Rovati, and E. Bassoli, *Using Additive Manufacturing for the Optomechanical Design of a Compact Ophthalmic Instrument for Pupillary Light Reflex Analysis*, University of Modena and Reggio Emilia, 2022.
- V. Di Pinto, **G. Gibertoni**, and L. Rovati, *A Device For Investigating The ipRGC Contribution To Pupillary Light Reflex With Silent Substitution Technique*, University of Modena and Reggio Emilia, 2021.
- G. Bellocchi, **G. Gibertoni**, and L. Rovati, *Characterization and performance improvement of a pupillometer prototype for flicker annoyance measurement*, University of Modena and Reggio Emilia, 2019.
- **G. Gibertoni**, S. Cattini, and L. Rovati, *Design and realization of a binocular pupillometer for RGB flicker annoyance estimation*, University of Modena and Reggio Emilia, 2019.

Bibliography

[1] B. Feigl and A. Zele, "Melanopsin-expressing intrinsically photosensitive retinal ganglion cells in retinal disease," *Optometry and vision science : official publication of the American Academy of Optometry*, vol. 91, 05 2014.

[2] P. T. Yuhas, "Isolation of iprgc contribution to the human pupillary light response," Ph.D. dissertation, The Ohio State University, 2014.

[3] "What to document and report in studies of ipRGC-influenced responses to light | CIE," Dec 2021, [Online]. [Online]. Available: https://cie.co.at/publications/what-document-and-report-studies-iprgc-influenced-responses-light

[4] S. Standring, *Gray's Anatomy International Edition: The Anatomical Basis of Clinical Practice*. Elsevier Health Sciences, 2015.

[5] E. Britannica, "Sensory reception: human vision: structure and function of the human eye," *Encyclopedia Brittanica*, vol. 27, p. 179, 1987.

[6] V. Y. Arshavsky and M. E. Burns, "Photoreceptor signaling: supporting vision across a wide range of light intensities," *Journal of Biological Chemistry*, vol. 287, no. 3, pp. 1620–1626, 2012.

[7] A. F. Goldberg, O. L. Moritz, and D. S. Williams, "Molecular basis for photoreceptor outer segment architecture," *Progress in retinal and eye research*, vol. 55, pp. 52–81, 2016.

[8] C. A. Curcio, K. R. Sloan, R. E. Kalina, and A. E. Hendrickson, "Human photoreceptor topography," *Journal of comparative neurology*, vol. 292, no. 4, pp. 497–523, 1990.

[9] E. R. Kandel, J. H. Schwartz, T. M. Jessell, D. of Biochemistry, M. B. T. Jessell, S. Siegelbaum, and A. Hudspeth, *Principles of neural science*. McGraw-hill New York, 2000, vol. 4.

[10] S. Li, J. Mitchell, D. J. Briggs, J. K. Young, S. S. Long, and P. G. Fuerst, "Morphological diversity of the rod spherule: a study of serially reconstructed electron micrographs," *PloS one*, vol. 11, no. 3, p. e0150024, 2016.

[11] A. Roorda and D. R. Williams, "The arrangement of the three cone classes in the living human eye," *Nature*, vol. 397, no. 6719, pp. 520–522, 1999, iSBN: 0028-0836 Publisher: Nature Publishing Group UK London.

[12] F. Grassi, D. Negrini, and C. Porro, *Fisiologia umana*. Poletto, 2015. [Online]. Available: https://books.google.it/books?id=AbbRjwEACAAJ

[13] C. E. Keeler, "Iris movements in blind mice," *American Journal of Physiology-Legacy Content*, vol. 81, no. 1, pp. 107–112, Jun. 1927, publisher: American Physiological Society. [Online]. Available: https://journals.physiology.org/doi/abs/10.1152/ajplegacy.1927.81.1.107

[14] ——, "Blind mice," *Journal of Experimental Zoology*, vol. 51, no. 4, pp. 495–508, 1928, _eprint: https://onlinelibrary.wiley.com/doi/pdf/10.1002/jez.1400510404. [Online]. Available: https://onlinelibrary.wiley.com/doi/abs/10.1002/jez.1400510404

[15] M. T. H. Do and K.-W. Yau, "Intrinsically photosensitive retinal ganglion cells," *Physiological reviews*, 2010, publisher: American Physiological Society Bethesda, MD.

[16] L. S. Mure, "Intrinsically Photosensitive Retinal Ganglion Cells of the Human Retina," *Front. Neurol.*, vol. 0, 2021.

[17] J. L. Ecker, O. N. Dumitrescu, K. Y. Wong, N. M. Alam, S.-K. Chen, T. LeGates, J. M. Renna, G. T. Prusky, D. M. Berson, and S. Hattar, "Melanopsin-Expressing Retinal Ganglion-Cell Photoreceptors: Cellular Diversity and Role in Pattern Vision," *Neuron*, vol. 67, no. 1, pp. 49–60, Jul. 2010. [Online]. Available: http://www.sciencedirect.com/science/article/pii/S0896627310004198

[18] F. H. Zaidi, J. T. Hull, S. N. Peirson, K. Wulff, D. Aeschbach, J. J. Gooley, G. C. Brainard, K. Gregory-Evans, J. F. Rizzo III, C. A. Czeisler *et al.*, "Short-wavelength light sensitivity of circadian, pupillary, and visual awareness in humans lacking an outer retina," *Current Biology*, vol. 17, no. 24, pp. 2122–2128, 2007.

[19] M. Bernabei, "High brightness solid state optical sources and visually safe lighting," PhD Thesis, Università di Modena e Reggio emilia, May 2016. [Online]. Available: https://morethesis.unimore.it/theses/available/etd-03052016-111857/

[20] H. J. Wyatt, "The form of the human pupil," *Vision Research*, vol. 35, no. 14, pp. 2021–2036, Jul. 1995. [Online]. Available: http://linkinghub.elsevier.com/retrieve/pii/004269899400268Q

[21] P. A. Barrionuevo, N. Nicandro, J. J. McAnany, A. J. Zele, P. Gamlin, and D. Cao, "Assessing Rod, Cone, and Melanopsin Contributions to Human Pupil Flicker Responses," *Investigative Ophthalmology & Visual Science*, vol. 55, no. 2, pp. 719–727, Feb. 2014. [Online]. Available: https://iovs.arvojournals.org/article.aspx?articleid=2189826

[22] W. A. H. Rushton, D. S. Powell, and K. D. White, "Exchange thresholds in dichromats," *Vision Research*, vol. 13, no. 11, pp. 1993–2002, Nov. 1973. [Online]. Available: https://www.sciencedirect.com/science/article/pii/0042698973901776

[23] S. Usui and L. Stark, "A model for nonlinear stochastic behavior of the pupil," *Biological Cybernetics*, vol. 45, no. 1, pp. 13–21, Aug. 1982. [Online]. Available: http://link.springer.com/10.1007/BF00387209

[24] P. Reeves, "The Response of the Average Pupil to Various Intensities of Light," *JOSA*, vol. 4, no. 2, pp. 35–43, Mar. 1920, publisher: Optical Society of America. [Online]. Available: https://www.osapublishing.org/josa/abstract.cfm?uri=josa-4-2-35

[25] P. Moon and D. E. Spencer, "On the Stiles-Crawford Effect," *JOSA*, vol. 34, no. 6, pp. 319–329, Jun. 1944, publisher: Optical Society of America. [Online]. Available: https://www.osapublishing.org/josa/abstract.cfm?uri=josa-34-6-319

[26] F. Sun, P. Tauchi, and L. Stark, "Dynamic pupillary response controlled by the pupil size effect," *Experimental Neurology*, vol. 82, no. 2, pp. 313–324, Nov. 1983. [Online]. Available: http://www.sciencedirect.com/science/article/pii/0014488683904041

[27] L. W. Stark, "The Pupil as a Paradigm for Neurological Control Systems," *IEEE Transactions on Biomedical Engineering*, vol. BME-31, no. 12, pp. 919–924, Dec. 1984.

[28] V. F. Pamplona, M. M. Oliveira, and G. V. G. Baranoski, "Photorealistic models for pupil light reflex and iridal pattern deformation," *ACM Transactions on Graphics*, vol. 28, no. 4, pp. 106:1–106:12, Sep. 2009. [Online]. Available: https://doi.org/10.1145/1559755.1559763

[29] C. M. Privitera and L. W. Stark, "A Binocular Pupil Model for Simulation of Relative Afferent Pupil Defects and the Swinging Flashlight Test," *Biological Cybernetics*, vol. 94, no. 3, pp. 215–224, Mar. 2006. [Online]. Available: https://doi.org/10.1007/s00422-005-0042-8

[30] X. Fan and G. Yao, "Modeling Transient Pupillary Light Reflex Induced by a Short Light Flash," *IEEE Transactions on Biomedical Engineering*, vol. 58, no. 1, pp. 36–42, Jan. 2011.

[31] C. Privitera and L. Stark, "A binocular pupil model for simulation of relative afferent pupil defect, RAPD," in *The 26th Annual International Conference of the IEEE Engineering in Medicine and Biology Society*, vol. 1, Sep. 2004, pp. 711–714, iSSN: null.

[32] C. M. Privitera and L. W. Stark, "A Binocular Pupil Model for Simulation of Relative Afferent Pupil Defects and the Swinging Flashlight Test," *Biological Cybernetics*, vol. 94, no. 3, pp. 215–224, Mar. 2006. [Online]. Available: http://link.springer.com/10.1007/s00422-005-0042-8

[33] S. Usui and Y. Hirata, "Estimation of autonomic nervous activity using the inverse dynamic model of the pupil muscle plant," *Annals of Biomedical Engineering*, vol. 23, pp. 375–387, Jul. 1995.

[34] Y. Hirata and S. Usui, "Estimation of the autonomic nervous activity from pupillary response," in *Proceedings of 16th Annual International Conference of the IEEE Engineering in Medicine and Biology Society*, vol. 2, Nov. 1994, pp. 1170–1171 vol.2, iSSN: null.

[35] A. Gilchrist and J. Nobbs, "Colorimetry, theory," in *Encyclopedia of Spectroscopy and Spectrometry (Third Edition)*, 3rd ed., J. C. Lindon, G. E. Tranter, and D. W. Koppenaal, Eds. Oxford: Academic Press, 2017, pp. 328–333. [Online]. Available: https://www.sciencedirect.com/science/article/pii/B9780128032244001242

[36] M. Shaw and M. Fairchild, "Evaluating the 1931 CIE color-matching functions," *Color Research & Application: Endorsed by Inter-Society Color Council, The Colour Group (Great Britain), Canadian Society for Color, Color Science Association of Japan, Dutch Society for the Study of Color, The Swedish Colour Centre Foundation, Colour Society of Australia, Centre Français de la Couleur*, vol. 27, no. 5, pp. 316–329, 2002, iSBN: 0361-2317 Publisher: Wiley Online Library.

[37] H. S. Fairman, M. H. Brill, and H. Hemmendinger, "How the CIE 1931 color-matching functions were derived from Wright-Guild data," *Color Research & Application: Endorsed by Inter-Society Color Council, The Colour Group (Great Britain), Canadian Society for Color, Color Science Association of Japan, Dutch Society for the Study of Color, The Swedish Colour Centre Foundation, Colour Society of Australia, Centre Français de la Couleur*, vol. 22, no. 1, pp. 11–23, 1997, iSBN: 0361-2317 Publisher: Wiley Online Library.

[38] P. W. Trezona, "Derivation of the 1964 CIE 10° XYZ colour-matching functions and their applicability in photometry," *Color Research & Application: Endorsed by Inter-Society Color Council, The Colour Group (Great Britain), Canadian Society for Color, Color Science Association of Japan, Dutch Society for the Study of Color, The Swedish Colour Centre Foundation, Colour Society of Australia, Centre Français de la Couleur*, vol. 26, no. 1, pp. 67–75, 2001, iSBN: 0361-2317 Publisher: Wiley Online Library.

[39] A. Stockman, L. T. Sharpe, and C. Fach, "The spectral sensitivity of the human short-wavelength sensitive cones derived from thresholds and color matches," *Vision Research*, vol. 39, no. 17, pp. 2901–2927, Aug. 1999. [Online]. Available: https://www.sciencedirect.com/science/article/pii/S0042698998002259

[40] A. Stockman and L. T. Sharpe, "The spectral sensitivities of the middle- and long-wavelength-sensitive cones derived from measurements in observers of known genotype," *Vision Research*, vol. 40, no. 13, pp. 1711–1737, Jun. 2000. [Online]. Available: https://www.sciencedirect.com/science/article/pii/S0042698900000213

[41] F. W. Billmeyer Jr., "Color Science: Concepts and Methods, Quantitative Data and Formulae, 2nd ed., by Gunter Wyszecki and W. S. Stiles, John Wiley and Sons, New York, 1982, 950 pp. Price: $75.00," *Color Research & Application*, vol. 8, no. 4, pp. 262–263, 1983, _eprint: https://onlinelibrary.wiley.com/doi/pdf/10.1002/col.5080080421. [Online]. Available: https://onlinelibrary.wiley.com/doi/abs/10.1002/col.5080080421

[42] A. Stockman, "CIE Physiologically Based Color Matching Functions and Chromaticity Diagrams," in *Encyclopedia of Color Science and Technology*, R. Luo, Ed. Berlin, Heidelberg: Springer, 2014, pp. 1–10. [Online]. Available: https://doi.org/10.1007/978-3-642-27851-8_326-1

[43] J. Schanda, *Colorimetry: Understanding the CIE System*. John Wiley & Sons, Oct. 2007, google-Books-ID: uZadszSGe9MC.

[44] M. D. Fairchild, *Color Appearance Models*. John Wiley & Sons, Aug. 2013, google-Books-ID: hh3lXMJ4bDIC.

[45] B. Smits, "An RGB-to-spectrum conversion for reflectances," *Journal of Graphics Tools*, vol. 4, no. 4, pp. 11–22, 1999, iSBN: 1086-7651 Publisher: Taylor & Francis.

[46] N. Ohta and A. R. Robertson, *Colorimetry: Fundamentals and Applications*. Wiley, 2005.

[47] M. Magnusson, J. Sigurdsson, S. E. Armansson, M. O. Ulfarsson, H. Deborah, and J. R. Sveinsson, "Creating rgb images from hyperspectral images using a color matching function," in *IGARSS 2020-2020 IEEE International Geoscience and Remote Sensing Symposium*. Ieee, 2020, pp. 2045–2048.

[48] Cie, "CIE S 026/E:2018 CIE System for Metrology of Optical Radiation for ipRGC-Influenced Responses to Light," International Commission on Illumination (CIE), Tech. Rep., Dec. 2018. [Online]. Available: https://cie.co.at/publications/cie-system-metrology-optical-radiation-iprgc-influenced-responses-light-0

[49] D. M. Berson, "Strange vision: ganglion cells as circadian photoreceptors," *Trends in Neurosciences*, vol. 26, no. 6, pp. 314–320, Jun. 2003. [Online]. Available: https://www.sciencedirect.com/science/article/pii/S0166223603001309

[50] A. Terakita, "The opsins," *Genome Biology*, vol. 6, no. 3, pp. 1–9, Mar 2005.

[51] R. J. Lucas, S. N. Peirson, D. M. Berson, T. M. Brown, H. M. Cooper, C. A. Czeisler, M. G. Figueiro, P. D. Gamlin, S. W. Lockley, J. B. O'Hagan, L. L. A. Price, I. Provencio, D. J. Skene, and G. C. Brainard, "Measuring and using light in the melanopsin age," *Trends in Neurosciences*, vol. 37, no. 1, pp. 1–9, Jan. 2014. [Online]. Available: https://www.sciencedirect.com/science/article/pii/S0166223613001975

[52] J. a. Enezi, V. Revell, T. Brown, J. Wynne, L. Schlangen, and R. Lucas, "A "Melanopic" Spectral Efficiency Function Predicts the Sensitivity of Melanopsin Photoreceptors to Polychromatic Lights," *Journal of Biological Rhythms*, vol. 26, no. 4, pp. 314–323, Aug. 2011, publisher: SAGE Publications Inc. [Online]. Available: https://doi.org/10.1177/0748730411409719

[53] S. Cie, "Cie international standard (cie s 026/e:2018) "system for metrology of optical radiation for iprgc-influenced responses to light"," *CIE Central Bureau: Vienna, Austria*, vol. 26, 12 2018.

[54] M. Spitschan and T. Woelders, "The Method of Silent Substitution for Examining Melanopsin Contributions to Pupil Control," *Frontiers in Neurology*, vol. 0, 2018, publisher: Frontiers. [Online]. Available: https://www.frontiersin.org/articles/10.3389/fneur.2018.00941/full

[55] O. Estévez and H. Spekreijse, "The "silent substitution" method in visual research," *Vision Research*, vol. 22, no. 6, pp. 681–691, Jan. 1982. [Online]. Available: https://www.sciencedirect.com/science/article/pii/0042698982901043

[56] K. O. Donner and W. A. H. Rushton, "Retinal stimulation by light substitution," *The Journal of Physiology*, vol. 149, no. 2, pp. 288–302, Dec. 1959. [Online]. Available: https://www.ncbi.nlm.nih.gov/pmc/articles/PMC1363090/

[57] V. Conus and M. Geiser, "A Review of Silent Substitution Devices for Melanopsin Stimulation in Humans," *Photonics*, vol. 7, no. 4, p. 121, Nov. 2020. [Online]. Available: https://www.mdpi.com/2304-6732/7/4/121

[58] G. Evéquoz, F. Truffer, and M. Geiser, "Maximum possible contrast level for silent substitution: a theoretical model applied to melanopsin stimulation," *JOSA A*, vol. 38, no. 9, pp. 1312–1319, Sep. 2021, publisher: Optica Publishing Group. [Online]. Available: https://opg.optica.org/josaa/abstract.cfm?uri=josaa-38-9-1312

[59] G. Wyszecki and W. S. Stiles, *Color science: Concepts and methods, quantitative data and formulas*, ser. Color science: Concepts and methods, quantitative data and formulas. Oxford, England: John Wiley, 1967.

[60] "International Lighting Vocabulary - CIE S 017/E:2011," 2012. [Online]. Available: https://cie.co.at/publications/international-lighting-vocabulary

[61] F. Viénot, S. Bailacq, and J. L. Rohellec, "The effect of controlled photopigment excitations on pupil aperture," *Ophthalmic and Physiological Optics*, vol. 30, no. 5, pp. 484–491, 2010, _eprint: https://onlinelibrary.wiley.com/doi/pdf/10.1111/j.1475-1313.2010.00754.x. [Online]. Available: https://onlinelibrary.wiley.com/doi/abs/10.1111/j.1475-1313.2010.00754.x

[62] M. Saito, K. Miyamoto, Y. Uchiyama, and I. Murakami, "Invisible light inside the natural blind spot alters brightness at a remote location," *Scientific Reports*, vol. 8, no. 1, pp. 1–9, May 2018. [Online]. Available: https://www.nature.com/articles/s41598-018-25920-9

[63] F. Patrick, S. Jessica, E. Gilles, B. Pierre, and G. Martial, "Homogeneous light stimulation of melanopsin and cones with a Maxwellian view device for the human eye," in *2021 IEEE International Instrumentation and Measurement Technology Conference (I2MTC)*, May 2021, pp. 1–5, iSSN: 2642-2077.

[64] A. J. Zele, P. Adhikari, D. Cao, and B. Feigl, "Melanopsin and Cone Photoreceptor Inputs to the Afferent Pupil Light Response," *Frontiers in Neurology*, vol. 10, p. 529, 2019. [Online]. Available: https://www.frontiersin.org/article/10.3389/fneur.2019.00529

[65] G. Gibertoni, V. D. Pinto, S. Cattini, F. Tramarin, M. Geiser, and L. Rovati, "A simple Maxwellian optical system to investigate the photoreceptors contribution to pupillary light reflex," in *Ophthalmic Technologies XXXII*, vol. 11941. SPIE, Mar. 2022, pp. 52–60. [Online]. Available: https://www.spiedigitallibrary.org/conference-proceedings-of-spie/11941/119410G/A-simple-Maxwellian-optical-system-to-investigate-the-photoreceptors-contribution/10.1117/12.2608129.full

[66] G. Gibertoni, "Design and realization of a binocular pupillometer for RGB flicker annoyance estimation," Tesi Magistrale, Università di Modena e Reggio Emilia, https://morethesis.unimore.it/theses/available/etd-03172019-233428/, Nov. 2019.

[67] L. S. Lasdon, R. L. Fox, and M. W. Ratner, "Nonlinear optimization using the generalized reduced gradient method," *Revue française d'automatique, informatique, recherche opérationnelle. Recherche opérationnelle*, vol. 8, no. V3, pp. 73–103, 1974, iSBN: 0397-9350 Publisher: EDP Sciences.

[68] M. Herzberger, "Gaussian Optics and Gaussian Brackets*†," *JOSA*, vol. 33, no. 12, pp. 651–655, Dec. 1943, publisher: Optica Publishing Group. [Online]. Available: https://opg.optica.org/josa/abstract.cfm?uri=josa-33-12-651

[69] P. Mouroulis and J. Macdonald, "Geometrical optics and optical design," *Choice Reviews Online*, vol. 34, no. 08, pp. 34–4535–34–4535, Apr. 1997, publisher: American Library Association. [Online]. Available: https://doi.org/10.5860%2Fchoice.34-4535

[70] B. E. A. Saleh and M. C. Teich, *Fundamentals of Photonics, 2 Volume Set*. Wiley, Feb. 2019, google-Books-ID: BDXoswEACAAJ.

[71] E. Hecht, *Optics*. Addison-Wesley, 2002, google-Books-ID: T3ofAQAAMAAJ.

[72] G. P. Agrawal and D. N. Pattanayak, "Gaussian beam propagation beyond the paraxial approximation," *JOSA*, vol. 69, no. 4, pp. 575–578, Apr. 1979, publisher: Optica Publishing Group. [Online]. Available: https://opg.optica.org/josa/abstract.cfm?uri=josa-69-4-575

[73] M. Lax, W. H. Louisell, and W. B. McKnight, "From Maxwell to paraxial wave optics," *Physical Review A*, vol. 11, no. 4, pp. 1365–1370, Apr. 1975, publisher: American Physical Society. [Online]. Available: https://link.aps.org/doi/10.1103/PhysRevA.11.1365

[74] V. N. Mahajan, *Optical imaging and aberrations: Ray geometrical optics*. SPIE press, 1998, vol. 45.

[75] W. T. Welford, *Aberrations of optical systems*. Routledge, 2017.

[76] G. Black and E. H. Linfoot, "Spherical aberration and the information content of optical images," *Proceedings of the Royal Society of London. Series A. Mathematical and Physical Sciences*, vol. 239, no. 1219, pp. 522–540, 1957, iSBN: 0080-4630 Publisher: The Royal Society London.

[77] M. Koomen, R. Tousey, and R. Scolnik, "The spherical aberration of the eye," *JOSA*, vol. 39, no. 5, pp. 370–376, 1949, publisher: Optica Publishing Group.

[78] B. Braunecker and H. J. Tiziani, *Advanced optics using aspherical elements*. Spie Press, 2008, vol. 173.

[79] L. N. Thibos, A. Bradley, D. L. Still, X. Zhang, and P. A. Howarth, "Theory and measurement of ocular chromatic aberration," *Vision research*, vol. 30, no. 1, pp. 33–49, 1990, iSBN: 0042-6989 Publisher: Elsevier.

[80] T. T. Smith, "The color correction of an achromatic doublet," *JOSA*, vol. 10, no. 1, pp. 39–63, 1925, publisher: Optica Publishing Group.

[81] M. Goggin, *Astigmatism: Optics, Physiology and Management*. BoD – Books on Demand, Feb. 2012, google-Books-ID: AuuPDwAAQBAJ.

[82] R. Bellucci, S. Morselli, and V. Pucci, "Spherical aberration and coma with an aspherical and a spherical intraocular lens in normal age-matched eyes," *Journal of Cataract & Refractive Surgery*, vol. 33, no. 2, pp. 203–209, 2007, iSBN: 0886-3350 Publisher: Elsevier.

[83] N. López-Gil, H. C. Howland, B. Howland, N. Charman, and R. Applegate, "Generation of third-order spherical and coma aberrations by use of radially symmetrical fourth-order lenses," *JOSA A*, vol. 15, no. 9, pp. 2563–2571, 1998, iSBN: 1520-8532 Publisher: Optical Society of America.

[84] "Aberrations - Opto Engineering," Dec 2021, [Online; accessed 16. Dec. 2021]. [Online]. Available: https://www.opto-e.com/basics/aberrations

[85] E. Santamato and Y. R. Shen, "Field-curvature effect on the diffraction ring pattern of a laser beam dressed by spatial self-phase modulation in a nematic film," *Optics letters*, vol. 9, no. 12, pp. 564–566, 1984, iSBN: 1539-4794 Publisher: Optica Publishing Group.

[86] M. A. González-Galicia, J. Garduño-Mejía, M. Rosete-Aguilar, N. C. Bruce, and R. Ortega-Martínez, "Effects of primary spherical aberration, coma, astigmatism, and field curvature on the focusing of ultrashort pulses: Gaussian illumination and experiment," *JOSA A*, vol. 28, no. 10, pp. 1990–1994, 2011, iSBN: 1520-8532 Publisher: Optical Society of America.

[87] E. DeHoog and J. Schwiegerling, "Fundus camera systems: a comparative analysis," *Applied optics*, vol. 48, no. 2, pp. 221–228, 2009, iSBN: 2155-3165 Publisher: Optica Publishing Group.

[88] R. W. Ehlen, "Distortion and its photography," Ph.D. dissertation, Pacific University, 1991.

[89] Z. Gao, Q. Zhang, Y. Su, and S. Wu, "Accuracy evaluation of optical distortion calibration by digital image correlation," *Optics and Lasers in Engineering*, vol. 98, pp. 143–152, 2017, iSBN: 0143-8166 Publisher: Elsevier.

[90] H. Ojanen, "Automatic correction of lens distortion by using digital image processing," *Rutgers University, Dept. of Mathematics technical report*, 1999, publisher: Citeseer.

[91] S. Ortiz, D. Siedlecki, I. Grulkowski, L. Remon, D. Pascual, M. Wojtkowski, and S. Marcos, "Optical distortion correction in optical coherence tomography for quantitative ocular anterior segment by three-dimensional imaging," *Optics express*, vol. 18, no. 3, pp. 2782–2796, 2010, iSBN: 1094-4087 Publisher: Optical Society of America.

[92] B. A. Watson and L. F. Hodges, "Using texture maps to correct for optical distortion in head-mounted displays," in *Proceedings Virtual Reality Annual International Symposium'95*. IEEE, 1995, pp. 172–178.

[93] X. Ma, D. Liu, F. Zhang, and Y. Yan, "Non-polarizing broadband dichroic mirror," *Journal of Optics A: Pure and Applied Optics*, vol. 9, no. 7, p. 573, 2007, iSBN: 1464-4258 Publisher: IOP Publishing.

[94] H. Kinoshita, K. Kurihara, Y. Ishii, and Y. Torii, "Soft x-ray reduction lithography using multilayer mirrors," *Journal of Vacuum Science & Technology B: Microelectronics Processing and Phenomena*, vol. 7, no. 6, pp. 1648–1651, 1989, iSBN: 0734-211X Publisher: American Vacuum Society.

[95] "Introduction to Optical Prisms | Edmund Optics." [Online]. Available: https://www.edmundoptics.com/knowledge-center/application-notes/optics/introduction-to-optical-prisms/

[96] M. H. Asghar, M. B. Khan, S. Naseem, and Z. A. Khan, "Design and preparation of antireflection films on glass substrate," *Turkish Journal of Physics*, vol. 29, no. 1, pp. 43–53, 2005, iSBN: 1300-0101.

[97] "Light basics - Opto Engineering," Dec 2021, [Online; accessed 17. Dec. 2021]. [Online]. Available: https://www.opto-e.com/basics/light-basics

[98] S. Yaguchi, Y. Kora, H. Takahashi, Y. Fukado, A. Yamanaka, M. Kusakabe, and S. Ishibashi, *A new endoscope for ophthalmic microsurgery*. SLACK Incorporated Thorofare, NJ, 1992, vol. 23, issue: 12 Pages: 838-841 Publication Title: Ophthalmic Surgery, Lasers and Imaging Retina.

[99] F. K. Yam and Z. Hassan, "Innovative advances in LED technology," *Microelectronics Journal*, vol. 36, no. 2, pp. 129–137, 2005, iSBN: 0026-2692 Publisher: Elsevier.

[100] S. Eguchi, T. Kohzuka, and M. Araie, "Stereoscopic ophthalmic microendoscope system," *Archives of Ophthalmology*, vol. 115, no. 10, pp. 1336–1338, 1997, iSBN: 0003-9950 Publisher: American Medical Association.

[101] W. T. Ham Jr, H. A. Mueller, J. J. Ruffolo Jr, D. Guerry III, and R. K. Guerry, "Action spectrum for retinal injury from near-ultraviolet radiation in the aphakic monkey," *American journal of ophthalmology*, vol. 93, no. 3, pp. 299–306, 1982, iSBN: 0002-9394 Publisher: Elsevier.

[102] J. M. Krauss and C. A. Puliafito, "Lasers in ophthalmology," *Lasers in surgery and medicine*, vol. 17, no. 2, pp. 102–159, 1995, iSBN: 0196-8092 Publisher: Wiley Online Library.

[103] N. Narendran and Y. Gu, "Life of LED-based white light sources," *Journal of display technology*, vol. 1, no. 1, p. 167, 2005, publisher: IEEE.

[104] "What is an LED?" Dec 2015, [Online; accessed 17. Dec. 2021]. [Online]. Available: https://www.ledsmagazine.com/leds-ssl-design/materials/article/16701292/what-is-an-led

[105] M. Wood, "Photopic curves–the old and the new," *Mike Wood Consulting: Out of the Wood*, 2014.

[106] G. Wyszecki and W. S. Stiles, *Color science*. Wiley New York, 1982, vol. 8.

[107] J. Gordon and I. Abramov, "Color appearance: Maxwellian vs. Newtonian views," *Vision Research*, vol. 48, no. 18, pp. 1879–1883, Aug. 2008. [Online]. Available: https://www.sciencedirect.com/science/article/pii/S0042698908003027

[108] A. M. Oliveira, H. E. S. Velten, J. C. Fabris, and I. G. Salako, "Newtonian view of general relativistic stars," *The European Physical Journal C*, vol. 74, no. 11, pp. 1–6, 2014, iSBN: 1434-6052 Publisher: Springer.

[109] G. Westheimer, "The maxwellian view," *Vision Research*, vol. 6, no. 11, pp. 669–682, Dec. 1966. [Online]. Available: https://www.sciencedirect.com/science/article/pii/0042698966900782

[110] L. L. Avant, "Vision in the Ganzfeld," *Psychological Bulletin*, vol. 64, pp. 246–258, 1965, place: US Publisher: American Psychological Association.

[111] C. W. Oyster, "The human eye," *Sunderland, MA: Sinauer*, 1999.

[112] F. C. Delori, R. H. Webb, and D. H. Sliney, "Maximum permissible exposures for ocular safety (ANSI 2000), with emphasis on ophthalmic devices," *J. Opt. Soc. Am. A*, vol. 24, no. 5, pp. 1250–65, Jun 2007.

[113] J. R. Meyer-Arendt, "Radiometry and Photometry: Units and Conversion Factors," *Applied Optics*, vol. 7, no. 10, pp. 2081–2084, Oct. 1968, publisher: Optica Publishing Group. [Online]. Available: https://opg.optica.org/ao/abstract.cfm?uri=ao-7-10-2081

[114] E. S. dos Santos, W. B. Xavier, R. N. Rodrigues, S. S. da C. Botelho, and A. V. Werhli, "Vision based measurement applied to industrial instrumentation," *IFAC-PapersOnLine*, vol. 50, no. 1, pp. 788–793, 2017, 20th IFAC World Congress.

[115] L. G. Shapiro, G. C. Stockman *et al.*, *Computer vision*. Prentice Hall New Jersey, 2001, vol. 3.

[116] B. Mahesh, "Machine learning algorithms-a review," *International Journal of Science and Research (IJSR).[Internet]*, vol. 9, pp. 381–386, 2020.

[117] Y. LeCun, Y. Bengio, and G. Hinton, "Deep learning," *nature*, vol. 521, no. 7553, pp. 436–444, 2015.

[118] B. G. Buchanan and R. G. Smith, "Fundamentals of expert systems," *Annual review of computer science*, vol. 3, no. 1, pp. 23–58, 1988.

[119] C. V. Gallagher, K. Bruton, K. Leahy, and D. T. O'Sullivan, "The suitability of machine learning to minimise uncertainty in the measurement and verification of energy savings," *Energy and Buildings*, vol. 158, pp. 647–655, 2018.

[120] T. Yao, C. Qu, Q. Liu, R. Deng, Y. Tian, J. Xu, A. Jha, S. Bao, M. Zhao, A. B. Fogo, B. A. Landman, C. Chang, H. Yang, and Y. Huo, "Compound Figure Separation of Biomedical Images with Side Loss," in *Deep Generative Models, and Data Augmentation, Labelling, and Imperfections*, ser. Lecture Notes in Computer Science, S. Engelhardt, I. Oksuz, D. Zhu, Y. Yuan, A. Mukhopadhyay, N. Heller, S. X. Huang, H. Nguyen, R. Sznitman, and Y. Xue, Eds. Cham: Springer International Publishing, 2021, pp. 173–183.

[121] M. Zhao, A. Jha, Q. Liu, B. A. Millis, A. Mahadevan-Jansen, L. Lu, B. A. Landman, M. J. Tyska, and Y. Huo, "Faster Mean-shift: GPU-accelerated clustering for cosine embedding-based cell segmentation and tracking," *Medical Image Analysis*, vol. 71, p. 102048, jul 2021. [Online]. Available: https://www.sciencedirect.com/science/article/pii/S1361841521000943

[122] S. J. Kim, K. J. Cho, and S. Oh, "Development of machine learning models for diagnosis of glaucoma," *Plos One*, vol. 12, no. 5, p. e0177726, may 2017.

[123] R. Asaoka, H. Murata, A. Iwase, and M. Araie, "Detecting Preperimetric Glaucoma with Standard Automated Perimetry Using a Deep Learning Classifier," *Ophthalmology*, vol. 123, no. 9, pp. 1974–1980, Sep 2016.

[124] Q. Li, B. Feng, L. Xie, P. Liang, H. Zhang, and T. Wang, "A Cross-Modality Learning Approach for Vessel Segmentation in Retinal Images," *IEEE Transactions on Medical Imaging*, vol. 35, no. 1, pp. 109–118, Jul 2015.

[125] P. Varun Gulshan, "Development and Validation of a Deep Learning Algorithm for Detection of Diabetic Retinopathy in Retinal," *Jama*, vol. 316, no. 22, pp. 2402–2410, Dec 2016.

[126] M. Daniel Shu Wei Ting, "Development and Validation of a Deep Learning System for Diabetic Retinopathy and Related Eye Diseases Using," *Jama*, vol. 318, no. 22, pp. 2211–2223, Dec 2017.

[127] L. Balyen and T. Peto, "Promising Artificial Intelligence-Machine Learning-Deep Learning Algorithms in Ophthalmology," *The Asia-Pacific Journal of Ophthalmology*, vol. 8, no. 3, pp. 264–272, Jun 2019. [Online]. Available: https://journals.lww.com/apjoo/fulltext/2019/05000/promising%5Fartificial%5Fintelligence%5Fmachine.13.aspx

[128] T. A. Schmidt, "On slit-lamp microscopy," *Documenta Ophthalmologica*, vol. 39, no. 1, pp. 117–153, 1975.

[129] A. G. Podoleanu, "Optical coherence tomography," *Journal of microscopy*, vol. 247, no. 3, pp. 209–219, 2012.

[130] E. Roberts, R. Morgan, D. King, and L. Clerkin, "Funduscopy: a forgotten art?" *Postgraduate medical journal*, vol. 75, no. 883, pp. 282–284, 1999.

[131] S. Sirois and J. Brisson, "Pupillometry," *Wiley Interdisciplinary Reviews: Cognitive Science*, vol. 5, no. 6, pp. 679–692, 2014.

[132] E. Osman, "Laser refractive surgery in glaucoma patients," *Saudi journal of ophthalmology*, vol. 25, no. 2, pp. 169–173, 2011.

[133] G. Davis, "The evolution of cataract surgery," *Missouri medicine*, vol. 113, no. 1, p. 58, 2016.

[134] B. G. Buchanan and R. G. Smith, "Fundamentals of expert systems," *Annual review of computer science*, vol. 3, no. 1, pp. 23–58, 1988, iSBN: 8756-7016.

[135] T. G. Dietterich, "Machine learning," *Annual review of computer science*, vol. 4, no. 1, pp. 255–306, 1990, iSBN: 8756-7016 Publisher: Annual Reviews 4139 El Camino Way, PO Box 10139, Palo Alto, CA 94303-0139, USA.

[136] B. Mahesh, "Machine learning algorithms-a review," *International Journal of Science and Research (IJSR).[Internet]*, vol. 9, pp. 381–386, 2020.

[137] Z.-H. Zhou, *Machine learning*. Springer Nature, 2021.

[138] P. Cunningham, M. Cord, and S. J. Delany, "Supervised learning," in *Machine learning techniques for multimedia*. Springer, 2008, pp. 21–49.

[139] H. B. Barlow, "Unsupervised learning," *Neural computation*, vol. 1, no. 3, pp. 295–311, 1989, iSBN: 0899-7667 Publisher: MIT Press One Rogers Street, Cambridge, MA 02142-1209, USA journals-info ....

[140] L. P. Kaelbling, M. L. Littman, and A. W. Moore, "Reinforcement learning: A survey," *Journal of artificial intelligence research*, vol. 4, pp. 237–285, 1996, iSBN: 1076-9757.

[141] M.-L. Zhang and Z.-H. Zhou, "ML-KNN: A lazy learning approach to multi-label learning," *Pattern recognition*, vol. 40, no. 7, pp. 2038–2048, 2007, iSBN: 0031-3203 Publisher: Elsevier.

[142] H. Zhang, A. C. Berg, M. Maire, and J. Malik, "SVM-KNN: Discriminative nearest neighbor classification for visual category recognition," in *2006 IEEE Computer Society Conference on Computer Vision and Pattern Recognition (CVPR'06)*, vol. 2. IEEE, 2006, pp. 2126–2136.

[143] S. Ruder, "An overview of gradient descent optimization algorithms," *arXiv preprint arXiv:1609.04747*, 2016.

[144] N. Ketkar, "Stochastic gradient descent," in *Deep learning with Python*. Springer, 2017, pp. 113–132.

[145] D. P. Kingma and J. Ba, "Adam: A method for stochastic optimization," *arXiv preprint arXiv:1412.6980*, 2014.

[146] Y. LeCun, Y. Bengio, and G. Hinton, "Deep learning," *nature*, vol. 521, no. 7553, pp. 436–444, 2015, iSBN: 1476-4687 Publisher: Nature Publishing Group.

[147] S. Albawi, T. A. Mohammed, and S. Al-Zawi, "Understanding of a convolutional neural network," in *2017 international conference on engineering and technology (ICET)*. Ieee, 2017, pp. 1–6.

[148] L. Alzubaidi, J. Zhang, A. J. Humaidi, A. Al-Dujaili, Y. Duan, O. Al-Shamma, J. Santamaría, M. A. Fadhel, M. Al-Amidie, and L. Farhan, "Review of deep learning: Concepts, CNN architectures, challenges, applications, future directions," *Journal of big Data*, vol. 8, no. 1, pp. 1–74, 2021, iSBN: 2196-1115 Publisher: Springer.

[149] L. R. Medsker and L. C. Jain, "Recurrent neural networks," *Design and Applications*, vol. 5, pp. 64–67, 2001.

[150] I. Goodfellow, J. Pouget-Abadie, M. Mirza, B. Xu, D. Warde-Farley, S. Ozair, A. Courville, and Y. Bengio, "Generative adversarial networks," *Communications of the ACM*, vol. 63, no. 11, pp. 139–144, 2020, iSBN: 0001-0782 Publisher: ACM New York, NY, USA.

[151] B. Laeng, S. Sirois, and G. Gredebäck, "Pupillometry: A window to the preconscious?" *Perspectives on psychological science*, vol. 7, no. 1, pp. 18–27, 2012, iSBN: 1745-6916 Publisher: Sage Publications Sage CA: Los Angeles, CA.

[152] S. Sirois and J. Brisson, "Pupillometry," *Wiley Interdisciplinary Reviews: Cognitive Science*, vol. 5, no. 6, pp. 679–692, 2014, iSBN: 1939-5078 Publisher: Wiley Online Library.

[153] J. B. Jonas, F.-M. Zäch, and G. O. Naumann, "Quantitative pupillometry of relative afferent defects in glaucoma," *Archives of Ophthalmology*, vol. 108, no. 4, pp. 479–480, 1990, iSBN: 0003-9950 Publisher: American Medical Association.

[154] M. C. Ortube, A. Kiderman, Y. Eydelman, F. Yu, N. Aguilar, S. Nusinowitz, and M. B. Gorin, "Comparative regional pupillography as a noninvasive biosensor screening method for diabetic retinopathy," *Investigative ophthalmology & visual science*, vol. 54, no. 1, pp. 9–18, 2013, iSBN: 1552-5783 Publisher: The Association for Research in Vision and Ophthalmology.

[155] M. L. Maynard, A. J. Zele, and B. Feigl, "Melanopsin-mediated post-illumination pupil response in early age-related macular degeneration," *Investigative ophthalmology & visual science*, vol. 56, no. 11, pp. 6906–6913, 2015, iSBN: 1552-5783 Publisher: The Association for Research in Vision and Ophthalmology.

[156] A. Vassilieva, M. H. Olsen, C. Peinkhofer, G. M. Knudsen, and D. Kondziella, "Automated pupillometry to detect command following in neurological patients: a proof-of-concept study," *PeerJ*, vol. 7, p. e6929, 2019, iSBN: 2167-8359 Publisher: PeerJ Inc.

[157] F.-P. Jahns, J. P. Miroz, M. Messerer, R. T. Daniel, F. S. Taccone, P. Eckert, and M. Oddo, "Quantitative pupillometry for the monitoring of intracranial hypertension in patients with severe traumatic brain injury," *Critical care*, vol. 23, no. 1, pp. 1–9, 2019, iSBN: 1364-8535 Publisher: Springer.

[158] D. F. Fotiou, V. Stergiou, D. Tsiptsios, C. Lithari, M. Nakou, and A. Karlovasitou, "Cholinergic deficiency in Alzheimer's and Parkinson's disease: evaluation with pupillometry," *International Journal of Psychophysiology*, vol. 73, no. 2, pp. 143–149, 2009, iSBN: 0167-8760 Publisher: Elsevier.

[159] P. P. Patwari, T. M. Stewart, C. M. Rand, M. S. Carroll, N. L. Kuntz, A. S. Kenny, C. D. Brogadir, and D. E. Weese-Mayer, "Pupillometry in congenital central hypoventilation syndrome (CCHS): quantitative evidence of autonomic nervous system dysregulation," *Pediatric research*, vol. 71, no. 3, pp. 280–285, 2012, iSBN: 1530-0447 Publisher: Nature Publishing Group.

[160] K. S. Chiew and T. S. Braver, "Temporal dynamics of motivation-cognitive control interactions revealed by high-resolution pupillometry," *Frontiers in psychology*, vol. 4, p. 15, 2013, iSBN: 1664-1078 Publisher: Frontiers Media SA.

[161] R. Murillo, C. Crucilla, J. Schmittner, E. Hotchkiss, and W. B. Pickworth, "Pupillometry in the detection of concomitant drug use in opioid-maintained patients," *Methods Find Exp Clin Pharmacol*, vol. 26, no. 4, pp. 271–275, 2004.

[162] M. Bernabei, L. Rovati, L. Peretto, and R. Tinarelli, "A simple portable polychromatic pupillometer for human eye annoyance measurement," in *2014 IEEE International Instrumentation and Measurement Technology Conference (I2MTC) Proceedings*, May 2014, pp. 1207–1211.

[163] P. Drew, R. Sayres, K. Watanabe, and S. Shimojo, "Pupillary response to chromatic flicker," *Experimental Brain Research*, vol. 136, no. 2, pp. 256–262, Jan. 2001. [Online]. Available: https://doi.org/10.1007/s002210000605

[164] I. E. Loewenfeld, "Pupillary changes to age," *Topics in neuro-ophthalmology*, 1979, publisher: William & amp; Wilkins.

[165] A. Kristek, "PHYSIOLOGICAL PUPILLOGRAM OF THE HUMAN EYE.(I. PUPILLARY STATICS)," *Ceskoslovenska oftalmologie*, vol. 21, pp. 28–35, 1965, iSBN: 0009-059X.

[166] D. H. Szczęsna and H. T. Kasprzak, "The modelling of the influence of a corneal geometry on the pupil image of the human eye," *Optik*, vol. 117, no. 7, pp. 341–347, Jul. 2006. [Online]. Available: http://www.sciencedirect.com/science/article/pii/S0030402605002615

[167] L.-K. Huang and M.-J. J. Wang, "Image thresholding by minimizing the measures of fuzziness," *Pattern recognition*, vol. 28, no. 1, pp. 41–51, 1995, iSBN: 0031-3203 Publisher: Elsevier.

[168] R. G. Van Schyndel, A. Z. Tirkel, and C. F. Osborne, "A digital watermark," in *Proceedings of 1st international conference on image processing*, vol. 2. IEEE, 1994, pp. 86–90.

[169] C. H. Morimoto, D. Koons, A. Amir, and M. Flickner, "Pupil detection and tracking using multiple light sources," *Image and vision computing*, vol. 18, no. 4, pp. 331–335, 2000, iSBN: 0262-8856 Publisher: Elsevier.

[170] X. Lin, J. Craig, G. Klette, and R. Klette, "Accurately Measuring the Size of the Pupil of the Eye," CITR, The University of Auckland, New Zealand, Technical Report, 2003. [Online]. Available: https://researchspace.auckland.ac.nz/handle/2292/2840

[171] P. H. Alsbirk, "Primary angle-closure glaucoma. Oculometry, epidemiology, and genetics in a high risk population." *Acta Ophthalmologica. Supplementum*, no. 127, pp. 5–31, 1976, iSBN: 0065-1451.

[172] A. Javed, M. Loutfi, S. Kaye, and M. Batterbury, "Interobserver reliability when using the Van Herick method to measure anterior chamber depth," *Oman Journal of Ophthalmology*, vol. 10, no. 1, p. 9, 2017, publisher: Wolters Kluwer–Medknow Publications.

[173] J. L. Wiggs and L. R. Pasquale, "Genetics of glaucoma," *Human molecular genetics*, vol. 26, no. R1, pp. R21–R27, 2017, iSBN: 0964-6906 Publisher: Oxford University Press.

[174] H. C. Geijssen, *Studies on normal pressure glaucoma*. Kugler Publications, 1991.

[175] R. N. Weinreb, T. Aung, and F. A. Medeiros, "The pathophysiology and treatment of glaucoma: a review," *Jama*, vol. 311, no. 18, pp. 1901–1911, 2014, iSBN: 0098-7484 Publisher: American Medical Association.

[176] Y.-C. Tham, X. Li, T. Y. Wong, H. A. Quigley, T. Aung, and C.-Y. Cheng, "Global prevalence of glaucoma and projections of glaucoma burden through 2040: A systematic review and meta-analysis," *Ophthalmology*, vol. 121, no. 11, pp. 2081–2090, 2014.

[177] C. Wright, M. A. Tawfik, M. Waisbourd, and L. J. Katz, "Primary angle-closure glaucoma: an update," *Acta ophthalmologica*, vol. 94, no. 3, pp. 217–225, 2016, iSBN: 1755-375X Publisher: Wiley Online Library.

[178] Y. G. Oh, S. Minelli, G. L. Spaeth, and W. C. Steinman, "The anterior chamber angle is different in different racial groups: a gonioscopic study," *Eye*, vol. 8, no. 1, pp. 104–108, 1994, iSBN: 1476-5454 Publisher: Nature Publishing Group.

[179] C. A. Bruno and W. L. Alward, "Gonioscopy in primary angle closure glaucoma," in *Seminars in ophthalmology*, vol. 17. Taylor & Francis, 2002, pp. 59–68, issue: 2.

[180] C. J. Pavlin, K. Harasiewicz, M. D. Sherar, and F. S. Foster, "Clinical use of ultrasound biomicroscopy," *Ophthalmology*, vol. 98, no. 3, pp. 287–295, 1991, iSBN: 0161-6420 Publisher: Elsevier.

[181] I. Riva, E. Micheletti, F. Oddone, C. Bruttini, S. Montescani, G. De Angelis, L. Rovati, R. N. Weinreb, and L. Quaranta, "Anterior Chamber Angle Assessment Techniques: A Review," *Journal of Clinical Medicine*, vol. 9, no. 12, p. 3814, Dec. 2020, number: 12 Publisher: Multidisciplinary Digital Publishing Institute. [Online]. Available: https://www.mdpi.com/2077-0383/9/12/3814

[182] W. van Herick, R. N. Shaffer, and A. Schwartz, "Estimation of Width of Angle of Anterior Chamber: Incidence and Significance of the Narrow Angle," *American Journal of Ophthalmology*, vol. 68, no. 4, pp. 626–629, Oct. 1969. [Online]. Available: https://www.sciencedirect.com/science/article/pii/0002939469912410

[183] J. Gispets, G. Cardona, M. Verdú, and N. Tomàs, "Sources of variability of the van Herick technique for anterior angle estimation," *Clinical and Experimental Optometry*, vol. 97, no. 2, pp. 147–151, 2014, _eprint: https://onlinelibrary.wiley.com/doi/pdf/10.1111/cxo.12094. [Online]. Available: https://onlinelibrary.wiley.com/doi/abs/10.1111/cxo.12094

[184] P. L. Dabasia, D. F. Edgar, I. E. Murdoch, and J. G. Lawrenson, "Noncontact screening methods for the detection of narrow anterior chamber angles," *Investigative ophthalmology & visual science*, vol. 56, no. 6, pp. 3929–3935, 2015, iSBN: 1552-5783 Publisher: The Association for Research in Vision and Ophthalmology.

[185] P. J. Foster, J. G. Devereux, P. H. Alsbirk, P. S. Lee, D. Uranchimeg, D. Machin, G. J. Johnson, and J. Baasanhu, "Detection of gonioscopically occludable angles and primary angle closure glaucoma by estimation of limbal chamber depth in Asians: modified grading scheme," *British Journal of Ophthalmology*, vol. 84, no. 2, pp. 186–192, 2000, iSBN: 0007-1161 Publisher: BMJ Publishing Group Ltd.

[186] M. Leung, S. S. O. Kang, J. Turuwhenua, and R. Jacobs, "Effects of illumination and observation angle on the Van Herick procedure," *Clin Exp Optom.*, vol. 95(1), pp. 72–77, Jan 2012.

[187] A. Jindal, J. Myint, D. F. Edgar, W. P. Nolan, and J. G. Lawrenson, "Agreement among optometrists and ophthalmologists in estimating limbal anterior chamber depth using the van Herick method," *Ophthalmic and Physiological Optics*, vol. 35, no. 2, pp. 179–185, 2015, iSBN: 0275-5408 Publisher: Wiley Online Library.

[188] I. S. Ardakani, W. Kongprawechnon, T. Theeramunkong, P. Bunnun, T. Isshiki, and A. Manassakorn, "Parameterization of Limbus Distance in Van Herick method's angle closure glaucoma diagnosis," in *2016 7th International Conference of Information and Communication Technology for Embedded Systems (IC-ICTES)*, Mar. 2016, pp. 7–13.

[189] C. Theeraworn, W. Kongprawechnon, T. Kondo, P. Bunnun, A. Nishihara, and A. Manassakorn, "Automatic screening algorithm for narrow anterior chamber angle and angle-closure glaucoma based on slit-lamp image analysis," *Agriculture and Natural Resources*, vol. 47, no. 6, pp. 940–952, 2013, iSBN: 2452-316X.

[190] "NeurOptics | Measure Pupil Reactivity with NPi-200 Pupillometer." [Online]. Available: https://neuroptics.com/npi-200-pupillometer/

[191] "Microperimetro MP-3." [Online]. Available: https://www.nidek.it/diagnostica/microperimetro-mp-3/

[192] "EyeLink 1000 Plus." [Online]. Available: https://www.sr-research.com/eyelink-1000-plus/

[193] J. Kotani, H. Nakao, I. Yamada, A. Miyawaki, N. Mambo, and Y. Ono, "A Novel Method for Measuring the Pupil Diameter and Pupillary Light Reflex of Healthy Volunteers and Patients With Intracranial Lesions Using a Newly Developed Pupilometer," *Front. Med.*, vol. 0, 2021.

[194] T.-H. Kim and J.-I. Youn, "Development of a Smartphone-based Pupillometer," *Journal of the Optical Society of Korea*, vol. 17, no. 3, pp. 249–254, 2013, publisher: Optical Society of Korea.

[195] A. Mariakakis, J. Baudin, E. Whitmire, V. Mehta, M. A. Banks, A. Law, L. Mcgrath, and S. N. Patel, "PupilScreen: using smartphones to assess traumatic brain injury," *Proceedings of the ACM on Interactive, Mobile, Wearable and Ubiquitous Technologies*, vol. 1, no. 3, pp. 1–27, 2017, iSBN: 2474-9567 Publisher: ACM New York, NY, USA.

[196] "Pupilometer - Apps on Google Play." [Online]. Available: https://play.google.com/store/apps/details?id=com.anesthemr.pupilometer&hl=en_US&gl=US

[197] K. Krafka, A. Khosla, P. Kellnhofer, H. Kannan, S. Bhandarkar, W. Matusik, and A. Torralba, "Eye tracking for everyone," in *Proceedings of the IEEE conference on computer vision and pattern recognition*, 2016, pp. 2176–2184.

[198] A. Kar and P. Corcoran, "A review and analysis of eye-gaze estimation systems, algorithms and performance evaluation methods in consumer platforms," *IEEE Access*, vol. 5, pp. 16 495–16 519, 2017.

[199] H. R. Chennamma and X. Yuan, "A Survey on Eye-Gaze Tracking Techniques," *ArXiv e-prints*, dec 2013.

[200] T. Fedullo, E. Masetti, G. Gibertoni, F. Tramarin, and L. Rovati, "On the Use of an Hyperspectral Imaging Vision Based Measurement System and Machine Learning for Iris Pigmentation Grading," in *2022 IEEE International Instrumentation and Measurement Technology Conference (I2MTC)*, may 2022, pp. 1–6, issn: 2642-2077.

[201] S. Winkler and R. Subramanian, "Overview of Eye tracking Datasets," in *2013 Fifth International Workshop on Quality of Multimedia Experience (QoMEX)*. Ieee, jul 2013, pp. 212–217.

[202] T. Fischer, H. J. Chang, and Y. Demiris, "Rt-gene: Real-time eye gaze estimation in natural environments," in *Proceedings of the European conference on computer vision (ECCV)*, 2018, pp. 334–352.

[203] B. Brousseau, J. Rose, and M. Eizenman, "Hybrid Eye-Tracking on a Smartphone with CNN Feature Extraction and an Infrared 3D Model," *Sensors*, vol. 20, no. 2, p. 543, jan 2020.

[204] H. Rahman, M. U. Ahmed, S. Barua, P. Funk, and S. Begum, "Vision-Based Driver's Cognitive Load Classification Considering Eye Movement Using Machine Learning and Deep Learning," *Sensors*, vol. 21, no. 23, p. 8019, Jan 2021, number: 23 Publisher: Multidisciplinary Digital Publishing Institute. [Online]. Available: https://www.mdpi.com/1424-8220/21/23/8019

[205] I. Vajs, V. Ković, T. Papić, A. M. Savić, and M. M. Janković, "Spatiotemporal Eye-Tracking Feature Set for Improved Recognition of Dyslexic Reading Patterns in Children," *Sensors*, vol. 22, no. 13, p. 4900, Jan 2022, number: 13 Publisher: Multidisciplinary Digital Publishing Institute. [Online]. Available: https://www.mdpi.com/1424-8220/22/13/4900

[206] L. A. Granka, T. Joachims, and G. Gay, "Eye-tracking analysis of user behavior in WWW search," in *Proceedings of the 27th annual international ACM SIGIR conference on Research and development in information retrieval*, ser. Sigir '04. New York, NY, USA: Association for Computing Machinery, jul 2004, pp. 478–479. [Online]. Available: https://doi.org/10.1145/1008992.1009079

[207] M. Agarwal and R. Sivakumar, "Blink: A Fully Automated Unsupervised Algorithm for Eye-Blink Detection in EEG Signals," in *2019 57th Annual Allerton Conference on Communication, Control, and Computing (Allerton)*, sep 2019, pp. 1113–1121.

[208] J. Cech and T. Soukupova, "Real-time eye blink detection using facial landmarks," *Cent. Mach. Perception, Dep. Cybern. Fac. Electr. Eng. Czech Tech. Univ. Prague*, pp. 1–8, 2016.

[209] K. Cortacero, T. Fischer, and Y. Demiris, "Rt-bene: a dataset and baselines for real-time blink estimation in natural environments," in *Proceedings of the IEEE/CVF International Conference on Computer Vision Workshops*, 2019, pp. 0–0.

[210] W. Fuhl, G. Kasneci, and E. Kasneci, "TEyeD: Over 20 million real-world eye images with Pupil, Eyelid, and Iris 2D and 3D Segmentations, 2D and 3D Landmarks, 3D Eyeball, Gaze Vector, and Eye Movement Types," *ArXiv e-prints*, feb 2021.

[211] M. Tonsen, X. Zhang, Y. Sugano, and A. Bulling, "Labelled pupils in the wild: a dataset for studying pupil detection in unconstrained environments," in *Proceedings of the Ninth Biennial ACM Symposium on Eye Tracking Research & Applications*, ser. Etra '16. New York, NY, USA: Association for Computing Machinery, mar 2016, pp. 139–142. [Online]. Available: https://doi.org/10.1145/2857491.2857520

[212] L. Omelina, J. Goga, J. Pavlovicova, M. Oravec, and B. Jansen, "A survey of iris datasets," *Image and Vision Computing*, vol. 108, p. 104109, apr 2021. [Online]. Available: https://www.sciencedirect.com/science/article/pii/S0262885621000147

[213] F. Timm and E. Barth, "Accurate eye centre localisation by means of gradients." *Visapp*, vol. 11, pp. 125–130, 2011.

[214] L. Świrski, A. Bulling, and N. Dodgson, "Robust real-time pupil tracking in highly off-axis images," in *Proceedings of the Symposium on Eye Tracking Research and Applications*, ser. Etra '12. New York, NY, USA: Association for Computing Machinery, mar 2012, pp. 173–176. [Online]. Available: https://doi.org/10.1145/2168556.2168585

[215] S. Chen and C. Liu, "Eye detection using discriminatory Haar features and a new efficient SVM," *Image and Vision Computing*, vol. 33, pp. 68–77, jan 2015.

[216] O. Jesorsky, K. J. Kirchberg, and R. W. Frischholz, "Robust Face Detection Using the Hausdorff Distance," in *Audio- and Video-Based Biometric Person Authentication*, ser. Lecture Notes in Computer Science, J. Bigun and F. Smeraldi, Eds. Berlin, Heidelberg: Springer, 2001, pp. 90–95.

[217] W. Fuhl, T. Santini, G. Kasneci, and E. Kasneci, "PupilNet: Convolutional Neural Networks for Robust Pupil Detection," *ArXiv e-prints*, jan 2016.

[218] F. J. Vera-Olmos, E. Pardo, H. Melero, and N. Malpica, "DeepEye: Deep convolutional network for pupil detection in real environments," *Integrated Computer-Aided Engineering*, vol. 26, no. 1, pp. 85–95, jan 2019.

[219] T. Fedullo, D. Cassanelli, G. Gibertoni, F. Tramarin, L. Quaranta, I. Riva, L. Tanga, F. Oddone, and L. Rovati, "Assessment of a Vision-Based Technique for an Automatic Van Herick Measurement System," *IEEE Transactions on Instrumentation and Measurement*, vol. 71, pp. 1–11, 2022, conference Name: IEEE Transactions on Instrumentation and Measurement.

[220] W. Khan, A. Hussain, K. Kuru, and H. Al-askar, "Pupil Localisation and Eye Centre Estimation Using Machine Learning and Computer Vision," *Sensors*, vol. 20, no. 13, p. 3785, Jan 2020, number: 13 Publisher: Multidisciplinary Digital Publishing Institute. [Online]. Available: https://www.mdpi.com/1424-8220/20/13/3785

[221] "Talking Face Video," jun 2008, [Online; accessed 30. Nov. 2022]. [Online]. Available: https://personalpages.manchester.ac.uk/staff/timothy.f.cootes/data/talking%5Fface/talking%5Fface.html

[222] A. Villanueva, V. Ponz, L. Sesma-Sanchez, M. Ariz, S. Porta, and R. Cabeza, "Hybrid method based on topography for robust detection of iris center and eye corners," *ACM Transactions on Multimedia Computing, Communications, and Applications*, vol. 9, no. 4, pp. 1–20, aug 2013. [Online]. Available: https://dl.acm.org/doi/10.1145/2501643.2501647

[223] A. Kacete, J. Royan, R. Seguier, M. Collobert, and C. Soladie, "Real-time eye pupil localization using Hough regression forest," in *2016 IEEE Winter Conference on Applications of Computer Vision (WACV)*, mar 2016, pp. 1–8.

[224] B. Jin, L. Cruz, and N. Gonçalves, "Pseudo RGB-D Face Recognition," *IEEE Sensors Journal*, vol. 22, no. 22, pp. 21 780–21 794, nov 2022, conference Name: IEEE Sensors Journal.

[225] Q. Zheng, M. Yang, J. Yang, Q. Zhang, and X. Zhang, "Improvement of Generalization Ability of Deep CNN via Implicit Regularization in Two-Stage Training Process," *IEEE Access*, vol. 6, pp. 15 844–15 869, 2018, conference Name: IEEE Access.

[226] "OSRAM TOPLED®, SFH 4253 | OSRAM Opto Semiconductors." [Online]. Available: https://www.osram.com/ecat/TOPLED%C2%AE%20SFH%204253/com/en/class_pim_web_catalog_103489/prd_pim_device_2219747/

[227] Oct 2019, [Online; accessed 1. Mar. 2022]. [Online]. Available: https://docs.rs-online.com/abeb/0900766b815fe30b.pdf

[228] "Fibre Ottiche," Feb 2001, [Online; accessed 27. Dec. 2021]. [Online]. Available: http://www.sunfiberoptic.com/prod01%5FFO.htm

[229] Dr. R. Paschotta, "Numerical Aperture," *RP Photonics*, Dec 2021. [Online]. Available: https://www.rp-photonics.com/numerical%5Faperture.html

[230] "45° AOI, 35.0mm Square, Hot Mirror | Edmund Optics," Dec 2021, [Online; accessed 26. Dec. 2021]. [Online]. Available: https://www.edmundoptics.com/p/45deg-aoi-350mm-square-hot-mirror/19181

[231] D. Couret, D. Boumaza, C. Grisotto, T. Triglia, L. Pellegrini, P. Ocquidant, N. J. Bruder, and L. J. Velly, "Reliability of standard pupillometry practice in neurocritical care: an observational, double-blinded study," *Crit. Care*, vol. 20, 2016.

[232] M. D. Christina L. Master, "Utility of Pupillary Light Reflex Metrics as a Physiologic Biomarker for Adolescent Sport-Related Concussion," *JAMA Ophthalmol.*, vol. 138, no. 11, pp. 1135–1141, nov 2020.

[233] Arduino. Arduino due. [Online]. Available: https://store-usa.arduino.cc/products/arduino-due

[234] *SAM3X8E ARM Cortex-M3 Datasheet*, Atmel, 03 2015. [Online]. Available: https://ww1.microchip.com/downloads/en/devicedoc/atmel-11057-32-bit-cortex-m3-microcontroller-sam3x-sam3a%5Fdatasheet.pdf

[235] *ATmega 2560 Datasheet*, Atmel, 02 2014. [Online]. Available: https://ww1.microchip.com/downloads/en/devicedoc/atmel-2549-8-bit-avr-microcontroller-atmega640-1280-1281-2560-2561%5Fdatasheet.pdf

[236] ON-Semiconductor, *CAT4238: LED Driver, Boost Converter, High Efficiency*. [Online]. Available: https://www.onsemi.com/PowerSolutions/product.do?id=CAT4238

[237] Renesas Electronics, *ISL21080 NanoPower Voltage Reference*. [Online]. Available: https://www.renesas.com/eu/en/www/doc/datasheet/isl21080.pdf

[238] A. Devices, "1-/2-/4-Channel Digital Potentiometers, AD8400/AD8402/AD8403." [Online]. Available: https://www.analog.com/en/products/ad8403.html#product-overview

[239] ON-Semiconductor, "mc33078, MC33079, NCV33078, NCV33079 - Low Noise Dual/Quad Operational Amplifiers," p. 14.

[240] "OpenCV: Introduction." [Online]. Available: https://docs.opencv.org/3.4.5/d1/dfb/intro.html

[241] R. J. Jacobs, I. L. Bailey, and M. A. Bullimore, "Artificial pupils and Maxwellian view," *Appl. Opt.*, vol. 31, no. 19, pp. 3668–3677, Jul 1992.

[242] "45° AOI, 35.0mm Square, Hot Mirror | Edmund Optics." [Online]. Available: https://www.edmundoptics.com/p/45deg-aoi-350mm-square-hot-mirror/19181/

[243] "90° Specialty Mirrors | Edmund Optics." [Online]. Available: https://www.edmundoptics.com/f/90-specialty-mirrors/12623/

[244] "20mm, Protected Gold Coated, N-BK7 90° Specialty Mirror," Mar 2022, [Online; accessed 4. Mar. 2022]. [Online]. Available: https://www.edmundoptics.com/p/20mm-protected-gold-coated-n-bk7-90deg-specialty-mirror/20369

[245] "20.0mm 750 - 1100nm Coated, N-BK7 Right Angle Mirror," Dec 2021, [Online; accessed 26. Dec. 2021]. [Online]. Available: https://www.edmundoptics.com/p/200mm-750-1100nm-coated-n-bk7-right-angle-mirror/29771

[246] N. A. Dodgson, "Variation and extrema of human interpupillary distance," in *Stereoscopic displays and virtual reality systems XI*, vol. 5291. SPIE, 2004, pp. 36–46.

[247] HAMAMATSU, *Photonic Multichannel Spectral Analyzer Model: PMA-11*. [Online]. Available: http://pdf.datasheetcatalog.com/datasheet/hamamatsu/C8147-38.pdf

[248] Hamamatsu. Pma-11 datasheet. [Online]. Available: https://datasheetspdf.com/datasheet/PMA-11.html

[249] M. V. Orna, "Light and Color in Nature and Art, by Samuel J. Williamson and Herman Z. Cummins, John Wiley and Sons, New York, 1983, 488 pp. Price: $30.95," *Color Research & Application*, vol. 10, no. 2, pp. 123–124, 1985. [Online]. Available: https://onlinelibrary.wiley.com/doi/abs/10.1002/col.5080100214

[250] ANSI - American National Standard Insitute, "ANSI Z80.36-2016 - Ophthalmics - Light Hazard Protection for Ophthalmic Instruments," Mar. 2016.

[251] B. En, "62471: 2008," *Photobiological Safety of Lamps and Lamp Systems*, 2008.

[252] J. Wu, S. Seregard, and P. V. Algvere, "Photochemical Damage of the Retina," *Survey of Ophthalmology*, vol. 51, no. 5, pp. 461–481, Sep. 2006. [Online]. Available: http://www.sciencedirect.com/science/article/pii/S003962570600124X

[253] I. Riva, E. Micheletti, F. Oddone, C. Bruttini, S. Montescani, G. De Angelis, L. Rovati, R. N. Weinreb, and L. Quaranta, "Anterior chamber angle assessment techniques: A review," *Journal of Clinical Medicine*, vol. 9, no. 12, p. 3814, Nov 2020.

[254] D. Ferreiro, S. García-Montero, J. Garcia-Queiruga, E. P. Dorrio, and E. Yebra-Pimentel, "Assessment of Van Herick technique by using ImageJ software," in *Fourth International Conference on Applications of Optics and Photonics*. Spie, Oct 2019, vol. 11207, pp. 310–315.

[255] J. Gispets, G. Cardona, M. Verdú, and N. Tomàs, "Sources of variability of the van Herick technique for anterior angle estimation," *Clinical and Experimental Optometry*, vol. 97, no. 2, pp. 147–151, Mar 2014.

[256] P. J. Foster, J. G. Devereux, P. H. Alsbirk, P. S. Lee, D. Uranchimeg, D. Machin, G. J. Johnson, and J. Baasanhu, "Detection of gonioscopically occludable angles and primary angle closure glaucoma by estimation of limbal chamber depth in Asians: modified grading scheme," *Br J Ophthalmol.*, vol. 84 (2), no. 2, pp. 186–192, Feb. 2000.

[257] R. Sihota, N. Kamble, A. K. Sharma, A. Bhari, A. Gupta, N. Midha, H. Selvan, T. Dada, V. Gupta, and R. M. Pandey, "'Van Herick Plus': a modified grading scheme for the assessment of peripheral anterior chamber depth and angle," *British Journal of Ophthalmology*, vol. 103, no. 7, pp. 960–965, 2019, publisher: BMJ Publishing Group Ltd _eprint: https://bjo.bmj.com/content/103/7/960.full.pdf. [Online]. Available: https://bjo.bmj.com/content/103/7/960

[258] C. Theeraworn, W. Kongprawechnon, T. Kondo, P. Bunnun, A. Nishihara, and A. Manassakorn, "Automatic screening of narrow anterior chamber angle and angle-closure glaucoma based on slit-lamp image analysis by using support vector machine," in *2013 35th Annual International Conference of the IEEE Engineering in Medicine and Biology Society (EMBC)*, 2013, pp. 5887–5890.

[259] ——, "Automatic screening algorithm for narrow anterior chamber angle and angle-closure glaucoma based on slit-lamp image analysis," *Kasetsart Journal - Natural Science*, vol. 47, no. 6, p. 940 – 952, 01 2013.

[260] F. Teixeira, D. C. Sousa, I. Leal, A. Barata, C. M. Neves, and L. A. Pinto, "Automated gonioscopy photography for iridocorneal angle grading," *European Journal of Ophthalmology*, vol. 30, no. 1, pp. 112–118, 2020, pmid: 30360660. [Online]. Available: https://doi.org/10.1177/1120672118806436

[261] H. Fu, M. Baskaran, Y. Xu, S. Lin, D. W. K. Wong, J. Liu, T. A. Tun, M. Mahesh, S. A. Perera, and T. Aung, "A Deep Learning System for Automated Angle-Closure Detection in Anterior Segment Optical Coherence Tomography Images," *American Journal of Ophthalmology*, vol. 203, pp. 37–45, 2019. [Online]. Available: https://www.sciencedirect.com/science/article/pii/S000293941930087X

[262] E. Shimizu, H. Yazu, N. Aketa, R. Yokoiwa, S. Sato, J. Yajima, T. Katayama, R. Sato, M. Tanji, Y. Sato, Y. Ogawa, and K. Tsubota, "A Study Validating the Estimation of Anterior Chamber Depth and Iridocorneal Angle with Portable and Non-Portable Slit-Lamp Microscopy," *Sensors*, vol. 21, no. 4, p. 1436, Feb 2021.

[263] M. Khanafer and S. Shirmohammadi, "Applied ai in instrumentation and measurement: The deep learning revolution," *IEEE Instrumentation Measurement Magazine*, vol. 23, no. 6, pp. 10–17, Oct 2020.

[264] G. Lee and H. Fujita, *Deep learning in medical image analysis: challenges and applications*. Springer, 2020, vol. 1213.

[265] J. Zhong, Z. Liu, Z. Han, Y. Han, and W. Zhang, "A cnn-based defect inspection method for catenary split pins in high-speed railway," *IEEE Transactions on Instrumentation and Measurement*, vol. 68, no. 8, pp. 2849–2860, Aug 2019.

[266] M. Venturelli, G. Borghi, R. Vezzani, and R. Cucchiara, "Deep Head Pose Estimation from Depth Data for In-Car Automotive Applications," in *Understanding Human Activities Through 3D Sensors*, ser. Lecture Notes in Computer Science, H. Wannous, P. Pala, M. Daoudi, and F. Flórez-Revuelta, Eds. Cham: Springer International Publishing, 2018, pp. 74–85.

[267] Y. Tong, W. Lu, Y. Yu, and Y. Shen, "Application of machine learning in ophthalmic imaging modalities," *Eye and Vision*, vol. 7, 2020. [Online]. Available: https://doi.org/10.1186/s40662-020-00183-6

[268] A. Krizhevsky, I. Sutskever, and G. Hinton, "Imagenet classification with deep convolutional neural networks," *Neural Information Processing Systems*, vol. 25, 01 2012.

[269] C. Szegedy, W. Liu, Y. Jia, P. Sermanet, S. Reed, D. Anguelov, D. Erhan, V. Vanhoucke, and A. Rabinovich, "Going deeper with convolutions," 2014.

[270] K. He, X. Zhang, S. Ren, and J. Sun, "Deep residual learning for image recognition," 2015.

[271] O. Russakovsky, J. Deng, H. Su, J. Krause, S. Satheesh, S. Ma, Z. Huang, A. Karpathy, A. Khosla, M. Bernstein, A. C. Berg, and L. Fei-Fei, "ImageNet Large Scale Visual Recognition Challenge," *International Journal of Computer Vision (IJCV)*, vol. 115, no. 3, pp. 211–252, 2015.

[272] M. Leung, S. S. O. Kang, J. Turuwhenua, and R. Jacobs, "Effects of illumination and observation angle on the van Herick procedure," *Clinical and Experimental Optometry*, vol. 95, no. 1, pp. 72–77, Jan 2012.

[273] Z. Sheng and A. Lyubarsky, "Optical Engine Reference Design for DLP2010 Digital Micromirror Device," 2017.

[274] "DLP2010EVM-LC DLP® 2010 Light Control Evaluation Module | TI.com." [Online]. Available: https://www.ti.com/tool/DLP2010EVM-LC

[275] G. S. Brindley, "The colour of light of very long wavelength," *The Journal of Physiology*, vol. 130, no. 1, pp. 35–44, Oct. 1955. [Online]. Available: https://www.ncbi.nlm.nih.gov/pmc/articles/PMC1363450/

[276] D. B. JUDD, "Report of U.S. secretariat committee on colorimetry and artificial daylight," *Proceedings of the 12th Session of the CIE, 1951*, vol. 1, p. 11, 1951. [Online]. Available: https://ci.nii.ac.jp/naid/10016149511/

[277] J. J. Vos, "Colorimetric and photometric properties of a 2° fundamental observer," *Color Research & Application*, vol. 3, no. 3, pp. 125–128, 1978. [Online]. Available: https://onlinelibrary.wiley.com/doi/abs/10.1002/col.5080030309

[278] C. CIE, "Commission internationale de l'eclairage proceedings, 1931," *Cambridge University, Cambridge*, 1932.

[279] S. J. Williamson and H. Z. Cummins, "Light and Color in Nature and Art," *Light and Color in Nature and Art, by Samuel J. Williamson, Herman Z. Cummins, pp. 512. ISBN 0-471-08374-7. Wiley-VCH , February 1983.*, Feb. 1983. [Online]. Available: http://adsabs.harvard.edu/abs/1983lcna.book.....W

[280] F. C. Delori, R. H. Webb, and D. H. Sliney, "Maximum permissible exposures for ocular safety (ANSI 2000), with emphasis on ophthalmic devices," *JOSA A*, vol. 24, no. 5, pp. 1250–1265, 2007, iSBN: 1520-8532 Publisher: Optica Publishing Group.

[281] I. 62471, "Photobiological safety of lamps and lamp systems," 2006, publisher: International Electrotechnical Commission Geneva.

[282] OSRAM Opto Semiconductors, "OSRAM OSTAR®Projection Compact LE BA Q6WM."

[283] ——, "OSRAM OSTAR® Projection Cube, LCG H9RM | OSRAM Opto Semiconductors." [Online]. Available: https://www.osram.com/ecat/OSRAM%20OSTAR%C2%AE%20Projection%20Cube%20LCG%20H9RM/com/en/class_pim_web_catalog_103489/global/prd_pim_device_2190826/

[284] G. Bellocchi, Gibertoni, Giovanni, and Rovati, Luigi, "Characterization and performance improvement of a pupillometer prototype for flicker annoyance measurement." Ph.D. dissertation, University of Modena and Reggio Emilia, Nov. 2019. [Online]. Available: https://morethesis.unimore.it/theses/available/etd-10302019-143123/

[285] G. Gibertoni, "Design and realization of a binocular pupillometer for RGB flicker annoyance estimation," Master Degree Thesis, Università di Modena e Reggio emilia, Apr. 2019. [Online]. Available: https://morethesis.unimore.it/theses/available/etd-03172019-233428/

[286] J. Barbur and A. Stockman, "Photopic, mesopic and scotopic vision and changes in visual performance," *Encyclopedia of the Eye*, vol. 3, pp. 323–331, 2010.

[287] S.-i. Tsujimura and Y. Tokuda, "Delayed response of human melanopsin retinal ganglion cells on the pupillary light reflex," *Ophthalmic and Physiological Optics*, vol. 31, no. 5, pp. 469–479, 2011, _eprint: https://onlinelibrary.wiley.com/doi/pdf/10.1111/j.1475-1313.2011.00846.x. [Online]. Available: https://onlinelibrary.wiley.com/doi/abs/10.1111/j.1475-1313.2011.00846.x

[288] N. Link and L. Stark, "Latency of the pupillary response," *IEEE Transactions on Biomedical Engineering*, vol. 35, no. 3, pp. 214–218, Mar. 1988, conference Name: IEEE Transactions on Biomedical Engineering.

[289] A. J. Zele, P. Adhikari, D. Cao, and B. Feigl, "Melanopsin and Cone Photoreceptor Inputs to the Afferent Pupil Light Response," *Frontiers in Neurology*, vol. 0, 2019.

[290] D. S. Joyce, B. Feigl, D. Cao, and A. J. Zele, "Temporal characteristics of melanopsin inputs to the human pupil light reflex," *Vision Research*, vol. 107, pp. 58–66, Feb 2015.

[291] R. S. L. Young and E. Kimura, "Pupillary correlates of light-evoked melanopsin activity in humans," *Vision Research*, vol. 48, no. 7, pp. 862–871, Mar 2008.

[292] H. McAdams, A. Igdalova, M. Spitschan, D. H. Brainard, and G. K. Aguirre, "Pulses of Melanopsin-Directed Contrast Produce Highly Reproducible Pupil Responses That Are Insensitive to a Change in Background Radiance," *Investigative Ophthalmology & Visual Science*, vol. 59, no. 13, pp. 5615–5626, Nov 2018.

[293] I. Perlman, *The Electroretinogram: ERG.* Salt Lake City (UT): University of Utah Health Sciences Center, 1995. [Online]. Available: http://www.ncbi.nlm.nih.gov/books/NBK11554/

[294] J. J. McAnany, J. C. Park, G. A. Fishman, and F. T. Collison, "Full-Field Electroretinography, Pupillometry, and Luminance Thresholds in X-Linked Retinoschisis," *Investigative Ophthalmology & Visual Science*, vol. 61, no. 6, p. 53, Jun. 2020. [Online]. Available: https://doi.org/10.1167/iovs.61.6.53

[295] R. Kardon, "Pupillary light reflex," *Current opinion in ophthalmology*, vol. 6, no. 6, pp. 20–26, Dec. 1995. [Online]. Available: https://doi.org/10.1097/00055735-199512000-00004

[296] P. H. Heller, F. Perry, D. L. Jewett, and J. D. Levine, "Autonomic components of the human pupillary light reflex." *Investigative Ophthalmology & Visual Science*, vol. 31, no. 1, pp. 156–162, Jan. 1990.

[297] O. R. Marmoy and S. Viswanathan, "Clinical electrophysiology of the optic nerve and retinal ganglion cells," *Eye*, vol. 35, no. 9, pp. 2386–2405, Sep. 2021, number: 9 Publisher: Nature Publishing Group. [Online]. Available: https://www.nature.com/articles/s41433-021-01614-x

[298] S. Usui and L. Stark, "A model for nonlinear stochastic behavior of the pupil," *Biological Cybernetics*, vol. 45, no. 1, pp. 13–21, Aug. 1982. [Online]. Available: http://link.springer.com/10.1007/BF00387209

[299] F. Zhang, K. Kurokawa, A. Lassoued, J. A. Crowell, and D. T. Miller, "Cone photoreceptor classification in the living human eye from photostimulation-induced phase dynamics," *Proceedings of the National Academy of Sciences of the United States of America*, vol. 116, no. 16, pp. 7951–7956, Apr. 2019. [Online]. Available: https://www.ncbi.nlm.nih.gov/pmc/articles/PMC6475411/

[300] J. Maguire, N. R. A. Parry, J. Kremers, I. J. Murray, and D. McKeefry, "Human S-cone electroretinograms obtained by silent substitution stimulation," *Josa A*, vol. 35, no. 4, pp. B11–b18, Apr. 2018, publisher: Optica Publishing Group. [Online]. Available: https://opg.optica.org/josaa/abstract.cfm?uri=josaa-35-4-B11

[301] D. A. Thompson, K. Fujinami, I. Perlman, R. Hamilton, and A. G. Robson, "ISCEV extended protocol for the dark-adapted red flash ERG," *Documenta Ophthalmologica*, vol. 136, no. 3, pp. 191–197, Jun. 2018. [Online]. Available: https://doi.org/10.1007/s10633-018-9644-z

[302] X. Fan and G. Yao, "Modeling Transient Pupillary Light Reflex Induced by a Short Light Flash," *IEEE Transactions on Biomedical Engineering*, vol. 58, no. 1, pp. 36–42, Jan. 2011.

[303] K. Yamaji, Y. Hirata, and S. Usui, "A method for monitoring autonomic nervous activity by pupillary flash response," *Systems and Computers in Japan*, vol. 31, no. 4, pp. 22–31, 2000, _eprint: https://onlinelibrary.wiley.com/doi/pdf/10.1002/%28SICI%291520-684X%28200004%2931%3A4%3C22%3A%3AAID-SCJ3%3E3.0.CO%3B2-W. [Online]. Available: https://onlinelibrary.wiley.com/doi/abs/10.1002/%28SICI%291520-684X%28200004%2931%3A4%3C22%3A%3AAID-SCJ3%3E3.0.CO%3B2-W

[304] D. L. McCulloch, M. F. Marmor, M. G. Brigell, R. Hamilton, G. E. Holder, R. Tzekov, and M. Bach, "ISCEV Standard for full-field clinical electroretinography (2015 update)," *Documenta Ophthalmologica*, vol. 130, no. 1, pp. 1–12, Feb. 2015. [Online]. Available: https://doi.org/10.1007/s10633-014-9473-7

[305] J. Maguire, "The Isolation of Human Rod and Cone Photoreceptor Activity combining Electroretinography and Silent Substitution Techniques," Ph.D. dissertation, University of Bradford, 2017. [Online]. Available: https://bradscholars.brad.ac.uk/handle/10454/16833

[306] P. Craven and G. Wahba, "Smoothing noisy data with spline functions," *Numer. Math.*, vol. 31, no. 4, pp. 377–403, Dec. 1978.

[307] N. Drasdo, Y. H. Aldebasi, Z. Chiti, K. E. Mortlock, J. E. Morgan, and R. V. North, "The S-Cone PhNR and Pattern ERG in Primary Open Angle Glaucoma," *Investigative Ophthalmology & Visual Science*, vol. 42, no. 6, pp. 1266–1272, May 2001.

[308] S. Machida, "Clinical Applications of the Photopic Negative Response to Optic Nerve and Retinal Diseases," *Journal of Ophthalmology*, vol. 2012, p. e397178, Oct. 2012, publisher: Hindawi. [Online]. Available: https://www.hindawi.com/journals/joph/2012/397178/

[309] G. Gibertoni, V. D. Pinto, S. Cattini, F. Tramarin, M. Geiser, and L. Rovati, "A simple Maxwellian optical system to investigate the photoreceptors contribution to pupillary light reflex," in *Ophthalmic Technologies XXXII*, vol. 11941. Spie, mar 2022, pp. 52–60. [Online]. Available: https://www.spiedigitallibrary.org/conference-proceedings-of-spie/11941/119410G/A-simple-Maxwellian-optical-system-to-investigate-the-photoreceptors-contribution/10.1117/12.2608129.full

[310] G. Gibertoni, G. Borghi, and L. Rovati, "Vision-Based Eye Image Classification for Ophthalmic Measurement Systems," *Sensors*, vol. 23, no. 1, p. 386, Jan. 2023, number: 1 Publisher: Multidisciplinary Digital Publishing Institute. [Online]. Available: https://www.mdpi.com/1424-8220/23/1/386

[311] T. Fedullo, D. Cassanelli, G. Gibertoni, F. Tramarin, L. Quaranta, I. Riva, L. Tanga, F. Oddone, and L. Rovati, "Assessment of a Vision-Based Technique for an Automatic Van Herick Measurement System," *IEEE Transactions on Instrumentation and Measurement*, vol. 71, pp. 1–11, 2022, conference Name: IEEE Transactions on Instrumentation and Measurement.

[312] D. Cassanelli, T. Fedullo, G. Gibertoni, G. Saporito, M. Ferrazza, F. Oddone, I. Riva, L. Quaranta, F. Tramarin, and L. Rovati, "Training of an artificial intelligence algorithm for automatic detection of the Van Herick grade," in *Ophthalmic Technologies XXXII*, vol. 11941. SPIE, Mar. 2022, pp. 35–41. [Online]. Available: https://www.spiedigitallibrary.org/conference-proceedings-of-spie/11941/119410C/Training-of-an-artificial-intelligence-algorithm-for-automatic-detection-of/10.1117/12.2607610.full

[313] "NI LabVIEW," dec 2022. [Online]. Available: https://www.ni.com/en-us/shop/labview.html

[314] G. Graffieti, G. Borghi, and D. Maltoni, "Continual learning in real-life applications," *IEEE Robotics and Automation Letters*, vol. 7, no. 3, pp. 6195–6202, 2022.

[315] N. Dalal and B. Triggs, "Histograms of oriented gradients for human detection," in *2005 IEEE computer society conference on computer vision and pattern recognition (CVPR'05)*, vol. 1. Ieee, 2005, pp. 886–893.

[316] T. Ojala, M. Pietikäinen, and D. Harwood, "A comparative study of texture measures with classification based on featured distributions," *Pattern recognition*, vol. 29, no. 1, pp. 51–59, 1996.

[317] M. Andriluka, S. Roth, and B. Schiele, "People-tracking-by-detection and people-detection-by-tracking," in *2008 IEEE Conference on computer vision and pattern recognition*. Ieee, 2008, pp. 1–8.

[318] F. Bolelli, G. Borghi, and C. Grana, "Historical handwritten text images word spotting through sliding window hog features," in *International Conference on Image Analysis and Processing*. Springer, 2017, pp. 729–738.

[319] S. Liao, X. Zhu, Z. Lei, L. Zhang, and S. Z. Li, "Learning multi-scale block local binary patterns for face recognition," in *International conference on biometrics*. Springer, 2007, pp. 828–837.

[320] M. A. Hearst, S. T. Dumais, E. Osuna, J. Platt, and B. Scholkopf, "Support vector machines," *IEEE Intelligent Systems and their applications*, vol. 13, no. 4, pp. 18–28, 1998.

[321] M. Riedmiller and A. Lernen, "Multi layer perceptron," *Machine Learning Lab Special Lecture, University of Freiburg*, pp. 7–24, 2014.

[322] S. J. Rigatti, "Random forest," *Journal of Insurance Medicine*, vol. 47, no. 1, pp. 31–39, 2017.

[323] M. Pal and P. M. Mather, "An assessment of the effectiveness of decision tree methods for land cover classification," *Remote sensing of environment*, vol. 86, no. 4, pp. 554–565, 2003.

[324] S. Raschka, "Naive bayes and text classification i-introduction and theory," *arXiv preprint arXiv:1410.5329*, 2014.

[325] L. E. Peterson, "K-nearest neighbor," *Scholarpedia*, vol. 4, no. 2, p. 1883, 2009.

[326] Y. Sun, Z. Liu, S. Todorovic, and J. Li, "Adaptive boosting for sar automatic target recognition," *IEEE Transactions on Aerospace and Electronic Systems*, vol. 43, no. 1, pp. 112–125, 2007.

[327] S. Srivastava, M. R. Gupta, and B. A. Frigyik, "Bayesian quadratic discriminant analysis." *Journal of Machine Learning Research*, vol. 8, no. 6, 2007.

[328] X. Ding, J. Liu, F. Yang, and J. Cao, "Random radial basis function kernel-based support vector machine," *Journal of the Franklin Institute*, vol. 358, no. 18, pp. 10 121–10 140, 2021.

[329] A. F. Agarap, "Deep learning using rectified linear units (relu)," *arXiv preprint arXiv:1803.08375*, 2018.

[330] D. P. Kingma and J. Ba, "Adam: A method for stochastic optimization," *arXiv preprint arXiv:1412.6980*, 2014.

[331] R. I. Lerman and S. Yitzhaki, "A note on the calculation and interpretation of the gini index," *Economics Letters*, vol. 15, no. 3-4, pp. 363–368, 1984.

[332] A. G. Howard, M. Zhu, B. Chen, D. Kalenichenko, W. Wang, T. Weyand, M. Andreetto, and H. Adam, "Mobilenets: Efficient convolutional neural networks for mobile vision applications," *arXiv preprint arXiv:1704.04861*, 2017.

[333] J. Deng, W. Dong, R. Socher, L.-J. Li, K. Li, and L. Fei-Fei, "Imagenet: A large-scale hierarchical image database," in *2009 IEEE conference on computer vision and pattern recognition*. Ieee, 2009, pp. 248–255.

[334] M. Sandler, A. Howard, M. Zhu, A. Zhmoginov, and L.-C. Chen, "Mobilenetv2: Inverted residuals and linear bottlenecks," in *Proceedings of the IEEE conference on computer vision and pattern recognition*, 2018, pp. 4510–4520.

[335] K. He, X. Zhang, S. Ren, and J. Sun, "Deep residual learning for image recognition," in *Proceedings of the IEEE conference on computer vision and pattern recognition*, 2016, pp. 770–778.

[336] C. Szegedy, W. Liu, Y. Jia, P. Sermanet, S. Reed, D. Anguelov, D. Erhan, V. Vanhoucke, and A. Rabinovich, "Going deeper with convolutions," in *Proceedings of the IEEE conference on computer vision and pattern recognition*, 2015, pp. 1–9.

[337] M. Tan and Q. Le, "Efficientnet: Rethinking model scaling for convolutional neural networks," in *International conference on machine learning*. Pmlr, 2019, pp. 6105–6114.

[338] C. Szegedy, V. Vanhoucke, S. Ioffe, J. Shlens, and Z. Wojna, "Rethinking the inception architecture for computer vision," in *Proceedings of the IEEE conference on computer vision and pattern recognition*, 2016, pp. 2818–2826.

[339] M. Abadi, A. Agarwal, P. Barham, E. Brevdo, Z. Chen, C. Citro, G. S. Corrado, A. Davis, J. Dean, M. Devin, S. Ghemawat, I. Goodfellow, A. Harp, G. Irving, M. Isard, Y. Jia, R. Jozefowicz, L. Kaiser, M. Kudlur, J. Levenberg, D. Mané, R. Monga, S. Moore, D. Murray, C. Olah, M. Schuster, J. Shlens, B. Steiner, I. Sutskever, K. Talwar, P. Tucker, V. Vanhoucke, V. Vasudevan, F. Viégas, O. Vinyals, P. Warden, M. Wattenberg, M. Wicke, Y. Yu, and X. Zheng, "TensorFlow: Large-scale machine learning on heterogeneous systems," 2015, software available from tensorflow.org. [Online]. Available: https://www.tensorflow.org/

[340] F. Chollet *et al.*, "Keras," 2015. [Online]. Available: https://github.com/fchollet/keras

[341] E. Antoniou, P. Bozios, V. Christou, K. D. Tzimourta, K. Kalafatakis, M. G. Tsipouras, N. Giannakeas, and A. T. Tzallas, "EEG-Based Eye Movement Recognition Using Brain–Computer Interface and Random Forests," *Sensors*, vol. 21, no. 7, p. 2339, Jan 2021, number: 7 Publisher: Multidisciplinary Digital Publishing Institute. [Online]. Available: https://www.mdpi.com/1424-8220/21/7/2339

[342] T. Fedullo, D. Cassanelli, G. Gibertoni, F. Tramarin, L. Quaranta, G. de Angelis, and L. Rovati, "A Machine Learning Approach for a Vision-Based Van-Herick Measurement System," in *2021 IEEE International Instrumentation and Measurement Technology Conference (I2MTC)*, May 2021, pp. 1–6, iSSN: 2642-2077.

[343] K. Simonyan and A. Zisserman, "Very deep convolutional networks for large-scale image recognition," in *3rd International Conference on Learning Representations, ICLR 2015, San Diego, CA, USA, May 7-9, 2015, Conference Track Proceedings*, Y. Bengio and Y. LeCun, Eds., 2015. [Online]. Available: http://arxiv.org/abs/1409.1556

[344] Y. Wang, Y. Li, Y. Song, and X. Rong, "The influence of the activation function in a convolution neural network model of facial expression recognition," *Applied Sciences*, vol. 10, no. 5, p. 1897, 2020.

[345] D. P. Kingma and J. Ba, "Adam: A method for stochastic optimization," 2017.

[346] B. H. Pui, B. Hayes-Gill, M. Clark, M. Somekh, C. See, J.-F. Piéri, S. Morgan, and A. Ng, "The Design and Characterisation of an Optical VLSI Processor for Real Time Centroid Detection," *Analog Integrated Circuits and Signal Processing*, vol. 32, pp. 67–75, Jul. 2002.

[347] K. K. Chavali, P. M. Furth, and P. R. Surkanti, "A low-voltage, adaptive CMOS centroid image sensor with improved bandwidth," in *2014 IEEE 57th International Midwest Symposium on Circuits and Systems (MWSCAS)*, Aug. 2014, pp. 937–940, issn: 1558-3899.

[348] W. Van Herick, R. N. Shaffer, and A. Schwartz, "Estimation of width of angle of anterior chamber. incidence and significance of the narrow angle. incidence and significance of the narrow angle," *Am J Ophthalmol.*, vol. 68(4), pp. 626–629, Oct 1969.

[349] Newport, *Newport-Optical Power Meter-1918-R*. [Online]. Available: https://neurophysics.ucsd.edu/Manuals/Newport/1918_Power_Meter_User's_Manual.pdf

[350] ——, *Optical Head -918D-UV-OD3R*. [Online]. Available: https://www.newport.com/p/918D-UV-OD3R

[351] M. Spitschan and T. Woelders, "The Method of Silent Substitution for Examining Melanopsin Contributions to Pupil Control," *Frontiers in Neurology*, vol. 9, Nov. 2018. [Online]. Available: https://www.frontiersin.org/article/10.3389/fneur.2018.00941/full

[352] J. Lin, D. Cheng, C. Yao, and Y. Wang, "Retinal projection head-mounted display," *Frontiers of Optoelectronics*, vol. 10, Nov. 2016.

[353] L. Hahn, "Photometric Units," *Retina Anatomy, University of Pennsylvania. viewed June*, 2005.

[354] G. Mischler, "Lighting design glossary," *Retrieved January*, vol. 30, p. 2006, 2004.

[355] L. Halonen and G. Bizjak, "CIE Mesopic photometry – implementation for outdoor lighting," *CIE*, p. 10, 2013.

[356] P. Schlyter, "Radiometry and photometry in astronomy," *Online at http://stjarnhimlen. se/comp/radfaq. html*, vol. 10, 2017. [Online]. Available: http://stjarnhimlen.se/comp/radfaq.html

[357] Philips Lighting Academy, "Basics of light and lighting," 2008. [Online]. Available: http://images.philips.com/is/content/PhilipsConsumer/PDFDownloads/China/ODLI20150914_001-UPD-zh_CN-basics_of_light.pdf

[358] ON-Semiconductor, *mc33078, MC33079, NCV33078, NCV33079 - Low Noise Dual/Quad Operational Amplifiers*.